DEVELOPMENT OF HYBRID-CONSTRUCT BIOPRINTING AND SYNCHROTRON-BASED NON-INVASIVE ASSESSMENT TECHNIQUES FOR CARTILAGE TISSUE ENGINEERING

A Thesis Submitted to the College of
Graduate Studies and Research
In Partial Fulfillment of the Requirements
For the Degree of Doctor of Philosophy
In the Division of Biomedical Engineering
University of Saskatchewan
Saskatoon

By

ZOHREH IZADIFAR

PERMISSION TO USE

In presenting this thesis in partial fulfilment of the requirements for a Postgraduate degree from the University of Saskatchewan, I agree that the Libraries of this University may make it freely available for inspection. I further agree that permission for copying of this thesis in any manner, in whole or in part, for scholarly purposes may be granted by the professor or professors who supervised my thesis work or, in their absence, by the Head of the Department or the Dean of the College in which my thesis work was done. It is understood that any copying or publication or use of this thesis or parts thereof for financial gain shall not be allowed without my written permission. It is also understood that due recognition shall be given to me and to the University of Saskatchewan in any scholarly use which may be made of any material in my thesis.

Requests for permission to copy or to make other use of material in this thesis in whole or part should be addressed to:

Head of the Division of Biomedical Engineering

57 Campus Drive, University of Saskatchewan

Saskatoon, Saskatchewan S7N 5A9

Canada

ABSTRACT

Cartilage tissue engineering has been emerging as a promising therapeutic approach, where engineered constructs or scaffolds are used as temporary supports to promote regeneration of functional cartilage tissue. Hybrid constructs fabricated from cells, hydrogels, and solid polymeric materials show the most potential for their enhanced biological and mechanical properties. However, fabrication of customized hybrid constructs with impregnated cells is still in its infancy and many issues related to their structural integrity and the cell functions need to be addressed by research. Meanwhile, it is noticed that nowadays monitoring the success of tissue engineered constructs must rely on animal models, which have to be sacrificed for subsequent examination based on histological techniques. This becomes a critical issue as tissue engineering advances from animal to human studies, thus raising a great need for non-invasive assessments of engineered constructs *in situ*. To address the aforementioned issues, this research is aimed to (1) develop novel fabrication processes to fabricate hybrid constructs incorporating living cells (hereafter referred as "construct biofabrication") for cartilage tissue regeneration and (2) develop non-invasive monitoring methods based on synchrotron X-ray imaging techniques for examining cartilage tissue constructs *in situ*.

Based on three-dimensional (3D) printing techniques, novel biofabrication processes were developed to create constructs from synthetic polycaprolactone (PCL) polymer framework and cell-impregnated alginate hydrogel, so as to provide both structural and biological properties as desired in cartilage tissue engineering. To ensure the structural integrity of the constructs, the influence of both PCL polymer and alginate was examined, thus forming a basis to prepare materials for subsequent construct biofabrication. To ensure the biological properties, three types of cells, i.e., two primary cell populations from embryonic chick sternum and an established chondrocyte cell line of ATDC5 were chosen to be incorporated in the construct biofabrication.

The biological performance of the cells in the construct were examined along with the influence of the polymer melting temperature on them. The promising results of cell viability and proliferation as well as cartilage matrix production demonstrate that the developed processes are appropriate for fabricating hybrid constructs for cartilage tissue engineering.

To develop non-invasive *in situ* assessment methods for cartilage and other soft tissue engineering applications, synchrotron phase-based X-ray imaging techniques of diffraction enhanced imaging (DEI), analyzer based imaging (ABI), and inline phase contrast imaging (PCI) were investigated, respectively, with samples prepared from pig knees implanted with low density scaffolds. The results from the computed-tomography (CT)-DEI, CT-ABI, and extended-distance CT-PCI showed the scaffold implanted in pig knee cartilage *in situ* with structural properties more clearly than conventional PCI and clinical MRI, thus providing information and means for tracking the success of scaffolds in tissue repair and remodeling. To optimize the methods for live animal and eventually for human patients, strategies with the aim to reduce the radiation dose during the imaging process were developed by reducing the number of CT projections, region of imaging, and imaging resolution. The results of the developed strategies illustrate that effective dose for CT-DEI, CT-ABI, and extended-distance CT-PCI could be reduced to 0.3-10 mSv, comparable to the dose for clinical X-ray scans, without compromising the image quality. Taken together, synchrotron X-ray imaging techniques were illustrated promising for developing non-invasive monitoring methods for examining cartilage tissue constructs in live animals and eventually in human patients.

ACKNOWLEDGMENTS

I would like to express my gratitude to my supervisors, Dr. Daniel Chen and Dr. Dean Chapman, for their research advices and encouraging supports throughout my Ph.D. studies.

I would like to thank the Advisory Committee members, Dr. Assem Hedayat, Dr. Bill Kulyk, and Dr. Ning Zhu, for their valuable comments and suggestions. Also, I appreciate Dr. Brian Eames for his invaluable guidance on the biological experiments of my thesis performed in his lab, Dr. Tuanjie Chang for his great assistance in the biological experiments, and Dr. Ali Honaramooz for his lab facilities and assistance with animal sample preparation for synchrotron imaging experiments. My thanks also go to Doug Bitner, Louis Roth, Rob Peace, and Ning Cao at the College of Engineering for their great technical support. The scientific help from Dr. Sheldon Wiebe, Dr. David Cooper, Dr. Zhouping Wei, Mr. Alain Lalonde, Dr. Stewart Walker, and Glendon Rhoades is also greatly appreciated. In addition, I would like to thank my friends from the Tissue Engineering Research Group (TERG) and Dr. Brian Eames's Laboratory for their kind friendship, encouragements, and helps.

Special thanks are due to the Canadian Light Source (CLS) where I performed all the synchrotron imaging experiments. The CLS is supported by Natural Sciences and Engineering Research Council of Canada (NSERC), CIHR, the National Research Council Canada, the Province of Saskatchewan, Western Economic Diversification Canada, and the University of Saskatchewan. In particular, the dedicated technical support and advices received from Dr. George Beleve and other scientists at the CLS Biomedical Imaging and Therapy Beamline is highly appreciated.

I acknowledge the financial supports from the University of Saskatchewan (through the Dean's Scholarship), Division of Biomedical Engineering (through the Devolved Scholarship),

the Saskatchewan Health Research Foundation (SHRF) (through the research funding to the TERG), and the CIHR-THRUST training program (through the fellowship to me).

Finally, my deep gratitude goes to my family for my dearest parents' constant unconditional love, heartwarming supports and encouragements throughout my life, for my lovely sisters' cheer-ups and always being there for me in hard times, and for my kind brother's priceless motivations.

TABLE OF CONTENTS

LIST OF TABLES

LIST OF FIGURES

CHAPTER 1: INTRODUCTION

1.1 Health challenge of cartilage damage

Osteoarthritis (OA) is the leading cause of joint disability in North America [1,2]; Approximately 4.4 million Canadians aged 15 years and older (more than 10% of the total population) are reported to suffer from OA [2, 3]. Although osteoarthritis can emerge at any time, regardless of age, physical condition or ethnic background, it is most common among seniors aged 75 years and older [4]. The prevalence of OA is observed to be higher among women than men: average women to man ratio of 1.5 [3]. It is expected that due to the aging of the population and the obesity epidemic [1], the number of affected Canadians will increase to approximately 10.4 million by 2040 [3]. Cartilage injuries in weight-bearing articulating joints caused by traumatic and sport-related events are also serious health problems that mainly affect young populations [5]. In addition to causing disability in the joints, cartilage injuries can be the onset for gradual degeneration of the tissue and initiation and progression of OA. OA and traumatic cartilage injuries pose large financial and lifestyle costs to the patients [5]. Significant clinical challenges with management of cartilage defects mainly stem from the limited intrinsic ability of cartilage to regenerate; the lack of vascular supply and sparse amount of cells (chondrocytes) residing in mature cartilage contribute to such limited healing capacity [6]. Although different clinical techniques are currently used for resurfacing the articular cartilage defects to alleviate the pain and restore some of the function, the results are inconsistent and not successful for long-term treatment [7, 8]. This often results in arthroplasty or total joint replacement procedure for end-stage cartilage or joint pathology.

1.2 Cartilage tissue engineering

New techniques that aim to promote regeneration of functional cartilage through different approaches, referred to as tissue engineering (TE) and regenerative medicine, could revolutionize joint treatments over the next decades [7]. The three main elements of the TE approaches are cells, scaffolds and biological-biomechanical signals. Scaffolds are three-dimensional (3D) structures contain characteristics essential for tissue regeneration, and can perform as carriers of cells and/or biological signals (e.g. growth factors, proteins, serum). The emerging TE techniques include categories of cellular and acellular (cell-free), and scaffold-based and

scaffold-free techniques. Clinical results from cell-based techniques that do not use scaffolds, such as autologous chondrocyte implantation, have shown variable results, which can partly be related to the lack of a supportive scaffold to guide and organize tissue matrix synthesis [7]. The major advantages of scaffold-based techniques over scaffold-free approaches include increased control over the geometry and size of the engineered tissue graft with better stability, possibility of *in vitro* culture and tissue synthesis prior to implantation, a less technically challenging procedure during *in situ* implantation, and, most importantly, providing a 3D environment favorable for cellular activities [7, 9].

In scaffold-based approaches, a suitable biomaterial scaffold could be incorporated with cells (primary chondrocytes or undifferentiated stem cells) and/or bioactive molecules (e.g., growth factors) [10, 11] to produce a supportive environment in which the cells can lay down cartilaginous extracellular matrix (ECM) as the foundation for new tissue formation. Cell-free scaffolds are often incorporated with bioactive molecules to encourage infiltration of native cells from the body into the scaffold upon implantation. When cell-based scaffold techniques are used the construct could initiate synthesis of tissue matrix *in vitro* prior to implantation; other cell sources (such as stem cells and allogenic chondrocytes) could be used in case of limited available autologous chondrocytes. In either case, the dynamic interaction of cells, scaffold, and bioactive molecules is believed to be essential in the success of TE approach [12, 13].

A wide range of materials and approaches have been used for developing 3D scaffolds for regenerating cartilage tissue. When cartilage tissue scaffolds are designed, different initial properties are often considered such as scaffold material biocompatibility, degradability, suitability for cellular activities, and mechanical strength. Mechanical characteristics are required to maintain the structural integrity of the scaffold throughout fabrication and handling (*in vitro* and/or during implantation procedure), protect the in-scaffold cells from excessive forces, and withstand the *in vivo* loading environment until the newly regenerated tissue can assume a load-bearing function [14].

1.3 Design and fabrication of cartilage tissue scaffolds

Exceptional biomechanical behavior of articular cartilage is largely attributed to its biphasic composition as well as the complex biochemistry and physical structure of its ECM. Natural articular cartilage is usually described as a biphasic material comprised of a fluid phase

(mainly water); 65-80 % (by weight), and a solid phase (collagen and proteoglycan); 20-35% [15]. The interaction of the liquid and solid phases results in the highly elastic and load absorbing performance of the articular cartilage. Furthermore, mature articular cartilage is organized into four different zones; superficial, middle (or transitional), deep, and calcified zones, from the articulating surface down to the subchondral bone [16]. Cartilage ECM composition and structure, as well as chondrocytes morphology and arrangement, vary through these zones, which results in zonal variation of mechanical properties and functionality against different types of mechanical loadings, e.g. tensile, shear, and compression. To develop more functional tissue scaffolds that can provide conducive environments for cellular activities and cartilage tissue regeneration, some of the natural characteristics of articular cartilage tissue can be incorporated in the structure and/or material composition of the scaffold. For example, biphasic and zonal-structure tissue scaffolds, inspired by natural properties and organization of cartilage tissue, could directly or indirectly introduce stimulations beneficial for formation of more natural-like cartilage tissue substitutes [17]. Successful development of such designed and relatively complicated 3D scaffolds is dependent on employed fabrication methods.

Hydrogels (highly hydrated polymer networks) and solid synthetic polymers are typical materials used for constructing cartilage scaffolds. Hydrogels are easy to be prepared and embedded with chondrocytes, and are able to retain chondrocyte phenotype and morphology through cell impregnation [18, 19]. However, hydrogels have poor mechanical strength, which limits their application to cartilage TE [20]. Polyester-based materials could be used for making scaffolds with superior mechanical characteristics [5, 21], but are less favorable for cellular activities than hydrogels. One approach to develop more functional scaffolds is to recruit both types of materials--hydrogels and solid polymers--in making hybrid constructs with synergistic properties. In such hybrid scaffold, polyester-based solid structure provides a reinforcing skeleton for mechanical strength and hydrogel provides a cell delivery/supportive matrix within the solid framework [21, 22]. By meeting these two essential properties, hydrogel-solid hybrid scaffold emerges as effective strategy for articular cartilage TE through mimicking the biphasic nature and function of the articular cartilage [5]. Successful implementation of such synergistic properties into the tissue scaffold or construct depends on the employed fabrication technique.

Fabrication of scaffold is one of the important factors in the success of cartilage TE as it can influence the scaffold properties including structural architecture, mechanical properties,

biocompatibility, and biological properties [23]. Conventional fabrication methods often rely on prefabrication of the solid framework and then manual perfusion of the hydrogel (with or without cells) into the framework. Such methods result in non-uniform distribution of hydrogel and cells throughout the construct, and do not allow design-based, reproducible fabrication of structurally complex hybrid construct from dissimilar materials of cells, hydrogels, bioactive molecules, and polyester polymers (e.g. constructs with designed cell distribution). The conventional fabrication techniques also demand post-fabrication cell seeding which is inefficient, time consuming, and cumbersome. The aforementioned fabrication issues negatively affect the scaffold function, the quality of regenerated tissue, and clinical translation of the technique due to limited reproducibility at economic cost and speed [24]. Advances in this regard can be achieved by using high-end technologies such as 3D printing for biofabrication of tissue engineering constructs. Computer-controlled, design-based, and multi-material fabrication features of the 3D printing technology can facilitate fabrication of hybrid 3D constructs from cells and multiple scaffold materials (e.g. polyester polymers and hydrogels). The 3D printing can also address the issues of reproducibility and difficulties with making constructs that have customized external geometry and internal architecture.

In order to develop a hybrid 3D printing-based method that can print living cells along with other materials into a construct, hereafter referred to as biofabrication process, parameters of materials processing condition are required to be studied and optimized. Materials printability, physical stability, and processing conditions cytocompatibility are factors that can potentially affect the success of 3D printing hybrid biofabrication. Often fabrication processing conditions that are suitable for accurate printing of polyesters and hydrogels are not cytocompatible or optimally suitable for biological activities of incorporated cells. Organic solvent-dissolved or high temperature-melted polyesters, stiff, high concentration or cross-linked hydrogels are examples of materials conditions suitable for 3D printing of physically and mechanically stable constructs [25]. However, organic solvent-free, low temperature-melted polymers, soft and low concentration hydrogels are more favourable conditions for cell viability, proliferation, and differentiation. Therefore, 3D printing-based hybrid biofabrication processes that maintain both physical and structural integrity as well as cytocompatibility and conducive cellular environment in the construct must be sought. The performance of the optimized biofabrication process must be verified by long-term assessment of cellular activities in the hybrid constructs. It is

noteworthy to mention that cell types from different tissue origins or differentiation phases could have different sensitivity or resistance to 3D printing process and materials conditions. As such, evaluating the biocompatibility of hybrid 3D printing process for incorporating different cell types is also importance to be investigated.

1.4 Non-invasive assessment of cartilage tissue engineering

The success of TE in repairing damaged cartilage tissue has to be verified both *in vitro* and *in vivo*. The functionality of employed strategies must be monitored and assessed at different time points throughout the tissue regeneration in order to understand the TE repair process and further modify and improve the approach for better regeneration results. Different conventional methods, such as histological and molecular biology techniques and microscopy, have long been used for evaluating the structure and biochemical composition of tissue constructs *in vitro*. However, conventional methods have limitations for application to animal *in vivo* studies and human trials. Due to the destructive and invasive procedure involved in the conventional methods, animals of *in vivo* studies have to be sacrificed at different time points during a longitudinal study in order to excise the repaired tissue/constructs for further assessments. With the advances in TE technology and the need for performing more animal model studies and eventually clinical human trials, the conventional assessment methods will not be efficient. As such, new assessment methods are required to be developed to enable longitudinal non-invasive evaluation of cartilage TE repair *in vivo* through a follow-up intermediate assessment on individual animal models. Advanced biomedical imaging techniques can significantly facilitate tissue engineering technology through non-invasive imaging and evaluation methods.

Synchrotron radiation (SR)-based X-ray imaging techniques have shown great promise for non-invasive, quantitative, and qualitative visualization of soft tissues with detailed structural information. Novel X-ray imaging techniques that are based on refraction contrast mechanisms-phase-based imaging- rather than absorption mechanisms have shown promising capabilities for resolving histological and structural details of low density materials such as cartilage [26-29], which is invisible in clinical radiography. Such phase-based X-ray imaging techniques hold promise for non-invasive imaging of low density TE scaffolds and newly formed cartilage tissue *in situ* (in the body). Therefore, new non-invasive assessment methods can be developed based on phase-based imaging techniques to monitor the functionality of tissue scaffolds and new

tissue regeneration dynamically throughout longitudinal *in vivo* studies. By using non-invasive assessment methods, longitudinal *in vivo* studies can be performed more realistically, efficiently, and economically without the need for scarifying a large number of animals. Furthermore, dynamic information on the functionality and degradation of TE scaffolds as well as neocartilage tissue formation and remodeling could be obtained at intermediate time-points throughout the repair process *in situ*. Such information would largely contribute to the improvement and optimization of tissue engineering strategies including the design and material properties of the tissue scaffolds for promoting better repair results.

1.5 Research objectives

This research is aimed to develop 3D hybrid scaffold bioprinting and non-invasive assessment techniques for cartilage tissue engineering applications. Advanced 3D printing technology has the potential for fabricating tissue constructs with advanced properties such as making biphasic (solid-gel) structure with spatially-controlled distribution of cells in the construct. It is hypothesised that a cytocompatible 3D printing-based hybrid biofabrication process, based on co-deposition of melt-polymer and cell-impregnated hydrogel solution, can be developed which enables maintaining of both reproducible physical integrity and biological functionality of the printed hybrid construct. Furthermore, advanced phase-based X-ray imaging techniques have great potential to be investigated and employed for non-invasive assessment of tissue scaffolds and cartilage repair *in situ*. Potentials of such biomedical imaging techniques are needed to be investigated for developing non-invasive methods that can facilitate current longitudinal animal *in vivo* studies as well as follow-up assessments of the future human trials. Therefore, the specific objectives of this thesis are as follow:

1) To develop a 3D printing-based biofabrication process for making reproducible hybrid tissue constructs from cartilage cells, hydrogel, and solid polyester materials,
2) To identify suitable processing conditions of melted polymer and non-cross-linked, low concentration hydrogel for cytocompatible 3D bioprinting of cell-impregnated hybrid constructs with structural integrity and biological functionality,

3) To evaluate the cytocompatibility of the 3D hybrid printing process with different cell types (two primary cell populations and one chondrogenic cell line), and to assess their long term biological activities in the 3D hybrid constructs *in vitro*,
4) To develop non-invasive assessment methods for visualization and characterization of cartilage tissue scaffolds *in situ* using different synchrotron radiation, phase-based X-ray imaging techniques; and
5) To develop low dose non-invasive assessment methods for safe and efficient cartilage tissue engineering applications to future longitudinal animal *in vivo* studies and possible human clinical trials.

1.6 Organization of the dissertation

The dissertation is organized into 6 chapters. In addition to this Introduction (Chapter 1), it includes four manuscripts (Chapters 2, 3, 4, and 5), followed by a final section (Chapter 6) summarizing the Conclusions drawn from this research and suggestions for future studies.

Chapter 2 is a comprehensive literature review on the two main aspects of this research--scaffold design and fabrication techniques for cartilage tissue repair and imaging-based evaluation techniques for cartilage tissue engineering applications. The first section of the literature review focuses on cartilage tissue injuries and clinical treatments, the importance of scaffold design and the effect of scaffold properties on tissue regeneration, cartilage scaffold fabrication techniques, and recent strategic designs of hybrid and zonal scaffolds for cartilage tissue regeneration. The second section of the literature review chapter focuses on the conventional assessment techniques in tissue engineering, major synchrotron phase-based X-ray imaging techniques, and their applications in cartilage tissue engineering.

Chapter 3 describes development of a hybrid 3D printing biofabrication process for making designed hydrogel-solid (alginate-polycaprolactone(PCL)) constructs impregnated with cartilage cells. The thermal effect induced during melted-polymer printing is investigated for identifying the cytocompatible processing condition of PCL polymer. A suitable processing condition is also identified for structurally stable, 3D printing of non-cross-linked, low concentration alginate into the hybrid construct. Long-term biological performance and chondrogenic activities of different cell populations, 3D-printed in the hybrid constructs, are also discussed.

Chapter 4 presents a novel synchrotron-based X-ray imaging technique for visualization and characterization of low density cartilage tissue scaffold implanted *in situ* in the knee joint of an animal model. The explored technique is also compared with clinical gold standard imaging technique of MRI as well as a conventional synchrotron X-ray imaging method.

In **Chapter 5**, three SR phase-based X-ray biomedical imaging techniques of computed tomography (CT)-diffraction enhanced imaging, CT-analyzer-based imaging, and CT-phase-contrast imaging are examined and compared for development of a non-invasive assessment method for cartilage tissue engineering applications. Furthermore, different strategies are investigated in this chapter to optimize the radiation dose and scan time of the developed non-invasive methods for safe and practical applications to future animal *in vivo* studies. Different quantitative and qualitative assessment criteria were developed and used for evaluation and comparison of the low dose imaging strategies. Moreover, the potential of the techniques for other soft tissue imaging and assessments applications such as in rheomotology diagnosis was also discussed.

Chapter 6 presents the conclusions drawn from this research and the suggestions and recommendations for possible future research.

1.7 Contributions of the primary investigator

The manuscripts included in this thesis are co-authored; however it is the mutual understanding of all authors that Zohreh Izadifar, as the first author, is the primary investigator of the research work. The contributions of other authors are greatly appreciated and acknowledged in this thesis.

1.8 References

1. Zhang, Y.; Jordan, J.M. Epidemiology of osteoarthritis. *Clin Geriatr Med* **2010**, 26, 355-369.

2. Public Health Agency of Canada (PHAC), *Life with Arthritis in Canada: A Personal and Public Health Challenge*. 2011.

3. Bombardier, C.; Hawker, G.; Mosher, D., *The Impact of Arthritis in Canada: Today and Over 30 Years*. 2011, Arthritis Alliance of Canada. p. 1-51.

4. The Chief Public Health Officer's Report on the State of Public Health in Canada, *Growing Older – Adding Life to Years*. 2010.

5. Athanasiou, K.A.; Darling, E.M.; Hu, J. Articular cartilage tissue engineering, In *Synthesis Lectures on Tissue Engineering*;Editor^Editors, Eds.; Morgan & Claypool: San Rafael, CA, USA, 2009. pp 182.

6. Haleem, M.A.; Chu, C.R. Advances in Tissue Engineering Techniques for Articular Cartilage Repair. *Oper Tech Orthop* **2010**, 20, 76-89.

7. Makris, E.A.; Gomoll, A.H.; Malizos, K.N.; Hu, J.C.; Athanasiou, K.A. Repair and tissue engineering techniques for articular cartilage. *Nat Rev Rheumatol* **2015**, 11, 21-34.

8. Alford, J.W.; Cole, B.J. Cartilage restoration, part 2: techniques, outcomes, and future directions. *Am J Sports Med* **2005**, 33, 443-460.

9. Caron, M.M.; Emans, P.J.; Coolsen, M.M.; Voss, L.; Surtel, D.A.; Cremers, A.; van Rhijn, L.W.; Welting, T.J. Redifferentiation of dedifferentiated human articular chondrocytes: comparison of 2D and 3D cultures. *Osteoarthritis Cartilage* **2012**, 20, 1170-1178.

10. Lavik, E.; Langer, R. Tissue engineering: current state and perspectives. *Appl Microbiol Biotechnol* **2004**, 65, 1-8.

11. Mikos, A.G.; Herring, S.W.; Ochareon, P.; Elisseeff, J.; Lu, H.H.; Kandel, R.; Schoen, F.J.; Toner, M.; Mooney, D.; Atala, A.; Van Dyke, M.E.; Kaplan, D.; Vunjak-Novakovic, G. Engineering complex tissues. *Tissue Eng* **2006**, 12, 3307-3339.

12. Niklason, L.E.; Langer, R. Prospects for organ and tissue replacement. *JAMA* **2001**, 285, 573-576.

13. Goldberg, M.; Langer, R.; Jia, X. Nanostructured materials for applications in drug delivery and tissue engineering. *J Biomater Sci Polym Ed* **2007**, 18, 241-268.

14. Hutmacher, D.W. Scaffolds in tissue engineering bone and cartilage. *Biomaterials* **2000**, 21, 2529-2543.

15. Guilak, F.; Setton, L.A.; Kraus, V.B. Structure and function of articular cartilage, In *Principles And Practice Of Orthopaedic Sports Medicine*;Editor^Editors, Eds.; Lippincott Williams & Wilkins: Philadelphia, PA, USA, 2000. pp 53-73.

16. Hunziker, E.B.; Michel, M.; Studer, D. Ultrastructure of adult human articular cartilage matrix after cryotechnical processing. *Microsc Res Tech* **1997**, 37, 271-284.

17. Klein, T.J.; Malda, J.; Sah, R.L.; Hutmacher, D.W. Tissue engineering of articular cartilage with biomimetic zones. *Tissue Eng Part B Rev* **2009**, 15, 143-157.

18. Li, W.J.; Laurencin, C.T.; Caterson, E.J.; Tuan, R.S.; Ko, F.K. Electrospun nanofibrous structure: a novel scaffold for tissue engineering. *J Biomed Mater Res* **2002**, 60, 613-621.

19. Sechriest, V.F.; Miao, Y.J.; Niyibizi, C.; Westerhausen-Larson, A.; Matthew, H.W.; Evans, C.H.; Fu, F.H.; Suh, J.K. GAG-augmented polysaccharide hydrogel: a novel biocompatible and biodegradable material to support chondrogenesis. *J Biomed Mater Res* **2000**, 49, 534-541.

20. Reddy, N.; Yang, Y. Potential of plant proteins for medical applications. *Trends Biotechnol* **2011**, 29, 490-498.

21. Moutos, F.T.; Guilak, F. Composite scaffolds for cartilage tissue engineering. *Biorheology* **2008**, 45, 501-512.

22. Chang, C.-H.; Lin, F.-H.; Kuo, T.-F.; Liu, H.-C. Cartilage tissue engineering. *Biomed Eng (Singapore)* **2005**, 17, 61-71.

23. Edwards, S.L.; Mitchell, W.; Matthews, J.B.; Ingham, E.; Russell, S.J. Design of Nonwoven Scaffolds Structures for Tissue Engineering of the Anterior Cruciate Ligament. *Autex Res J* **2004**, 4, 86-94.

24. van Blitterswijk, C., *Tissue Engineering*. 2008, San Diego, USA: Elsevier Academic Press.

25. Otto, I. A.; Melchels, F.P.; Zhao, X.; Randolph, M.A.; Kon, M.; Breugem, C.C.; Malda, J. Auricular reconstruction using biofabrication-based tissue engineering strategies. *Biofabrication* **2015**,7, 032001.

26. Mollenhauer, J.; Aurich, M.E.; Zhong, Z.; Muehleman, C.; Cole, A.A.; Hasnah, M.; Oltulu, O.; Kuettner, K.E.; Margulis, A.; Chapman, L.D. Diffraction-enhanced X-ray imaging of articular cartilage. *Osteoarthritis Cartilage* **2002**, 10, 163-171.

27. Muehleman, C.; Chapman, L.D.; Kuettner, K.E.; Rieff, J.; Mollenhauer, J.A.; Massuda, K.; Zhong, Z. Radiography of rabbit articular cartilage with diffraction-enhanced imaging. *Anat Rec A Discov Mol Cell Evol Biol* **2003**, 272, 392-397.

28. Muehleman, C.; Li, J.; Zhong, Z. Preliminary study on diffraction enhanced radiographic imaging for a canine model of cartilage damage. *Osteoarthritis Cartilage* **2006**, 14, 882-888.

29. Muehleman, C.; Zhong, Z.; Williams, J.M.; Kuettner, K.E.; Aurich, M.; Han, B.; Mollenhauer, J.; Chapman, L.D. Diffraction enhanced X-ray imaging of the articular cartilage of experimental animals In *Annual Meeting Orthopaedic Research Society*. Dallas, TX. USA. 2002.

CHAPTER 2: LITERATURE REVIEW

This chapter provides a literature review on the two main aspects of this thesis: (1) biofabrication of strategically designed tissue scaffolds for cartilage repair, and (2) synchrotron-based X-ray imaging techniques for cartilage tissue engineering assessment applications. The contents of this chapter are divided into two sections, which have been published as "Izadifar Z, Chen X, Kulyk W. (2012) Strategic design and fabrication of engineered scaffolds for articular cartilage repair. *Journal of Functional Biomaterials*. 3(4): 799-838", and published as parts of "Olubamiji AD, Izadifar Z, Chen DX. (2014) Synchrotron imaging techniques for bone and cartilage tissue engineering: potential, current trends, and future directions. *Tissue Engineering Part B Reviews*. 20(5): 503-522". "According to the Copyright Agreement, "the authors retain the right to include the journal article, in full or in part, in a thesis or dissertation". The most recent literature review (2013-2015) on these two aspects of the thesis are provided in the Chapters 3-5.

2.1 STRATEGIC DESIGN AND FABRICATION OF ENGINEERED SCAFFOLDS FOR ARTICULAR CARTILAGE REPAIR

2.1.1 Abstract

Tissue Engineering has raised the hope for the repair of articular cartilage with the help of biocompatible supportive structures, called scaffolds. Over the past two decades, different designs and fabrication techniques have been investigated for developing TE scaffolds suitable for the construction of transplantable artificial cartilage tissue substitutes. Advances in fabrication technologies now enable the strategic design of scaffolds with complex, biomimetic structures and properties. In particular, scaffolds with hybrid and/or biomimetic zonal designs have recently been developed for cartilage tissue engineering applications. This review discusses critical aspects of the design of engineered scaffolds for articular cartilage repair as well as the available advanced fabrication techniques. In addition, recent studies on the design of hybrid and zonal scaffolds for use in cartilage tissue repair are highlighted.

2.1.2 Introduction

Articular cartilage is a specialized tissue that covers the ends of the bones in articulating joints. It provides a low friction, highly elastic surface [1] that can withstand dynamic compressive loads several times body weight [2]. This behavior is attributed to the complex biochemistry and physical structure of the cartilage extracellular matrix (ECM), which is secreted by the chondrocyte cells that reside therein. Unfortunately, the natural healing ability of human articular cartilage is extremely limited, which poses significant clinical challenges for the treatment of joint cartilage defects [3]. These include articular cartilage degeneration resulting from osteoarthritis (OA), a debilitating joint disease that affects ~70% of the population aged 65 years and older [4]. In addition, articular cartilage lesions resulting from traumatic joint injuries in children and young adults are a serious health problem with, at present, no entirely satisfactory clinical management solution [5]. Although some clinical treatments are available for articular cartilage repair [6], their success to date has been limited as they do not result in long-term correction of cartilage pathologies [1].

Tissue engineering (TE) aims to replace damaged articular cartilage with a long-lasting biomanufactured replacement tissue, and holds great promise as an effective treatment for joint repair. Most cartilage tissue engineering strategies incorporate three main components: a suitable biocompatible scaffold, live chondrocytes or multipotent mesenchymal cells capable of developing into chondrocytes, and a combination of appropriate bioactive molecules (e.g., growth factor proteins (GFs)) [7,8]. It is hoped the dynamic interaction of these components will generate a transplantable artificial tissue construct that integrates well with normal articular cartilage and approximates its unique biomechanical properties [9,10]. The TE scaffold is typically a three-dimensional (3-D) structure manufactured from synthetic polymers and/or natural biopolymers to provide temporary mechanical physical and biological support for the embedded chondrocytic cells; this in turn promotes their growth *ex vivo*, maintains their phenotype, and encourages their production of cartilage-specific extracellular matrix components. In addition, the fabricated scaffold exerts control over the shape and volume of the engineered cartilage tissue construct [11–14]. Accordingly, scaffold design and manufacturing techniques are critical elements for successful cartilage tissue engineering.

Because cartilage tissue engineering is aimed at creating artificial constructs for use in joint cartilage repair, this review will begin with a synopsis of relevant features of normal

articular cartilage structure and the pathology of osteoarthritic cartilage breakdown. The main body of this review will focus on critical considerations in the design of scaffolds for cartilage TE and the fabrication techniques currently available. Finally, I discuss recent and promising advances in biomimetic scaffold construction, including the use of hybrid solid polymer/hydrogel scaffolds and zonal scaffolds to manufacture cartilage tissue substitutes that more closely replicate the biomechanical characteristics and stratified organization of natural articular cartilage.

2.1.2.1 Structure and organization of natural articular cartilage

Articular cartilage is a smooth, partially translucent tissue that covers the distal ends of bones in diarthrodial joints of the body, such as the knee and elbow. It provides a deformable, low friction surface that facilitates the movement of articulating bones within the joint and is capable of supporting high dynamic compressive loads. The unique biomechanical properties of articular cartilage are attributable to the composition of its specialized extracellular matrix (ECM), which is the secretory product of its single resident cell type: chondrocytes. Although cartilage ECM contains a plethora of molecular components [5,15], it is primarily comprised of fibrils of *type II collagen* protein together with a cartilage-specific proteoglycan, *aggrecan* (Figure 2.1A). The collagen II fibrils, which account for up to 60% of articular cartilage dry weight [16], provide the tissue with high tensile strength and the ability to withstand shear stresses. In contrast, the aggrecan proteoglycans (which comprise ~35% of cartilage dry weight) confer cartilage tissue with the ability to support high compressive loads. Each individual aggrecan molecule consists of a polypeptide core protein from which extend numerous covalently linked glycosaminoglycan (GAG) side chains, specifically chondroitin sulfate and keratan sulfate polysaccharides. Molecules of *link protein,* which associate with the base of each aggrecan core protein, mediate the attachment of numerous aggrecan monomers to a common long *hyaluronan* polysaccharide chain (Figure 2.1A). This creates huge supramolecular cartilage proteoglycan complexes embedded within the collagen II fibril network. The high negative charge densities of the chondroitin sulfate and keratan sulfate GAG side chains of the entrapped aggrecan complex create an osmotic potential that draws water into the cartilage ECM from the synovial fluid of the joint cavity and other adjacent tissues. Therefore, articular cartilage consists of up to

80% water with respect to total wet weight. Indeed, the fluid phase of articular cartilage is a critical factor for its load-bearing function [16].

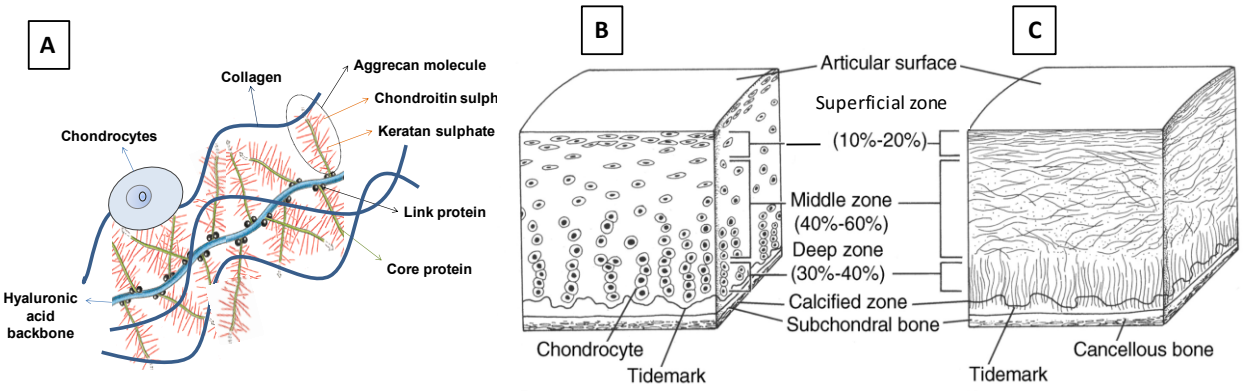

Figure 2.1 Principal components and zonal organization of articular cartilage tissue: (**A**) fibrils of type II collagen, proteoglycan complexes composed of aggrecan and hyaluronan, and chondrocytes cells; (**B**) zonal chondrocytes; and (**C**) zonal collagen fibers. ((**B**) and (**C**) are reproduced from Buckwalter *et al*. [17]).

Natural articular cartilage has a layered or "zonal" organization (Figure 2.1B,C). Its four layers, going from the articular surface down to underlying subchondral bone, are usually termed the *superficial zone*, the *middle (or transitional) zone*, the *deep zone*, and the *calcified zone* [18]. These zones differ with respect to the molecular composition and organization of the cartilage ECM, the shape and density of the resident chondrocytes, and their mechanical properties. The superficial zone, which faces the synovial joint cavity, represents 10%–20% of total articular cartilage thickness. It is characterized by densely packed, tangentially oriented, fine collagen fibrils [19] and a relatively low proteoglycan content [20]. The superficial zone is the layer primarily responsible for bearing tensile and shear stresses [21]. The middle zone (40%–60% of articular cartilage thickness) is characterized by randomly oriented collagen fibrils [18] and the highest proteoglycan content [2], which may contribute to the higher compression modulus in this zone [22] caused by the larger osmotic water swelling effect. The deep zone (30%–40% of articular cartilage thickness) exhibits radially oriented, larger diameter collagen fibers and a lower proteoglycan content than the middle zone [20,23]. The cell density of chondrocytes decreases from the superficial zone to the deep zone, and their morphology changes from a flattened discoidal shape in the superficial zone, to a more spherical shape in the middle zone, to a slightly elongated form in the deep zone [24] (Figure 2.1B). The calcified zone provides a transition between the hyaline cartilage tissue of the overlying zones and the basal *subchondral*

bone [5]. Within the calcified zone, the cartilage ECM is mineralized and type II collagen is replaced by a distinct type X collagen.

2.1.2.2 Cartilage injuries, osteoarthritis (OA), and traditional cartilage repair strategies

Traumatic joint injuries, abnormal joint loading, and degenerative joint diseases can all cause defects in articular cartilage tissue. Unfortunately, cartilage tissue has an extremely limited ability for self repair. This is attributed to its lack of both a vascular supply and any intrinsic mesenchymal stem cell population to facilitate tissue regeneration. Physical trauma to the knee or other articular joints can lead to several types of focal cartilage lesions, which are classified as chondral lesions, osteochondral lesions, and microfractures. Chondral defects solely affect the articular cartilage layer and do not extend to the underlying subchondral bone. In osteochondral lesions, the damage extends through the articular cartilage into the subchondral bone [5]. Microfractures, or fractures in the cartilage that are not visible to the naked eye but affect the collagen network [25], can lead to further matrix destruction upon repeated loading [17]. Because of the inability of articular cartilage to repair itself, the initial focal cartilage damage leads to abnormal compressive loading and increased mechanical stress in the surrounding healthy cartilage, which gradually expands the area of articular damage. Over a period of years, this leads to a gradual erosion of the articular cartilage layer of the joint, resulting in osteoarthritic disease. In the end stages of osteoarthritic disease progression, the articular cartilage is totally destroyed thus exposing the subchondral bone [5]. This results in debilitating joint pain and severely reduced joint mobility. Due to the potential of traumatic joint injuries to initiate osteoarthritic disease progression, and the serious clinical consequences of late stage OA, there is tremendous interest in developing improved therapies for articular cartilage repair.

Nonsurgical treatment of OA includes activity modification, physical therapy, dietary supplements, weight loss, anti-inflammatory drugs (e.g., aspirin, ibuprofen, Celebrex), and injections of viscous hyaluronan preparations into the synovial cavity [5]. These mainly alleviate the pain and discomfort in the arthritic joint without correcting the underlying pathology. Current surgical therapies include arthroscopic microfracture, autologous chondrocyte implantation (ACI) [26], osteotomy, and arthroplasty. In microfracture surgery, damaged cartilage is removed at the site of lesion and the subchondral bone is microfractured to stimulate a healing response from subchondral bone mesenchymal stem cells and growth factors. However, the repair tissue

induced by microfracture treatment is predominantly fibrocartilage that contains more type I collagen than type II collagen and has inferior biomechanical properties to articular cartilage [27]. In ACI, articular chondrocytes isolated from a healthy non-load-bearing region of a patient's joint are expanded in tissue culture and subsequently reimplanted into the site of the cartilage lesion [28]. The tissue formed following ACI can be hyaline articular cartilage (~15% of cases) or fibrocartilage [29,30]. The scarcity of source material, donor site morbidity, and the requirement for multiple invasive surgeries limit the use of ACI [5]. Osteotomy decreases pressure in the defected area by reshaping the bone to shift the mechanical axis of bearing load to the healthier part of the joint. Osteotomy can temporarily restore knee function and decrease osteoarthritic pain, but over the long term often results in joint deterioration and eventual arthroplasty [31]. Arthroplasty, or joint replacement surgery, is the treatment for end-stage OA and involves replacement of the arthritic joint by an artificial prosthesis. Eventual loosening and deterioration of the prosthetic implant, and possible stress shielding effect induced damage to the adjacent bone, are some limitations of arthroplasty surgery. Moreover, arthroplasty is unsuitable for child and adolescent patients whose skeletons are still growing and who require a long-term solution [5]. Indeed, the common problem in most current therapies is their inability to provide long-term relief and resumption of activity [5]. The aim of cartilage tissue engineering is to promote long-lasting, functional repair of defective articular cartilage lesions through the development and *ex vivo* manufacture of implantable artificial cartilage tissue substitutes.

2.1.3 Scaffold design for cartilage tissue engineering

Design of TE scaffolds for cartilage repair generally includes customization of biochemical and physical properties for better engineering of cartilage tissue constructs [32]. Biochemical design concerns chemical composition and biological properties of the scaffold, which mainly affect the cellular behavior and activity. Physical design concerns the internal and external scaffold architecture, mechanical properties, and degradation properties. This review discusses physical design considerations of engineered scaffolds with a brief discussion of the typical backbone materials used for cartilage tissue engineering.

2.1.3.1 Scaffold backbone materials

The scaffold material is one of the main design factors to be considered in scaffold-based cartilage TE. The chosen material should meet several criteria, including biocompatibility, mechanical strength, cell affinity and ability to promote cartilage tissue formation, and adjustable biodegradability. The mechanical properties of the material are particularly important for cartilage TE applications due to the load-bearing nature of the target tissue. More precisely, a scaffold material must maintain its structural integrity and stability during fabrication, clinical handling, and fixation at the implant site [33]. It should also protect the embedded cells from harmful mechanical stresses and withstand the *in vivo* loading environment until the newly formed tissue can assume the load-bearing function. Furthermore, it should provide a desirable environment for biological activities such as cell attachment, proliferation, differentiation, and cell–cell interaction [5,32,33]. Hydrogels (highly hydrated polymer networks) and solid polymers are typical scaffold materials and have been widely investigated for cartilage tissue engineering (Figure 2.2).

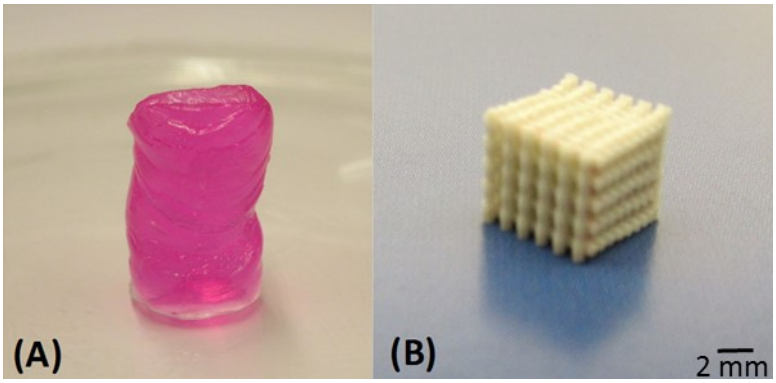

Figure 2.2 Examples of (**A**) hydrogel; and (**B**) solid scaffolds.

Hydrogels are easily prepared and embedded with chondrocytes, which retain their phenotype and morphology through impregnation [34,35]. Hydrogels can be made of a wide variety of biomaterials, including natural materials, which may be carbohydrate-based (e.g., alginate, agarose, chitosan, hyaluronic acid (HA)), protein-based (e.g., fibrin glue, collagen type I and II, silk) [5,28], or some combination of the two, and synthetic materials, such as poly(hydroxyethyl methacrylate), polyethylene glycol and its derivatives, or poly(vinyl alcohol) (PVA) [36]. Hydrogels exhibit characteristics similar to soft tissues and therefore provide a supportive matrix for chondrocyte activity and cartilage ECM secretion both *in vitro* and *in vivo*

[37–40]. High efficiency of cell encapsulation and uniform cell distribution within the hydrogel are advantages that influence the quality of formed tissue. However, hydrogels have very weak mechanical properties that limit their application for cartilage TE [41]; for example, their compression moduli can range from 10% to 20% [42,43] to 50% [44] of natural cartilage values. Limited control over shape and internal structure is another issue that makes architectural design of hydrogel scaffolds difficult. A comprehensive review of hydrogel scaffolds for cartilage TE is given in [45].

Polyester-based solid scaffolds are generally created from biocompatible synthetic materials and have superior biomechanical properties to those based on hydrogels [1,5]. Furthermore, these materials allow easier fabrication of scaffolds with designed shapes and internal architectures. Some frequently used synthetic polymers in cartilage TE include poly (glycolic acid) (PGA), poly(lactic acid) (PLA), poly(lactic-co-glycolic acid) (PLGA), poly-caprolactone (PCL), and poly(ethyl glycol) (PEG), all of which received FDA approval more than 20 years ago. Created by chemical processes, synthetic polymers allow for easier customization of material properties, e.g., mechanical and degradation properties, compared to hydrogel materials. PCL- and PGA-based scaffolds with exactly the same structure exhibit markedly different mechanical properties; for example, the aggregate modulus of a PCL-based scaffold was 0.787 MPa compared to 0.173 MPa for a PGA-based scaffold [46]. Mechanical modulus values of scaffolds made of poly(glycerol sebacate) (PGS) polymer, a newly developed biomaterial, can be increased to the range of native articular cartilage by material modifications that include changing the molar ratios of glycerol:sebacic acid and increasing the polymer curing time [47]. Although their adjustment can improve scaffold mechanical strength, material properties should still allow for gradual hydrolytic attack and degradation of the temporary scaffold [48] and replacement by neocartilage. Although mechanically suitable for cartilage TE, solid synthetic scaffolds have shown less affinity for cell adhesion and activity than hydrogels [28]. Different techniques have been used to improve surface cell adhesion and bioactivity of synthetic polymers, such as blending or copolymerization with hydrophilic/hydrophobic materials including chitosan [49], polymethacrylic acid [50], fibronectin and collagen [51,52], and chondroitin sulfate molecules [36]. A review of polymeric materials for cartilage tissue engineering is given in Puppi *et al*. [53]. Recently, decellularized tissue materials (*i.e*., shattered natural cartilage ECM) have been used to create solid scaffolds for cartilage TE [54–56]; natural

ECM proteins and structures present in the decellularized scaffolds promote good cell affinity and ECM formation.

2.1.3.2 Scaffold physical architecture

As natural cartilage tissue originally develops in a 3D environment, there are distinct advantages of using 3D *vs.* 2D scaffold structures, including better maintenance of chondrocyte morphology and differentiation [48,57] and higher expression of genes that regulate cell activities and ECM production [58,59]. The most commonly used 3D scaffold architectures in cartilage TE are porous 3D sponges and nonwoven fibrous structures (Figure 2.3A,B) [60]. Gradient fibrous structures [61], whose architectural properties vary through the depth of scaffold (Figure 2.3C), and woven architectures [46] (Figure 2.3D) have also been developed for cartilage TE. Different design parameters within these architectures, including pore size and geometry, pore distribution, pore accessibility and tortuosity, and porosity, play significant roles in the morphology, composition, mechanical properties, and functionality of the neocartilage [48,62–64].

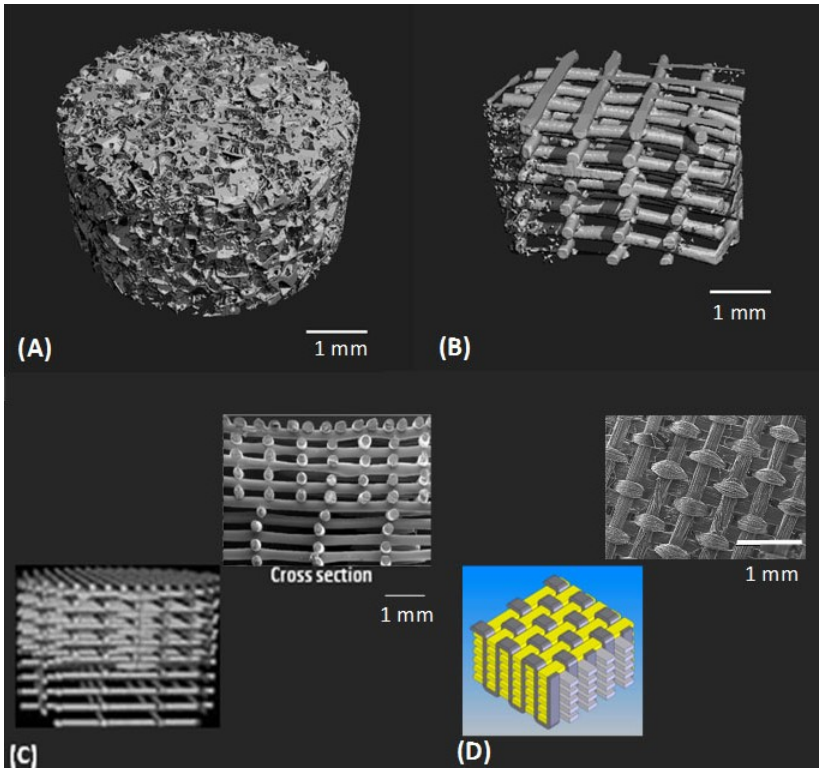

Figure 2.3 Different scaffold structural designs for cartilage tissue engineering: (**A**) 3D sponge [57]; (**B**) fibrous [57]; (**C**) gradient [61]; and (**D**) woven [46].

The influence of scaffold pore size on cartilage formation has been studied [65–67]. The presence of both macro and micropores are important in 3D scaffolds, as macropores (>50 μm) promote cell migration [68] and micropores promote cell–cell interaction and mass transport, which improve tissue formation especially *in vivo* [69]. Titanium alloy constructs with a small average pore size (13 μm) form thicker cartilage tissue with significantly greater proteoglycan and cell density than those with larger pore sizes (43 and 68 μm) [67]. Larger pore sizes (400 μm) in nonwoven fibrous scaffolds cultured with cells result in a significantly larger GAG content compared to constructs with 100 and 200 μm pore sizes [70]. Lien *et al*. [71] show that pore sizes between 250 and 500 μm in scaffolds are appropriate for chondrocyte proliferation and ECM secretion. Cell response and chondrogenesis may vary with pore size and influence different components of tissue formation, such as cell phenotype and activity as well as the amount and composition of ECM; small pore sizes might help maintain chondrocyte phenotypes, as chondrocytes are more likely to differentiate when the pore size is about 30 times the cell diameter (10–15 μm) [72–74]. On the other hand, larger pore sizes increase the extension of ECM. In other words, small pore sizes increase the tendency for cell proliferation, while large pore sizes benefit the formation of ECM [71]. Gradient structures [61] or composite scaffolds (micro to macropore structures [69]) that exhibit a range of pore sizes can better facilitate both chondrocyte activity and secretion of ECM. In addition to pore size, scaffold fiber size affects the cell activity. Relatively large fiber diameters (hundreds of micrometers) in fibrous scaffolds negatively influence cell function because they present as a more two dimensional (2D) attachment surface for individual cells [21]. Chondrocytes seeded on nanofiber meshes show better chondrogenesis than on larger fiber scaffolds [75].

High degrees of porosity and pore interconnectivity are essential factors in the design of scaffolds, because they allow for initial cell or cell–carrier substance impregnation into and through the scaffold, further cell–cell interactions, mass transfer of nutrients and metabolites, and tissue growth [32]. Highly porous substrates provide for more cell attachment (about four times) than less porous substrates and result in more cartilage tissue formation [76]. Although this might be due to a greater chance of nutrient and metabolite transfer in more porous scaffolds, the exact factor(s) responsible for higher cell spreading and ECM production in the highly porous substrate are not known. Practically speaking, there is a compromise between porosity and mechanical properties of the scaffold, where the degree of stiffness tends to decrease as porosity

increases [77]. As a result, scaffolds should be designed to provide an interconnected pore network with enough overall porosity while maintaining sufficient strength and stiffness [69,78]. Sponge scaffold designs generally have higher porosities than fibrous scaffolds [57], although the porosity of fibrous scaffolds can be precisely controlled in the fabrication process [61]. Woven scaffolds have compact structures with low porosity (70% [79]) and limited interconnectivity [21], which may cause inhomogeneous cell seeding and tissue growth as well as reduced nutrition transfer throughout the scaffold [46,80,81]. Gradient structures with varying porosities might allow tailoring of both mechanical and architectural properties with minimal compromise.

Pore interconnectivity can influence the ability of a scaffold to support chondrogenesis as well as the quality of formed tissue, even in scaffolds with similar porosities [57,82]. Interconnected structures with open pores are more capable of facilitating homogeneous cell seeding and better nutrient dispersion throughout the construct [21]. Lack of sufficient pore interconnectivity can cause inhomogeneous chondrogenesis, with cartilage formation only evident on the peripheral boundaries of TE constructs [83,84]. Sponge scaffold architecture is largely controlled by the fabrication process rather than design parameters [85], and thus there is no control over the interconnectivity of the pores. A comparison of 3D sponge and organized fibrous scaffolds shows that the sponge scaffold contains random pores with tortuous paths, a lower average pore size (about five times smaller), and a higher specific area [57]. In addition, sponge architectures have a higher chance of pore blockage (filtration effect) than fibrous architectures. As the diffusion coefficient of a structure is directly proportional to porosity and inversely proportional to tortuosity, diffusion of nutrients is less in sponge structures than organized fibrous structures despite both architectures having similar porosities. This difference may not result in different cartilaginous tissue growth *in vitro* [57]; however, *in vivo* implantation revealed more chondrogenesis in the organized fibrous scaffold that had a denser and more homogeneous structure. These results demonstrate the effect of scaffold architecture as well as the importance of considering differences between *in vitro* and *in vivo* environments when designing scaffolds.

The design of pore distribution using natural cartilage as a model has also been investigated in oriented porous polymer scaffolds [86], fiber-reinforced scaffolds [87], and gradient pore size structures [61]. In the latter study, growth of cartilaginous tissue in fibrous

scaffolds with three different fiber spacings along the length of scaffold (large to small spacing from bottom to top) was investigated for mimicking the zonal structure of natural cartilage. Results indicate that an anisotropic scaffold architecture can promote inhomogeneous tissue formation; however, it cannot produce zonal cartilage matrix similar to natural tissue. Different parameters in the architectural design of a scaffold may not have similar effects on all components of engineered cartilage, and different combinations of these parameters may differently influence cartilage tissue formation. For instance, scaffold architecture and pore size may not influence the formation of collage type II [57,66] and total collagen content [67]. However, chondrocyte proliferation and GAG content are improved in scaffolds with small pore sizes (<20 μm) (more cell–cell interaction) [65]. Thus, it is important to investigate how the various components of scaffold architectural design influence the individual biological properties of the engineered cartilage construct. Table 2.1 summarizes some of the architectural properties of scaffolds, with ranges of associated values for two commonly studied designs (sponge and fibrous) in cartilage TE applications.

In contrast to solid scaffolds, hydrogels do not provide much flexibility for creating structures with defined internal architectures. Few efforts have been able to develop architecturally designed hydrogel scaffolds [88–91] and, therefore, the effect of architectural parameters on chondrogenesis, as has been considered for solid scaffolds, is yet to be determined. However, the significant influence of other hydrogel scaffold design parameters, such as macromere molecular weight and wt % concentration [92,93], as well as the structure of the polymer network (e.g., mesh size) [94–96], on the synthesis and distribution of engineered cartilage ECM has been investigated. Higher wt % concentration of HA hydrogels can better upregulate collagen type II and proteoglycan content [92]. However, the higher density of the hydrogel network impedes the distribution of deposited ECM, which interferes with the mechanical properties of the formed tissue construct [93]. The structure of the hydrogel network, controlled by the polymer chemistry and gelation mechanism [94,96,97] can dictate the spatial distribution of formed ECM by influencing the diffusion of nutrients and the degradation profile. To engineer a functional cartilage tissue construct, a fine balance among these design parameters must be achieved. A review of design aspects for hydrogel scaffolds along with examples of successful hydrogel systems for impregnation of chondrocytes are given in Nicodemus and Bryant [97].

Table 2.1 Typical architectural properties of sponge and fibrous scaffold structures.

Scaffold	Avg. Pore size (μm)	Porosity	Surface area (mm^2/mm^3)	Interconnectivity	Fiber size	References
Sponge	50–500	48%–95%	55.6	<100% (low cut off value*)	--	[37,98–102]
Fibrous	100–1650	48%–87%	16.5	100% (high cut off value)	30–250 μm	[21,34,61,70,
Macro fibers	20–80	84%–90%	--	--	60–100 μm	85,103–106]
Micro/nano fibers						

*cut off value; fraction of total pores that are 100% interconnected.

2.1.3.3 Mechanical properties

The load-bearing nature of the joint environment in which the engineered scaffold/construct will be implanted must be considered when designing the mechanical properties of the scaffold. Design considerations with respect to mechanical strength will depend on whether the scaffold will be used *in vitro* or *in vivo*. If the scaffold will be implanted into an articular joint *in vivo* shortly after fabrication, its mechanical characteristics should ideally match those of natural cartilage to support the loads encountered in the joint. The peak force applied to knee cartilage during normal physiological loading ranges from 1.9 to 7.2 times body weight [107], which corresponds to about 0.84 to 3 MPa for a 70 kg person [108]. If the scaffold is designed to initially promote engineered tissue growth *in vitro* before implantation *in vivo*, it may not require the same level of mechanical strength as natural cartilage. This is because the scaffold will largely act as a supportive environment to help formation of the tissue construct. Rather, the newly formed tissue or neocartilage–scaffold construct (partially developed cartilage) must achieve the required mechanical properties to replace the damaged tissue *in vivo* [5].

In addition to the initial strength of the backbone material, architectural properties can play an important role with respect to the overall mechanical properties of the scaffold. The dynamic stiffness of 3D fibrous scaffolds [57] is higher than 3D sponge scaffolds, and close to that of bovine articular cartilage [85] and human knee cartilage [109], even when both scaffolds are made of exactly the same material. Poly-l-lactide acid (PLLA) sponge scaffolds (300 μm pore sizes and 90% and 95% porosities) and fibrous scaffolds (1 mm pore sizes and 85% porosity) can all exhibit mechanical properties (compression Young's modulus) similar to that of natural cartilage [110].

Mechanical properties of scaffolds are also influenced by the variation of architectural parameters, such as porosity [69,111], pore size [70,111], pore shape [112,113], fiber diameter [1], and fiber spacing [85]. Fibrous scaffolds with different macropore and macro/micropore porosities have varying mechanical properties [69]. El-Ayoubi *et al*. [69] demonstrated the design of scaffold architectures that result in similar mechanical properties to bovine articular cartilage and a good environment for cell attachment and activity. Sponge scaffolds with macropores ranging from 300 to 500 μm have varying mechanical properties, with those of lower porosity best resembling the performance of rabbit articular cartilage in compression and stress relaxation tests [111].

The effect of pore size on the mechanical properties of woven chitosan-HA copolymeric fibrous scaffolds was studied by Yamane *et al*. [70]. Chondrocyte-seeded scaffolds with the smallest pore size (100 μm) had a larger compression modulus than scaffolds with 200 or 400 μm pore sizes. However, after 28 days of cultivation, the scaffolds with the smaller pore sizes had reduced compression moduli while the two others (specifically 400 μm) had increased compression moduli and significantly enhanced ECM production. Thus, the scaffold with the larger pore size presents a better environment for developing a stronger tissue substitute. Increased ECM content can also be accompanied by improved mechanical properties [114,115]. The influence of pore shape on the mechanical properties of cartilage TE scaffolds [112,113] and constructs [113] as well as chondrogenesis [116,117] has also been studied. Chondrocytes produce more robust ECM (higher sulfated GAGs) in the presence of ellipsoidal pores than cubical pores. Jeong and Hollister [113] show that a 3D spherical pore-shaped scaffold enhances chondrogenic activity compared to cubical pore shapes. When the porosity and surface area of the scaffolds were kept similar, increased chondrogenesis in spherical pore-shaped scaffolds was attributed to the lower permeability, subsequent higher cell aggregation and GAG retention, and lower oxygen tension within the scaffold. The significant influence of a pore shape on scaffold mechanical properties (i.e., stiffness and nonlinearity) and *in vivo*-generated cartilage tissue constructs has also been demonstrated [113]. Scaffolds with pore size gradients [61] or oriented structural parameters [46] exhibit associated anisotropic mechanical properties, which can be employed to mimic anisotropic biomechanical properties of natural articular cartilage. These observations demonstrate the importance of simultaneously considering different factors for achieving the most appropriate design for cartilage TE scaffolds.

Hydrogel scaffolds have intrinsically weak mechanical properties for *in situ* placement in cartilage. Although architectural properties, similar to those used for solid scaffold design, may not be used for modifying hydrogel properties, other strategies have been investigated for improving the initial mechanical properties of hydrogels; this includes mixing with other molecules or polymers [118–121], using cross-linking agents [122], and changing macromere chemistry, molecular weight, and polymer concentration [96,121,123]. In the latter two studies, the compression modulus of the scaffolds created ranged from 0.005 to 2.6 MPa, comparable to that of healthy human articular cartilage. However, these modification methods can introduce chemical toxicity and impair nutrient diffusion [124]. Hydrogels with low initial mechanical properties can promote the formation of constructs with high mechanical strength (*i.e.*, compressive and dynamic modulus) compared to hydrogels whose mechanical strength is initially higher [93]. As a result, design considerations for the initial mechanical properties of hydrogels should be balanced with parameters that control the synthesis of tissue ECM.

The design of TE scaffolds for cartilage repair should also consider mechanical compression, tensile, and shear properties to achieve functionality similar to natural cartilage. However, scaffolds in most studies have been designed and tested with respect to one or two mechanical properties at the expense of others. Compression properties have received more attention in scaffold mechanical design than tensile and shear properties. 3D-woven structures made of polymeric biocompatible yarns [46,70] demonstrate considerable improvements in some mechanical properties, such as nonlinear, anisotropic mechanical properties, as well as high tensile strength and stiffness. One potential research area for the mechanical design of scaffolds is the investigation of the optimum architecture for improved mechanical properties. A study of the molecular/cellular structure and organization of the human body's musculoskeletal/cytoskeletal system shows that the specific architectural framework of a structure (e.g., a tensegrity structure) can maximize its strength, flexibility, and structural integrity with minimum employed mass [125]. Such framework architectures could be investigated with respect to TE scaffolds for cartilage applications.

Overall, the design of scaffolds with adequate mechanical strength is challenging. Currently available cartilage TE scaffolds still require mechanical property improvements, as mostly remain inferior to natural human cartilage with respect to supporting the loads at the damaged site. Moreover, excellent mechanical properties of TE scaffolds do not guarantee the growth of cartilage

tissue substitutes with mechanical properties similar to natural cartilage. To date, the mechanical properties of most engineered hyaline cartilage substitutes remain largely inferior to natural cartilage [68,126–129]. For instance, mechanically stimulated agarose disks with seeded cells had an aggregate modulus of 0.1 MPa (0.1–2.0 MPa for natural cartilage) [68], and agarose and chitosan constructs cultivated for 20 days had compression moduli of 0.028 and 0.011 MPa, respectively [130], both of which are lower than values for native cartilage (Table 2.2). Although scaffolds with sufficient mechanical strength can protect the healing site and may indirectly influence the quality of neocartilage, numerous factors should be considered with respect to the regeneration of native-like engineered cartilage in terms of mechanical properties. Furthermore, changes in mechanical properties during *in vitro* culture or after *in situ* implantation are very important considerations for scaffold design. Such changes are closely linked to the degradation rate and profile of the scaffold *in vitro* or *in vivo*. This relationship has been explored to advance designs that consider changes in scaffold mechanical properties in culture or during *in vivo* healing time. Time-dependent mechanical properties have been modeled during degradation based on the change in microstructure and/or material properties of the scaffold [131]. A profile of change in scaffold mechanical properties has also been designed [132] based on a proposed profile of degradation [48]. Consequently, the variation of scaffold mechanical properties while *in vitro* or *in vivo* can be controlled/customized using factors that govern the degradation process. Table 2.2 shows the range of some biomechanical properties for natural human cartilage and cartilage TE constructs. Different mechanical tests (e.g., compression, tensile, and shear tests) have been used to evaluate the mechanical function of TE cartilage scaffolds, constructs, and natural cartilage. These mechanical properties have been described in detail and the associated testing procedures for cartilage TE applications have been comprehensively reviewed in Little *et al*. [133].

Table 2.2 Biomechanical properties of natural human cartilage and cartilage tissue engineering constructs with associated ranges.

Mechanical properties	**Healthy human articular cartilage**	**References**	**Cartilage TE construct**	**References**
Tensile Young's modulus (MPa)	5–25	[134–136]	0.089–400	[34,46,137,138]
Ultimate tensile stress (MPa)	15–35	[139,140]	5.27–85	[34,46,137]
Compression Young's modulus (MPa)	0.24–0.85	[141–143]	0.005–5.9	[46,70,123]
Complex shear modulus (MPa)	0.2–2.0	[144]	0.023–0.11	[46,145]

2.1.3.4 Degradation properties

Scaffold degradation is an important aspect in the design of TE scaffolds as it can affect the formation and/or functionality of new tissue, as well as the response of host tissue [146]. Ideally, the rate of scaffold degradation should be proportional to the rate of tissue formation to ensure sufficient mechanical support at the defect site until the new tissue can fully assume load-bearing function [48]. The implementation of this strategy is practically challenging. The degradation properties of scaffolds depend on and can be modified by variables including biomaterial type and composition [18], surface chemistry [147], scaffold local environment [132], and architecture [148]. These factors can be used in the design of scaffolds to customize their degradation behavior during cartilage tissue growth *in vitro* or *in vivo*. Manipulation of the scaffold material has been a common strategy to control degradation behavior. The degradation behavior of naturally-derived scaffolds is largely influenced by the intrinsic properties of the material, over which there is very limited control. Some strategies used for controlling the degradation rate in naturally derived solid/hydrogel scaffolds include change of material deacetylation degree [5,149], chemistry [150], molecular weight, wt % concentration [151,152], and combination with other polymers [94]. For polymeric scaffolds, strategies such as alteration of polymer/copolymer composition and molecular weight [153,154], crystallinity [155], and incorporation of additives [155] have been undertaken to modify degradation behavior. Local environmental parameters such as temperature and pH are also factors that affect material degradation [155,156] by accelerating/decelerating hydrolysis processes. Mechanical loading (i.e., dynamic loading) also accelerates degradation of scaffolds *in vitro* [157], which is an important factor to be considered with respect to the design of scaffolds for *in vivo* cartilage TE applications.

Architectural properties affect the degradation of polymeric scaffolds [158–160], with scaffolds of higher porosity or smaller pore sizes degrading more slowly than those with lower porosity or larger pore sizes. This is attributed to the greater thickness of pore walls and the associated earlier autocatalysis hydrolysis inside the struts [156], and domination of bulk degradation over surface degradation. Although the exact involvement of each degradation mechanism has not been quantitatively determined, both pore wall thickness (bulk degradation) and surface area (surface degradation) of the scaffold should be considered with respect to scaffold degradation. For hydrogels, the structure of the gel, namely the mesh size of the cross-

linked network, influences the degradation profile [161], with highly cross-linked hydrogels (smaller mesh size) exhibiting longer degradation times. The difference between scaffold degradation behavior in *in vitro* and *in vivo* microenvironments [162–164] indicates the importance of considering the properties of the actual *in vivo* microenvironment (e.g., the presence of enzymes) when strategies for scaffold degradation control are developed for cartilage TE applications.

2.1.4 Fabrication of designed scaffolds

Creation of TE cartilage scaffolds can be as challenging as scaffold design. The fabrication process must generate a scaffold with a reproducible architecture, which can function as designed for a specific period of time in the load-bearing environment of a joint (if implanted shortly after implantation) [32,48]. The choice of manufacturing method can influence different characteristics of the scaffold, including structural architecture, mechanical properties, biocompatibility, and biochemical properties (cell/bioactive agent incorporation) [165].

Current fabrication techniques include solvent casting, particulate leaching, melt molding, phase separation, freeze-drying, and gas foaming [48,58,166]. Some methods, such as freeze-drying, can generate porous scaffolds containing both small (e.g., 15 to 35 μm) and large (>200 μm) pore sizes [167,168]. Using these conventional techniques, scaffold properties can only be controlled by process and equipment parameters rather than design parameters [85]. Thus, scaffold architectural design parameters (e.g., pore size, geometry, interconnectivity, distribution) cannot be precisely controlled or customized. Extensive use of highly toxic solvents and extreme processing conditions (e.g., high temperature, pressure) in most of the current fabrication methods [48] are disadvantages for advanced designs and strategies, such as incorporation of viable cells and bioactive molecules during scaffold fabrication (termed biofabrication) [165]. Detailed information along with the pros and cons associated with these current techniques are summarized by Hutmacher [48] and Sachlos and Czernuszka [169].

Textile technologies, including classical nonwoven textile and electrospinning, are other methods for fabrication of highly porous scaffolds from polymer fibers. Electrospinning methods build scaffolds from micron/submicron fibers that are similar to the size of collagens in the ECM of cartilage [34]. Briefly, the electrospinning process involves creations of an electrically charged jet of polymer that is ejected across a high voltage electric field. The spinning polymer

fibers lay randomly on a grounded collecting screen to create a scaffold. These fine-fiber-based electrospun structures can have better mechanical properties than other fiber-based scaffolds [34,170,171], such as similar tensile properties to human cartilage [171]. Although electrospun scaffolds can have superior stiffness and tensile strength, more studies are required to test their mechanical performance (e.g., compression, shear strength) in both dry and hydrated conditions. Some advantages and limitations of electrospinning techniques that should be considered in designed-based scaffold fabrication are summarized in Table 2.3. In terms of design-based scaffold fabrication, electrospinning has the capacity to create meshes with aligned nanofibers that resemble the anisotropic structure and mechanical properties of cartilage tissue [172–174]. Although electrospinning methods can create oriented fibers, to date the anisotropy of the electrospun fibers is only controllable in one direction; therefore, scaffolds with greater architectural complexity (e.g., gradient structure, spatially controlled properties) cannot be easily created. Focused melt electrospinning has introduced some improvements by enabling deposition of patterned nanofibers [175], which could be advanced to fabrication of 3D scaffolds with more complex, designed structures for cartilage TE. Melt electrospinning has also been successfully tested for direct deposition of nanofibrous polymers onto the cells *in vitro* [176], which has the potential to be improved for biofabrication of scaffolds with incorporated cells and/or bioactive molecules for cartilage TE applications.

Additive manufacturing (AM) techniques, also known as rapid prototyping (RP), is a computer-controlled fabrication technique that enables reproducible fabrication of scaffolds with designed internal and external architecture [32,169]. In brief, the scaffold model, designed or customized (*i.e.*, based on medical images of defect area) by computer-aided design (CAD) software, is physically built layer by layer using selective materials as specified by a computer program [32,48]. Two main categories of AM techniques used for cartilage TE include extrusion-based (e.g., melt/dissolution plotting [57,177,178]) and particle/polymer bonding (e.g., stereolithography [179], selective laser sintering [180]). The main advantages of the AM techniques in strategic TE of cartilage include developing scaffolds with a range of designed mechanical and architectural properties, including copolymer composition, porosity, and pore geometry with high precision [85,181–183]. These capabilities of AM approaches have made strategic study of the cellular response to scaffold architectural design possible [61,184–186]. Some modern AM techniques, such as 3D printing, 3D plotting, sterolithography, and laser-

assisted systems, can be adopted to operate at biocompatible conditions [187], which make them good candidates for biofabrication of scaffolds with incorporated viable cells and/or bioactive molecules. Hydrogel-based scaffolds with designed patterns of encapsulated cells have been fabricated with AM techniques [89–91,188]. Designed patterns of growth factors immobilized to a biomaterial have also been precisely printed using an AM technique (*i.e.*, inkjet printing) to study cellular response to engineered bio-guidance [189]. AM techniques have also been used to integrate nano-/micro-scaled features into scaffolds [69,190]. Microspheres or nanoparticles loaded with bioactive materials have been blended with backbone materials and dispenses by AM to make TE scaffolds [190]. These capabilities are of special interest for strategic cartilage TE because they can provide precise, design-based fabrication in biocompatible processing conditions. AM and indirect AM [191] techniques also have the potential to be integrated with other approaches for developing scaffolds with additional features and functionalities. For example, conventional porogen leaching and advanced AM techniques have been integrated to create scaffolds with both macro- and micro-features [69,192].

3D plotting techniques (Figure 2.4) have become more common in TE [69,193,194] because a wide range of biomaterials (e.g., from polyester polymers to cell-/bioactive-laden hydrogels) can be employed during fabrication [195,196]. This is desirable for developing and studying complex scaffolds that have enhanced mechanical and biological functions for cartilage TE. Some of the important merits and demerits of 3D plotting for designed-based scaffold fabrication are listed in Table 2.3. Although theoretically possible, few studies have investigated the potential for building biomimetic designs and complexities into cartilage TE scaffolds using these fabrication techniques. In particular, the capability of 3D plotters for biofabrication of cartilage TE scaffolds (incorporating cells/bioactive molecules during fabrication) has received limited attention, yet could alleviate the low efficiency, nonuniform cell seeding issue that usually requires the additional step of dynamic seeding or culture [197–199]. Updated reviews of AM systems for TE of scaffolds, along with their detailed advantages and disadvantages, are available in the literature [187,200,201]. Some of the recent strategic designs of scaffolds investigated for cartilage TE using advanced fabrication techniques are reviewed in the following section.

Table 2.3 Merits and demerits of electrospinning and bioplotter fabrication techniques for design-based scaffold fabrication.

Merits and demerits	Electrospinning	Bioplotter-additive manufacturing
Merits	• Fine fibers (25–100 μm), ECM-like structure (good for cellular activities) [34,106] • Use of minimum amount of material [202], minimizing material–cell/tissue interaction [171] • Potential biofabrication capacity [106,203] • Capable of incorporating multiple polymers [204,205]	• Reproducible fabrication [69,209] • Computer controlled • Building of designed, specified structures; patient-specific grafts [169,209] • Processing the widest range of biomaterials: hydrogels to polymer melts and hard substances [85,196] • Design-based biofabrication capacity [195]
Demerits	• Densely packed structure, small pore size, nonuniform cell infiltration/tissue formation [206,207] • Need of postfabrication process, e.g., direct perfusion [105] and dynamic culturing [173,208] • Limited design-based architectural/properties	• Limited at high spatial resolution [69,192]

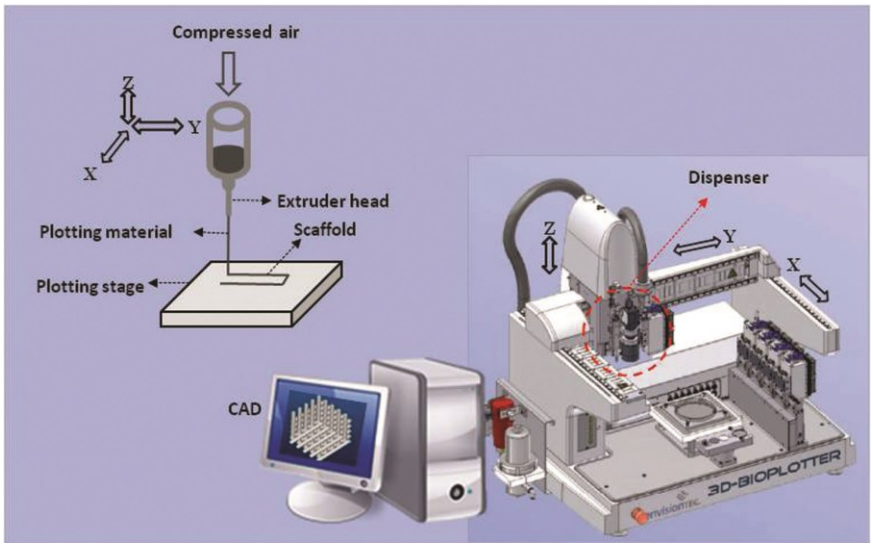

Figure 2.4 Schematic diagram of a 3D plotter additive manufacturing fabrication technique (Image courtesy of Envisiontec GmbH [210]).

2.1.5 Strategic scaffold designs for cartilage tissue engineering

Recent efforts have been directed toward developing more functional, biomimetic scaffolds using designed structures, combined strategies, advanced fabrication techniques, and/or novel

methodologies. This review focuses on the two strategies of hybrid and zonal TE scaffolds for cartilage repair.

2.1.5.1 Hybrid scaffolds

Hydrogel and solid polymer backbone materials have advantages and disadvantages with respect to cartilage TE. However, the use of both materials in hybrid scaffolds can result in unique synergistic properties for better engineering of cartilage. In such hybrid designs, the polyester solid material provides a reinforcing skeleton for mechanical strength and the hydrogel provides a cell supportive/delivery matrix within the scaffold [1,28]. Composed of two essential components, hydrogel–solid hybrid scaffolds resemble the biphasic nature of articular cartilage (water and solid phases) and might be an effective strategy for TE cartilage repair. The superiority of hybrid scaffold over hydrogel- or solid-only scaffolds for cartilage TE has been demonstrated. Some reported advantages of hydrogels within solid scaffolds include retaining cells in the 3D, cell-friendly environment of the hydrogel, even distribution of cells in the solid scaffold pores, preventing cells from floating out of the scaffold, confining growth factors within the scaffold for better interaction with cells [211], and retaining the initial geometry (shape) of the scaffold. Synthetic PLGA mesh has been combined with chondrocyte-embedded fibrin glue to both preserve cell phenotype and provide controllable scaffold degradation properties [212]. The accumulation of GAGs after four weeks was 2.6 times more than in a pure PLGA scaffold [5]. Composite PLGA/cell-embedded alginate scaffolds enhanced expression of collagen type II [213]. An *in vivo* study of a cell-seeded collagen (type I)/PLGA scaffold showed homogeneous distribution of morphologically stable (round shape) cells and collagen type II formation [214]. Other similar examples in cartilage repair include combinations of PGA/alginate [215], PLA/alginate [216], PLGA/HA [217], and PLGA/fibrin [162,218].

Different approaches and designs have been investigated for creating hybrid scaffolds. Here, the most recent different designs for hybrid scaffolds in cartilage TE are reviewed. Infiltration of hydrogels into solid scaffolds has been very popular in cartilage TE. In brief, the method takes a solid scaffold framework and then loads it with hydrogel, which may or may not contain cells and/or bioactive molecules. The base solid framework is typically fiber/textile [87,112,212], sponge [162,211,216,218], or rapid prototyped structures [219]. The hydrogel loading procedure may be as simple as dropping the hydrogel cell suspension onto the solid

scaffold and then molding the hybrid scaffold, or just seeding the solid scaffold with a hydrogel cell suspension [220]. Jung *et al*. [220] hybridized a synthetic poly (L-lactide-co-ε-caprolactone) (PLCL) polymer with chondrocyte-embedded fibrin gels (FG) and hyaluronan (HA) hydrogel. The porous solid framework was created by press-molding, salt leaching, and then freeze-drying of the PLCL-NaCl mixture. The chondrocyte-hydrogel suspensions were incubated in the PLCL scaffolds quickly after preparation. The solid PLCL framework (85% porosity and 300–500 μm pore size) possessed rubber-like elasticity, which could deliver stimulating mechanical signals to the cells. The round cellular morphology of the chondrocytes was properly retained in the inoculated hydrogels. Hybrid scaffolds made with higher viscosity hydrogels (*i.e.*, FG and HA) exhibited the highest cell adhesion efficiency among other created hybrid scaffolds. Overall, these observations indicate how the design of hydrogel properties can affect the scaffold biofunctionality. An eight-week *in vivo* study showed formation of a well-developed, homogeneously distributed cartilage construct that had comparable compression properties (0.57–0.77 MPa) to natural articular cartilage (Table 2.2) [220]; the fabrication method used did not allow any design-based control over the structural organization of the formed tissue, and ECM formed in the randomly distributed pores of the PLCL scaffold [220] (Figure 2.5A).

Vacuum-assisted infusion of hydrogel/cell–hydrogel biomaterials is another approach that provides uniform infiltration of hydrogels into solid scaffolds (*i.e.*, dense structures) [46]. Moutos [46] hybridized an agarose/fibrin hydrogel with 3D woven PCL or PGA scaffolds (porosity of 70%~75%) using a vacuum-based infusion technique (Figure 2.5B). The design of a woven reinforcing component significantly improved the initial mechanical properties (tensile and compression) of the hybrid scaffold to within the range of natural articular cartilage. The structural design of the hybrid scaffold provided biomimetic mechanical properties including anisotropy, viscoelasticity, and tension-compression nonlinearity. The hydrogel component was observed to improve viscoelastic creep behavior and stiffness. However, the highly intense design of the solid framework resulted in the accumulation of ECM around the perimeter of the hybrid scaffold (Figure 2.5B) and lower mechanical properties in the engineered construct [46].

Tanaka *et al*. [110] systematically studied the effect of design (architecture and composition) on the functionality of atelocollagen/synthetic polymer hybrid scaffolds. Two groups of sponge and nonwoven fibrous poly-L-lactide acid (PLLA) scaffolds were fabricated, with each design created at different pore sizes and porosities (Figure 2.5C). Chondrocyte-

embedded atelocollagen was injected into the porous solid scaffolds, incubated for gelation, and then the scaffolds subcutaneously implanted *in vivo*. Retention of the cell–atelocollagen mixture was highest in the scaffolds with the highest pore sizes and porosities. Sponge scaffolds show higher retention of the hydrogel than fibrous scaffolds, mainly due to their generally higher porosity, at 90%–95% compared to 85%–90%. The hybrid scaffold designs that demonstrated superior accumulation of collagen type II and GAGs include sponge-based scaffolds, with a pore size of 0.3 mm and porosity of 95%, and fibrous-based scaffolds, with a pore size of 1.5 mm and porosity of 88%. Collagen type I was generally higher in fibrous-reinforced *vs.* sponge-reinforced constructs. Accumulation of macrophages was also observed on and around the polymeric part of the hybrid scaffolds [110]. Unfortunately, the mechanical properties of the hybrid scaffolds and TE constructs were not investigated despite this information being of great value for cartilage TE applications. One limitation of fibrous-reinforced scaffolds is the large fiber size (smallest achievable diameter of 1 mm), which inhibits fabrication of scaffolds with higher porosities and consequently inhibits formation of larger tissue volumes. Advanced AM fabrication techniques can address this issue through higher achievable resolutions [110].

Kawazoe *et al*. [221] developed a PLGA-collagen hybrid scaffold for cartilage repair that was specifically designed to prevent the cells from leaking out of the scaffold during seeding. The design included a bilayered, cup-shaped mesh membrane of PLGA filled with collagen sponge (freeze-dried collagen) (Figure 2.5D). Knitted and woven PLGA meshes, with big and small interstices, respectively, were glued to each other to maintain the 3D structure of the collagen (to prevent shrinking) and protect against cell leakage. The developed hybrid scaffold had comparable mechanical properties (e.g., compression Young's modulus) to articular cartilage and was successful in preventing cell leakage, having a cell seeding efficiency four times higher than a nonhybrid scaffold. This and similar hybrid scaffold designs [114,222,223] still require postfabrication cell seeding, which may involve noncontrollable/-reproducible cell infiltration and distribution.

Dai *et al*. [214] developed three designs of hybrid PLGA-collagen scaffolds for cartilage TE: a knitted PLGA mesh with collagen sponge in its interstices (called THIN), a knitted PLGA mesh with 3 mm collagen sponge on one side (called SEMI), and a knitted PLGA mesh with 3mm collagen sponge on both sides (called SANDWICH) (Figure 2.5E). Scaffolds were seeded with chondrocytes after fabrication and transplanted *in vivo*. Cell seeding efficiencies were

higher in SEMI and SANDWICH designs than the THIN design. Two to eight weeks after transplantation, cartilage-like tissues that formed in SEMI and SANDWICH designs were thicker and higher in GAGs and collagen type II than in the THIN design. The maximum achieved Young's modulus and stiffness was associated with the SEMI design; 54.8% and 68.8%, respectively, of that of natural cartilage [214]. This indicates how the initial design of the hybrid scaffold can affect the mechanical properties of the engineered construct. No significant difference was reported between the mechanical and biochemical properties of the constructs formed by SEMI and SANDWICH designs.

Comparison of the appearance of the tissue formed in different hybrid scaffold designs (Figure 2.5) shows the influence of scaffold design on the structural organization of formed tissue. Despite the number of hybrid scaffolds tested for cartilage TE, few studies have investigated the development of hybrid scaffolds with reproducible solid and hydrogel components throughout the scaffold. More specifically, the customized spatial distribution of hydrogels and/or cells and varying the composition of hydrogels throughout hybrid scaffolds, have not yet been investigated for cartilage TE.

Recently, hybrid scaffolds with controlled spatial distribution of hydrogels and solid polymers have been developed using advances in fabrication techniques. Although these studies were not specifically aimed at cartilage TE, they shed light into potential advances that could be achieved in cartilage TE. Lee *et al*. [225] combined AM and electrospinning fabrication techniques to develop hybrid scaffolds from PCL and collagen biomaterials. Melted PCL was plotted in two layers of perpendicular strands and then collagen nanofibers electrospun on top of the PCL strands. This pattern was repeated to make a 3D hybrid scaffold (Figure2.6A), which was later seeded with cells. This hybrid scaffold showed better mechanical properties (tensile Young's modulus) and biological activity than a pure PCL scaffold. Although not tested by Lee *et al*. [225], electrospinning could be used to incorporate viable cells during fabrication [203] and, therefore, achieve the design of a biological hybrid scaffold.

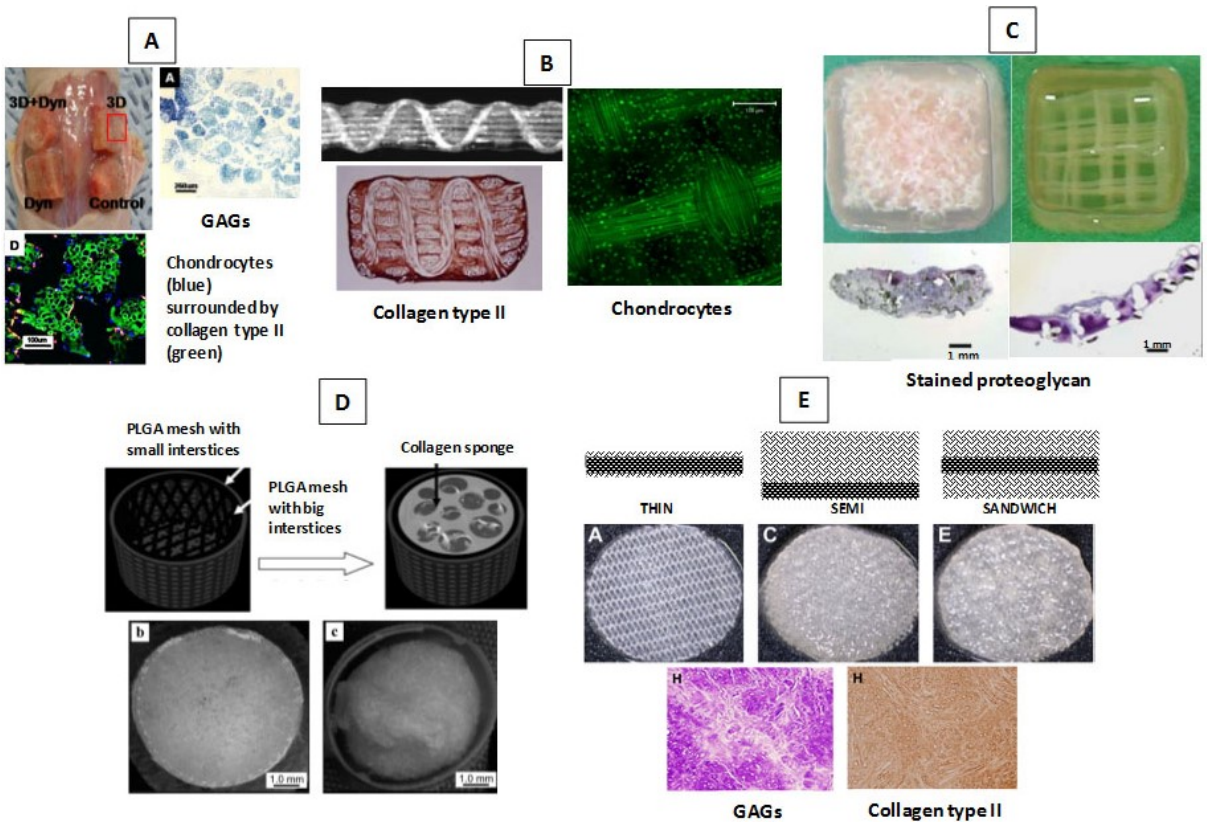

Figure 2.5 Different designs of hybrid scaffolds developed for cartilage TE: (**A**) PLCL-FG/HA [220,224]; (**B**) woven PGA/PCL-agarose/fibrin [46]; (**C**) PLLA-atelocollagen [110]; (**D**) PLGA-collagen [221]; and (**E**) PLGA-collagen [214].

Shim *et al*. [196] employed a multihead deposition system to create a hybrid scaffold from synthetic polymers and hydrogel. A mixture of PCL-PLGA was deposited in three layers (nonperpendicular pattern), then hydrogel (hyaluronic acid, gelatin, and atelocollagen) infused into the canals created between the solid strands. The same pattern was repeated to produce a 3D hybrid scaffold (Figure 2.6B). Using this fabrication technique, the dispensing position of both synthetic polymer and hydrogel inside the scaffold was exactly controlled. Shim *et al*. [196] also used this fabrication process to make one layer of a hybrid scaffold with a cell-laden hydrogel. The viability of the dispensed cells was 97.8% and 94.8% at 4 and 10 days after dispensing, respectively, which indicates that cell printing may not affect cell viability. Due to limitations of the fabrication process, only one cell-embedded layer was included in the hybrid scaffold (Figure 2.6B). Practical challenges of the fabrication process that may influence the biological integrity of the hybrid scaffold were not addressed, including use of toxic organic solvents during fabrication.

Schuurman *et al*. [195] created 3D hybrid scaffolds from CAD models using PCL and a cell-embedded alginate hydrogel, demonstrating the feasibility of making hybrid scaffolds with customized shapes, internal architectural designs, and depth-varying hydrogel materials (Figure 2.6C). Viability of cells in this type of hybrid scaffold, three days after fabrication, was reported to be within the same range as those in a nonprinted, hydrogel-only scaffold. The Young's modulus of the developed hybrid scaffold was within the range of natural articular cartilage. The results of these studies confirm the feasibility of using advanced fabrication techniques to develop multiphase hybrid scaffolds with controlled and designed distribution of cells, hydrogel, and synthetic materials. These strategies and fabrication techniques could be employed for developing more functional cartilage TE scaffolds that have customized biological and mechanical properties.

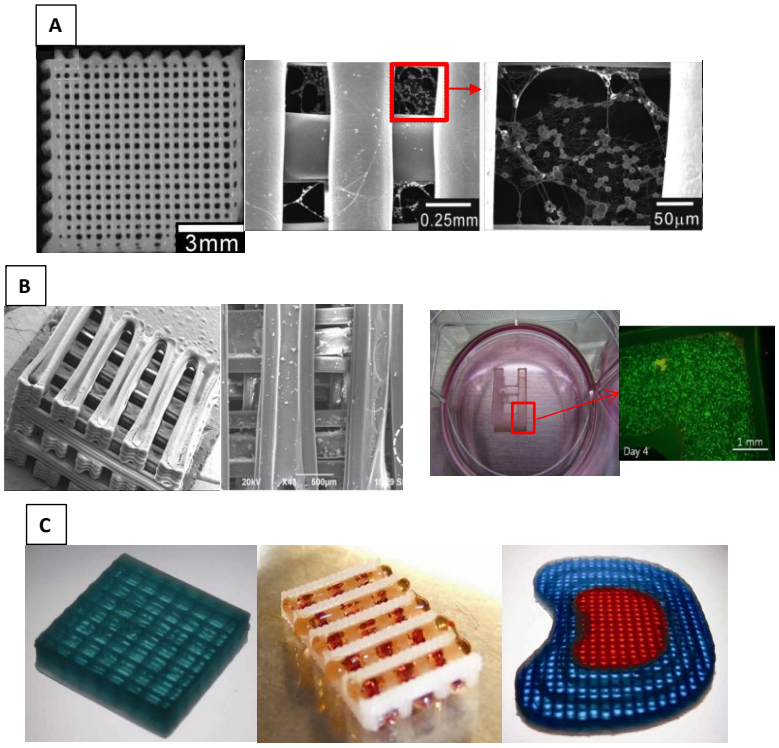

Figure 2.6 Controlled deposition hybrid scaffolds: (**A**) PCL-electrospun collagen [225]; (**B**) PCL/PLGA-hydrogel [196]; and (**C**) PCL-alginate [195].

2.1.5.2 Zonal scaffolds

The exceptional mechanical functionality of natural articular cartilage can be attributed to the distinctive organization of cartilage into four zones from the articular surface down to subchondral bone. As discussed in the introduction, the variation in cell morphology and ECM matrix composition/structure across these regions is believed to be a key factor in the mechanical

functionality of the cartilage. One problem with current engineered cartilage constructs is the absence of normal cell and ECM zonal organization, which is critical to natural cartilage function. Recently, researchers have attempted to replicate this zonal variation in scaffold design to improve the functionality of the resulting TE cartilage constructs. Cartilage TE scaffolds with a zonal design, as described by Klein *et al*. [21], can be categorized into either scaffold-free (cell-based) or scaffold-based approaches. The scaffold-based approach may use zonal solid, hydrogel, or hybrid scaffolds. Some efforts have been made to design scaffolds that promote engineered cartilage with zonally specific structure/function.

In a scaffold-free approach, zonal chondrocytes, which have been isolated from different zones of natural cartilage, are zonally layered to replicate the normal zonal organization of cells. This approach can induce cartilage ECM with a structure on the upper surface similar to the superficial zone of natural cartilage [115,226,227]. Self-assembling fabrication techniques [228] could potentially facilitate scaffold-free approaches for zonal cartilage TE. Although the initial mechanical properties of such cell-based structures are low, strategies can be taken to improve the mechanical properties of the self-assembled TE constructs [228–231]. Advances in AM technology (*i.e.*, bioprinting self-assembly) [232] could significantly contribute to the design and customization of physical/biochemical properties of assembled structures. One limitation of zonal cell-based TE is the difficulty in isolating cells from separate zones in articular cartilage, especially in human cartilage [61].

Zonally varying structural/biochemical designs in solid scaffolds is another approach for replicating cartilage zonal organization. Oriented nanofibrous scaffolds can induce cartilage tissue with oriented mechanical and cellular properties similar to the superficial zone of natural cartilage [233]. Cartilage TE scaffolds with designed zonally varied physical parameters (no variation in biological properties) [61] can mimic the anisotropic distribution of cells but not the zonal ECM organization. Natural and synthetic hydrogels with zonal-varying properties have also been investigated for cartilage zonal TE [234–239]. Zonal chondrocytes have been successfully expanded/cultured separately in hydrogels for zonal cartilage TE [238,240,241]. Zonal hydrogel scaffolds with a spatial gradient of embedded chondrocyte concentration [43] or type (zonal chondrocytes) [242,243] have been developed using a multilayer scaffold design. The interaction between superficial and deep/middle zone chondrocytes in a bilayer scaffold design resulted in depth-varying cellular activity and heterogeneous ECM formation. A depth-

dependent compression modulus [242] and enhanced mechanical properties (shear and compression strength) [243] have been observed in zonal constructs when compared to single-layer hydrogel scaffolds. Nguyen *et al*. [239] designed a hydrogel with zonally varying biochemical composition that can drive mesenchymal stem cells into zone-specific chondrocytes and promote zone-specific chondrogenesis similar to natural cartilage. The developed hydrogels [239] are intended to be incorporated into a layered hydrogel scaffold for zonal cartilage TE. In this type of zonal scaffold, the hydrogel for each layer is prepared separately and then assembled to make a multilayer, zonal scaffold. One limitation of this approach is the delamination of distinct layers by shear stress of applied loads. Efficient layering strategies, which ensure sufficient integration/stability of these heterogeneous biomimetic gels, are required to address this issue.

In a very recent study, Fedorovich *et al*. [88] investigated the use of AM fabrication technique for making cell-laden heterogeneous (layered) hydrogel scaffolds for cartilage TE. Two different hydrogel layers with different cell types were successfully fabricated into a 3D zonal scaffold. Hydrogel scaffolds designed with varying architectural (*i.e.*, fiber spacing, angle, and porosity) and mechanical properties (*i.e.*, elastic modulus) have been successfully fabricated and tested both *in vitro* and *in vivo* [88]. A method has also been developed for engineering multiphase structures with controlled and designed properties in each phase, as well as at the interfaces [244]. More specifically, multiple phases of collagen fibers, the density and size of which were modulated by varying collagen concentration and gelling temperature, were integrated into an engineered structure. Using this technique, significant adhesion strength was achieved at the interfaces of the multiphase construct [244], which could be important for layered cartilage TE design.

Hybrid scaffolds have also been designed and created to promote the formation of a zonal cartilage–bone interface (continuous gradations in formed ECM) [88,245,246]. A review of current strategies for developing TE osteochondral (bone–cartilage) grafts is given by O'Shea and Miao [247]. The effectiveness of bioreactors and mechanical loadings for stimulating the deposition of zone-specific cartilage ECM in TE scaffolds has also been demonstrated [248–250]. A thorough review of zonal cartilage TE strategies can be found in Klein *et al*. [21,251].

2.1.6 Conclusions and recommendations for future research

During the last 20 years, significant advances have been made in cartilage TE with respect to scaffold biomaterials, design, and fabrication. Hopes have been increased with respect to the development of a tissue engineering-based treatment for osteoarthritis, as well as cartilage lesions in young patients. This review discussed design considerations along with techniques used for fabrication of designed scaffolds for cartilage TE. Progress and advances in two strategic designs of hybrid and biomimetic zonal scaffolds were also reviewed. Although encouraging progress has been made, the major challenge in TE cartilage repair remains the insufficient resemblance of engineered cartilage to natural hyaline cartilage, in terms of biochemical composition, structural organization, and biomechanical properties [252]. To systematically improve this limitation using bioengineered scaffolds, strategic scaffold designs should be developed and investigated toward creating more functional cartilage TE constructs. One approach could be to learn from previous designs, with the mechanisms and/or factors that are currently inhibiting successful formation of functional cartilage tissue investigated and addressed in scaffold design and/or therapeutic strategies. Another approach is to develop and investigate biomimetic scaffold designs using knowledge from natural cartilage tissue systems and/or the healing process. This could include introduction of biological (e.g., bioactive molecules/cells) and structural (e.g., ECM-like architecture) complexities, similar to natural cartilage, into the scaffold design. Using the available advanced fabrication techniques, highly complex and designed scaffolds with a biomimetic distribution of cells and/or bioactive molecules within the scaffold could be created and investigated for design-based functional cartilage TE. Furthermore, different designs that have been successfully developed could be integrated and combined into new scaffold designs to achieve improved functionality for better cartilage TE. A current example of this approach is hybrid scaffolds with a hydrogel formulation designed for successful chondrogenesis and a solid framework designed for sufficient biomechanical functionality and formed tissue affinity. Hybrid scaffolds with biomimetic (e.g., zonal) designs are another interesting option to be investigated for cartilage TE; the solid framework structure and cell–hydrogel formulation could be designed to vary at different zones of a hybrid scaffold to achieve biomimetic zonal properties and signals. Biomimetic zonal cartilage TE is still in its infancy and more work in the development of design and fabrication methods is required to obtain zonally tailored TE scaffolds that promote zonal cartilage tissue

formation. Furthermore, whether or not a biomimetic zonal design will actually result in functional (mechanically and/or biologically) engineered cartilage, as compared to a nonzonal TE strategy, remains to be determined [21].

Although available advanced fabrication techniques have several benefits and capabilities, limited work has been done to investigate scaffolds designed with built-in biological/structural properties for cartilage TE; this should be conducted in future cartilage TE studies. More complex scaffold designs may not be easily achieved and studied without sophisticated fabrication techniques. Advancements in fabrication techniques for facilitating the development of precisely designed bioengineered scaffolds are urgently needed. Specifically, programmable, multifunctional, computer-controlled biofabrication techniques with higher resolution (*i.e.*, smaller fiber diameter and spacing) could significantly contribute to advances in cartilage TE. The reproducibility of scaffolds in a sterile, nontoxic environment could reduce the steps required for scaffold preparation and thus accelerate the economical transition of cartilage TE strategies to clinical applications. Fabrication systems that are able to facilitate this transition, by accommodating multiple functions, are of great interest with respect to development and commercialization. Some efforts have been made to develop integrated fabrication systems that prepare cell-incorporated biological samples [253] or TE scaffolds [254] in a sterile environment, including the nanoplotter-laminar flow hood [253] and stereolithography system-laminar flow hood [254]. Ongoing advances in technology and instrumentation could significantly contribute to this task.

Although the effect of different scaffold properties on chondrogenesis has been widely investigated, the exact mechanisms by which these properties affect neocartilage structure/composition are not fully understood. Investigating the rationale behind this cause and effect relationship will help to efficiently optimize scaffold design parameters and achieve better results. Developing mathematical models that can simulate the tissue formation process and subsequently relate scaffold properties to engineered tissue properties would be of special interest and benefit to scaffold optimization. One shortcoming in the cartilage TE literature is the lack of consistent mechanical and biological tests and/or evaluation criteria, which inhibits valid comparisons of designs and strategies. Most of the results reported are based on a variety of different testing conditions and criteria, and thus the development of standard evaluation

protocols for mechanical and biological assessment of cartilage TE constructs will be beneficial for the comparison of different studies and the development of better strategies.

Different results observed from *in vivo* and *in vitro* studies of the same scaffold design demonstrate the need and importance of in *vivo* studies for better understanding real-life scaffold performance. Published *in vivo* studies are considerably fewer in number than *in vitro* studies; this issue becomes especially important when meticulously designed scaffolds, based on *in vitro* tests, perform differently *in vivo* [255,256]. Because the *in vivo* environment is where the scaffold will finally perform [21], cartilage TE studies should move toward more *in vivo* experiments. Sterilization techniques and their influence on the integrity of TE scaffolds (e.g., scaffold material mechanical properties) should also be given more attention in scaffold design. Secure fixation of the engineered construct or TE scaffold in the transplantation site, which will be highly load-bearing joint, is another issue that should be considered in the design and/or fabrication of TE scaffolds/constructs. Weak or inappropriate implantation may significantly affect neocartilage formation, structural organization, integration with host tissue, and its remodeling.

2.2 SYNCHROTRON X-RAY IMAGING FOR CARTILAGE TISSUE ENGINEERING APPLICATIONS

2.2.1 Abstract

Biomedical imaging is crucial to the success of cartilage tissue engineering by providing detailed three-dimensional information on tissue-engineered scaffolds and associated cartilage growth during the healing process. Synchrotron radiation (SR)-based biomedical imaging is an emerging technique for this purpose that has been recently drawing considerable attention. Due to the unique properties of synchrotron light, novel SR X-ray biomedical imaging techniques are capable of providing information that conventional imaging techniques are not able to capture. SR phase-based X-ray imaging techniques use contrast mechanisms different from conventional X-ray imaging, which makes them particularly suitable for high resolution biomedical imaging of low density materials and soft tissues such as in cartilage tissue engineering applications. In the following, conventional methods used for cartilage tissue engineering assessments and novel

SR phase-based X-ray imaging techniques are briefly reviewed. Furthermore, recent applications of these SR biomedical imaging techniques to cartilage tissue engineering is discussed.

2.2.2 Introduction

The success of tissue engineering (TE) scaffold in repairing cartilage tissue may not be verified without appropriate monitoring and assessment techniques. Methods for assessing engineered scaffolds and tissue constructs can be generally categorized into invasive and non-invasive methods. Invasive methods mainly include histological and biochemical analysis, light microscopy, and electron optical methods. Non-invasive methods include the techniques that can image the tissue or structure *in situ* (in the body) without the need for excising the specimen from the body. Examples of non-invasive evaluation methods are the currently used clinical diagnostic imaging techniques such as magnetic resonance imaging (MRI), ultrasound, X-ray and computed-tomography (CT) imaging. Non-invasive assessment methods are important from two perspectives. First, obtaining better understanding of the long term repair process *in situ* can improve current TE approaches towards more effective strategies. However, the *in situ* condition under which the *de facto* process of TE repair occurs in animal or human bodies is almost impossible to replicate in the lab environment. As such, development of assessment methods that can enable obtaining such *de facto* information non-invasively during longitudinal animals or humans *in vivo* studies would be highly beneficial. Secondly, the conventional invasive methods cannot be used for assessments of future clinical human trials. Therefore, developing robust non-invasive assessment methods for future clinical tissue engineering applications is inevitable.

2.2.3 Conventional assessment methods

Conventional assessment methods in TE, such as histological analysis, light microscopy, and electron optical methods are destructive, involved with invasive analysis and complex preparation procedures. Light microscopy methods used for characterization of the biological structures have the disadvantage of low penetration depth that inhibits their application for analysis of opaque structures [257]. The most developed confocal and multiphoton microscopy methods [258, 259] allow imaging of structures with a depth less than 100 and 400 μm, respectively. Larger depth of structures can be imaged by serial sectioning technique, which is invasive, destroys the volumetric structure, do not allow complete reconstruction of 3D structure,

and also prevents in-depth quantification of structural details [257]. Electron optical methods--scanning electron microscope (SEM) and transmission electron microscope (TEM)--provide high resolution images at the nanometer scale. However, due to the limited penetration depth these methods are only able to resolve peripheral information and/or volumetric information of small, thin, and highly detailed samples [257, 260]. Furthermore, required specimen preparations such as fixation and dehydration can alter the organization of tissue constructs and impose artifacts in images [257, 261]. The invasive nature of the histological techniques requires scarifying of animal models at intermediate timepoints during longitudinal *in vivo* studies in order to excise the tissue construct or repaired tissue for further assessments. Such invasive procedure interrupts the repair process, make the long term *in vivo* studies inefficient and uneconomical with potential individual-dependent, variable results.

The conventional assessment techniques cannot be used for future clinical human trials which will, consequently, make the evaluation and approval of TE therapeutic strategies challenging. Therefore, the TE field demands development of non-invasive methods for non-destructive, volumetric, qualitative, and quantitative assessments of TE scaffolds and constructs *in situ* throughout the repair process. Common non-invasive clinical imaging methods used for cartilage diagnosis include MRI, ultrasound, and conventional radiographic X-ray imaging. MRI can provide image resolution of <50 μm [262]. Through newly developed modalities, MRI has also enabled imaging of the cartilage matrix structure [263] as well as qualitative and quantitative assessments of soft tissue regeneration [264]. However, MRI has shown limitations for non-invasive tissue engineering assessments such as lower image resolutions than X-ray imaging, being applicable to small animal imaging only [264], and requiring exogenous contrast materials for large animal imaging [265]. Furthermore, MR-based techniques mainly enable assessment of new tissue growth and fall short in imaging and evaluating polymeric tissue scaffolds *in situ* [264]. Ultrasound imaging provides information about the surface of the cartilage and have limited resolution and ability to resolve inner structure of the cartilage [266, 267]. Ultrasound imaging of the cartilage is also limited by the geometry and location of the articular cartilage because the sound head cannot resolve non-straight signals [266]. Ultrasound-based non-invasive evaluation methods for cartilage tissue engineering assessments are based on comparison of acoustic properties of the natural cartilage tissue, newly growth tissue, or

hydrogel scaffold [268-271]. The capability of these techniques for *in vivo* TE assessments has not been reported in the literature.

X-ray has high penetration depth and better image resolution than MRI and ultrasound [272]. Theoretically, it has a resolution between optical and electron microscopy [257]. This makes X-ray imaging a potential candidate for non-invasive assessment of TE scaffolds/constructs and regenerated tissue in large animal models and human patients *in vivo*. Conventional X-ray radiography is based on absorption contrast mechanism in which cartilage as a soft tissue is invisible; cartilage and soft tissues are mainly constitute of low X-ray-absorbing elements of hydrogen, oxygen, carbon, and nitrogen. Soft tissue scaffolds and constructs are made of comparably low density materials that are not visualizable in absorption-based X-ray imaging. Therefore, clinical radiographs cannot be used for assessment of cartilage tissue and low density TE scaffolds. To overcome this issue, researchers have tried to either use contrast agents, such as heavy metals for enhancing the absorption contrast [273-276], or develop new X-ray imaging techniques to improve the image contrast [277-281]. The use of contrast agents (staining) may impose cytotoxicity issues [282], artifact effect, and non-uniform staining of the tissue/biological construct [283], and, as such, are not optimal for longitudinal *in situ* TE assessments.

2.2.4 Synchrotron X-ray imaging

Synchrotron radiation (SR) X-ray is produced from charged particles (i.e. electrons) accelerated in a storage ring. The electron particles are initially ejected from an electron gun by electric field and speed up in a linear accelerator. The particles are then further accelerated to near the speed of light in a booster ring before being transferred to storage ring. In the storage ring, bend magnets cause the electrons to change direction and this results in a change in their velocity vector and consequently the radiation of synchrotron light. The produced X-ray has advanced properties such as high photon flux over large range of energies, high brilliance, small angular beam divergence, high level of coherence, and capability of monochromatization compared to conventional X-ray tube sources [284, 285]. These properties of the synchrotron X-ray have resulted in development of advanced biomedical imaging techniques [277-281] with superior imaging capabilities [286, 287] and potential for TE applications such as non-invasive

and longitudinal delineation of TE construct morphometry, neotissue growth, construct degradation kinetics, and host-implant interface dynamic [288-290].

2.2.5 Phase-based X-ray imaging

When X-ray enters an object, its propagation behavior through the object material is described by a dimensionless number called complex refractive index (n) and is defined as:

$$n = 1 - \alpha - i\beta \qquad 2.1$$

where α is the refractive index decrement (typically 10^{-6} for hard X-rays) and β is the absorption index (typically 10^{-11} for hard X-rays in soft tissues). The real part of the index n, 1-α, is referred to as refractive index, which indicates the phase velocity and for hard X-ray energy range (10-100 keV) is very close to (but less than) 1. The absorption index (β) indicates attenuation of the X-ray photons as they propagate through the material. In conventional X-ray imaging, e.g. clinical radiography, the imaginary part of the complex refractive index, $i\beta$, is used as the source of absorption contrast. However, in phase contrast imaging the contrast mechanism relies on the variations of the real part of the complex refractive index, 1-α (the phase shift), that is several orders of magnitude larger than the imaginary part. Using the phase shift variations as the source of contrast, the interface of microstructures and soft tissues constitutes of similar low density materials is imaged without using exogenous contrast agents [291-293]. Based on different implementations of this principle, several phase contrast X-ray imaging techniques have been developed [277-281, 285, 294]. Here three phase-based imaging techniques of inline phase-contrast imaging (PCI), diffraction enhanced imaging (DEI), and analyzer based imaging (ABI) are reviewed.

2.2.5.1 Inline phase-contrast imaging

Inline phase contrast imaging (PCI), also called propagation-based imaging, has a simple experimental setup similar to the clinical radiograph except using a sample-to-detector distance and/or a small effective X-ray source (Fig. 2.7a) [295-297]. When the X-ray travels through the object, the phase information of the wave front is disturbed at the interfaces of tissues and microstructures that have different refractive index. Such wave disturbance results in a phase shift and refraction of the X-ray, which is further developed over a free sample-to-detector propagation distance. The detector, then, collects the travelled beam at a distance downstream

the object. This is in contrast to conventional absorption-based radiograph where the emerged X-rays is collected immediately after the object. The continuous phase variations in the propagated X-rays result in photon intensity variation and enhanced contrast at the boundaries of tissues and microstructures [295-298]. Phase contrast imaging using conventional X-ray tube source involves limitations such as intense attenuation and scattering, which result in poor contrast images. Such effect is attributed to the polychromatic nature of the X-ray tube source and the employed imaging set up in which the transmitted beam must travel over a distance before hitting the detector [299]. Superior properties of SR X-ray beam can make substantial improvements in this regard. PCI technique has shown improved contrast compared to absorption-based images and has enabled resolving of soft tissue structures without using contrast agents [257].

2.2.5.2 Diffraction enhanced imaging

Diffraction enhanced imaging (DEI) utilizes contrast mechanisms of X-ray refraction, ultra-small angle X-ray scattering (USAXS), and scatter rejection of small angle X-ray scattering (SAXS), in addition to the absorption mechanism[261]. A three crystals setup that consists of a double crystal monochromator and an analyzer crystal with asymmetric reflection plane is employed in this technique (Fig. 2.7b) [277]. The double crystal monochromator selects a monochromatic X-ray beam with a small energy bandwidth from the incident polychromatic synchrotron beam [300]. The monochromatic X-ray beam transverse the object and is deflected at the interfaces of features with varying refractive index. Upon exiting the object and hitting the analyzer crystal, the X-rays that align within an acceptance angular bandwidth of the analyzer will be reflected off the analyzer to the detector with an angle-dependent modulation in the photon intensity given by analyzer rocking curve (RC). This mechanism along with the rejection of any photon that falls out of the angular acceptance window of the analyzer RC--scatter rejection effect--result in an enhanced contrast at interfaces and boundaries of features in a pure refraction image. Implementation of DEI system involves collecting two sets of images at two opposing (low and high) angles of the RC (e.g. at half maximum reflectivity angles), and then extracting the apparent refraction and absorption images from the two collected images. Currently, implementation of the DEI technique is mainly possible with the nearly monochromatic and highly collimated X-ray beam of synchrotron. However, DEI method can

also be implemented using any other X-ray source that can produce similar level of X-ray intensity [301]. Development of a table-top DEI system in laboratory (with X-ray tube source) has been reported in the literature for the imaging of cartilage tissue [302].

2.2.5.3 Analyzer based imaging

Analyzer-based imaging (ABI) is a version of DEI technique [303] that uses the same three crystals setup as DEI, however, only one set of images is collected at one side of the analyzer RC (e.g. half maximum reflectivity at high or low angle side). Similar to DEI, the contrast mechanism involves the slightly refracted X-ray beam that exits the sample and is amplified by the analyzer crystal, which, thereby, generate intensity variations that enhances the boundaries contrast. Unlike DEI, ABI system does not give pure refraction image, however, easier implementation, shorter imaging time, amplified contrast signal, and scatter rejection properties, enhance the potentials of this technique for live animal imaging [303].

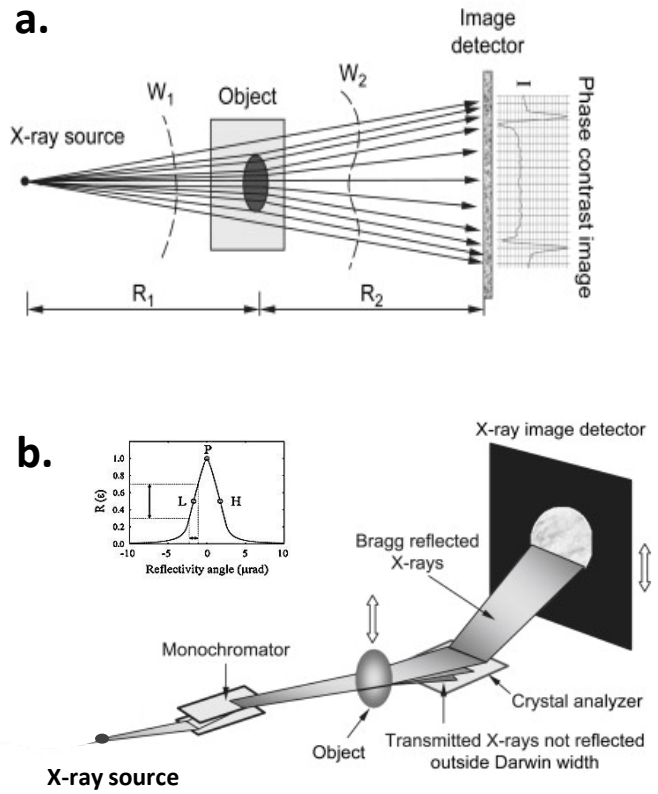

Figure 2.7 Schematic diagrams illustrating the image acquisition setup of (a) inline PCI and (b) DEI [304]

2.2.6 Computed tomography imaging

Computed tomography (CT) [305] is a unique technique for non-destructive, three-dimensional (3D) imaging of an object. It employs a series of 2D images, collected at different angles around the object, to produce cross-sectional images-virtual slices- without physical sectioning of the object. Reconstruction of CT slices resolve detailed spatial structures that are superimposed and not distinguishable in projected 2D images. The reconstructed slices can be stacked to produce 3D volume of the imaged object, which allows non-invasive qualitative and quantitative characterization of the specimen. Furthermore, combining CT modality with high resolution imaging emerged micro-CT (μCT) imaging systems [306] that when implemented with advanced X-ray sources can enable CT imaging at resolutions as high as <1 μm [307]. These capabilities have increased the popularity of μCT imaging for many medical and industrial research applications [308, 309]. Non-invasive property of CT imaging is particularly of interest for assessments of tissue engineering scaffolds [299, 308, 310-315] and regenerated tissues, such as bone [309, 316-319]. Being a computational method, quantification of numerous microarchitectural parameters of scaffold, such as material volume, surface area, strut width, pore size, pore network, and interconnectivity have become possible using μCT imaging [308]. Such quantitative architectural information is very valuable for assessing degradation behavior of tissue scaffolds and constructs, and evaluating mechanical properties and fluid dynamics in the engineered construct using solid and fluid mechanical testing and finite element modeling (FEM).

One of the limitations associated with the conventional CT system at high resolution (1-50 μm pixel size) is beam hardening effect that is caused by the polychromatic X-ray beam that contain lower energy X-rays. In other words, lower energy X-rays are readily attenuated in the sample and result in higher exposure time at the sample center (beam hardening), higher radiation dose, and difficult image segmentation/thresholding [308]. Superior properties of the SR X-ray such as high photon flux (typically about 10^8 photons/s), high brilliance, small angular beam divergence, and the ability to obtain monochromatic beam offer higher quality and more efficient CT imaging than conventional CT imaging. These advantages enable improved spatial resolution, high signal-to-noise ratio, faster acquisition time, and less beam hardening artifacts [320-326]. Combining advanced properties of CT modality, SR X-ray, and the phase-based imaging techniques would enable development of robust non-invasive imaging systems that have

more sensitivity to soft tissues and low density scaffolds for quantitative and qualitative TE assessments *in situ*.

2.2.7 Synchrotron phase-based imaging applications in cartilage tissue engineering

The high water content and low density of cartilage tissue produce negligible X-ray attenuations that limits visualization of cartilage using conventional absorption-based X-ray imaging techniques [307, 327]. MRI is commonly used to examine the cartilage and to identify damages and loss of the tissue without contrast media [328]. Nevertheless, the poor spatial resolution of MRI and inability to resolve specific tissue types when compared with synchrotron-based imaging techniques is the bottle-neck of this modality [328, 329]. Synchrotron imaging techniques were initially attracted by researchers in medical diagnosis field, where superior imaging techniques have always been on demand for early and accurate diagnosis of cartilage damages and diseases, e.g. detection of osteoarthritis in early stages. As such, most of the reported studies in the literature concentrate on the application of synchrotron imaging techniques for visualization and characterization of healthy and damaged/diseased cartilage tissue and cartilage-bone interface. Very few studies have investigated these techniques for cartilage and/or soft tissue engineering assessments, with no report on the *in situ* applications for cartilage TE. Since the bone tissue has high absorption coefficient that enables easier X-ray imaging, several studies have explored SR X-ray imaging techniques for quantitative and qualitative evaluation of bone TE scaffolds and newly regenerated bone tissue [307, 309, 316-319, 330]. The results of these studies indicate the feasibility of using such advanced X-ray imaging techniques for assessing and characterization of TE scaffolds architectural properties, degradation kinetics, regenerated tissue quality, and its integration with surrounding host tissue. Similarly, by developing SR X-ray imaging techniques capable of imaging low density materials and soft tissues *in situ* such information could also be obtained for *in vivo* cartilage TE assessment applications.

2.2.7.1 PCI

The simplicity of implementation, provision of outstanding contrast of less dense samples without using contrast agents, and edge enhancement are notable advantages of inline PCI. Inline PCI is a powerful tool for characterization of cell-scaffold matrix, new tissue ingrowth and bone-

cartilage interface where the refractive indices vary greatly [296, 304, 328]. The combination of inline PCI with either CT or μCT has been studied for 3D visualization of the articular cartilage [328]. One of such studies was conducted by Ismail and colleagues who used bench-top microfocus X-ray source with polychromatic, incoherent X-rays as well as synchrotron coherent X-rays for examining the cartilage-bone interface and different zones of cartilage [328]. They recorded edge enhancement, especially using synchrotron X-rays that was enough to visualize low density cartilage and cartilage-bone interface with transitional zones from articulating surface down to subchondral bone [328]. In a similar study, Zehbe et al. [257] used PC-μCT for 3D qualitative and quantitative characterization of articular cartilage; the 3D rendered images revealed information that was superior to that obtained from conventional serial histology (Fig. 2.8). Using the 3D images, various tissues under physiological and pathological conditions were differentiated. In addition, tissues structure and cellular level changes such as spatial cell density, shape and orientation of the lacunae inside soft tissues, were quantified without destruction of the tissues [257]. Using high resolution PCI, Choi et al. [331] characterized microstructural features of healthy cartilage as well as inflammatory and pathological changes in the arthritic joint of mice *in vivo*, also showing results comparable to those of μCT or histological analysis. Most of the reported studies imaged microstructure of the cartilage and scaffold, visualized early signs of cartilage disease, and quantified cellular activities in the scaffolds on excised *ex vivo* biological specimens, as opposed to intact specimens *in situ*. New techniques and ideas need to be explored for expanding similar applications to *in situ* samples for future *in vivo* studies.

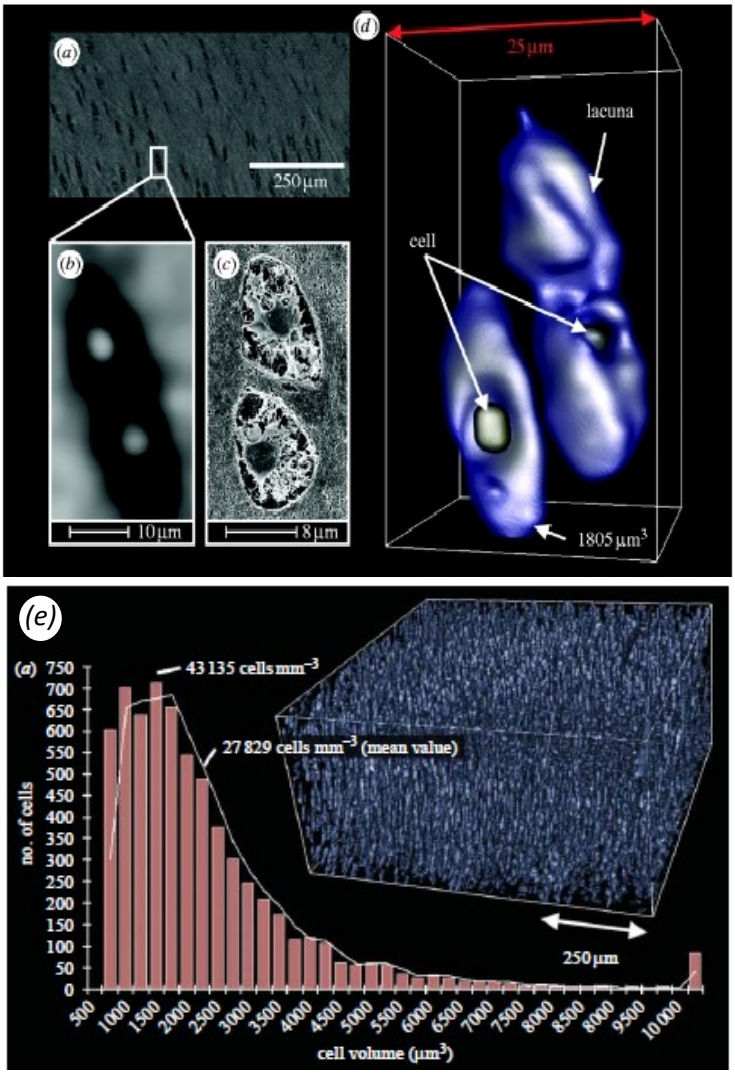

Figure 2.8 Images showing cellular information from the frontal lacuna in the soft tissue of an articular cartilage: (a) original slice image from inline PC-µCT ; (b) magnified region of interest containing lacuna doublet with chondrocytes in the centres; (c) corresponding SEM image ; (d) 3D rendering of (c); and (e) quantitative analysis of cell density from inline PC-µCT (adapted from [257]).

2.2.7.2 DEI and ABI

DEI is capable of scatter rejection, is sensitive to density differences in tissues, can be optimized through varying the analyzer angular setting without increasing the radiation dose, and provides multiple types of information such as absorption, refraction, and extinction images [332]. Hence, this method is promising for the 3D characterization of microstructural properties of regions with varying densities, especially in low X-ray absorbing materials such as native and tissue-engineered cartilage. DEI has been used to visualize cartilage tissue with appreciable

structural detail in both *ex vivo* [261, 333, 334] and *in situ* samples [301, 302, 335]. High levels of detail in the cartilage structure, such as the structural organization of collagen fiber bundles within the articular cartilage, have been revealed using DEI system [276]. Issever et al. [333] reported the visualization of cartilage matrix including changes in hypodensities that were strongly hypothesized to be chondrocyte lacunes. Similarly, Wagner et al. [334] used color-coding DEI to explore the internal structure of healthy and pathological joints. In their study, comparison of DEI with MRI showed that the same level of structural detail may be revealed by MRI but only after a much prolonged exposure that might not be practical with a patient. Muehleman et al. [302] differentiated stages of a cartilage lesion from a normal state to a down-to-bone erosion state in intact canine joints *in situ* using a DEI system. The high spatial resolution combined with the refraction-based mechanism of DEI enabled visualization of early-stage cartilage degeneration and defects in intact human knee and ankle joints *in situ* [302]. These results were further confirmed by histological and gross analysis [301].

AB-PCI was also used for characterization of osteoarthritic and normal cartilage matrices both *ex vivo* and *in vivo* [303, 336, 337]. In fact, the investigated technique enabled quantitative and qualitative characterization of the zonal pattern in the cartilage matrix, zonal thicknesses, chondrocyte homogeneity and alignment, and matrix fibrillation (Fig. 2.9b,c) [336]. Coan et al. [337] tested this imaging modality on *in vivo* samples and observed a high level of contrast for depicting anatomic structural details and pathological features of an osteoarthritic articular joint [337]. Similarly, Li et al. [303] imaged intact human knee and obtained structural details such as cartilage tissue, cruciate ligaments, loose connective tissue, menisci, and chondrocalcinosis (Fig. 2.9a).

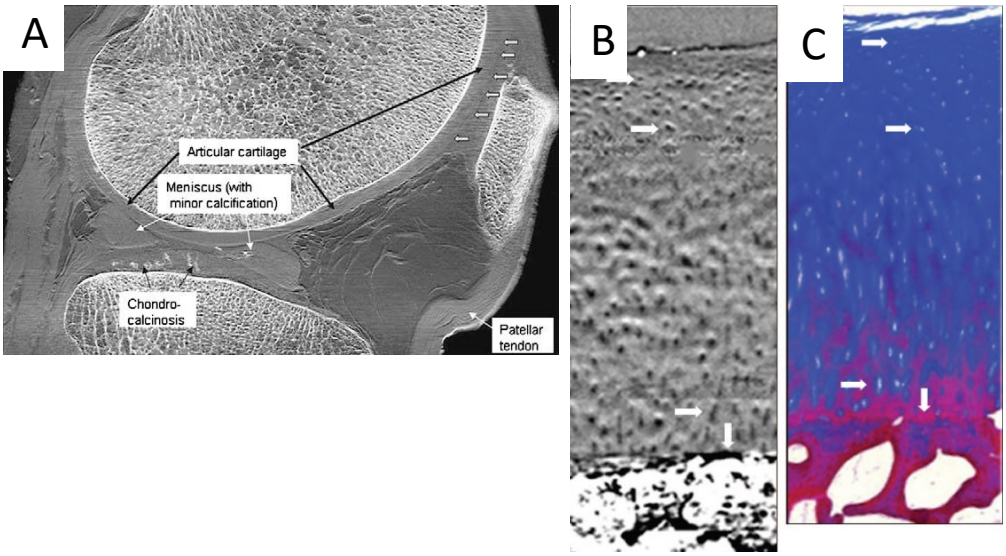

Figure 2.9 (A) Analyzer-based (AB) imaging of cadaveric human knee joint showing enhanced contrast imaging of soft tissues and bone with structural details *in situ*[303], and CT-AB imaging of cartilage specimen *ex vivo* with zonal structural detail comparable to (c) histological analysis [336]

Researchers have conducted extensive studies in cartilage imaging and diagnosis of cartilage disease using DEI and ABI systems. The reported results suggest the potential of these techniques for cartilage and other soft TE applications, and for developing non-invasive imaging-based assessment methods. DEI can enable visualizing both soft and hard tissues at the same time [337], which can give a unique potential in monitoring and assessing scaffold-based TE strategies for osteochondral (full thickness) cartilage repair. PCI, DEI, and ABI systems demonstrated capabilities in providing information similar to the gross and histological assessments of the cartilage tissue [338] that suggest their potential for evaluation of the cartilage repair success. Yet, very few studies have explored the potential of the phase contrast imaging techniques for non-invasive characterization of cartilage and soft tissue scaffolds [339, 340]. Zhu et al. [339] investigated imaging of soft tissue scaffolds *in vitro*, and compared DEI with laboratory-based radiography, SR-radiography, and inline PCI at the same energy. Their results showed that DEI offered better structural and microstructural quantification of soft tissues over the other three methods because of its ability to reject X-ray scatter [339]. Apple et al. [340] showed the capability of μCT phase-based imaging technique using synchrotron and conventional X-ray tube sources for non-invasive evaluation of cell-embedded tissue constructs. The structure of the tissue constructs and the newly formed tissue were characterized at various

time points during the culture time in a perfusion bioreactors [340]. The majority of the reported studies in the literature focused on imaging and characterization of low density TE scaffold in air or *ex vivo*. This indicates that the limitations of the currently investigated methods for *in situ* assessments is yet to be investigated and addressed. As a result, there is a high demand for exploring advanced imaging techniques such as SR phase-based imaging for visualization and characterization of TE scaffolds and regenerated tissue *in situ*. This is particularly important for verification of these techniques for animal *in vivo* studies and future clinical applications.

2.3 References

1. Moutos, F.T.; Guilak, F. Composite scaffolds for cartilage tissue engineering. *J. Biorheol.* **2008**, *45*, 501–512.

2. Mow, V.C.; Ratcliffe, A.; Poole, A.R. Cartilage and diarthrodial joints as paradigms for hierarchical materials and structures. *Biomaterials* **1992**, *13*, 67–97.

3. Haleem, A.M.; Chu, C.R. Advances in tissue engineering techniques for articular cartilage repair. *Oper. Tech. Orthop.* **2010**, *20*, 76–89.

4. Gillogly, S.D.; Voightm, M.; Blackburn, T. Treatment of articular cartilage defects of the knee with autologous chondrocyte implantation. *J. Orthop. Sports Phys. Ther.* **1998**, *28*, 241–251.

5. Athanasiou, K.A.; Darling, E.M.; Hu, J.C. Articular cartilage tissue engineering. In *Synthesis Lectures on Tissue Engineering*, 1st ed.; Athanasiou K.A., Leach J.K., Eds.; Morgan & Claypool: San Rafael, CA, USA, 2009; pp. 1–182.

6. Alford, J.W.; Cole, B.J. Cartilage restoration, Part 2: Techniques, outcomes, and future directions. *Am. J. Sports Med.* **2005**, *33*, 443–460.

7. Lavik, E.; Langer, R. Tissue engineering: Current state and perspectives. *Appl. Microbiol. Biotechnol.* **2004**, *65*, 1–8.

8. Mikos, A.G.; Herring, S.W.; Ochareon, P.; Elisseeff, J.; Lu, H.H.; Kandel, R.; Schoen, F.J.; Toner, M.; Mooney, D.; Atala, A.; Van Dyke, M.E.; Kaplan, D.; Vunjak-Novakovic, G. Engineering complex tissues. *Tissue Eng.* **2006**, *12*, 3307–3339.

9. Niklason, L.E.; Langer, R. Prospects for organ and tissue replacement. *JAMA* **2001**, *285*, 573–576.

10. Goldberg, M.; Langer, R.; Jia, X. Nanostructured materials for applications in drug delivery and tissue engineering. *J. Biomater. Sci. Polym. Ed*. **2007**, *18*, 241–268.

11. Athanasiou, K.A.; Niederauer, G.G.; Agrawal, C.M. Sterilization, toxicity, biocompatibility and clinical applications of polylactic Acid/Polyglycolic acid copolymers. *Biomaterials* **1996**, *17*, 93–102.

12. Cima, L.G.; Vacanti, J.P.; Vacanti, C.; Ingber, D.; Mooney, D.; Langer, R. Tissue engineering by cell transplantation using degradable polymer substrates. *J. Biomech. Eng.* **1991**, *113*, 143–151.

13. Freed, L.E.; Vunjak-Novakovic, G.; Biron, R.J.; Eagles, D.B.; Lesnoy, D.C.; Barlow, S.K.; Langer, R. Biodegradable polymer scaffolds for tissue engineering. *Biotechnology* **1994**, *12*, 689–693.

14. Mikos, A.G.; Bao, Y.; Cima, L.G.; Ingber, D.E.; Vacanti, J.P.; Langer, R. Preparation of poly(glycolic acid) bonded fiber structures for cell attachment and transplantation. *J Biomed. Mater. Res.* **1993**, *27*, 183–189.

15. Buckwalter, J.A.; Mankin, H.J.; Grodzinsky, A.J. Articular cartilage and osteoarthritis. *Instr. Course Lect.* **2005**, *54*, 465–480.

16. Ateshian, G.A.; Lai, W.M.; Zhu, W.B.; Mow, V.C. An asymptotic solution for the contact of two biphasic cartilage layers. *J. Biomech.* **1994**, *27*, 1347–1360.

17. Buckwalter, J.A.; Mow, V.C.; Ratcliffe, A. Restoration of injured or degenerated articular cartilage. *J. Am. Acad. Orthop. Surg.* **1994**, *2*, 192–201.

18. Buckwalter, J.A.; Hunziker, E.B.; Rosenberg, L.C.; Coutts, R.D.; Adams, M.E.; Eyre, D.R. Articular cartilage. Composition and structure. In *Injury and Repair of the Musculoskeletal Soft Tissues*; Woo, S.L.-Y., Buckwalter, J.A., Eds.; The American Academy of Orthopaedic Surgeons: Park Ridge, IL, USA, 1988; pp. 405–425.

19. Meachim, G.; Sheffield, S.R. Surface ultrastructure of mature adult human articular cartilage.
J. Bone Joint. Surg. Br. **1969**, *51*, 529–539.

20. Muir, H.; Bullough, P.; Maroudas, A. The distribution of collagen in human articular cartilage with some of its physiological implications. *J. Bone Joint. Surg. Br.* **1970**, *52*, 554–563.

21. Klein, T.J.; Malda, J.; Sah, R.L.; Hutmacher, D.W. Tissue engineering of articular cartilage with biomimetic zones. *Tissue Eng. Part B* **2009**, *15*, 143–157.

22. Huang, C.Y.; Stankiewicz, A.; Ateshian, G.A.; Mow, V.C. Anisotropy, inhomogeneity, and tension-compression nonlinearity of human glenohumeral cartilage in finite deformation. *J. Biomech.* **2005**, *38*, 799–809.

23. Venn, M.; Maroudas, A. Chemical composition and swelling of normal and osteoarthrotic femoral head cartilage. I. Chemical composition. *Ann. Rheum. Dis.* **1977**, *36*, 121–129.

24. Eggli, P.S.; Hunziker, E.B.; Schenk, R.K. Quantitation of structural features characterizing weight- and less- weight-bearing regions in articular cartilage: A stereological analysis of medial femoral condyles in young adult rabbits. *Anat. Rec.* **1988**, *222*, 217–227.

25. Radin, E.L.; Ehrlich, M.G.; Chernack, R.; Abernethy, P.; Paul, I.L.; Rose, R.M. Effect of repetitive impulsive loading on the knee joints of rabbits. *Clin. Orthop. Relat. Res.* **1978**, *131*, 288–293.

26. Brittberg, M.; Lindahl, A.; Nilsson, A.; Ohlsson, C.; Isaksson, O.; Peterson, L. Treatment of deep cartilage defects in the knee with autologous chondrocyte transplantation. *N. Engl. J. Med.* **1994**, *331*, 889–995.

27. Bi, X.; Li, G.; Doty, S.B.; Camacho, N.P. A novel method for determination of collagen orientation in cartilage by fourier transform infrared imaging spectroscopy (FT-IRIS). *Osteoarth. Cart.* **2005**, *13*, 1050–1058.

28. Chang, C.H.; Lin, F.H; Kuo, T.F.; Liu, H.C. Cartilage tissue engineering. *Biomed. Eng. Appl. Basis Comm*. **2005**, *17*, 1–11.

29. Horas, U.; Pelinkovic, D.; Herr, G.; Aigner, T.; Schnettler, R. Autologous chondrocyte implantation and osteochondral cylinder transplantation in cartilage repair of the knee joint: A prospective, comparative trial. *J. Bone Joint Surg. Am.* **2003**, *85*, 185–192.

30. Roberts, S.; Menage, J.; Sandell, L.J.; Evans, E.H.; Richardson, J.B. Immunohistochemical study of collagen types I and II and procollagen IIa in human cartilage repair tissue following autologous chondrocyte implantation. *Knee* **2009**, *16*, 398–404.

31. Osteotomy of the knee. AAOS (American Academy of Orthopaedic Surgeons) Website. Available online: http://orthoinfo.aaos.org/topic.cfm?topic=A00591 (accessed on 26 October 2012).

32. Hutmacher, D.; Woodfield, T.; Dalton, P.D.; Lewis, J.A. Scaffold design and fabrication. In *Tissue Engineering*; van Blitterswijk, C., Thomsen, P., Hubbell, J., Cancedda, R., de Bruijn, J., Lindahl, A., Sohier, J., Williams, D.F., Eds.; Elsevier Academic Press: London, UK, 2008; pp. 403–454.

33. Stoop, R. Smart biomaterials for tissue engineering of cartilage injury. *Int. J. Care Injured* **2008**, *39*, 77–87.

34. Li, W.J.; Laurencin, C.T.; Caterson, E.J.; Tuan, R.S.; Ko, F.K. Electrospun nanofibrous structure: a novel scaffold for tissue engineering. *J. Biomed. Mater. Res.* **2002**, *60*, 613–621.

35. Sechriest, V.; Miao, Y.; Niyibizi, C.; Westerhausen-Larson, A.; Matthew, H.; Evans, C.H.; Fu, F.H.; Suh, J.K. GAG-augmented polysaccharide hydrogel: A novel biocompatible and biodegradable material to support chondrogenesis. *J. Biomed. Mater. Res.* **2000**, *49*, 534–541.

36. Gibas, I.; Janik, H. Review: Synthetic polymer hydrogels for biomedical applications. *Chem. Chem. Technol.* **2010**, *4*, 297–304.

37. Lin, Y.J.; Yen, C.N.; Hu, Y.C.; Wu, Y.C.; Liao, C.J.; Chu, I.M. Chondrocytes culture in three-dimensional porous alginate scaffolds enhanced cell proliferation, matrix synthesis and gene expression. *J. Biomed. Mater. Res. Part A* **2009**, *88*, 23–33.

38. Perka, C.; Schultz, O.; Spitzer, R.; Lindenhayn, K. The influence of transforming growth factor beta1 on mesenchymal cell repair of full-thickness cartilage defects. *J. Biomed. Mater. Res.* **2000**, *52*, 543–552.

39. Mouw, J.K.; Case, N.D.; Guldberg, R.E.; Plaas, A.H.; Levenston, M.E. Variations in matrix composition and gag fine structure among scaffolds for cartilage tissue engineering. *Osteoarth. Cart.* **2005**, *13*, 828–836.

40. Rahfoth, B.; Weisser, J.; Sternkopf, F.; Aigner, T.; von der Mark, K.; Brauer, R. Transplantation of allograft chondrocytes embedded in agarose gel into cartilage defects of rabbits. *Osteoarth. Cart.* **1996**, *6*, 50–65.

41. Reddy, N.; Yang, Y. Potential of plant proteins for medical applications. *Trends Biotechnol.* **2011**, *29*, 490–498.

42. Lee, K.Y.; Rowley, J.; Moy, E.; Bouhadir, K.H.; Mooney, D.J. Controlling mechanical and swelling properties of alginate hydrogels independently by cross-linker type and cross-linking density. *Macromolecules* **2000**, *33*, 4291–4294.

43. Buschmann, M.D.; Gluzband, Y.A.; Grodzinsky, A.J.; Hunziker, E.B. Mechanical compression modulates matrix biosynthesis in chondrocyte/agarose culture. *J. Cell Sci.* **1995**, *108*, 1497–1508.

44. Bryant, S.J.; Anseth, K.S. Hydrogel properties influence ECM production by chondrocytes PHotoencapsulated in poly (ethylene glycol) hydrogels. *J. Biomed. Mater. Res.* **2002**, *59*, 63–72.

45. Balakrishnan, B.; Banerjee, R. Biopolymer-based hydrogels for cartilage tissue engineering. *Chem. Rev.* **2011**, *111*, 4453–4474.

46. Moutos, F.T. Biomimetic Composite Scaffold for the Functional Tissue Engineering of Articular Cartilage. Ph.D. thesis, Duke University, Durham, NC, USA, 2009.

47. Kemppainen, J.M.; Hollister, S.J. Tailoring the mechanical properties of 3D-designed poly(glycerol sebacate) scaffolds for cartilage applications. *J. Biomed. Mater. Res. A* **2010**, *94*, 9–18.

48. Hutmacher, D.W. Scaffolds in tissue engineering bone and cartilage. *Biomaterials* **2000**, *21*, 2529–2543.

49. Yang, Z.; Wu, Y.; Li, C.; Zhang, T.; Zou, Y.; Hui, J.H.; Ge, Z.; Lee, E.H. Improved mesenchymal stem cells attachment and *in vitro* cartilage tissue formation on chitosan-modified poly(L-lactide-co-epsilon-caprolactone) scaffold. *Tissue Eng. Part A*. **2012**, *18*, 242–251.

50. Ma, Z.; Gao, C.; Gong, Y.; Shen, J. Cartilage tissue engineering PLLA scaffold with surface immobilized collagen and basic fibroblast growth factor. *Biomaterials* **2005**, *26*, 1253–1259.

51. Bhati, R.S.; Mukherjee, D.P.; McCarthy, K.J.; Rogers, H.S.; Smith, D.F.; Shalaby, S.W. The growth of chondrocytes into a fibronectin-coated biodegradable scaffold. *J. Biomed. Mater. Res*. **2001**, *56*, 74–82.

52. Solchaga, L.A.; Gao, J.; Dennis, J.E.; Awadallah, A.; Lundberg, M.; Caplan, A.I.; Goldberg, V.M. Treatment of osteochondral defects with autologous bone marrow in a hyaluronan-based delivery vehicle. *Tissue Eng.* **2002**, *8*, 333–347.

53. Puppi, D.; Chiellini, F.; Piras, A.M.; Chiellini, E. Polymeric materials for bone and cartilage repair. *Prog. Polym. Sci.* **2010**, *35*, 403–440.

54. Yang, Q.; Peng, J.; Guo, Q.; Huang, J.; Zhang, L.; Yao, J.; Yang, F.; Wang, S.; Xu, W.; Wang, A.; Lu, S. A cartilage ECM-derived 3-D porous acellular matrix scaffold for *in vivo* cartilage tissue engineering with PKH26-labeled chondrogenic bone marrow-derived mesenchymal stem cells. *Biomaterials* **2008**, *29*, 2378–2387.

55. Yang, Z.; Shi, Y.; Wei, X.; He, J.; Yang, S.; Dickson, G.; Tang, J.; Xiang, J.; Song, C.; Li, G. Fabrication and repair of cartilage defects with a novel acellular cartilage matrix scaffold. *Tissue Eng. Part C* **2010**, *16*, 865–876.

56. Elder, B.D.; Eleswarapu, S.V.; Athanasiou, K.A. Extraction Techniques for the decellularization of tissue engineered articular cartilage constructs. *Biomaterials* **2009**, *30*, 3749–3756.

57. Malda, J.; Woodfield, T.B.F.; van der Vloodta, F.; Wilsond, C.; Martensc, D.E.; Tramperc, J.; van Blitterswijk, C.A.; Rieslea, J. The effect of PEGT/PBT scaffold architecture on the composition of tissue engineered cartilage. *Biomaterials* **2005**, *26*, 63–72.

58. Hwang, N.S.; Kim, M.S.; Sampattavanich, S.; Baek, J.H.; Zhang, Z.; Elisseeff, J. Effects of three-dimensional culture and growth factors on the chondrogenic differentiation of murine embryonic stem cells. *Stem Cells* **2006**, *24*, 284–291.

59. Liu, H.; Lin, J.; Roy, K. Effect of 3D scaffold and dynamic culture condition on the global gene expression profile of mouse embryonic stem cells. *Biomaterials* **2006**, *27*, 5978–5989.

60. Putnam, A.J.; Mooney, D.J. Tissue Engineering using synthetic extracellular matrices. *Nat. Med.* **1996**, *2*, 824–826.

61. Woodfield, T.B.F.; van Blitterswijk, C.A.; de Wijn, J.; Sims, T.J.; Hollander, A.P.; Riesle, J. Polymer scaffold fabricated with pore-size gradient as a model for studying the zonal organization within tissue-engineered cartilage constructs. *Tissue Eng.* **2005**, *11*, 1297–1311.

62. Woodfield, T.B.F.; Bezemer, J.M.; Pieper, J.S.; van Blitterswijk, C.A.; Riesle, J. Scaffolds for tissue engineering of cartilage. *Crit. Rev. Euk. Gene Exp.* **2002**, *12*, 207–235.

63. Zein, I.; Hutmacher, D.W.; Tan, K.C.; Teoh, S.H. Fused deposition modeling of novel scaffold architectures for tissue engineering applications. *Biomaterials* **2002**, *23*, 1169–1185.

64. Murphy, W.L.; Dennis, R.G.; Kileny, J.L.; Mooney, D.J. Salt fusion: An approach to improve pore interconnectivity within tissue engineering scaffolds. *Tissue Eng.* **2002**, *8*, 43–52.

65. Nehrer, S.; Breinan, H.A.; Ramappa, A.; Young, G.; Shortkroff, S.; Louie, L.K.; Sledge, C.B.; Yannas, I.V.; Spector, M. Matrix collagen type and pore size influence behaviour of seeded canine chondrocytes. *Biomaterials* **1997**, *18*, 769–776.

66. LiVecchi, A.B.; Tombes, R.M.; LaBerge, M. *In vitro* chondrocyte collagen deposition within porous HDPE: Substrate microstructure and wettability effects. *J. Biomed. Mater. Res.* **1994**, *28*, 839–850.

67. Bhardwaj, T.; Pilliar, R.M.; Grynpas, M.D.; Kandel, R.A. Effect of material geometry on cartilagenous tissue formation *in vitro*. *J. Biomed. Mater. Res.* **2001**, *57*, 190–199.

68. Silva, M.M.; Cyster, L.A.; Barry, J.J.; Yang, X.B.; Oreffo, R.O.; Grant, D.M.; Scotchford, C.A.; Howdle, S.M.; Shakesheff, K.M.; Rose, F.R. The effect of anisotropic architecture on cell and tissue infiltration into tissue engineering scaffolds. *Biomaterials* **2006**, *27*, 5909–5917.

69. El-Ayoubi, R.; Degrandpre, C.; Diraddo, R.; Yousef, A.M. design and dynamic culture of 3D-scaffolds for cartilage tissue engineering. *J. Biomater. Appl.* **2011**, *25*, 429–444.

70. Yamane, S.; Iwasaki, N.; Kasahara, Y.; Harada, K.; Majima, T.; Monde, K.; Nishimura, S.; Minami, A. effect of pore size on *in vitro* cartilage formation using chitosan-based hyaluronic acid hybrid polymer fibers. *J. Biomed. Mater. Res. Part A* **2007**, *81A*, 586–593.

71. Lien, S.M.; Ko, L.Y.; Huang, T.J. Effect of pore size on ecm secretion and cell growth in gelatin scaffold for articular cartilage tissue engineering. *Acta Biomater.* **2009**, *5*, 670–679.

72. Grad, S.; Zhou, L.; Gogolewski, S.; Alini, M. Chondrocytes seeded onto poly (L/DL-Lactide) 80%/20% porous scaffolds: A biochemical evaluation. *J. Biomed. Mater. Res. Part A* **2003**, *66*, 571–579.

73. Lefebvre, V.; Peeters-Joris, C.; Vaes, G. Production of collagens, collagenase and collagenase inhibitor during the dedifferentiation of articular chondrocytes by serial subcultures. *Biochem. Biophys. Acta* **1990**, *1051*, 266–275.

74. Rodriguez, A.M.; Vacanti, C.A. Tissue engineering of cartilage. In *Frontiers in Tissue Engineering*. Patrick, J.C.W., Mikos, A.G., McIntire, L.V., Eds.; Elsevier Scienc: New York, NY, USA, 1998; pp. 400–411.

75. Li, W.J.; Jiang, Y.J.; Tuan, R.S. Chondrocyte phenotype in engineered fibrous matrix is regulated by fiber size. *Tissue Eng.* **2006**, *12*, 1775–1785.

76. Spiteri, C.G.; Pilliar, R.M.; Kandel, R.A. Substrate porosity enhances chondrocyte attachment, spreading, and cartilage tissue formation *in vitro*. *J. Biomed. Mater. Res. Part A* **2006**, *78*, 677–683.

77. Gerecht, S.; Townsend, S.A.; Pressler, H.; Zhu, H.; Nijst, C.L.; Bruggeman, J.P.; Nichol, J.W.; Langer, R. A porous photocurable elastomer for cell encapsulation and culture. *Biomaterials* **2007**, *28*, 4826–4835.

78. El-Ayoubi, R.; Eliopoulus, N.; Diraddo, R.; Galipeau, J.; Yousefi, A.M. Design and fabrication of 3D porous scaffolds to facilitate cell-based gene therapy. *Tissue Eng. Part A* **2008**, *14*, 1037–1048.

79. Moutos, F.T.; Estes, B.T.; Guilak, F. Multifunctional hybrid three-dimensionally woven scaffolds for cartilage tissue engineering. *Macromol. Biosci*. **2010**, *10*, 1355–1364.

80. Sahoo, S.; Cho-Hong, J.G.; Siew-Lok, T. Development of hybrid polymer scaffolds for potential applications in ligament and tendon tissue engineering. *Biomed Mater*. **2007**, *2*, 169–173.

81. Cheng, Z.; Teoh, S.H. Surface modification of ultra thin poly (epsilon-caprolactone) films using acrylic acid and collagen. *Biomaterials* **2004**, *25*, 1991–2001.

82. Miot, S.; Woodfield, T.B.F.; Daniels, A.U.; Suetterlin, R.; Peterschmitt, I.; Heberer, M.; van Blitterswijk, C.A.; Riesle, J.; Martin, I. Effects of scaffold composition and architecture on human nasal chondrocyte redifferentiation and cartilaginous matrix deposition. *Biomaterials* **2005**, *26*, 2479–2489.

83. Freed, L.E.; Hollander, A.P.; Martin, I.; Barry, J.R.; Langer, R.; Vunjak-Novakovic, G. Chondrogenesis in a cell–polymer–bioreactor system. *Exp. Cell Res.* **1998**, *240*, 58–65.
84. Obradovic, B.; Meldon, J.H.; Freed, L.E.; Vunjak-Novakovic, G. Glycosaminoglycan deposition in engineered cartilage: Experiments and mathematical model. *AIChE J* **2000**, *46*, 1860–1871.
85. Woodfield, T.B.F.; Malda, J.; de Wijn, J.; Peters, F.; Riesle, J.; van Blitterswijk, C.A. Design of porous scaffolds for cartilage tissue engineering using a three-dimensional fiber-deposition technique. *Biomaterials* **2004**, *25*, 4149–4161.
86. Lin, A.S.; Barrows, T.H.; Cartmella, S.H.; Guldberg, R.E. Microarchitectural and mechanical characterization of oriented porous polymer scaffolds. *Biomaterials* **2003**, *24*, 481–489.
87. Slivka, M.A.; Leatherbury, N.C.; Kieswetter, K.; Niederauer, G.G. Porous, resorbable, fiber-reinforced scaffolds tailored for articular cartilage repair. *Tissue Eng.* **2001**, *7*, 767–780.
88. Fedorovich, N.E.; Schuurman, W.; Wijnberg, H.M.; Prins, H.J.; van Weeren, P.R.; Malda, J.; Alblas, J.; Dhert, W.J. Biofabrication of osteochondral tissue equivalents by printing topologically defined, cell-laden hydrogel scaffolds. *Tissue Eng. Part C* **2012**, *18*, 33–44.

89. Guillotin, B.; Souquet, A.; Catros, S.; Duocastella, M.; Pippenger, B.; Bellance, S.; Bareille, R.; Rémy, M.; Bordenave, L.; Amédée, J.; *et al.* Laser assisted bioprinting of engineered tissue with high cell density and microscale organization. *Biomaterials* **2010**, *31*, 7250–7256.

90. Cohen, D.L.; Malone, E.; Lipson, H.; Bonassar, L.J. Direct freeform fabrication of seeded hydrogels in arbitrary geometries. *Tissue Eng.* **2006**, *12*, 1325–1335.

91. Xu, T.; Jin, J.; Gregory, C.; Hickman, J.J.; Boland, T. Inkjet printing of viable mammalian cells. *Biomaterials* **2005**, *26*, 93–99.

92. Chung, C.; Mesa, J.; Randolph, M.A.; Yaremchuk, M.; Burdick, J.A. Influence of gel properties on neocartilage formation by auricular chondrocytes photoencapsulated in hyaluronic acid networks. *J. Biomed. Mater. Res. A* **2006**, *77*, 518–525.

93. Erickson, I.E.; Huang, A.H.; Sengupta, S.; Kestle, S.; Burdick, J.A.; Mauck, R.L. Macromer density influences mesenchymal stem cell chondrogenesis and maturation in photocrosslinked hyaluronic acid hydrogels. *Osteoarth. Cart.* **2009**, *17*, 1639–1648.

94. Bryant, S.J.; Anseth, K.S. Controlling the spatial distribution of ecm components in degradable PEG hydrogels for tissue engineering cartilage. *J. Biomed. Mater. Res.* **2003**, *64A*, 70–79.

95. Bryant, S.J.; Durand, K.L.; Anseth, K.S. Manipulations in hydrogel chemistry control photoencapsulated chondrocyte behavior and their extracellular matrix production. *J. Biomed. Mater. Res.* **2003**, *67A*, 1430–1436.

96. Sontjens, S.H.M.; Nettles, D.L.; Carnahan, M.A.; Setton, L.A.; Grinstaff, M.W. Biodendrimer-based hydrogel scaffolds for cartilage tissue repair. *Biomacromolecules* **2006**, *7*, 310–316.

97. Nicodemus, G.D.; Bryant, S.J. Cell encapsulation in biodegradable hydrogels for tissue engineering applications. *Tissue Eng. Part B Rev*. **2008**, *14*, 149–165.

98. Jeong, C.G.; Hollister, S.J. A comparison of the influence of material on in vitro cartilage tissue engineering with PCL, PGS, and POC 3D scaffold architecture seeded with chondrocytes. *Biomaterials* **2010**, *31*, 4304–4312.

99. Annabi, N.; Nichol, J.W.; Zhong, X.; Ji, C.; Koshy, S.; Khademhosseini, A.; Dehghani, F. Controlling the porosity and microarchitecture of hydrogels for tissue engineering. *Tissue Eng*. *Part B* **2010**, *16*, 371–383.

100. Mohan, N.; Nair, P.D. Polyvinyl alcohol-poly (caprolactone) semi IPN scaffold with implication for cartilage tissue engineering. *J. Biomed. Mater. Res. B Appl. Biomater.* **2007**, *84*, 584–594.

101. Park, J.S.; Woo, D.G.; Sun, B.K.; Chung, H.-M.; Im, S.J.; Choi, Y.M.; Park, K.; Huh, K.M.; Park, K.-H. *In vitro* and *in vivo* test of PEG/PCL-based hydrogel scaffold for cell delivery application. *J. Control Release* **2007**, *124*, 51–59.

102. Suh, S.W.; Shin, J.Y.; Kim, J.; Kim, J.; Beak, C.H.; Kim, D.I.; Kim, H.; Jeon, S.S.; Choo, I.W. Effect of different particles on cell proliferation in polymer scaffolds using a solvent-casting and particulate leaching technique. *ASAIO J.* **2002**, *48*, 460–464.

103. Kemppainen, J.M.; Hollister, S.J. Differential effects of designed scaffold permeability on chondrogenesis by chondrocytes and bone marrow stromal cells. *Biomaterials* **2010**, *31*, 279–287.

104. Heydarkhan-Hagvall, S.; Schenke-Layland, K.; Dhanasopon, A.P.; Rofail, F.; Smith, H.; Wu, B.M.; Shemin, R.; Beygui, R.E.; Maclellan, W.R. Three-dimensional electronspun ECM-based hybrid scaffolds for cardiovascular tissue engineering. *Biomaterials* **2008**, *29*, 2907–2914.

105. Pham, Q.P.; Sharma, U.; Mikos, A.G. Electrospun poly (e-caprolactone) microfiber and multilayer nanofiber- microfiber scaffolds: Characterization of scaffolds and measurement of cellular infiltration. *Biomacromolecules* **2006**, *7*, 2796–2805.
106. Matthews, J.A.; Boland, E.D.; Wnek, G.E.; Simpson, D.G.; Bowlin, G.L. Electrospinning of collagen type II: A feasibility study. *J. Bioact. Compat. Pol.* **2003**, *18*, 125–134.
107. Komistek, R.D.; Kane, T.R.; Mahfouz, M.; Ochoa, J.A.; Dennis, D.A. Knee mechanics: A review of past and present techniques to determine *in vivo* loads. *J. Biomech.* **2005**, *38*, 215–228.

108. Natoli, R.M.; Athanasiou, K.A. P188 reduces cell death and IGF-I reduces GAG release following single-impact loading of articular cartilage. *J. Biomech. Eng.* **2008**, *130*, doi: 10.1115/
1.2939368.

109. Treppo, S.; Koepp, H.; Quan, E.C.; Cole, A.A.; Kuettner, K.E.; Grodzinsky, A.J. Comparison of biomechanical and biochemical properties of cartilage from human knee and ankle pairs. *J. Orthop. Res.* **2000**, *18*, 739–748.

110. Tanaka, Y.; Yamaoka, H.; Nishizawa, S.; Nagata, S.; Ogasawara, T.; Asawa, Y.; Fujihara, Y.; Takato, T.; Hoshi, K. The optimization of porous polymeric scaffolds for chondrocyte/atelocollagen based tissue-engineered cartilage. *Biomaterials* **2010**, *31*, 4506–4516.

111. Xie, J.; Ihara, M.; Jung, Y.; Kwonk, K.; Kim, S.H.; Kim, Y.H.; Mastuda, T. Mechano-active scaffold design based on microporous poly(L-lactide-co-ε-caprolactone) for articular cartilage tissue engineering: Dependence of porosity on compression force-applied mechanical behaviors. *Tissue Eng.* **2006**, *12*, 449–458.

112. Moroni, L.; de Wijn, J.R.; van Blitterswijk, C.A. 3D fiber-deposited scaffolds for tissue engineering: Influence of pores geometry and architecture on dynamic mechanical properties. *Biomaterials* **2006**, *27*, 974–985.

113. Jeong, C.G.; Hollister, S.J. Mechanical and biochemical assessments of three-dimensional poly (1,8-Octanediol-co-Citrate) scaffold pore shape and permeability effects on *in vitro* chondrogenesis using primary chondrocytes. *Tissue Eng. Part A.* **2010**, *16*, 3759–3768.

114. Chen, G.; Sato, T.; Ushida, T.; Hirochika, R.; Shirasaki, Y.; Ochiai, N.; Tateishi, T. The use of a novel PLGA fiber/collagen composite web as a scaffold for engineering of articular cartilage tissue with adjustable thickness. *J. Biomed. Mater. Res. A* **2003**, *67*, 1170–1180.

115. Waldman, S.D.; Grynpas, M.D.; Pilliar, R.M.; Kandel, R.A. The use of specific chondrocyte populations to modulate the properties of tissue-engineered cartilage. *J. Orthop. Res.* **2003**, *21*, 132–138.

116. Liao, E.; Yaszemski, M.; Krebsbach, P.; Hollister, S. Tissue-engineered cartilage constructs using composite hyaluronic acid/collagen I hydrogels and designed poly (propylene fumarate) scaffolds. *Tissue Eng.* 2007, *13*, 537–550.

117. Liao, E.E. Enhancement of Chondrogenesis by Directing Cellular Condensation through Chondroinductive Microenvironments and Designed Solid Freeform Fabricated Scaffolds. Ph.D. Thesis, University of Michigan, Ann Arbor, MI, USA, 2007.

118. Chung, T.W.; Yang, J.; Akaike, T.; Cho, K.Y.; Nah, J.W.; Kim, S.I.; Cho, C.S. Preparation of alginate/galactosylated chitosan scaffold for hepatocyte attachment. *Biomaterials* **2002**, *23*, 2827–2834.

119. Chuang, W.Y.; Young, T.H.; Yao, C.H.; Chiu, W.Y. Properties of the poly (vinyl alcohol)/chitosan blend and its effect on the culture of fibroblast *in vitro*. *Biomaterials* **1999**, *20*, 1479–1487.

120. Zhang, M.; Li, X.H.; Gong, Y.D.; Zhao, N.M.; Zhang, X.F. Properties and biocompatibility of chitosan films modified by blending with PEG. *Biomaterials* **2002**, *23*, 2641–2648.

121. Bryant, S.J.; Davis-Arehart, K.A.; Luo, N.; Shoemaker, R.K.; Arthur, J.A.; Anseth, K.S. Synthesis and characterization of photopolymerized multifunctional hydrogels: Water soluble poly (vinyl alcohol) and chondroitin sulfate macromers for chondrocyte encapsulation. *Macromolecules* **2004**, *37*, 6726–6733.

122. Kuo, Y.C.; Lin, C.Y. Effect of Genipin-crosslinked chitin-chitosan scaffolds with hydroxyapatite modifications on the cultivation of bovine knee chrondrocytes. *Biotechnol. Bioeng.* **2006**, *95*, 132–137.

123. Bryant, S.J.; Bender, R.J.; Durand, K.L.; Anseth, K.S. Encapsulating chondrocytes in degrading PEG hydrogels with high modulus: Engineering gel structural changes to facilitate cartilaginous tissue production. *Biotechnol. Bioeng*. **2004**, *86*, 747–755.

124. Fedorovich, N.E.; Alblas, J.; de Wijn, J.R.; Hennink, W.E.; Verbout, A.J.; Dhert, W.J.A. Hydrogels as extracellular matrices for skeletal tissue engineering: state-of-the-art and novel application in organ printing. *Tissue Eng.* **2007**, *13*, 1905–1925.

125. Chen, C.S.; Ingber, D.E. Tensegrity and mechanoregulation: From skeleton to cytoskeleton. *Osteoarth. Cart.* **1999**, *7*, 81–94.

126. Martin, I.; Obradovic, B.; Treppo, S.; Grodzinsky, A.J.; Langer, R.; Freed, L.E.; Vunjak-Novakovic, G. Modulation of the mechanical properties of tissue engineered cartilage. *Biorheology* **2000**, *37*, 141–147.

127. Gratz, K.R.; Wong, V.W.; Chen, A.C.; Fortier, L.A.; Nixon, A.J.; Sah, R.L. Biomechanical assessment of tissue retrieved after *in vivo* cartilage defect repair: Tensile modulus of repair tissue and integration with host cartilage. *J. Biomech.* **2006**, *39*, 138–146.

128. Natoli, R.M.; Responte, D.J.; Lu, B.Y.; Athanasiou, K.A. Effects of multiple chondroitinase ABC applications on tissue engineered articular cartilage. *J. Orthop. Res.* **2009**, *27*, 949–956.

129. Natoli, R.M.; Revell, C.M.; Athanasiou, K.A. Chondroitinase ABC treatment results in greater tensile properties of self-assembled tissue-engineered articular cartilage. *Tissue Eng. Part A* **2009**, *15*, 3119–3128.

130. Hoemann, C.D.; Sun, J.; Legare, A.; McKee, M.D.; Buschmann, M.D. Tissue engineering of cartilage using an injectable and adhesive chitosan-based cell-delivery vehicle. *Osteoarth. Cart.* **2005**, *13*, 318–329.

131. Bawolin, N.K.; Li, M.G.; Chen, X.B.; Zhang, W.J. Modeling material-degradation-induced elastic property of tissue engineering scaffolds. *J. Biomech. Eng.* **2010**, *132*, doi: 10.1115/1.4002551.

132. Liebschner, M.; Bucklen, B.; Wettergreen, M. Mechanical aspects of tissue engineering. *Semin. Plast. Surg.* **2005**, *19*, 217–228.

133. Little, C.J.; Bawolin, N.K.; Chen, X. Mechanical properties of natural cartilage and tissue-engineered constructs. *Tissue Eng. Part B Rev*. **2011**, *17*, 213–227.

134. Akizuki, S.; Mow, V.C.; Müller, F.J.; Pita, J.C.; Howell, D.S.; Manicour, D.H. Tensile properties of human knee joint cartilage: I. Influence of ionic conditions, weight bearing, and fibrillation on the tensile modulus. *J. Orthop. Res.* **1986**, *4*, 379–392.

135. Setton, L.A.; Mow, V.C.; Müller, F.J.; Pita, J.C.; Howell, D.S. Mechanical properties of canine articular cartilage are significantly altered following transection of the anterior cruciate ligament. *J. Orthop. Res.* **1994**, *12*, 451–463.

136. Elliott, D.M.; Guilak, F.; Vail, T.P.; Wang, J.Y.; Setton, L.A. Tensile properties of articular cartilage are altered by meniscectomy in a canine model of osteoarthritis. *J. Orthop. Res.* **1999**, *17*, 503–508.

137. Sakkers, R.J.B.; de Wijn, J.R.; Dalmeyer, R.A.J.; Brand, R.; van Blitterswijk, C.A. Evaluation of copolymers of polyethylene oxide and poly buthylene terephthalate (polyactives): Mechanical behaviour. *J. Mater. Sci.* **1998**, *9*, 375–379.

138. Temenoff, J.S.; Athanasiou, K.A.; Lebaron, R.G.; Mikos, A.G. Effect of poly (ethylene glycol) molecular weight on tensile and swelling properties of oligo (poly (ethylene glycol) fumarate) hydrogels for cartilage tissue engineering. *J. Biomed. Mater. Res. A* **2002**, *59*, 429–437.

139. Kempson, G.E.; Muir, H.; Pollard, C.; Tuke, M. The tensile properties of the cartilage of human femoral condyles related to the content of collagen and glycosaminoglycans. *Biochim. Biophys. Acta* **1973**, *297*, 456–472.

140. Bader, D.L.; Kempson, G.E.; Barrett, A.J.; Webb, W. The effects of leucocyte elastase on the mechanical properties of adult human articular cartilage in tension. *Biochim. Biophys. Acta*. **1981**, *677*, 103–108.

141. Mow, V.C.; Guo, X. Mechano-electrochemical properties of articular cartilage: Their inhomogeneities and anisotropies. *Annu. Rev. Biomed. Eng.* **2002**, *4*, 175–209.

142. Mow, V.C.; Gibbs, M.C.; Lai, W.M.; Zhu, W.B.; Athanasiou, K.A. Biphasic indentation of articular cartilage—II. A numerical algorithm and an experimental Study. *J. Biomech.* **1989**, *22*, 853–861.

143. Jurvelin, J.S.; Buschmann, M.D.; Hunziker, E.B. Optical and mechanical determination of poisson's ratio of adult bovine humeral articular cartilage. *J. Biomech.* **1997**, *30*, 235–241.

144. Zhu, W.; Mow, V.C.; Koob, T.J.; Eyre, D.R. Viscoelastic shear properties of articular cartilage and the effects of glycosidase treatments. *J. Orthop. Res.* **1993**, *11*, 771–781.

145. LeRoux, M.A.; Guilak, F.; Setton, L.A. Compressive and shear properties of alginate gel: Effects of sodium ions and alginate concentration. *J. Biomed. Mater. Res.* **1999**, *47*, 46–53.

146. Babensee, J.E.; Anderson, J.M.; McIntire, L.V.; Mikos, A.G. Host response to tissue engineered devices. *Adv. Drug Deliver. Rev.* **1998,** *33*, 111–139.

147. Martins, A.M,; Pham, Q.P.; Malafaya, P.B.; Raphael, R.M.; Kasper, F.K.; Reis, R.L.; Mikos, A.G. Natural stimulus responsive scaffolds/cells for bone tissue engineering: Influence of lysozyme upon scaffold degradation and osteogenic differentiation of cultured marrow stromal cells induced by CaP coatings. *Tissue Eng. Part A*. **2009**, *15*, 1953–1963.

148. Jeong, C.G.; Hollister, S.J. Mechanical, permeability, and degradation properties of 3D designed poly (1,8 octanediol-co-citrate) scaffolds for soft tissue engineering. *J. Biomed. Mater. Res. B Appl. Biomater.* **2010**, *93*, 141–149.

149. Zhang, H.; Neau, S.H. *In vitro* degradation of chitosan by a commercial enzyme preparation: effect of molecular weight and degree of deacetylation. *Biomaterials* **2001**, *22*, 1653–1658.

150. Salinas, C.N.; Anseth, K.S. The influence of the RGD peptide motif and its contextual presentation in PEG gels on human mesenchymal stem cell viability. *J. Tissue Eng. Regen. Med.* **2008**, *2*, 296–304.

151. Sahoo, S.; Chung, C.; Khetan, S.; Burdick, J.A. Hydrolytically degradable hyaluronic acid hydrogels with controlled temporal structures. *Biomacromolecules* **2008**, *9*, 1088–1092.

152. Chung, C.; Beecham, M.; Mauck, R.L.; Burdick, J.A. The influence of degradation characteristics of hyaluronic acid hydrogels on *in vitro* neocartilage formation by mesenchymal stem cells. *Biomaterials* **2009**, *30*, 4287–4296.

153. Middleton, J.C.; Tipton, A.J. Synthetic biodegradable polymers as orthopedic devices. *Biomaterials* **2000**, *21*, 2335–2346.

154. Wu, L.B.; Ding, J.D. *In vitro* degradation of three-dimensional porous poly (D,L-lactide-co-glycolide) scaffolds for tissue engineering. *Biomaterials* **2004**, *25*, 5821–5830.

155. Kofron, M.D.; Griswold, A.; Kumbar, S.G.; Martin, K.; Wen, X.; Laurencin, C.T. The implications of polymer selection in regenerative medicine: A comparison of amorphous and semi-crystalline polymer for tissue regeneration. *Adv. Funct. Mater.* **2009**, *19*, 1351–1359.

156. Pan, Z.; Ding, J. Engineering and regenerative medicine poly (lactide-co-glycolide) porous scaffolds for tissue. *Interface Focus* **2012**, *2*, 366–377.

157. Yang, Y.; Zhao, Y.; Tang, G.; Li, H.; Yuan, X.; Fan, Y. *In vitro* degradation of porous poly (L-lactide-co-glycolide)/b-tricalcium phosphate (PLGA/b-TCP) scaffolds under dynamic and static conditions. *Polym. Degrad. Stabil.* **2008**, *93*, 1838–1845.

158. Yoshioka, T.; Kawazoe, N.; Tateishi, T.; Chen, G. *In vitro* evaluation of biodegradation of poly (lactic-coglycolic acid) sponges. *Biomaterials* **2008**, *29*, 3438–3443.

159. Odelius, K.; Hoglund, A.; Kumar, S.; Hakkarainen, M.; Ghosh, A.K.; Bhatnagar, N.; Albertsson, A.-C. Porosity and pore size regulate the degradation product profile of polylactide. *Biomacromolecules* **2011**, *12*, 1250–1258.

160. Wu, L.B.; Ding, J.D. Effects of porosity and pore size on in vitro degradation of three-dimensional porous poly (D,L-lactide-co-glycolide) scaffolds for tissue engineering. *J. Biomed. Mater. Res. Part A* **2005**, *75*, 767–777.

161. Sawhney, A.S.; Pathak, C.P.; Hubbell, J.A. Bioerodible hydrogels based on photopolymerized poly (ethylene glycol)-co-poly(alpha-hydroxy acid) diacrylate macromers. *Macromolecules* **1993**, *26*, 581–587.

162. Wang, W.; Li, B.; Li, Y.; Jiang, Y.; Ouyang, H.; Gao, C. *In vivo* restoration of full-thickness cartilage defects by poly (lactide-co-glycolide) sponges filled with fibrin gel, bone marrow mesenchymal stem cells and dna complexes. *Biomaterials* **2010**, *31*, 5953–5965.

163. Yu, L.; Zhang, Z.; Zhang, H.; Ding, J. Biodegradability and biocompatibility of thermoreversible hydrogels formed from mixing a sol and a precipitate of block copolymers in water. *Biomacromolecules* **2010**, *11*, 2169–2178.

164. Zhang, Z.; Ni, J.; Chen, L.; Yu, L.; Xu, J.; Ding, J. Biodegradable and thermoreversible PCLA-PEG-PCLA hydrogel as a barrier for prevention of post-operative adhesion. *Biomaterials* **2011**, *32*, 4725–4736.

165. Edwards, S.L.; Mitchell, W.; Matthews, J.B.; Ingham, E.; Russell, S.J. Design of nonwoven scaffolds structures for tissue engineering of the anterior cruciate ligament. *AUTEX Res. J.***2004**, *4*, 86–94.

166. Lu, L.; Mikos, A. The importance of new processing techniques in tissue engineering. *MRS Bull.* **1996**, *21*, 28–32.

167. Whang, K.; Thomas, C.H.; Healy, K.E.; Nuber, G. A novel method to fabricate bioabsorbable scaffolds. *Polymers* **1995**, *36*, 837–842.

168. Whang, K.; Tsai, D.C.; Nam, E.K.; Aitken, M.; Sprague, S.M.; Patel, P.K.; Healy, K.E. Ectopic bone formation via rhBMP-2 Delivery from porous bioresorbable polymer scaffolds. *J. Biomed. Mater. Res.* **1998**, *42*, 491–499.

169. Sachlos, E.; Czernuszka, J.T. Making tissue engineering scaffolds work. Review: The application of solid freeform fabrication technology to the production of tissue engineering scaffolds. *Eur. Cell. Mater.* **2003**, *5*, 29–39.

170. Kim, J.; Reneker, D.H. Mechanical properties of composites using ultrafine electrospun fibers. *Polym. Comp.* **1999**, *20*, 124–131.

171. Sittinger, M.; Bujia, J.; Rotter, N.; Reitzel, D.; Minuth, W.W.; Burmester, G.R. Tissue engineering and autologous transplant formation: practical approaches with resorbable biomaterials and new cell culture techniques. *Biomaterials* **1996**, *17*, 237–242.

172. Soliman, S.; Sant, S.; Nichol, J.W.; Khabiry, M.; Traversa, E.; Khademhosseini, A. Controlling the porosity of fibrous scaffolds by modulating the fiber diameter and packing density.
J. Biomed. Mater. Res. A **2011**, *96*, 566–574.

173. Nerurkar, N.L.; Sen, S.; Baker, B.M.; Elliott, D.M.; Mauck, R.L. Dynamic culture enhances stem cell infiltration and modulates extracellular matrix production on aligned electrospun nanofibrous scaffolds. *Acta Biomate.* **2011**, *7*, 485–491.

174. Li, W.J.; Mauck, R.L.; Cooper, J.A.; Yuan, X.; Tuan, R.S. Engineering controllable anisotropy in electrospun biodegradable nanofibrous scaffolds for musculoskeletal tissue engineering.
J. Biomech. **2007**, *40*, 1686–1693.

175. Dalton, P.D.; Joergensen, N.T.; Groll, J.; Moeller, M. Patterned melt electrospun substrates for tissue engineering. *Biomed. Mater.* **2008**, *3*, doi:10.1088/1748-6041/3/3/034109.

176. Dalton, P.D.; Klinkhammer, K.; Salber, J.; Klee, D.; Möller, M. Direct *in vitro* electrospinning with polymer melts. *Biomacromolecules* **2006**, *7*, 686–690.

177. Moroni, L.; Hendriks, J.A.A.; Schotel, R.; de Wijn, J.R.; van Blitterswijk, C.A. Design of biphasic polymeric 3-Dimensional fiber deposited scaffolds for cartilage tissue engineering applications. *Tissue Eng.* **2007**, *13*, 361–371.

178. Shao, X.; Goh, J.C.H.; Hutmacher, D.W.; Lee, E.H.; Zigang, G. Repair of large articular osteochondral defects using hybrid scaffolds and bone marrow-derived mesenchymal stem cells in a rabbit model. *Tissue Eng.* **2006**, *12*, 1539–1551.

179. Vozzi, G.; Flaim, C.; Ahluwalia, A.; Bhatia, S. Fabrication of PLGA scaffolds using soft lithography and microsyringe deposition. *Biomaterials* **2003**, *24*, 2533–2540.

180. Wiria, F.E.; Chua, C.K.; Leong, K.F.; Quah, Z.Y.; Chandrasekaran, M.; Lee, M.W. Improved biocomposite development of poly(vinyl alcohol) and hydroxyapatite for tissue engineering scaffold fabrication using selective laser sintering. *J. Mater. Sci. Mater. Med.* **2008**, *19*, 989–996.

181. Ramanath, H.S.; Chandrasekaran, M.; Chua, C.K.; Leong, K.F.; Shah, K.D. Melt flow behaviour of poly-ε-caprolactone in fused deposition modeling. *J. Mater. Sci. Mater. Med.* **2008**, *19*, 2541–2550.

182. Sudarmadji, N.; Tan, J.Y.; Leong, K.F.; Chua, C.K.; Loh, Y.T. Investigation of the mechanical properties and porosity relationships in selective laser-sintered polyhedral for functionally graded scaffolds. *Acta Biomater.* **2011**, *7*, 530–537.

183. Landers, R.; Mulhaupt, R. Desktop manufacturing of complex objects, prototypes and biomedical scaffolds by means of computer-assisted design combined with computer-guided 3d plotting of polymers and reactive oligomers. *Macromolec. Mater. Eng.* **2000**, *282*, 17–21.

184. Sobral, J.M.; Caridade, S.G.; Sousa, R.A.; Mano, J.F.; Reis, R.L. Three-dimensional plotted scaffolds with controlled pore size gradients: Effect of scaffold geometry on mechanical performance and cell seeding efficiency. *Acta Biomater.* **2011**, *7*, 1009–1018.

185. Maher, P.S.; Keatch, R.P.; Donnelly, K. Characterisation of rapid prototyping techniques for studies in cell behaviour. *Rapid Prototyp. J.* **2010**, *16*, 116–123.

186. Melchels, F.P.W.; Barradas, A.M.C.; van Blitterswijk, C.A.; de Boer, J.; Feijen, J.; Grijpma, D.W. Effects of the architecture of tissue engineering scaffolds on cell seeding and culturing. *Acta Biomater.* **2010**, *6*, 4208–4217.

187. Chua, C.K.; Liu, M.J.J.; Chou, S.M. Additive manufacturing-assisted scaffold-based tissue engineering. In *Innovative Developments in Virtual and Physical Prototyping*, Proceedings of the 5th International Conference on Advanced Research in Virtual and Rapid Prototyping, Leiria, Portugal, 28 September–1 October 2011; Bartolo, P.J., Ed.; CRC Press: London, UK, 2011.

188. Saunders, R.E.; Gough, J.E.; Derby, B. Delivery of human fibroblast cells by piezoelectric drop-on-demand inkjet printing. *Biomaterials* **2008**, *292*, 193–203.

189. Miller, E.D.; Li, K.; Kanade, T.; Weiss, L.E.; Walker, L.M.; Campbell, P.G. Spatially directed guidance of stem cell population migration by immobilized patterns of growth factors. *Biomaterials* **2011**, *32*, 2775–2785.

190. Duan, B.; Wang, M.; Zhou, W.Y.; Cheung, W.L.; Li, Z.Y.; Lu, W.W. Three-dimensional nanocomposite scaffolds fabricated via selective laser sintering for bone tissue engineering. *Acta Biomater.* **2010**, *6*, 4495–4505.

191. Li, X.; Li, D.; Lu, B.; Wang, C. Fabrication of bioceramic scaffolds with pre-designed internal architecture by gel casting and indirect stereolithography techniques. *J. Porous Mater.* **2008**, *15*, 667–671.

192. Taboas, J.M.; Maddox, R.D.; Krebsbach, P.H.; Hollister, S.J. Indirect solid free form fabrication of local and global porous, biomimetic and composite 3D polymer-ceramic scaffolds. *Biomaterials* **2003**, *24*, 181–194.

193. Vozzi, G. Microsyringe-based deposition of two-dimensional and three-dimensional polymer scaffolds with a well-defined geometry for application to tissue engineering. *Tissue Eng.* **2002**, *8*, 1089–1098.

194. Landers, R.; Pfister, A.; Hubner, U.; John, H.; Schmelzeisen, R.; Mulhaupt, R. Fabrication of soft tissue engineering scaffolds by means of rapid prototyping techniques. *J. Mater. Sci.* **2002**, *37*, 3107–3116.

195. Schuurman, W.; Khristov, V.; Pot, M.W.; van Weeren, P.R.; Dhert, W.J.A.; Malda, J. Bioprinting of hybrid tissue constructs with tailorable mechanical properties. *Biofabrication* **2011**, *3*, 021001.

196. Shim, J.H.; Kim, J.Y.; Park, M.; Park, J.; Cho, D.W. Development of a hybrid scaffold with synthetic biomaterials and hydrogel using solid freeform fabrication technology. *Biofabrication* **2011**, *3*, 034102.

197. Martin, I.; Wendt, D.; Heberer, M. The role of bioreactors in tissue engineering. *Trends Biotechnol.* **2004**, *22*, 80–86.

198. Wendt, D.; Marsano, A.; Jakob, M.; Heberer, M.; Martin, I. Oscillating perfusion of cell suspensions through three-dimensional scaffolds enhances cell seeding efficiency and uniformity. *Biotechnol. Bioeng.* **2003**, *84*, 205–214.

199. Davisson, T.; Sah, R.L.; Ratcliffe, A. Perfusion increases cell content and matrix synthesis in chondrocyte three-dimensional cultures. *Tissue Eng.* **2002**, *8*, 807–816.

200. Vlasea, M.; Shanjani, Y.; Basalah, A.; Toyserkani, E. Additive manufacturing of scaffolds for tissue engineering of bone and cartilage: Review. *IJAMS* **2011**, *13*, 123–141.

201. Melchels, F.P.W.; Domingos, M.A.N.; Klein, T.J.; Malda, J.; Bartolo, P.J.; Hutmacher, D.W. Additive manufacturing of tissues and organs. *Prog. Polym. Sci.* **2012**, *37*, 1079–1104.

202. Sittinger, M.; Reitzel, D.; Dauner, M.; Hierlemann, H.; Hammer, C.; Kastenbauer, E.; Planck, H.; Burmester, G.R.; Bujia, J. Resorbable polyesters in cartilage engineering: Affinity and biocompatibility of polymer fiber structures to chondrocytes. *J. Biomed. Mater. Res. Appl. Biomater.* **1996**, *33*, 57–63.

203. Stankus, J.J.; Guan, J.; Fujimoto, K.; Wagner, W.R. Microintegrating smooth muscle cells into a biodegradable, elastomeric fiber matrix. *Biomaterials* **2006**, *27*, 735–744.

204. Baker, B.M.; Gee, A.O.; Metter, R.B.; Nathan, A.S.; Marklein, R.A.; Burdick, J.A. The potential to improve cell infiltration in composite fiber-aligned electrospun scaffolds by the selective removal of sacrificial fibers. *Biomaterials* **2008**, *29*, 2348–2358.

205. Nam, J.; Huang, Y.; Agarwal, S.; Lannutti, J. Improved cellular infiltration in electrospun fiber via engineered porosity. *Tissue Eng.* **2007**, *13*, 2249–2257.

206. Baker, B.M.; Mauck, R.L. The effect of nanofiber alignment on the maturation of engineered meniscus constructs. *Biomaterials* **2007**, *28*, 1967–1977.

207. Baker, B.M.; Nathan, A.S.; Huffman, G.R.; Mauck, R.L. Tissue engineering with meniscus cells derived from surgical debris. *Osteoarth. Cart.* **2009**, *17*, 336–345.

208. Li, W.J.; Jiang, Y.J.; Tuan, R.S. Cell-nanofiber-based cartilage tissue engineering using improved cell seeding, growth factor, and bioreactor technologies. *Tissue Eng. Part A* **2008**, *14*, 639–648.

209. Yousefi, A.M.; Gauvin, C.; Sun, L.; DiRaddo, R.W.; Fernandes, J. Design and fabrication of
3D-plotted polymeric scaffolds in functional tissue engineering. *Polym. Eng. Sci.* **2007**, *47*, 608–618.

210. Envision TEC BioPlotter V4. Altair Consulting Website. Available online: http://www.altair-consulting.com/envisiontec_bioplotter_v4.htm (accessed on May 2011).

211. Caterson, E.J.; Nesti, L.J.; Li, W.J.; Danielson, K.G.; Albert, T.J.; Vaccaro, A.R.; Tuan, R.S. Three-dimensional cartilage formation by bone marrow-derived cells seeded ion polylactide/alginate amalgam. *J. Biomed. Mater. Res.* **2001**, *57*, 394–403.

212. Ameer, G.A.; Mahmood, T.A.; Langer, R. A biodegradable composite scaffold for cell transplantation. *J. Orthop. Res.* **2002**, *20*, 16–19.

213. Marijnissen, W.J.; van Osch, G.J.; Aigner, J.; Verwoerd-Verhoef, H.L.; Verhaar, J.A. Tissue-engineered cartilage using serially passaged articular chondrocytes. Chondrocytes in alginate, combined *in vivo* with a synthetic (E210) or biologic biodegradable carrier (DBM). *Biomaterials* **2000**, *21*, 571–580.

214. Dai, W.; Kawazoe, N.; Lin, X.; Dong, J.; Chen, G. The influence of structural design of PLGA/collagen hybrid scaffolds in cartilage tissue engineering. *Biomaterials* **2010**, *31*, 2141–2152.

215. Shahin, K. *In Vitro* Production of Human Hyaline Cartilage using Tissue Engineering. Ph.D. Thesis, University of New South Wales, Sydney, Australia, 2008.

216. Wayne, J.S.; McDowell, C.L.; Shields, K.J.; Tuan, R.S. *In vivo* response of polylactic acid-alginate scaffolds and bone marrow-derived cells for cartilage tissue engineering. *Tissue Eng.* **2005**, *11*, 953–963.

217. Sang, Y.H.; Lee, E.A.; Yoon, J.J.; Park, T.G. Hyaluronic acid modified biodegradable scaffolds for cartilage tissue engineering. *Biomaterials* **2005**, *26*, 1925–1933.

218. Wang, W.; Li, B.; Yang, J.; Xin, L.; Li, Y.; Yin, H.; Qi, Y.; Jiang, Y.; Ouyang, H.; Gao, C. The restoration of full-thickness cartilage defects with bmscs and tgf-beta 1 loaded PLGA/Fibrin gel constructs. *Biomaterials* **2010**, *31*, 8964–8973.

219. Schek, R.M.; Taboas, J.M.; Segvich, S.J.; Hollister, S.J.; Krebsbach, P.H. Engineered osteochondral grafts using biphasic composite solid free-form fabricated scaffolds. *Tissue Eng.* **2004**, *10*, 1376–1385.

220. Jung, Y.; Kim, S.H.; Kim, Y.H.; Kim, S.H. The effect of hybridization of hydrogels and poly (L-lactide-co-epsilon-caprolactone) scaffold on cartilage tissue engineering. *J. Biomat. Sci. Polym. E* **2010**, *21*, 581–592.

221. Kawazoe, N.; Inoue, C.; Tateishi, T.; Chen, G. A cell leakproof PLGA-collagen hybrid scaffold for cartilage tissue engineering. *Biotechnol. Prog*. **2010**, *26*, 819–826.

222. Chen, G.; Sato, T.; Ushida, T.; Ochiai, N.; Tateishi, T. Tissue engineering of cartilage using a hybrid scaffold of synthetic polymer and collagen. *Tissue Eng.* **2004**, *10*, 323–330.

223. Hiraoka, Y.; Kimura, Y.; Ueda, H.; Tabata, Y. fabrication and biocompatibility of collagen sponge reinforced with poly (glycolic acid) fiber. *Tissue Eng*. **2003**, *9*, 1101–1112.

224. Jung, Y.; Kim, S.-H.; Kim, Y.H.; Kim, S.H. The effects of dynamic and three-dimensional environments on chondrogenic differentiation of bone marrow stromal cells source. *Biomed. Mater.* **2009**, *4*, doi:10.1088/1748-6041/4/5/055009.

225. Lee, H.; Yeo, M.; Ahn, S.; Kang, D.O.; Jang, C.H.; Lee, H.; Park, G.M.; Kim, G.H. Designed hybrid scaffolds consisting of polycaprolactone microstrands and electrospun collagen-nanofibers for bone tissue regeneration. *J. Biomed. Mater. Res. B Appl. Biomater.* **2011**, *97*, 263–270.

226. Klein, T.J.; Schumacher, B.L.; Schmidt, T.A.; Li, K.W.; Voegtline, M.S.; Masuda, K.; Thonar, E.J.; Sah, R.L. Tissue engineering of stratified articular cartilage from chondrocyte subpopulations. *Osteoarth. Cart.* **2003**, *11*, 595–602.

227. Yu, H.; Grynpas, M.; Kandel, R.A. Composition of cartilagenous tissue with mineralized and non-mineralized zones formed *in vitro*. *Biomaterials* **1997**, *18*, 1425–1432.

228. Hu, J.C.; Athanasiou, K.A. A self-assembling process in articular cartilage tissue engineering. *Tissue Eng*. **2006**, *12*, 969–979.

229. Elder, B.D.; Athanasiou, K.A. Effects of temporal hydrostatic pressure on tissue-engineered bovine articular cartilage constructs. *Tissue Eng. Part A* **2009**, *15*, 1151–1158.

230. Elder, S.H.; Cooley, A.J., Jr.; Borazjani, A.; Sowell, B.L.; To, H.; Tran, S.C. Production of hyaline-like cartilage by bone marrow mesenchymal stem cells in a self-assembly model. *Tissue Eng. Part A* **2009**, *15*, 3025–3036.

231. Ofek, G.; Revell, C.M.; Hu, J.C.; Allison, D.D.; Grande-Allen, K.J.; Athanasiou, K.A. Matrix development in self-assembly of articular cartilage. *PLoS One* **2008**, *3*, e2795.

232. Jakab, K.; Norotte, C.; Marga, F.; Murphy, K.; Vunjak-Novakovic, G.; Forgacs, G. Tissue engineering by self-assembly and bio-printing of living cells. *Biofabrication* **2010**, *2*, 022001.

233. Wise, J.K.; Yarin, A.L.; Megaridis, C.M.; Cho, M. Chondrogenic differentiation of human mesenchymal stem cells on oriented nanofibrous scaffolds: engineering the superficial zone of articular cartilage. *Tissue Eng. A* **2009**, *15*, 913–921.

234. Ng, K.; Wang, C.C.; Guo, X.E.; Ateshian, G.A.; Hung, C.T. Characterization of inhomogeneous Bi-layered chondrocyte-seeded agarose constructs of differing agarose concentrations. In *Transactions of the Orthopedic Research Society*, Proceedings of 49th Annual Meeting; Orthopedic Research Society, Chicago, III, Ed.; The Orthopedic Research Society: New Orleans, LA, USA, 2003, Volume 28, Abstract no. 960.

235. Ng, K.W.; Wang, C.C.; Mauck, R.L.; Kelly, T.N.; Chahine, N.O.; Costa, K.D.; Ateshian, G.A.; Hung, C.T. A Layered agarose approach to fabricate depth-dependent inhomogeneity in chondrocyte-seeded constructs. *J. Orthop. Res.* **2005**, *23*, 134–141.

236. Kim, T.K.; Sharma, B.; Williams, C.G.; Ruffner, M.A.; Malik, A.; McFarland, E.G.; Elisseeff, J.H. Experimental model for cartilage tissue engineering to regenerate the zonal organization of articular cartilage. *Osteoarth. Cart.* **2003**, *11*, 653–664.

237. Sharma, B.; Williams, C.G.; Kim, T.K.; Malik, A.; Elisseeff, J.H. Multi-layered hydrogel constructs recreate zonal organization of articular cartilage. In *Transactions of the Orthopedic Research Society*, Proceedings of the 49th Annual Meeting, Orthopedic Research Society, Chicago, III, Ed.; The Orthopedic Research Society: New Orleans, LA, Volume 28, 2003, Abstract no. 948.

238. Klein, T.J.; Schumacher, B.L.; Li, K.W.; Voegtline, M.; Masuda, K.; Thonar, E.J.; Sah, R.L. Tissue engineered articular cartilage with functional stratification: Targeted delivery of chondrocytes expressing superficial zone protein. In *Transactions of the Orthopedic Research Society*, Proceedings of 48th Annual Meeting, Orthopedic Research Society, Chicago, III, Ed.; The Orthopedic Research Society: Dallas, TX, USA, 2002, Volume 27, abstract no.212.

239. Nguyen, L.H.; Kudva, A.K.; Guckert, N.L.; Linse, K.D.; Roy, K. Unique biomaterial compositions direct bone marrow stem cells into specific chondrocytic phenotypes corresponding to the various zones of articular cartilage. *Biomaterials* **2011**, *32*, 1327–1338.

240. Thomson, B.; Smith, M.; Boyer, S.; Turner, R.; Kidd, D.; Riggs, H.; Dowthwaite, G.; Archer, C. Coated biomaterials, zonal cell-seeding and cartilage tissue engineering. In *Transactions of the Orthopedic Research Society*, Proceedings of 48th Annual Meeting, Orthopedic Research Society, Chicago, III, Ed.; The Orthopedic Research Society: Dallas, TX, USA, 2002. Volume 27, abstract no. 477.

241. Hwang, N.S.; Varghese, S.; Janice, H.L.; Theprungsirikul, P.; Canver, A.; Sharma, B.; Elisseeff, J. Response of zonal chondrocytes to extracellular matrix-hydrogels. *FEBS Lett.* **2007**, *581*, 4172–4178.

242. Ng, K.W.; Ateshian, G.A.; Hung, C.T. Zonal chondrocytes seeded in a layered agarose hydrogel create engineered cartilage with depth-dependent cellular and mechanical inhomogeneity. *Tissue Eng. Part A* **2009**, *15*, 2315–2324.

243. Sharma, B.; Williams, C.G.; Kim, T.K.; Sun, D.; Malik, A.; Khan, M.; Leong, K.; Elisseeff, J.H. Designing zonal organization into tissue-engineered cartilage. *Tissue Eng.* **2007**, *13*, 405–414.

244. Gillette, B.M.; Rossen, N.S.; Das, N.; Leong, D.; Wang, M.; Dugar, A.; Sia, S.K. Engineering extracellular matrix structure in 3D multiphase tissues. *Biomaterials* **2011**, *32*, 8067–8076.

245. Grayson, W.L.; Bhumiratana, S.; Grace-Chao, P.H.; Hung, C.T.; Vunjak-Novakovic, G. Spatial regulation of human mesenchymal stem cell differentiation in engineered osteochondral constructs: Effects of pre-differentiation, soluble factors and medium perfusion. *Osteoarth. Cart.* **2010**, *18*, 714–723.

246. Erisken, C.; Kalyon, D.M.; Wang, H. Functionally graded electrospun polycaprolactone and beta-tricalcium phosphate nanocomposites for tissue engineering applications. *Biomaterials* **2008**, *29*, 4065–4073.

247. O'Shea, T.M.; Miao, X. Bilayered scaffolds for osteochondral tissue engineering. *Tissue Eng. Part B Rev.* **2008**, *14*, 447–464.

248. Jeon, J.E.; Schrobback, K.; Hutmacher, D.W.; Klein, T.J. Dynamic compression improves biosynthesis of human zonal chondrocytes from osteoarthritis patients. *Osteoarth. Cart.* **2012**, *20*, 906–915.

249. Marsano, A.; Wendt, D.; Quinn, T.M.; Sims, T.J.; Farhadi, J.; Jakob, M.; Heberer, M.; Martin, I. Bi-zonal cartilaginous tissues engineered in a rotary cell culture system. *Biorheology* **2006**, *43*, 553–560.

250. Mizuno, S. A novel method for assessing effects of hydrostatic fluid pressure on intracellular calcium: A study with bovine articular chondrocytes. *Am. J. Physiol. Cell. Physiol.* **2005**, *288*, C329–C337.

251. Klein, T.J.; Rizzi, S.C.; Reichert, J.C.; Georgi, N.; Malda, J.; Schuurman, W.; Crawford, R.W.; Hutmacher, D.W. Strategies for zonal cartilage repair using hydrogels. *Macromol. Biosci.* **2009**, *9*, 1049–1058.

252. Laasanen, M.S.; Toyras, J.; Korhonen, R.K.; Rieppo, J.; Saarakkala, S.; Nieminen, M.T.; Hirvonen, J.; Jurvelin, J.S. Biomechanical properties of knee articular cartilage. *Biorheology* **2003**, *40*, 133–140.

253. Gepp, M.M.; Ehrhart, F.; Shirley, S.G.; Howitz, S.; Zimmermann, H. Dispensing of very low volumes of ultra high viscosity alginate gels: A new tool for encapsulation of adherent cells and rapid prototyping of scaffolds and implants. *Biotechniques* **2009**, *46*, 31–34.

254. Tonde, M.P. Retrofitting a stereolithography system within a laminar flow hood. ETD Collection for University of Texas, El Paso. Paper AAI1473894. Avaliable online: http://digitalcommons.utep.edu/dissertations/AAI1473894 (accessed on 8 September, 2012)

255. Ostrander, R.V.; Goomer, R.S.; Tontz, W.L.; Khatod, M.; Harwood, F.L.; Maris, T.M.; Amiel, D. Donor cell fate in tissue engineering for articular cartilage repair. *Clin. Orthop. Relat. Res.* **2001**, *389*, 228–237.

256. Mierisch, C.M.; Wilson, H.A.; Turner, M.A.; Milbrandt, T.A.; Berthoux, L.; Hammarskjold, M.L.; Rekosh, D.; Balian, G.; Diduch, D.R. Chondrocyte transplantation into articular cartilage defects with use of calcium alginate: The fate of the cells. *J. Bone Joint Surg. Am.* **2003**, *85A*, 1757–1767.

257. Zehbe, R.; Haibel, A.; Riesemeier, H.; Gross, U.; Kirkpatrick, C.J.; Schubert, H.; Brochhausen, C. Going beyond histology. Synchrotron micro-computed tomography as a methodology for biological tissue characterization: from tissue morphology to individual cells. *J R Soc Interface* **2010**, 7, 49-59.

258. Cahalan, M.D.; Parker, I.; Wei, S.H.; Miller, M.J. Two-photon tissue imaging: seeing the immune system in a fresh light. *Nat Rev Immunol* **2002**, 2, 872-880.

259. Minsky, M., *Microscopy apparatus*. 1961, Google Patents.

260. DeRosier, D.; Klug, A. Reconstruction of three dimensional structures from electron micrographs. *Nature* **1968**, 217, 130-134.

261. Muehleman, C.; Majumdar, S.; Issever, A.S.; Arfelli, F.; Menk, R.H.; Rigon, L.; Heitner, G.; Reime, B.; Metge, J.; Wagner, A.; Kuettner, K.E.; Mollenhauer, J. X-ray detection of structural orientation in human articular cartilage. *Osteoarthritis Cartilage* **2004**, 12, 97-105.

262. Othman, S.F.; Li, J.; Abdullah, O.; J Moinnes, J.; L Magin, R.; Muehleman, C. High-resolution/high-contrast MRI of human articular cartilage lesions. *Acta orthop* **2007**, 78, 536-546.

263. Xia, Y.; Moody, J.; Burton-Wurster, N.; Lust, G. Quantitative in situ correlation between microscopic MRI and polarized light microscopy studies of articular cartilage. *Osteoarthritis and Cartilage* **2001**, 9, 393-406.

264. Kotecha, M.; Klatt, D.; Magin, R.L. Monitoring cartilage tissue engineering using magnetic resonance spectroscopy, imaging, and elastography. *Tissue Eng Part B Rev* **2013**, 19, 470-484.

265. Kwack, K.S.; Cho, J.H.; Kim, M.M.; Yoon, C.S.; Yoon, Y.S.; Choi, J.W.; Kwon, J.W.; Min, B.H.; Sun, J.S.; Kim, S.Y. Comparison study of intraarticular and intravenous gadolinium-enhanced magnetic resonance imaging of cartilage in a canine model. *Acta Radiol* **2008**, 49, 65-74.

266. Tarhan, S.; Unlu, Z. Magnetic resonance imaging and ultrasonographic evaluation of the patients with knee osteoarthritis: a comparative study. *Clin Rheumatol* **2003**, 22, 181-188.

267. Muehleman, C.; Chapman, L.D.; Kuettner, K.E.; Rieff, J.; Mollenhauer, J.A.; Massuda, K.; Zhong, Z. Radiography of rabbit articular cartilage with diffraction-enhanced imaging. *Anat Rec A Discov Mol Cell Evol Biol* **2003**, 272, 392-397.

268. Walker, J.; Myers, A.; Schluchter, M.; Goldberg, V.; Caplan, A.; Berilla, J.; Mansour, J.; Welter, J. Nondestructive Evaluation of Hydrogel Mechanical Properties Using Ultrasound. *Ann Biomed Eng* **2011**, 39, 2521-2530.

269. Kohles, S.S.; Mason, S.S.; Adams, A.P.; Berg, R.J.; Blank, J.; Gibson, F.; Righetti, J.; Washington, I.S.; Saha, A.K. Ultrasonic wave propagation assessment of native cartilage explants and hydrogel scaffolds for tissue engineering. *Int J Biomed Eng Technol* **2012**, 10, 296-307.

270. Hattori, K.; Takakura, Y.; Ohgushi, H.; Habata, T.; Uematsu, K.; Ikeuchi, K. Novel ultrasonic evaluation of tissue-engineered cartilage for large osteochondral defects--non-invasive judgment of tissue-engineered cartilage. *J Orthop Res* **2005**, 23, 1179-1183.

271. Hattori, K.; Takakura, Y.; Ohgushi, H.; Habata, T.; Uematsu, K.; Yamauchi, J.; Yamashita, K.; Fukuchi, T.; Sato, M.; Ikeuchi, K. Quantitative ultrasound can assess the regeneration process of tissue-engineered cartilage using a complex between adherent bone marrow cells and a three-dimensional scaffold. *Arthritis Res Ther* **2005**, 7, R552-559.

272. Wolbarst, A.B., *Physics of radiology*. 1993: McGraw-Hill/Appleton & Lange.

273. Bewer, B.; Zhang, H.; Zhu, Y.; Zhang, L.; George, G.N.; Pickering, I.J.; Chapman, D. Development of a combined K-edge subtraction and fluorescence subtraction imaging system for small animals. *Rev Sci Instrum* **2008**, 79, 085102.

274. Astolfo, A.; Arfelli, F.; Schültke, E.; James, S.; Mancini, L.; Menk, R.-H. A detailed study of gold-nanoparticle loaded cells using X-ray based techniques for cell-tracking applications with single-cell sensitivity. *Nanoscale* **2013**, 5, 3337-3345.

275. Astolfo, A.; Schultke, E.; Menk, R.H.; Kirch, R.D.; Juurlink, B.H.; Hall, C.; Harsan, L.A.; Stebel, M.; Barbetta, D.; Tromba, G.; Arfelli, F. In vivo visualization of gold-loaded cells in mice using x-ray computed tomography. *Nanomedicine* **2013**, 9, 284-292.

276. Zehbe, R.; Haibel, A.; Brochhausen, C.; Gross, U.; Kirkpatrick, C.J.; Schubert, H. Characterization of oriented protein-ceramic and protein-polymer-composites for cartilage tissue engineering using synchrotron μ-CT. *Int J Mater Res* **2007**, 98, 562-568.

277. Chapman, D.; Thomlinson, W.; Johnston, R.E.; Washburn, D.; Pisano, E.; Gmur, N.; Zhong, Z.; Menk, R.; Arfelli, F.; Sayers, D. Diffraction enhanced x-ray imaging. *Phys Med Biol* **1997**, 42, 2015-2025.

278. Momose, A.; Fukuda, J. Phase-contrast radiographs of nonstained rat cerebellar specimen. *Med Phys* **1995**, 22, 375-379.

279. Momose, A.; Takeda, T.; Itai, Y.; Hirano, K. Phase-contrast X-ray computed tomography for observing biological soft tissues. *Nat Med* **1996**, 2, 473-475.

280. Snigirev, A.; Snigireva, I.; Kohn, V.; Kuznetsov, S.; Schelokov, I. On the possibilities of x-ray phase contrast microimaging by coherent high-energy synchrotron radiation. *Rev Sci Instrum* **1995**, 66, 5486-5492.

281. Pfeiffer, F.; Weitkamp, T.; Bunk, O.; David, C. Phase retrieval and differential phase-contrast imaging with low-brilliance X-ray sources. *Nat Phys* **2006**, 2, 258-261.

282. Cooper, D.M.; Chapman, L.D.; Carter, Y.; Wu, Y.; Panahifar, A.; Britz, H.M.; Bewer, B.; Zhouping, W.; Duke, M.J.; Doschak, M. Three dimensional mapping of strontium in bone by dual energy K-edge subtraction imaging. *Phys Med Biol* **2012**, 57, 5777-5786.

283. Chien, C.C.; Chen, H.H.; Lai, S.F.; Wu, K.C.; Cai, X.; Hwu, Y.; Petibois, C.; Chu, Y.; Margaritondo, G. Gold nanoparticles as high-resolution X-ray imaging contrast agents for the analysis of tumor-related micro-vasculature. *J Nanobiotechnology* **2012**, 10, 10.

284. Dilmanian, F. Computed tomography with monochromatic x rays. *Am J Physiol Imaging* **1991**, 7, 175-193.

285. Bonse, U.; Hart, M. An X-ray interferometer with Bragg case beam splitting and beam recombination. *Z Phys* **1966**, 194, 1-17.

286. Bernhardt, R.; Scharnweber, D.; Müller, B.; Thurner, P.; Schliephake, H.; Wyss, P.; Beckmann, F.; Goebbels, J.; Worch, H. Comparison of microfocus-and synchrotron X-ray tomography for the analysis of osteointegration around Ti6Al4V implants. *Eur Cell Mater* **2004**, 7, C0.

287. Meuli, R.; Hwu, Y.; Je, J.H.; Margaritondo, G. Synchrotron radiation in radiology: radiology techniques based on synchrotron sources. *Eur Radiol* **2004**, 14, 1550-1560.

288. Guldberg, R.E.; Duvall, C.L.; Peister, A.; Oest, M.E.; Lin, A.S.; Palmer, A.W.; Levenston, M.E. 3D imaging of tissue integration with porous biomaterials. *Biomaterials* **2008**, 29, 3757-3761.

289. Zhu, N.; Chen, X.B.; Chapman, D. A brief review of visualization for nerve tissue engineering applications. *J Biomim Biomater Tissue Eng* **2010**, 7, 81-99.

290. Hendee, W.R.; Cleary, K.; Ehman, R.L.; Fullerton, G.D.; Grundfest, W.S.; Haller, J.; Kelley, C.A.; Meyer, A.E.; Murphy, R.F.; Phillips, W.; Torchilin, V.P. Bioengineering and imaging research opportunities workshop V: summary of findings on imaging and characterizing structure and function in native and engineered tissues. *Radiology* **2008**, 248, 342-347.

291. Zernike, F. How I discovered phase contrast. *Science* **1955**, 121, 345-349.

292. Gao, D.; Pogany, A.; Stevenson, A.W.; Wilkins, S.W. Phase-contrast radiography. *RadioGraphics* **1998**, 18, 1257-1267.

293. Greaves, A.W., *Phase contrast in x-ray imaging*, in *Engineering and Industrial Sciences. Centre for Atom Optics and Ultrafast Spectroscopy*. 2011, Swinburne University of Technology: Australasian Digital Thesis collection.

294. Pfeiffer, F.; Bech, M.; Bunk, O.; Kraft, P.; Eikenberry, E.F.; Brönnimann, C.; Grünzweig, C.; David, C. Hard-X-ray dark-field imaging using a grating interferometer. *Nat Mater* **2008**, 7, 134-137.

295. Wilkins, S.; Gureyev, T.; Gao, D.; Pogany, A.; Stevenson, A. Phase-contrast imaging using polychromatic hard X-rays. *Nature* **1996**, 384, 335-338.

296. Spanne, P.; Raven, C.; Snigireva, I.; Snigirev, A. In-line holography and phase-contrast microtomography with high energy x-rays. *Phys Med Biol* **1999**, 44, 741.

297. Krol, A.; Rosen, J., *In-line hard X-ray holography for biomedical imaging*. 2011: INTECH Open Access Publisher.

298. Kieffer, J.-C.; Krol, A.; Jiang, Z.; Chamberlain, C.C.; Scalzetti, E.; Ichalalene, Z. Future of laser-based X-ray sources for medical imaging. *Appl Phys B* **2002**, 74, s75-s81.

299. Guan, Y., *Characterization of alginate scaffolds using X-ray imaging techniques*, in *Biomedical Engineering*. 2010, University of Saskatchewan Saskatoon.

300. Zhong, Z.; Thomlinson, W.; Chapman, D.; Sayers, D. Implementation of diffraction-enhanced imaging experiments: at the NSLS and APS. *Nucl Instrum Methods Phys Res A* **2000**, 450, 556-567.

301. Mollenhauer, J.; Aurich, M.E.; Zhong, Z.; Muehleman, C.; Cole, A.A.; Hasnah, M.; Oltulu, O.; Kuettner, K.E.; Margulis, A.; Chapman, L.D. Diffraction-enhanced X-ray imaging of articular cartilage. *Osteoarthritis Cartilage* **2002**, 10, 163-171.

302. Muehleman, C.; Fogarty, D.; Reinhart, B.; Tzvetkov, T.; Li, J.; Nesch, I. In-laboratory diffraction-enhanced X-ray imaging for articular cartilage. *Clin Anat* **2010**, 23, 530-538.

303. Li, J.; Zhong, Z.; Connor, D.; Mollenhauer, J.; Muehleman, C. Phase-sensitive X-ray imaging of synovial joints. *Osteoarthritis and Cartilage* **2009**, 17, 1193-1196.

304. Zhou, S.-A.; Brahme, A. Development of phase-contrast X-ray imaging techniques and potential medical applications. *Physica Medica* **2008**, 24, 129-148.

305. Hounsfield, G. Computerized transverse axial scanning (tomography). 1. Description of system. *Br J Radiol* **1973**, 46, 1016-1022.

306. Feldkamp, L.A.; Goldstein, S.A.; Parfitt, M.A.; Jesion, G.; Kleerekoper, M. The direct examination of three-dimensional bone architecture in vitro by computed tomography. *J Bone Miner Res* **1989**, 4, 3-11.

307. Albertini, G.; Giuliani, A.; Komlev, V.; Moroncini, F.; Pugnaloni, A.; Pennesi, G.; Belicchi, M.; Rubini, C.; Rustichelli, F.; Tasso, R. Organization of extracellular matrix fibers within polyglycolic acid–polylactic acid scaffolds analyzed using X-ray synchrotron-radiation phase-contrast micro computed tomography. *Tissue Eng Part C- Methods* **2009**, 15, 403-411.

308. Ho, S.T.; Hutmacher, D.W. A comparison of micro CT with other techniques used in the characterization of scaffolds. *Biomaterials* **2006**, 27, 1362-1376.

309. Renghini, C.; Komlev, V.; Fiori, F.; Verné, E.; Baino, F.; Vitale-Brovarone, C. Micro-CT studies on 3-D bioactive glass–ceramic scaffolds for bone regeneration. *Acta biomater* **2009**, 5, 1328-1337.

310. Zehbe, R.; Goebbels, J.; Ibold, Y.; Gross, U.; Schubert, H. Three-dimensional visualization of in vitro cultivated chondrocytes inside porous gelatine scaffolds: a tomographic approach. *Acta biomater* **2010**, 6, 2097-2107.

311. Lin, A.S.; Barrows, T.H.; Cartmell, S.H.; Guldberg, R.E. Microarchitectural and mechanical characterization of oriented porous polymer scaffolds. *Biomaterials* **2003**, 24, 481-489.

312. Wang, F.; Shor, L.; Darling, A.; Khalil, S.; Sun, W.; Güçeri, S.; Lau, A. Precision extruding deposition and characterization of cellular poly-ϵ-caprolactone tissue scaffolds. *Rapid Prototyp J* **2004**, 10, 42-49.

313. Shao, X.X.; Hutmacher, D.W.; Ho, S.T.; Goh, J.C.; Lee, E.H. Evaluation of a hybrid scaffold/cell construct in repair of high-load-bearing osteochondral defects in rabbits. *Biomaterials* **2006**, 27, 1071-1080.

314. Atwood, R.; Jones, J.; Lee, P.; Hench, L. Analysis of pore interconnectivity in bioactive glass foams using X-ray microtomography. *Scr Mater* **2004**, 51, 1029-1033.

315. Jones, A.C.; Milthorpe, B.; Averdunk, H.; Limaye, A.; Senden, T.J.; Sakellariou, A.; Sheppard, A.P.; Sok, R.M.; Knackstedt, M.A.; Brandwood, A. Analysis of 3D bone ingrowth into polymer scaffolds via micro-computed tomography imaging. *Biomaterials* **2004**, 25, 4947-4954.

316. Verna, C.; Dalstra, M.; Wikesjö, U.M.; Trombelli, L. Healing patterns in calvarial bone defects following guided bone regeneration in rats. *J Clin Periodontol* **2002**, 29, 865-870.

317. Papadimitropoulos, A.; Mastrogiacomo, M.; Peyrin, F.; Molinari, E.; Komlev, V.; Rustichelli, F.; Cancedda, R. Kinetics of in vivo bone deposition by bone marrow stromal cells within a resorbable porous calcium phosphate scaffold: an X-ray computed microtomography study. *Biotechnol Bioeng* **2007**, 98, 271-281.

318. Cancedda, R.; Cedola, A.; Giuliani, A.; Komlev, V.; Lagomarsino, S.; Mastrogiacomo, M.; Peyrin, F.; Rustichelli, F. Bulk and interface investigations of scaffolds and tissue-engineered bones by X-ray microtomography and X-ray microdiffraction. *Biomaterials* **2007**, 28, 2505-2524.

319. Mastrogiacomo, M.; Komlev, V.; Hausard, M.; Peyrin, F.; Turquier, F.; Casari, S.; Cedola, A.; Rustichelli, F.; Cancedda, R. Synchrotron radiation microtomography of bone engineered from bone marrow stromal cells. *Tissue Eng* **2004**, 10, 1767-1774.

320. Peter, Z.-A.; Peyrin, F.; Homma, N. Synchrotron radiation micro-CT imaging of bone tissue, In *Theory and Applications of CT Imaging and Analysis*;Editor^Editors, Eds.; INTECH Open Access Publisher, 2011.

321. Stock, S. Recent advances in X-ray microtomography applied to materials. *Int Mater Rev* **2008**, 53, 129-181.

322. Cooper, D.; Erickson, B.; Peele, A.; Hannah, K.; Thomas, C.; Clement, J. Visualization of 3D osteon morphology by synchrotron radiation micro-CT. *J Anat* **2011**, 219, 481-489.

323. Yue, S.; Lee, P.D.; Poologasundarampillai, G.; Yao, Z.; Rockett, P.; Devlin, A.H.; Mitchell, C.A.; Konerding, M.A.; Jones, J.R. Synchrotron X-ray microtomography for assessment of bone tissue scaffolds. *J Mater Sci Mater Med* **2010**, 21, 847-853.

324. Landis, E.N.; Nagy, E.N.; Keane, D.T. Microstructure and fracture in three dimensions. *Eng Fract Mech* **2003**, 70, 911-925.

325. Weyland, M.; Midgley, P.A. Electron tomography. *Mater Today* **2004**, 7, 32-40.

326. Salomé, M.; Peyrin, F.; Cloetens, P.; Odet, C.; Laval-Jeantet, A.-M.; Baruchel, J.; Spanne, P. A synchrotron radiation microtomography system for the analysis of trabecular bone samples. *Med Phys* **1999**, 26, 2194-2204.

327. Komlev, V.; Peyrin, F.; Mastrogiacomo, M.; Cedola, A.; Papadimitropoulos, A.; Rustichelli, F.; Cancedda, R. Kinetics of in vivo bone deposition by bone marrow stromal cells into porous calcium phosphate scaffolds: an X-ray computed microtomography study. *Tissue Eng* **2006**, 12, 3449-3458.

328. Ismail, E.C.; Kaabar, W.; Garrity, D.; Gundogdu, O.; Bunk, O.; Pfeiffer, F.; Farquharson, M.; Bradley, D. X-ray phase contrast imaging of the bone–cartilage interface. *Appl Radiat Isotopes* **2010**, 68, 767-771.

329. Davis, T.; Gao, D.; Gureyev, T.; Stevenson, A.; Wilkins, S. Phase-contrast imaging of weakly absorbing materials using hard X-rays. *Nature* **1995**, 373, 595-598.

330. Weiss, P.; Obadia, L.; Magne, D.; Bourges, X.e.; Rau, C.; Weitkamp, T.; Khairoun, I.; Bouler, J.; Chappard, D.; Gauthier, O. Synchrotron X-ray microtomography (on a micron scale) provides three-dimensional imaging representation of bone ingrowth in calcium phosphate biomaterials. *Biomaterials* **2003**, 24, 4591-4601.

331. Choi, C.-H.; Kim, H.-T.; Choe, J.-Y.; Kim, S.-K.; Choi, G.-W.; Jheon, S.; Kim, J.-K. In vivo high-resolution synchrotron radiation imaging of collagen-induced arthritis in a rodent model. *J Synchrotron Radiat* **2010**, 17, 393-399.

332. Li, J.; Zhong, Z.; Lidtke, R.; Kuettner, K.E.; Peterfy, C.; Aliyeva, E.; Muehleman, C. Radiography of soft tissue of the foot and ankle with diffraction enhanced imaging. *J Anat* **2003**, 202, 463-470.

333. Issever, A.S.; Diederichs, G.; Majumdar, S.; Rogalla, P.; Hamm, B.K.; Lange, A.; Harwardt, M.; Hentschel, M.P.; Mueller, B.R. Analyser-based tomography images of cartilage. *J synchrotron radiat* **2008**, 15, 525-527.

334. Wagner, A.; Aurich, M.; Sieber, N.; Stoessel, M.; Wetzel, W.-D.; Schmuck, K.; Lohmann, M.; Reime, B.; Metge, J.; Coan, P. Options and limitations of joint cartilage imaging: DEI in comparison to MRI and sonography. *Nucl Instrum Methods Phys Res A* **2005**, 548, 47-53.

335. Rhoades, G.; Belev, G.; Rosenberg, A.; Chapman, D. A novel analyzer control system for diffraction enhanced imaging. *J Phys Conf Ser* **2013**, 425, 022003.

336. Coan, P.; Bamberg, F.; Diemoz, P.C.; Bravin, A.; Timpert, K.; Mützel, E.; Raya, J.G.; Adam-Neumair, S.; Reiser, M.F.; Glaser, C. Characterization of osteoarthritic and normal human patella cartilage by computed tomography X-ray phase-contrast imaging: a feasibility study. *Invest Radiol* **2010**, 45, 437-444.

337. Coan, P.; Wagner, A.; Bravin, A.; Diemoz, P.C.; Keyriläinen, J.; Mollenhauer, J. In vivo x-ray phase contrast analyzer-based imaging for longitudinal osteoarthritis studies in guinea pigs. *Phys Med Biol* **2010**, 55, 7649.

338. Muehleman, C.; Zhong, Z.; Williams, J.M.; Kuettner, K.E.; Aurich, M.; Han, B.; Mollenhauer, J.; Chapman, L.D. Diffraction enhanced X-ray imaging of the articular cartilage of experimental animals In *Annual Meeting Orthopaedic Research Society*. Dallas, TX. USA. 2002.

339. Zhu, N.; Chapman, D.; Cooper, D.; Schreyer, D.J.; Chen, X. X-ray diffraction enhanced imaging as a novel method to visualize low-density scaffolds in soft tissue engineering. *Tissue Eng Part C Methods* **2011**, 17, 1071-1080.

340. Appel, A.A.; Larson, J.C.; Garson, A.B., 3rd; Guan, H.; Zhong, Z.; Nguyen, B.N.; Fisher, J.P.; Anastasio, M.A.; Brey, E.M. X-ray phase contrast imaging of calcified tissue and biomaterial structure in bioreactor engineered tissues. *Biotechnol Bioeng* **2015**, 112, 612-620.

CHAPTER 3: 3D BIOPRINTING OF CELL-IMPREGNATED HYBRID CONSTRUCTS FOR CARTILAGE TISSUE ENGINEERING

This chapter has been published as "Izadifar Z., Change T., Kulyk W., Chen X.B., Eames B.F. (2015) Analyzing biological performance of 3D-printed, cell-impregnated hybrid constructs for cartilage tissue engineering. *Tissue Engineering Part C: Methods.* Epub ahead of print, In Press". According to the Copyright Agreement, "the authors retain the right to include the journal article, in full or in part, in a thesis or dissertation".

3.1 Abstract

Three-dimensional (3D) bioprinting of hybrid constructs is a promising biofabrication method for cartilage tissue engineering, because a synthetic polymer framework and cell-impregnated hydrogel provide structural and biological features of cartilage, respectively. During bioprinting, impregnated cells may be subjected to high temperatures (caused by the adjacent melted polymer) and process-induced mechanical forces, potentially compromising cell function. This study addresses these biofabrication issues, evaluating the heat distribution of printed polycaprolactone (PCL) strands and the rheological property and structural stability of alginate hydrogels at various temperatures and concentrations. The biocompatibility of parameters from these studies was tested by culturing 3D hybrid constructs bioprinted with primary cells from embryonic chick cartilage. During initial 2D culture expansion of these primary cells, two morphologically and molecularly distinct cell populations (“rounded” and “fibroblastic”) were isolated. The biological performance of each population was evaluated in 3D hybrid constructs separately. Cell viability, proliferation, and cartilage differentiation were observed at high levels in hybrid constructs of both cell populations, confirming the validity of these 3D bioprinting parameters for effective cartilage tissue engineering. Statistically significant performance variations were observed, however, between the “rounded” and “fibroblastic” cell populations. Molecular and morphological data support the notion that such performance differences may be attributed to the relative differentiation state of “rounded” versus “fibroblastic” cells (i.e., differentiated chondrocytes versus chondroprogenitors, respectively), which is a relevant issue for cell-based tissue engineering strategies. Taken together, this study demonstrates that bioprinting 3D hybrid constructs of PCL and cell-impregnated alginate hydrogel is a promising approach for cartilage tissue engineering.

3.2 Introduction

Although significant progress has been made over the last few decades in developing tissue engineering strategies for cartilage repair [1], regeneration of cartilage that functions similarly to natural cartilage remains a challenging task. The exceptional biomechanical functionality of cartilage at the articulating surfaces of skeletal joints in part derives from the structural intricacies [2] and the biphasic (solid-liquid) nature of cartilage extracellular matrix (ECM) [3]. Resembling a reinforced, highly hydrated material, cartilage ECM provides a favourable biological environment, so that impregnated chondrocytes can maintain tissue homeostasis, along with a non-compressible, load-bearing function [4-7]. A biomimetic cartilage tissue engineering approach creates scaffolds or constructs (i.e., cell-impregnated scaffolds) with structural and biological functionality similar to cartilage. Tissue constructs that lack such structural and biologically conducive properties can result in inferior performance, particularly after *in vivo* transplantation [8-10].

A hybrid cartilage tissue engineering strategy using both cell-impregnated hydrogels and polymeric scaffolds is emerging as an effective approach to mimic the biological and structural features of cartilage ECM. Hydrogels have many desirable properties for use in cartilage tissue engineering. They are highly hydrated and form tissue-like networks [11]. Furthermore, hydrogels are prepared easily, can be impregnated with cells, and provide an environment that is favourable for retaining the phenotype and morphology of chondrocytes [12, 13]. However, they have poor mechanical strength, which impairs their structural functionality for cartilage tissue engineering. Polymeric scaffolds, on the other hand, provide the required structural properties [14, 15], but they are inferior to the hydrogels in terms of providing a biologically favourable, highly hydrated 3D structure similar to natural cartilage matrix [8]. Therefore, combining both hydrogel and polymeric components into a hybrid construct can mimic the biologically and structurally supportive properties of cartilage, offering promise for optimizing cartilage tissue engineering strategies [16-20].

Conventional hybrid constructs often lack reproducible and/or customized properties, due to limitations of the fabrication methods. Conventional approaches, such as free-penetration or perfusion-assisted incorporation of hydrogel into scaffolds, do not allow customized cell-seeding into the construct, which can affect negatively the distribution and organization of cells and, consequently, the quality of regenerated tissue matrix [15, 17, 19]. For example, inefficient cell

penetration into the scaffold can lead to formation of cartilage matrix only at the periphery of the construct [15]. Indeed, lack of control over the spatial distribution of cells throughout the construct can lead to inferior matrix organization and function compared to that of natural cartilage [18]. Advanced additive manufacturing techniques, such as three-dimensional (3D) bioprinting, can produce custom-designed, computer-controlled hybrid tissue constructs, overcoming many limitations of current biofabrication methods [21, 22].

Three studies show the potential of 3D hybrid bioprinting as a superior fabrication technique for cartilage tissue engineering [23-25], but the biological performance of the impregnated cells has not been investigated comprehensively, and some critical fabrication parameters remain unexplored. Despite some positive results [25], 3D hybrid bioprinting may decrease chondrocyte viability, due to thermal stresses from dispensing heated polymers adjacent to cell-impregnated alginate [24]. Increases in chondrocyte numbers and cartilage ECM production were observed in long-term culture of 3D hybrid constructs, but no images were presented [24] or little cartilaginous matrix was produced [23]. These studies leave open the question of whether this fabrication technique affect the impregnated cells in producing enough matrix to replace defective cartilage. In addition, the amount of mechanical stresses that cells experience during biofabrication is determined by the viscosity of the alginate parameters used [26, 27]. Alginate parameters meanwhile can influence long-term biological performance, such as proliferation and chondrogenic differentiation. For example, very high alginate concentrations resulted in lower biological performance [24, 28, 29], and very low alginate concentrations compromise the structural integrity of constructs [30]. Therefore, PCL dispensing temperature and alginate rheological properties need to be carefully investigated, and the biological performance of impregnated cells, from viability to cartilage differentiation, should be evaluated qualitatively and quantitatively over long-term *in vitro* culture.

The success of engineered tissue constructs in promoting regeneration of cartilage is influenced largely by the type of employed cells [31]. Primary chondrocytes and stem cells are the most investigated cell sources for cartilage tissue engineering [32]. Because both cell sources offer advantages and disadvantages, there is still discussion and debate on which cell source is better suited for cartilage repair strategies. Primary chondrocytes more readily produce and maintain cartilage ECM, but they are obtained in low numbers from donor cartilage and do not proliferate easily [33, 34]. Stem cells proliferate readily, but they have to be directed carefully

towards chondrogenic differentiation [35]. Chondroprogenitors may represent a cell type intermediate to stem cells and chondrocytes, for they have the advantage of high expansion capability, while maintaining a predisposition to differentiate into chondrocytes [36]. Cartilage tissue engineering strategies can be optimized by investigating proliferation and differentiation of different cell types (e.g., chondrocytes vs. chondroprogenitors) in 3D biofabricated tissue constructs.

In this study, parameters of a 3D bioprinting technique, including thermal stress of melt-dispensed PCL and shear stress of dispensed alginate, were evaluated with respect to biocompatibility of hybrid cartilage constructs. The biological performance of hybrid constructs biofabricated with identified parameters of heat and alginate concentration/temperature were investigated during long-term *in vitro* culture using assays of cell survival, proliferation, and cartilage differentiation. To test whether cell source influences the biological performance of these constructs, two morphologically distinct cell populations, "rounded" and "fibroblastic", were isolated from primary cultures of embryonic chick chondrocytes. The biological performance of each population was very high, verifying the effectiveness of this cartilage tissue engineering approach. It is discussed whether differences observed between these cell populations may reflect the differentiation state of the "rounded" versus "fibroblastic" cells.

3.3 Materials and methods

3.3.1 Materials

LIVE/DEAD® Viability/Cytotoxicity Kit for mammalian cells (L-3224, Invitrogen, USA), anti-collagen type II antibody (II-II6B3—Developmental Studies Hybridoma Bank (DSHB), USA), collagen type X antibody (X-AC9—DSHB), Goat anti-mouse IgG-488 conjugate (A-11001, Millipore, USA), RNeasy Mini Kit (74104, Qiagen, Canada), RT^2 Easy First Strand Kit (330421, Qiagen, Canada), SYBER master mix (4472908, Life Technologies, USA), Acetone (Fisher Scientific, Canada), methanol (Fisher Scientific, Canada), acetic acid (Fisher Scientific, Canada), ethanol (Fisher Scientific, Canada), Gibco® fetal bovine serum (FBS, 12483-020, Thermo Fisher Scientific, Canada),. The rest of listed reagents and materials were purchased from Sigma-Aldrich (Oakville, Canada). Polycaprolactone (PCL) (704105-Aldrich, Mw 48,000-90,000), alginic acid sodium salt; low viscosity alginate (LVA) (A2158-Sigma), alginate powder (AP) (180947-Aldrich), medium viscosity alginate (MVA) (A2033-

Sigma), calcium chloride dehydrate ($CaCl_2$), Dulbecco's modified Eagle's medium (DMEM, D6429), Stemline® Keratinocyte Medium II-Calcium free (SKM, S0196), phosphate buffer saline (PBS), phosphate buffer saline Tween-20 (PBST), HEPES buffer, collagenase type IA, trypsin, Hank's buffered salt solution (HBSS), antibiotic antimycotic (AA; containing penicillin, streptomycin, and amphotericin), kanamycin sulfate, glutamine, ascorbate acid, sucrose. Ethylenediaminetetraacetic acid (EDTA), Alcian Blue, cacodylate buffer, sodium cacodylate, paraformaldehyde, glutaraldehyde, ruthenium (III) hexamine trichloride, normal goat serum, normal sheep serum, DMEM/F-12 Ham's medium (D8437), ascorbate-2-phosphate, insulin-transferrin-selenium (ITS, 12521).

3.3.2 Terminology

Due to variable usage of terms in the literature, it is defined here how a few terms are used in this manuscript. "Scaffold" will refer to materials printed without cells, whereas "construct" will refer to materials printed with cells. "Hybrid scaffold" will refer to a structure printed with two materials (in this case, PCL and alginate), but no cells, while "hybrid construct" will refer to a structure with two materials as well as cells.

3.3.3 Design and fabrication of the hybrid constructs

Three-dimensional (3D) models of the hybrid constructs were designed to have porous, non-woven structure consisting of polycaprolactone (PCL) framework scaffold and an embedded alginate hydrogel network in a box-shaped external geometry (Fig 3.1A). The PCL and alginate strands were designed to have 1 mm spacing with 0/90^o perpendicular pattern in two consecutive layers (Fig. 3.1A). The cell-impregnated alginate hydrogel was designed to be placed in the desired canals created between the PCL strands in each layer of the construct (Fig. 3.1C). The 3D computer-aided design (CAD) model of the hybrid construct was made using Magics Envisiontec (V13, Materialise, Belgium) software. The 3D hybrid model was then sliced into consecutive multiple layers using Bioplotter RP (V2.9, Envisiontec GmbH, Germany) software, and loaded to the interface software (VisualMachine BP, V2.2, Envisiontec GmbH, Germany) of the 3D-Bioplotter™ system (Envisiontec GmbH, Germany) for construct fabrication (Fig. 3.1B) , which was carried out in a sterile biosafety cabinet. PCL beads were loaded to high-temperature dispensing head (HTDH), melted and maintained at desired temperature (65-80^{o}C) for 15-20

minutes before dispensing. Dissolved alginate solution was loaded to low-temperature dispensing head (LTDH) of the machine, maintained at 10ºC for 10-20 minutes before dispensing. Following the CAD hybrid model, in each layer of the construct the PCL in the HTDH was first dispensed with the assigned pattern and then the alginate solution in LTDH was dispensed in the created canals between the PCL strands (Fig. 3.1C). This alternative dispensing pattern of PCL and alginate was repeated in subsequent layers to build the 3D hybrid constructs layer by layer as designed.

PCL was dispensed through 300 µm metal cylindrical needle (24G) using pneumatic pressure of 0.8 MPa at dispensing speed of 1 mm/sec. The alginate solution was dispensed through 200 µm conical needle, using 0.01 MPa pressure at dispensing speed of 25 mm/sec. Conical needles have been shown to be superior to cylindrical needles in dispensing live cells with lower shear-induced cell damage [37]. Since alginate gelation improves its stability and structural integrity [38], a partial cross-linking process was adopted throughout the construct fabrication. 170 mM $CaCl_2$ aerosol was produced with an ultrasonic nebulizer (MY-520) and was applied externally to the dispensing alginate, which takes about 10 seconds for each layer. Such partial cross-linking also keeps the construct moist and prevents it from drying during the fabrication. The partial cross-linking was followed by a 20 min full cross-linking of the finished 3D hybrid construct in 100 mM $CaCl_2$ solution to gel the alginate network within the PCL scaffold.

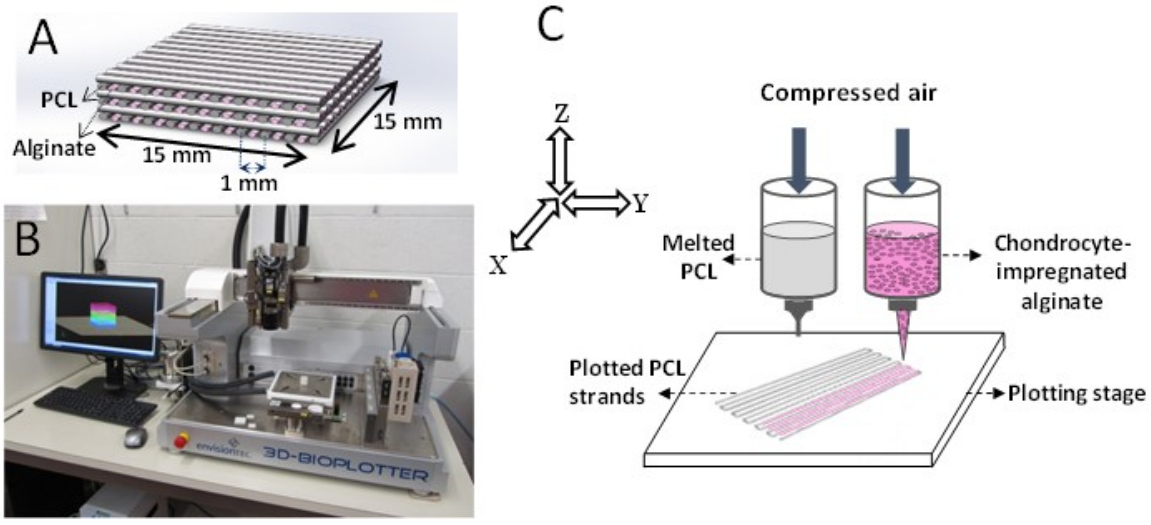

Figure 3.1 Design and 3D bioprinting of hybrid constructs with structural and biological features. (A) Schematic of designed 3D hybrid construct with alternating strands of PCL and chondrocyte-

impregnated alginate in each layer, (B) 3D-Bioplotter^{TM} system employed for biofabrication of designed hybrid constructs, and (C) hybrid biofabrication using pneumatic dispenser heads.

3.3.4 Characterization of hybrid scaffold fabrication

Different parameters of the fabrication process, such as materials characteristics and processing conditions were investigated to ensure the biocompatibility of the hybrid biofabrication for encapsulating cells. To identify a suitable processing temperature of PCL, scaffolds were made at different PCL temperatures (65, 70, 75, and 80 ºC) using a pressure of 0.8 MPa, and the heat distribution on the surface of dispensing PCL strands was monitored with an infrared thermal camera (FLIR i3, FLIR systems Inc., CA). Upon dispensing of a 10 mm-long PCL strand, infrared (IR) images were collected for analysis. Surface temperature profile along the length of the dispensed PCL strand was measured in the collected IR images using FLIR Therma CAM Researcher Software (FLIR systems Inc., CA). Prior to collecting images, the infrared thermal camera was calibrated with an ice-water mixture (0 ºC).

Three different sodium alginate stocks; namely, *alginate powder* (AP), *low viscosity alginate* (LVA), and *medium viscosity alginate* (MVA), were used for preparing alginate solutions (dissolving in dH_2O) and testing the fabrication of the hybrid scaffold. The effect of temperature on the viscosity of alginate solution (2% w/w) was investigated by using a programmable rheometer (Brookfield DV-III Ultra, USA). Alginate temperature was decreased from 25-26ºC to 10ºC by two degrees at a time and its viscosity was measured. At each temperature, at least 10 min wait time was given for the material to uniformly reach the desired temperature before viscosity was measured. The effect of temperature on the viscosity of higher concentrations of LVA solution (4% and 5%) was also investigated for comparison.

3.3.5 Cell isolation and culture

All experiments were carried out according to approved institutional and national standards of animal ethics. Primary chondrocytes were isolated from cartilaginous sternums of 14 day-old chick embryos. Embryonic chick cartilage was used as the cells source because of the easy accessibility of large numbers of cartilage-producing cells, and it is a well-characterized model for studying the development and differentiation of cartilage cells in different culture conditions [39-43] and tissue scaffolds [44-47]. Since monolayer passaging of the primary chondrocytes can negatively affect their chondrogenic differentiation capacity [48, 49], 20 to 24

embryos were used to obtain sufficient numbers of primary cells without needing to passage them (i.e., passage 0). The excised sternums of chick embryos were finely chopped and subsequently subjected to digestion in 0.2% collagenase and 0.25% trypsin in HBSS at 37ºC and 5% CO_2 for 2 hours with one gentle pipetting at 90 minute. The digestion was stopped by adding DMEM and 10% FBS to the digestion medium. The resulting cell suspension was passed through a sterile Nitex (70 µm mesh size) and centrifuged at 200g for 10 minutes. The collected cell pellets were suspended in culture medium containing DMEM, 10% FBS, 2 mM glutamine, 0.1 mg/mL kanamycin, 1% AA (100 U/mL penicillin, 0.1 mg/mL streptomycin, 0.25 µg/mL amphotericin B), and 0.01 mg/mL ascorbate. The isolated cells were seeded at a population of 2×10^6 cells/flask (T-75 flask, VWR, Canada) at 37ºC and 5% CO_2 and the medium was changed every three days. Of note, the culture medium used for 3D culture of cells in constructs did not contain additional growth factors, which are not needed for primary cells from embryonic cartilage to differentiate as chondrocytes [50-53], perhaps due to the self-expression of chondrogenic growth factors by these embryonic cells [54].

Two morphologically distinct cell types, “rounded” and “fibroblastic”, were observed in the primary cultures after 7 days of 2D culture *in vitro* (see Results and Fig. 3.4). Rounded and fibroblastic cells were collected separately from the culture at day 10 following the primary isolation. To collect rounded cells, the culture medium was gently pipetted up and down two times to dissociate any loosely-attached round cells. Then, the floating and dissociated cells were harvested and centrifuged at 300g for 10 min to pellet the cells. The remaining fibroblastic cells attached to the culture flasks were rinsed with PBS and incubated with 0.25% trypsin solution at 37ºC for 5 min. Following the incubation, the FBS-containing culture medium (described earlier) was added to the flask to neutralize the trypsin. The flask medium was gently pipetted up and down to disperse detached cell clumps, which was then centrifuged at 300g for 10 min to pellet the cells. Cell number and viability in the collected rounded and fibroblastic cell suspensions were determined using hemocytometer and Trypan blue exclusion assay, respectively.

3.3.6 Biofabrication of cell-impregnated hybrid construct

Medium viscosity alginate solution (3.5 % w/w) was prepared by stir-bar mixing of alginic acid sodium salt in Stemline® Keratinocyte Medium under sterile condition. For each cell type, the alginate solution was evenly mixed with cells suspended in fresh culture medium

(7:3, alginate volume :cell-suspension volume) using three-way stopcocks to a final alginate solution concentration of 2.5% and cell concentration of 5.68×10^6 cells/ml. The cell-embedded alginate was then loaded to the LTDH of the 3D-Bioplotter^{TM} machine and the 3D PCL-alginate constructs with impregnated cells were dispensed following the hybrid fabrication procedure described earlier. During the biofabrication, the temperature of the plotting stage was maintained at 10ºC. After crosslinking of the finished cell-embedded hybrid constructs in 100mM $CaCl_2$ in 4.2 mM HEPES, 0.35M sucrose solution (pH7.4), the constructs were washed in DMEM twice for 5 minutes each, and were moved to 12-well culture plates containing DMEM supplemented with 10% FBS, 2 mM glutamine, 0.1 mg/mL kanamycin, 0.01 mg/mL ascorbate, and 100 U/mL penicillin, 0.1 mg/mL streptomycin, 0.25 µg/mL amphotericin B. The hybrid constructs were maintained at 37ºC and 5% CO_2 condition with fresh medium change every three days.

For biological studies, hybrid constructs with two consecutive layers were fabricated and used. Furthermore, to better approximate the thickness of human articular cartilage (1.5-2.35 mm [55]), multilayer hybrid constructs with six consecutive layers were designed and fabricated using cells of the ATDC5 cell line previously employed for cartilage tissue engineering applications [56, 57]. ATDC5 mouse cells were purchased from Sigma and were cultured in culture flasks containing DMEM/F-12 HAM's medium supplemented with 5% FBS, penicillin (100 unit/ml), streptomycin (100 µg/ml), glutamine (2mM), ascorbate-2-phosphate (0.05mg/ml), and 1X ITS+. The medium was changed every two days. Confluent cells after one week of culture were collected, re-suspended in serum free DMEM/F-12 HAM's medium, and mixed with alginate (5.6×10^6 cells/ml in 2.5% alginate solution) for construct biofabrication following the procedure described earlier. The hybrid 6-layer constructs were then maintained at 37ºC and 5% CO_2 condition with fresh medium change every three days.

3.3.7 Cell viability and proliferation assay

Cell viability assay was conducted in the hybrid constructs using the two-color LIVE/DEAD® Kit and fluorescence microscopy. Green-fluorescent calcein-AM dye staining identifies live cells with normal intracellular esterase activity, whereas red-fluorescent ethidium homodimer-1 (EthD-1) dye staining identifies dead cells with compromised plasma membranes. The viability of cells in the hybrid constructs was assayed immediately after biofabrication (day 0), and at days 1, 3, 7, and 14 of subsequent *in vitro* culture. At each timepoint, the constructs

(n=3) were removed from the culture, washed with DMEM, and stained in 2μM calcein-AM and 0.5 μM EthD-1 solution in DMEM for 30 min in a 37°C, 5% CO_2 incubator. The constructs were washed with DMEM twice and imaged using a fluorescence microscope (Nikon, ECLIPSE E600, SPOT Insight™ Camera, USA).

Sequential images at different vertical focal planes were captured to investigate the spatial distribution and viability of the impregnated cells within the hydrogel. To quantitatively determine the cell viability in the hybrid constructs, the stained cells were released from the constructs by dissolving hydrogel matrix with 50 mM EDTA solution (diluted in DMEM) for 30 min at room temperature while protected from light. Using gentle pipetting, the medium was dispersed to give an even cell suspension mixture. Samples (N=3) were taken from the cell mixture of each construct and imaged under a coverslip on a standard glass microscope slide at 5-6 random locations for counting live and dead cells. The cell number in these isolated cell suspensions (n=3) was determined using a hemocytometer to indicate proliferation over the culture period. The cell viability and proliferation experiment was repeated three times in independent experiments and the collected data was used for quantitative viability and proliferation analysis.

3.3.8 Cell differentiation assessments

Cartilage differentiation of the cells was investigated by assaying glycosaminoglycans (GAGs) and Collagen type II (Col2) deposition in the hybrid constructs. Alcian blue staining was used to assaym sulfated GAGs at days 1, 7, 14 and 28 following biofabrication. At each timepoint, the constructs (n=3) were removed from the culture and washed twice with DMEM. The constructs were fixed in acetone and methanol solution (1:1) on ice for 30 minutes and then stained with 0.5 % Alcian blue diluted in 3% acetic acid solution (pH=1) overnight. The stained constructs were washed once with 25% ethanol in 3% acetic acid and once with 50% ethanol in 3% acetic acid, and were then imaged using light microscopy. Using ImageJ software [58] the amount of Alcian blue-stained matrix in the hybrid constructs was estimated by measuring the percentage area of the blue-stained matrix to the total field of view in the alginate of the constructs at days 7, 14, and 28 of culture.

Immunofluorescent staining was performed to detect Col2 or Col10 accumulation within the hybrid constructs. The constructs were harvested at days 1, 7, and 14 following

biofabrication, washed with DMEM and fixed in cacodylate buffer (200mM sodium cacodylate (pH7.4), 20 mM $CaCl_2$, 4% sucrose) contains 2% paraformaldehyde, 2% glutaraldehyde, and 0.7% ruthenium (III) hexamine trichloride for two hours at 4ºC on a shaking platform. The constructs were then washed once in cacodylate buffer, digested with 0.5% trypsin in PBS for 20 minutes at 37ºC for antigen retrieval, and then incubated in blocking buffer (4% normal goat serum and 2% normal sheep serum in PBST) for 2 hrs while shaking at room temperature. The constructs were then incubated in purified anti-Col2 or anti-Col10 antibody in blocking buffer (1:100) overnight at 4ºC while shaking. Next, the constructs were washed 6-8 times with blocking buffer over two hours and then incubated with goat anti-mouse IgG-488 conjugate in blocking buffer (1:1000) at 4ºC overnight. Constructs were then washed in PBST for at least two hours before fluorescence microscopy imaging. Histochemical and immunoflurescent staining experiments were repeated twice in independent experiments to confirm the obtained results.

Relative levels of *Collagen type I alpha 2* (*Col1a2*) and *Collagen type II alpha 1* (*Col2a1*) transcript expression in cells harvested from the hybrid constructs were investigated using quantitative polymerase chain reaction (qPCR) analysis following manufacturer's protocols. At day 0, rounded and fibroblastic cells were released from hybrid constructs, using the same procedure described earlier for cell viability and proliferation assays, and total RNA was extracted using RNeasy Mini Kit (Qiagen, Canada). For each sample, 100 ng of RNA was reverse transcribed into cDNA using RT^2 Easy First Strand Kit (Qiagen, Canada). qPCR was performed in 20 µl of reaction volume using 1 µl of cDNA products, gene-specific primers, and SYBR master mix with 46 cycles of denaturation (30 s, 95ºC), annealing (30 s, 55ºC), and extension (30 s, 72ºC) using a Stratagene™ Mx3005P qPCR system (Agilent Technologies, Inc. USA). Primer sets for chick *Col2a1* (Forward: aagggtgatcgtggtgagac, Reverse: tcgcctctgtctccttgttt), *Col1a2* (Forward: tgaagttggctttgatgcag, Reverse: gggttctttttggagccttc), and internal reference *Hprt1* (Forward: aagtggccagtttgttggtc, Reverse: ttgtagtcgagggcgtatcc) were synthesized by IDT. PCR efficiency was measured as 102% that was in the acceptable range of 95-110%. Ratio changes in gene expression were calculated using the ΔΔCt method [59, 60].

3.3.9 Statistical analysis of the data

Collected data are presented as mean ± standard deviation. Statistical significance difference among different timepoints and cell types was calculated using one-way or two-way

analysis of variance (ANOVA) and Tukey's multiple comparison test. Differences were significant when the calculated P-value was less than 0.05.

3.4 Results

3.4.1 Investigating parameters of hybrid construct fabrication for biocompatibility and structural integrity

To assess the level of potential heat stress on cells in adjacent alginate strands during hybrid construct fabrication (see Fig. 3.1), surface temperature of printed PCL strands was determined using an infrared camera. Although the PCL was dispensed at 65-80ºC, the surface temperature of the PCL strands dropped considerably once printed (Fig. 3.2). The temperature profiles along the 10 mm length of printed PCL (X axis and marked black line in Fig. 3.2 inset images) indicate that the PCL surface temperature dropped to room temperature (25ºC) within approximately 10 seconds after printing at 1 mm/sec. When PCL was printed at 65, 70, 75, and 80ºC, the maximum temperature at the surface of the printed PCL was 33.9, 38.1, 39, and 42.4ºC, respectively (Fig. 3.2), which was almost half the applied processing temperatures. Since cells are cultured at 37ºC, PCL temperatures of 65-75ºC should allow biocompatible printing of hybrid constructs with impregnated cells. Because of the lower viscosity and higher flow rate of PCL at higher temperatures, 75ºC PCL printing was used for all subsequent experiments of this study.

Stability of the alginate strands during printing is important for maintaining the designed structural properties of the hybrid construct. In order to identify parameters by which the stability of low concentration alginate could be controlled effectively, alginate viscosity was characterized as functions of temperature, concentration, and the polymer chain length of starting material. At 2% concentration, medium viscosity alginate (MVA) exhibited significantly ($P<0.001$) higher viscosity than the low viscosity alginates, LVA and AP, at every temperature tested between 25ºC and 10ºC (Fig. 3.3). A similar statistically significance ($P<0.001$) increase in viscosity was achieved by increasing the concentration of LVA from 2% to 5% (Fig. 3.3). Lowering the temperature from 25ºC to 10ºC significantly ($P<0.001$) increased alginate viscosity at all concentrations tested. However, the viscosity increase in 2% MVA and 4% and 5% LVA was 3-8 times larger than that in 2% LVA and 2% AP (Fig. 3.3), which was statistically significant ($P<0.001$). At 2% and 2.5% concentrations, printing of hybrid constructs with low

viscosity alginates (LVA and AP) was found to be very challenging, even by lowering the alginate temperature and employing partial cross-linking with $CaCl_2$ aerosol during fabrication. Low viscosity alginates did not have enough stability to maintain their 3D structures, and the alginate strands flattened after printing. However, hybrid constructs printed with 2% and 2.5% MVA at 10ºC maintained their structural integrity (see Fig. 3.6). As such, higher initial viscosity of alginate along with printing at a low temperature can provide a processing condition for making stable hybrid constructs with low alginate concentrations [see Appendix A], which is an alternative and more biocompatible approach than using high alginate concentrations.

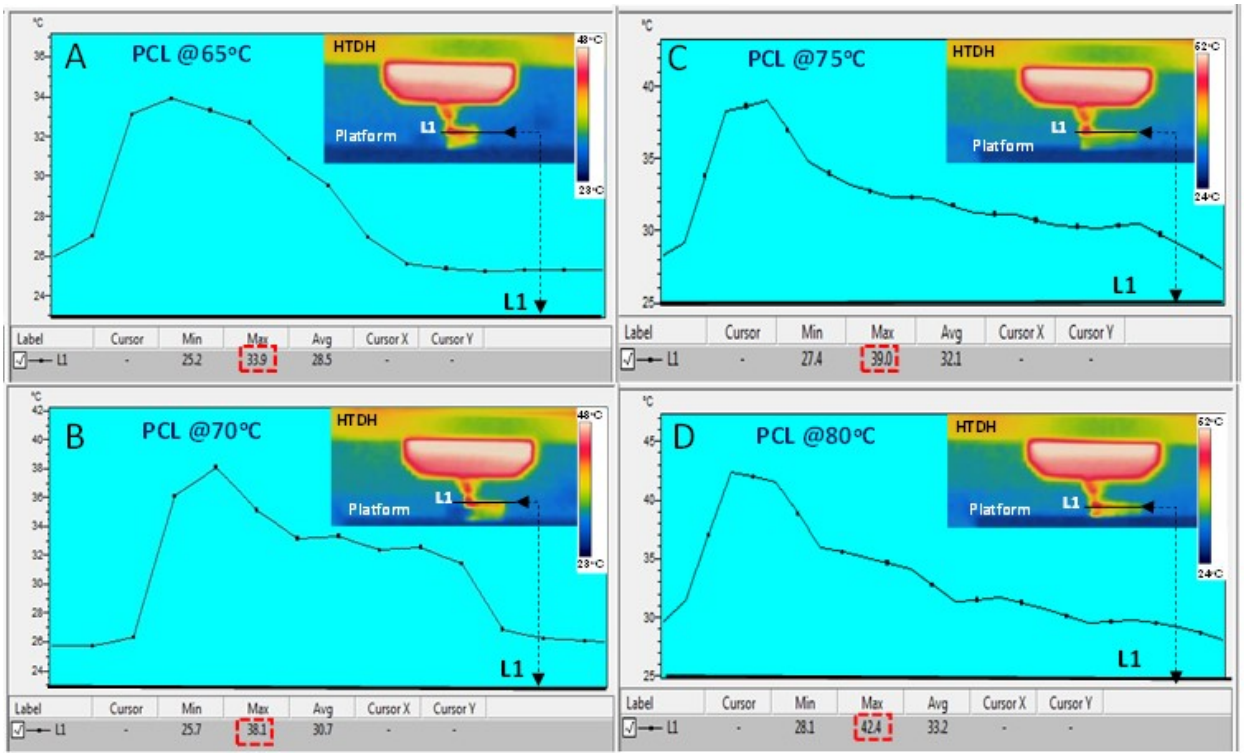

Figure 3.2 Thermal infrared (IR) imaging reveals that temperature decreases rapidly during PCL strand printing. Surface temperature profile along the length of printed PCL (L1 in the inset images) shows a rapid drop to ambient temperature after printing at (A) 65ºC, (B) 70ºC, (C) 75ºC, or (D) 80ºC. X axes in the graphs corresponds to the black line (L1) marked along the length of printed PCL in the inset IR images. HTDH: high temperature dispensing head. (The heat map scale bar was created automatically from the detected range of temperatures in each captured field of view).

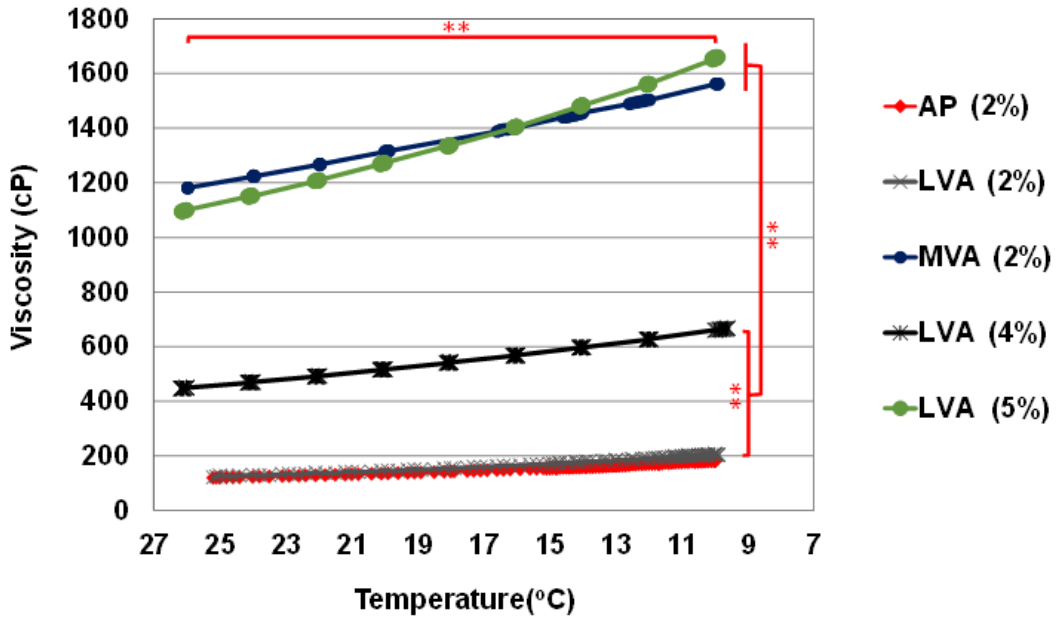

Figure 3.3 Increase of viscosity by temperature decrease in solutions of low viscosity alginate (LVA), medium viscosity alginate (MVA), and alginate powder (AP). Asterisks indicate statistically significant difference in viscosity from 25ºC to 10ºC for all tested solutions (horizontal asterisks), and at every tested temperature between 2% MVA & 5% LVA and 2% LVA, 2% AP and 4% LVA at $P<0.001$.

3.4.2 Two populations of primary cells were isolated from embryonic chick cartilage

Two morphologically distinct cell types, "rounded" and "fibroblastic", were observed in primary cultures of embryonic chick sternal chondrocytes after 7 days of 2D culture *in vitro* (Fig. 3.4). Rounded cells with spherical morphology floated in the culture medium or were attached loosely to the flask bottom (Fig. 3.4B and C, white arrowheads). Fibroblastic cells with flattened morphology were attached firmly to the flask bottom and could not be detached by simple pipetting (Fig. 3.4B and C, blue arrowheads). Interestingly, fibroblastic cells appeared to give rise to rounded cells when cultured after the floated and loosely attached rounded cells were removed (Fig. 3.4D-F).

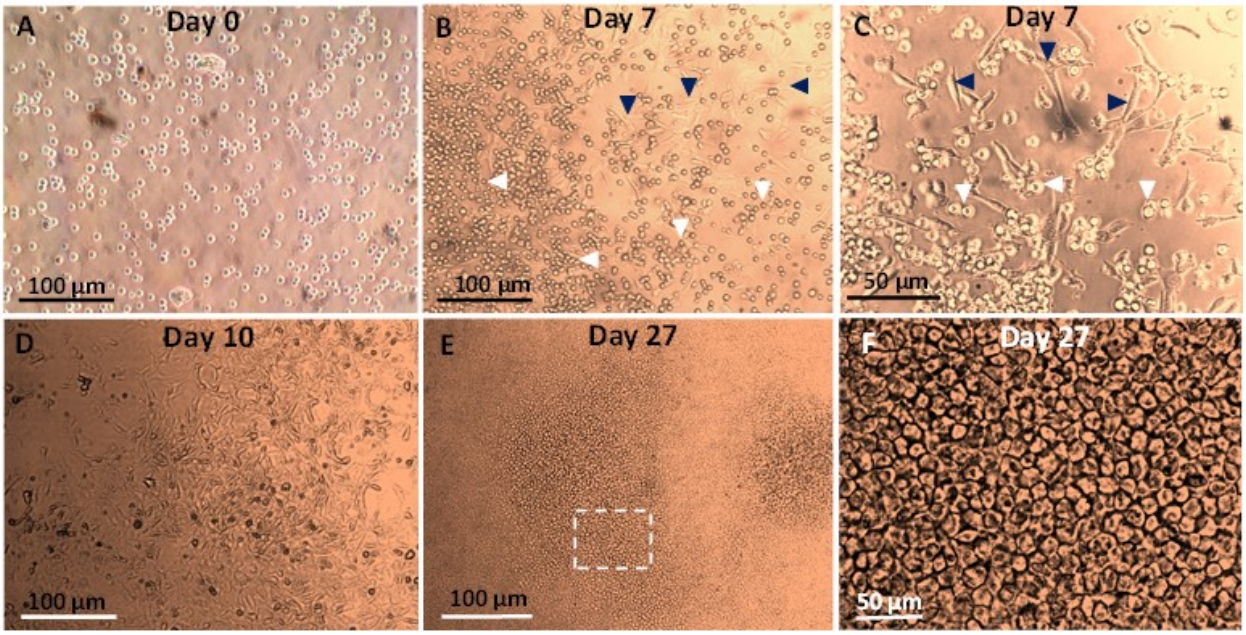

Figure 3.4 Two populations of cells were isolated from primary chick cartilage. Primary cells isolated from embryonic chick cartilage in 2D culture at (A) day 0 and (B,C) day 7. Panel C is higher magnification view of sample in panel B. Dark blue arrowheads point to fibroblastic cells, and white arrowheads point to rounded cells. (D) 2D culture at day 10 following removal of floated and loosely attached rounded cells. (E,F) Many rounded cells appeared by day 27, 17 days after removal of floated and loosely attached rounded cells. Panel F shows higher magnification view of dashed box in panel E.

In addition to the morphological differences between rounded and fibroblastic cells, molecular analyses indicated they had different gene expression profiles. Quantitative gene expression analysis using qPCR was performed to further investigate the difference between the rounded and fibroblastic cells. At day 0, immediately after biofabrication, rounded cells were observed to have statistically higher *Col2a1* mRNA levels than the fibroblastic cells, while fibroblastic cells were observed to have statistically higher *Col1a2* mRNA levels than the rounded cells (Fig. 3.5). Given these morphological and molecular differences, the biological performance of rounded and fibroblastic cell populations in 3D hybrid constructs was evaluated separately.

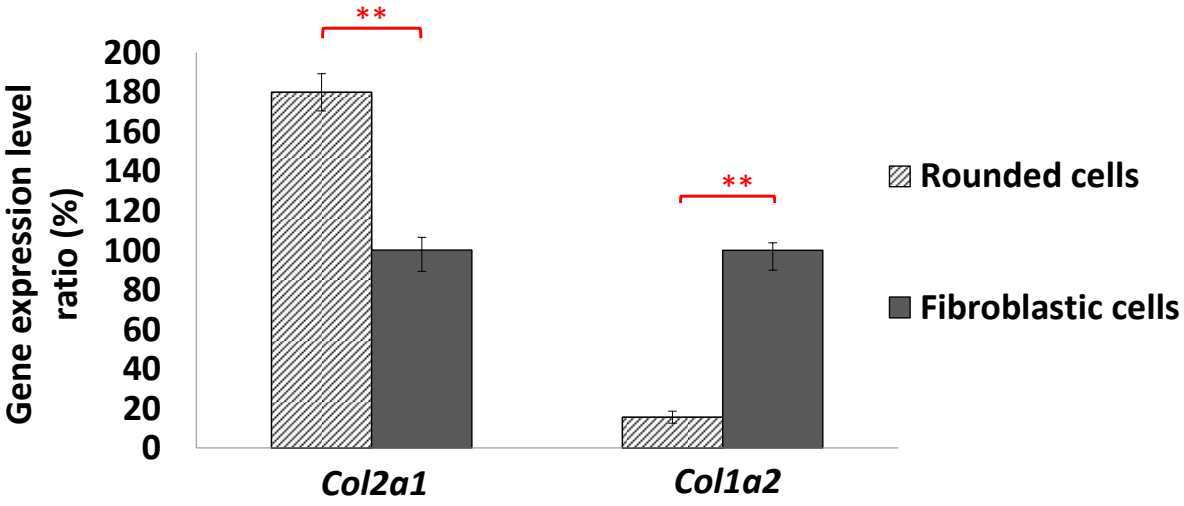

Figure 3.5 Rounded cells have distinct molecular characteristics from fibroblastic cells. qPCR analyses revealed higher levels of *Col1a2*, and lower levels of *Col2a1*, expression in fibroblastic cells than rounded cells at day 0 of hybrid construct biofabrication. Levels of *Col2a1* and *Col1a2* mRNAs are normalized with respect to those in fibroblastic cells. Asterisks indicate $P<0.001$.

3.4.3 Rounded and fibroblastic cells demonstrated high viability in hybrid constructs

Biocompatibility of the PCL temperature and alginate processing parameters identified above was measured using a fluorescent cell viability assay. After 3D hybrid construct printing (day 0), cells were observed to be distributed uniformly, without formation of cell clumps, throughout the alginate strands between the PCL strands (Fig. 3.6). Fluorescent imaging of stained constructs at day 0 showed uniform distribution of both live and dead cells throughout the alginate portion of the constructs immediately after printing (Fig. 3.7). The absence of increased cell death in regions of alginate that were immediately adjacent to the PCL strands confirms that the heat produced by melt-dispensed PCL does not harm considerably the viability of impregnated cells (Fig. 3.7A-F). No differences in distribution of cells were observed between rounded and fibroblastic cells.

Time course analysis indicated that both rounded and fibroblastic cells maintained high viability in hybrid constructs cultured *in vitro*. At day 0, constructs with rounded and fibroblastic cells both showed cell viability of more than 80% (Fig. 3.7G). Cell viability of constructs containing fibroblastic cells decreased to 76% by day 7, which was improved to about 85% by day 14 (Fig. 3.7G), although these changes were not statistically significant. For constructs with

rounded cells, the viability remained high (>80%) throughout the 14 days of culture, slightly increasing from days 3 to 14 (Fig. 3.7G), although not statistically significant. From days 1 to 14 during culture, rounded cells tended to exhibit slightly higher viability than fibroblastic cells, but this was only statistically significant on day 7 (Fig. 3.7G). In general, cell viability was high in hybrid constructs of both cell types, with a minimum viability of 77%.

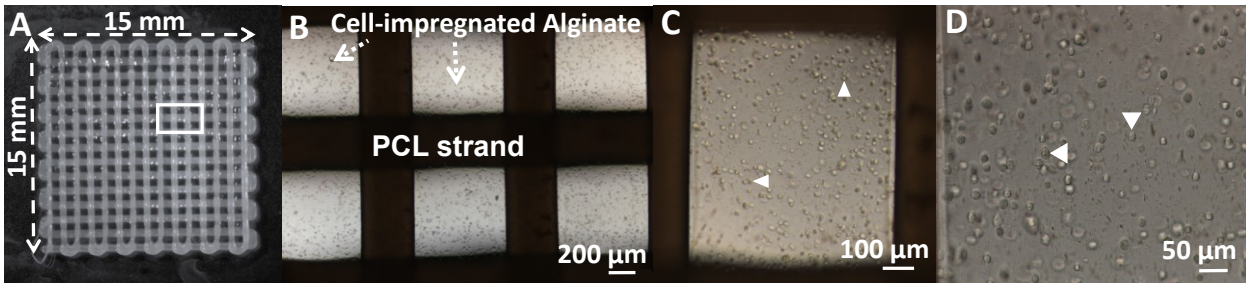

Figure 3.6 3D bioprinted hybrid constructs have uniformly distributed impregnated cells within the alginate hydrogel. (A) Gross and (B-D) magnified light microscopy views. Panel B is higher magnification view of the box in panel A. Dashed arrows point to cell-impregnated alginate strands, and white arrowheads point to cells impregnated in the alginate strand.

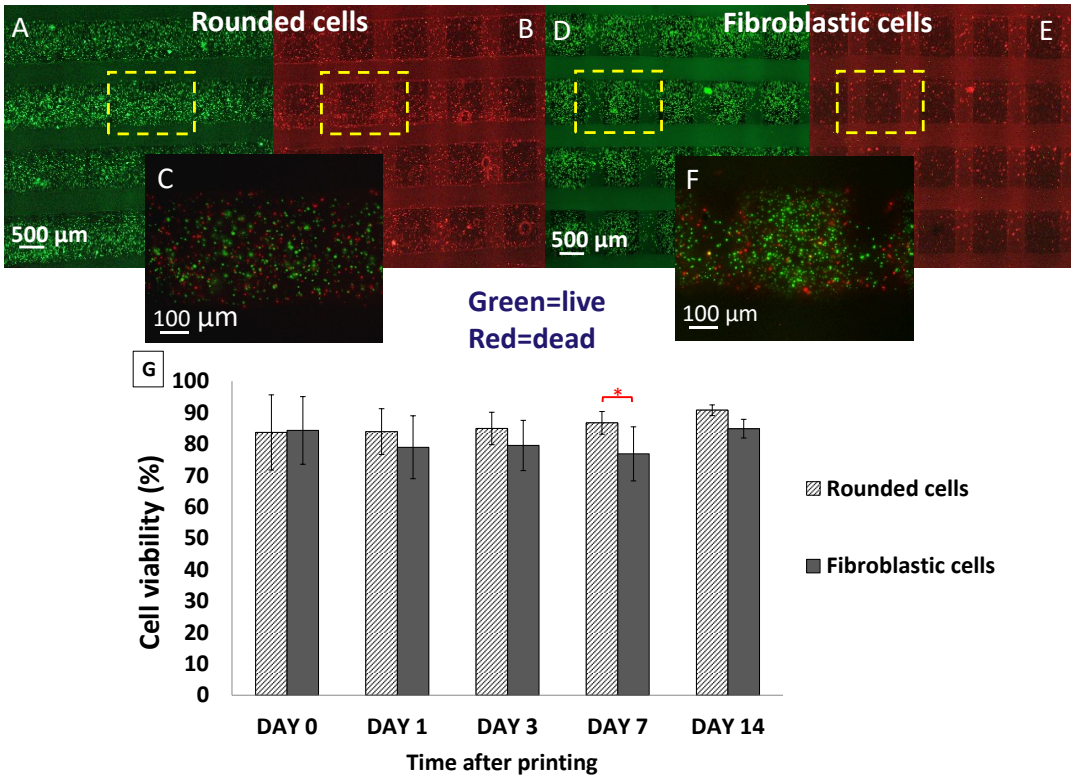

Figure 3.7 Cell viability was high for both rounded and fibroblastic cells in 3D bioprinted hybrid constructs. Uniform distribution of (A) live, (B) dead, (C) live and dead rounded cells, and (D)

live (E) dead, (F) live and dead fibroblastic cells in hybrid constructs confirms the harmless use of melted PCL in hybrid fabrication. (G) Time course cell viability analysis demonstrates high viability for rounded and fibroblastic cells in the hybrid constructs. Asterisk indicates a statistical significant difference with $P< 0.05$.

3.4.4 Fibroblastic cells had higher proliferation than rounded cells in hybrid constructs

To ensure that the hybrid construct provided a stable environment for cell proliferation during *in vitro* culture, cell number, cell organization, and the structural integrity of alginate were examined. Representative images of hybrid constructs (Fig. 3.8A-F) suggested that the number of live rounded and fibroblastic cells increased during culture. Quantitative analyses of the number of rounded and fibroblastic cells suggested that hybrid constructs provide a conducive environment for maintaining cell proliferation (Fig. 3.8I). Cell numbers steadily rose during the culture period for both rounded and fibroblastic cells, each showing a significant increase in cell number at day 14 compared to earlier culture times. Rounded and fibroblastic cells exhibited similar cell numbers at each timepoint during culture up to day 7, but at day 14, fibroblastic cells had significantly higher numbers (3.7-fold increase) than the rounded cells (2.5-fold increase) (Fig. 3.8I).

Cell proliferation was associated with the formation of cell clusters during *in vitro* culture of hybrid constructs. Most cells were dispersed individually throughout the alginate strands at day 1, but at later timepoints, discernible cell clusters became apparent (inset images in Fig 3.8A-F). A high resolution (0.83 μm pixel size) confocal image of the rounded cell hybrid construct taken at day 28 of culture revealed that most cells were in clusters rather than isolated (Fig. 3.8G, H). In addition, both rounded and fibroblastic cells displayed round morphologies that typify chondrocytes in native cartilage during *in vitro* culture of hybrid constructs (inset images in Fig.3.8A-F).

Throughout *in vitro* culture, the alginate strands retained both external and internal structural integrity. Alginate strands persisted in filling the space between PCL strands, maintaining the interconnectivity of pores within the hybrid constructs during 28 days of culture (Fig. 3.8A-G). At later times of culture (such as day 28), the size of alginate strands (its diameter) sometimes appeared to increase, perhaps due to osmotic swelling of the alginate or a gradual loosening of the internal microstructure of the hydrogel matrix. In contrast to this latter possibility, cells within the alginate strands displayed the same uniform distribution as seen after

initial fabrication, suggesting that the internal structure of alginate was preserved during *in vitro* culture.

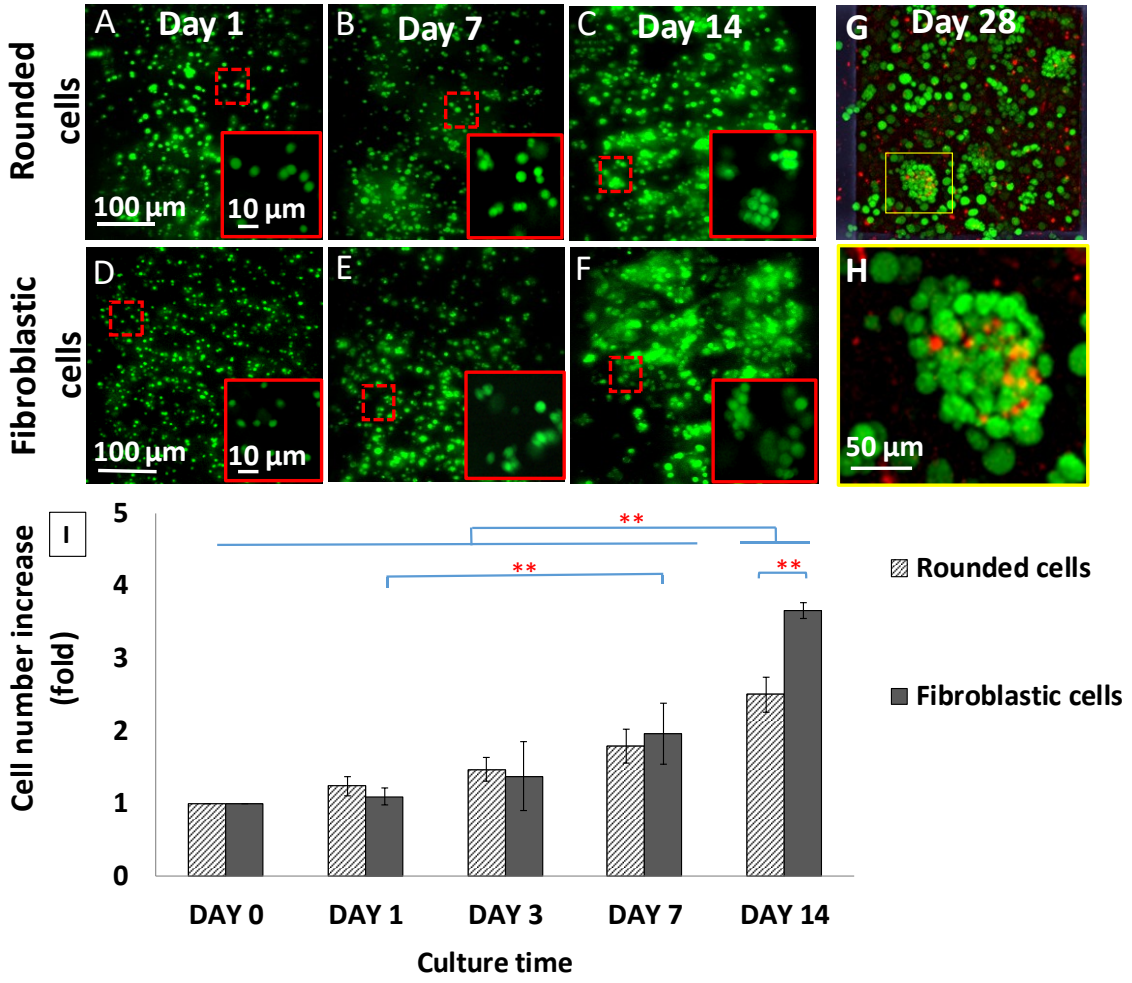

Figure 3.8 Qualitative and quantitative cell proliferation analyses indicate cell population increases in hybrid constructs with time in culture. Live-stained constructs impregnated with rounded (A-C) and fibroblastic cells (D-F) at day 1 (A,D), day 7 (B,E), and day 14 (C,F). (G,H) Confocal image of green and red stained rounded cells in a hybrid construct at day 28 of culture. Inset images and panel H are high magnification view of the cells in the constructs showing cell cluster formation in hybrid constructs over time. (I) Fold increases in cell numbers in hybrid constructs over time. Asterisks indicate statistically significant difference with $P < 0.001$.

3.4.5 Rounded and fibroblastic cells secrete abundant cartilage matrix within hybrid constructs

Abundant Alcian blue and Col2 immunofluorescence staining reflected secretion of the two main components of cartilage tissue matrix, glycosaminoglycans (GAGs) and Col2 [61], within hybrid constructs during *in vitro* culture. Alcian blue staining was localized around cells

in the alginate hydrogel of the hybrid constructs from both rounded and fibroblastic cells (Fig. 3.9A-L). Over the culture timepoints, regions of Alcian blue-stained matrix appeared to increase in size within both the rounded and fibroblastic cell hybrid constructs. At days 7 and 14, fibroblastic cells seemed to produce more Alcian blue-stained matrix than the rounded cells (Fig. 3.9C,D,I,J). At day 28, the Alcian blue-stained matrix almost filled the alginate strands of the hybrid constructs for both rounded and fibroblastic cells (Fig. 3.9E,F,K,L).

In order to quantitate these observations, the relative area of Alcian blue-positive matrix was measured at each timepoint during the culture period, and these measurements confirmed the trends observed in the images. Reflecting GAG secretion, Alcian blue-stained matrix increased over culture time for both rounded and fibroblastic cells, being significantly higher at day 28 compared to days 7 and 14 (Fig. 3.9M). Alcian blue-stained matrix significantly increased at day 14 compared to day 7 for fibroblastic cells. At each timepoint measured, fibroblastic cells showed larger regions of Alcian blue-stained matrix than rounded cells, with statistical significance at days 7 and 14. Alcian blue-stained matrix accounted for more than 80% of the measured area of alginate strands by day 28 in both rounded and fibroblastic cell constructs (Fig. 3.9M). In total, these data confirm that hybrid constructs provide a favourable environment for increased secretion of cartilaginous matrix during long culture periods.

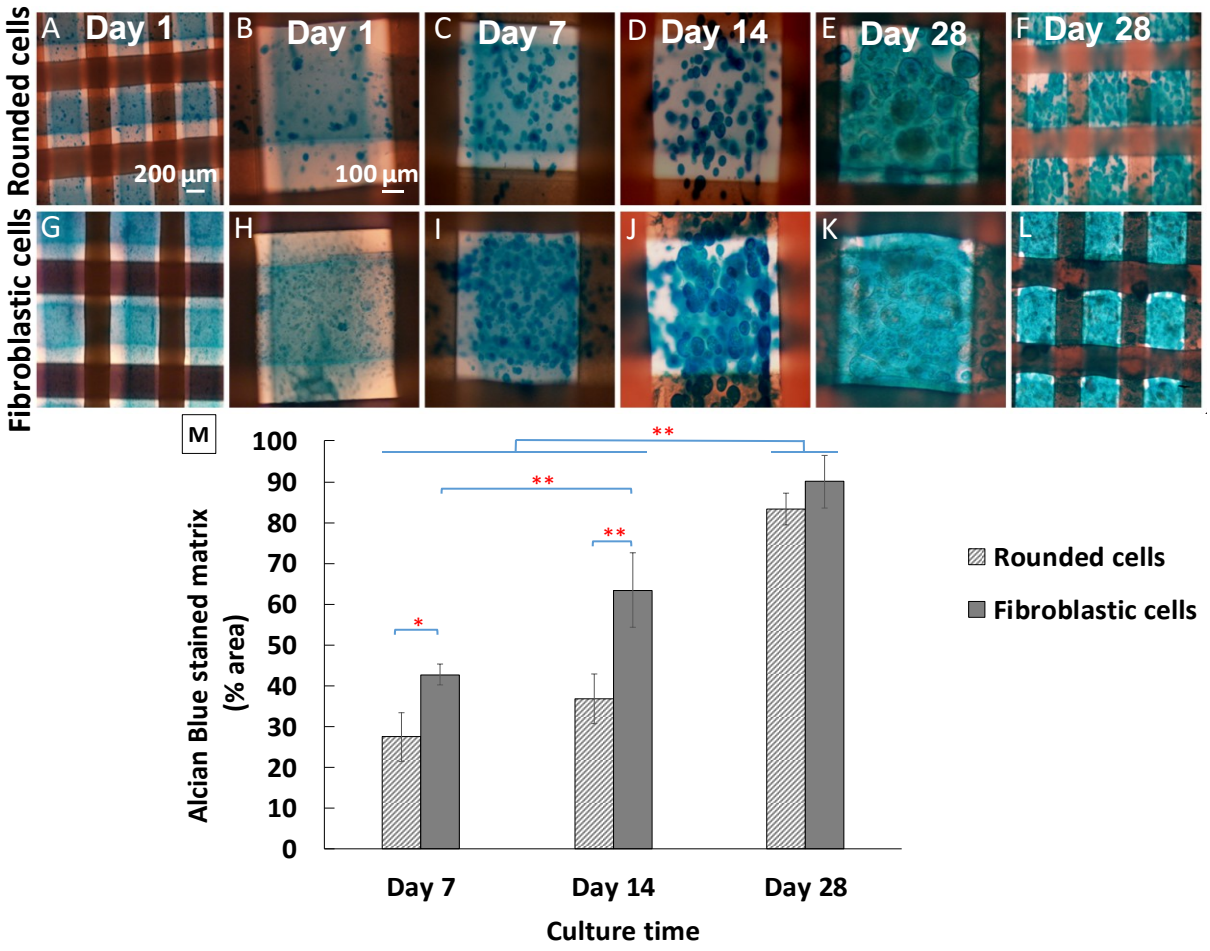

Figure 3.9 Increased secretion of Alcian blue-positive matrix in the 3D hybrid constructs over *in vitro* culture time. Alcian blue-stained 3D constructs impregnated with (A-F) rounded and (G-L) fibroblastic cells at day 1 (A,B,G, H), day 7 (C,I), day 14 (D,J), and day 28 (E,F,K,L). Panels B, E, H, and K are high magnification views of samples in panels A, F, G, and L, respectively. (M) Quantitative increase of Alcian blue-positive matrix in 3D hybrid constructs over time in culture for rounded and fibroblastic cells. Single asterisk and double asterisks indicate statistically significant differences with $P<0.05$ and $P<0.001$, respectively.

Col2 immunostaining demonstrated secretion of Collagen type II matrix around impregnated cells of the *in vitro*-cultured hybrid constructs. Similar to the Alcian blue staining results, Col2-stained matrix increased for both rounded and fibroblastic cells over time in culture (Fig. 3.10). At day 1 and 7, rounded and fibroblastic cells showed comparable Col2 matrix secretion. However, fibroblastic cell hybrid constructs seemed to have larger and more continuous Col2-stained matrix than the rounded cells by day 14 of culture (Fig. 3.10D,E,I,J). The cells impregnated in the constructs also secreted some Collagen type X (Col10) matrix after

long term *in vitro* culture (Fig. 3.11). In summary, these data demonstrate that hybrid constructs are permissive for chondrogenic differentiation and secretion of Collagen type II matrix by both rounded and fibroblastic cells.

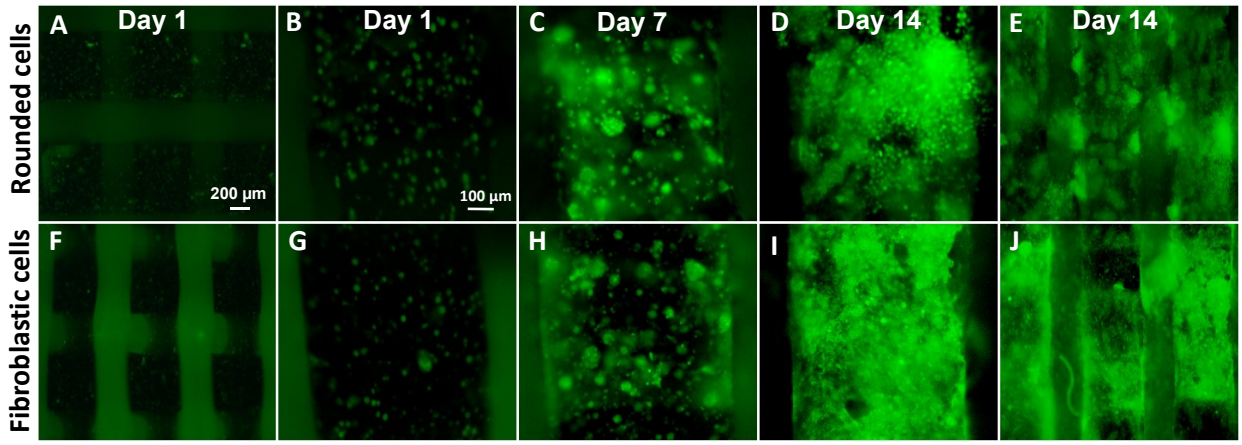

Figure 3.10 Collagen type II (Col2) immunofluorescence staining illustrates increase of Col2-positive matrix over time in 3D hybrid constructs. Fluorescent images of constructs impregnated with rounded (A-E) and fibroblastic cells (F-J) at day 1 (A,B, F,G), day 7 (C,H), and day 14 (D,E,I,J). The same exposure time was used for panels B-D and G-I to illustrate relative increase in Col2 immunostaining during culture.

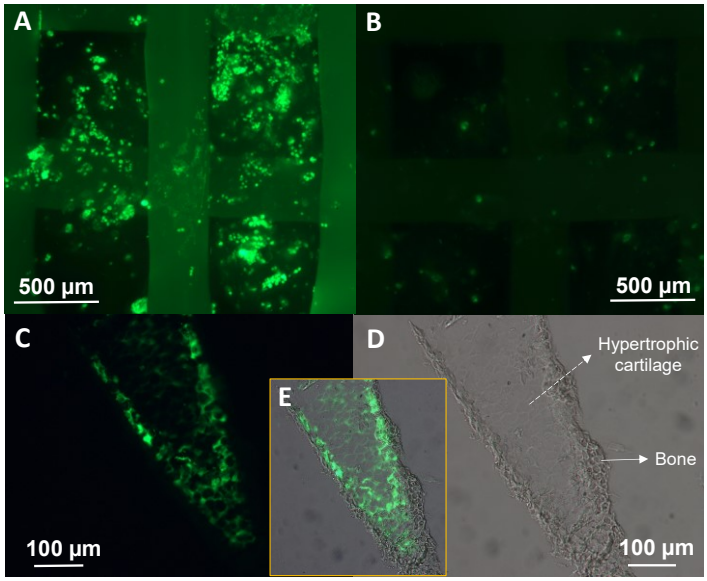

Figure 3.11 Collagen type II (Col2) and type X (Col10) immunofluorescence staining illustrates both (A) Col2-positive matrix and (B) some Col10-positive matrix in the 3D hybrid constructs. (C) Hypertrophic cartilage of developing limb in embryonic chick (HH35) was used as a positive control for Col10 immunostaining. (D) DIC image of HH35 chick section, and (E) overlay image of panels C and D demonstrate abundant Col10 in hypertrophic cartilage of the developing embryonic chick limb.

3.4.6 Biofabrication of cartilage hybrid constructs can be scaled up successfully

To confirm that this biofabrication method can be scaled up to make biologically functional constructs with a thickness approximating that of mature cartilage, 6-layer constructs were printed, and cell viability and matrix production were evaluated. For these experiments, the common chondrogenic cell line, ATDC5 [56, 57], was used. High cell viability and Alcian blue staining at days 14 and 28 of culture demonstrated that this hybrid biofabrication method can be scaled up to create multilayer constructs that maintain high cell viability and secretion of GAGs (Fig. 3.12, and data not shown). Cross section views further confirmed the biocompatibility of the PCL printing temperature. Similar to the two-layer hybrid constructs (Fig. 3.8A-G), uniform distribution of cells within the alginate throughout the thickness of six-layer constructs verified the integrity of the alginate hydrogel 3D structure during in vitro culture (Fig. 3.12). These results demonstrate not only the successful up-scaling of this biofabrication method, but also illustrate its versatility on multiple cell sources.

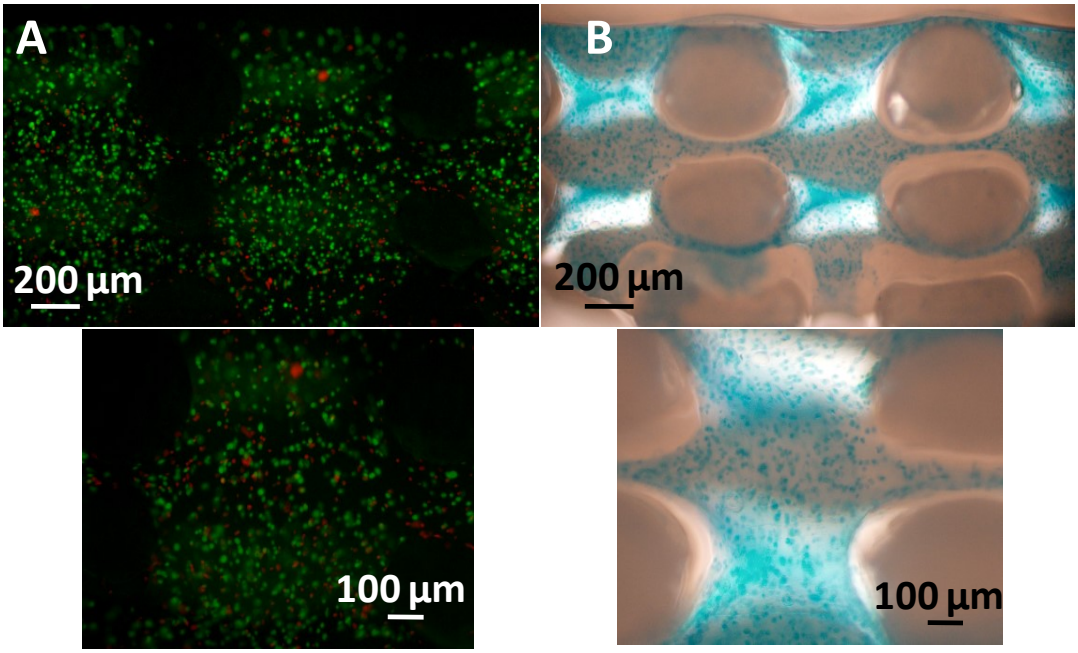

Figure 3.12 Six-layer hybrid constructs with impregnated ATDC5 cells also demonstrate good biofunctionality. Cross section views of six-layer constructs revealed promising biological performance by (A) live (green) and dead (red) cell viability assay, and (B) Alcian blue-positive matrix at day 14. Cross section of the PCL strands and the outline of the transverse PCL strands that make the 0/90º pattern in the stacked layers are seen in panel B.

3.5 Discussion

Identifying parameters of biofabrication that enable reproducible results, while ensuring biocompatibility, is critical to future clinical applications of tissue engineering. Recently, the sophisticated tissue engineering strategy of 3D bioprinting live cells into hybrid constructs has been attracting more attention, since it can generate customized structural and biological functions. Also, this biofabrication method is automated, hands-free, and economical, showing promise to improve cartilage tissue regeneration and facilitate clinical translations. The feasibility of using 3D bioprinting for cartilage tissue engineering had been shown by limited studies [23-25], and this study confirmed and significantly expanded the promising potential of this technique. Parameters of a hybrid biofabrication process that employs melt-dispensed PCL polymer and chondrocyte-impregnated alginate were identified to enable biocompatible impregnation of cells and allow maintenance of the construct's structural integrity [see Appendix A]. Throughout culture periods of four weeks, impregnated cells were distributed uniformly, and high cell viability was observed (Figs. 3.7,8). Although PCL was dispensed at high temperatures, there was a relatively fast (within seconds) and large decrease of temperature at the surface of the dispensed PCL strand (Fig. 3.2), presumably because the small size of the strands accelerated the cooling process. The high observed cell viability during biofabrication of hybrid constructs may result from this rapid cooling, since there was no spatial correlation between dead cells and dispensed PCL (Figs. 3.7,12)

Reproducible and biocompatible 3D printing of structurally stable hydrogels remains a challenge. The PCL scaffold provides mechanical properties to the hybrid construct [25], with the goal of withstanding loading of the joint after *in situ* implantation, yet still allowing some transfer of applied mechanical stimuli to the cells in the alginate. In the absence of any external loading, such as in the experiments reported here, the PCL scaffold likely does not affect the biological behaviour of cells encapsulated in alginate. The performance of the PCL scaffold in transferring customized mechanical stimuli (modulated by the PCL architectural design) to the cells in the alginate is recommended to be investigated in the future studies. Despite mechanical support from PCL, the alginate strands in hybrid constructs also need to exhibit some level of stability after fabrication in order to maintain the customized design properties. Crosslinking the hydrogel before dispensing can improve biofabrication [38], but the crosslinking process is progressive, leading to changes in hydrogel viscosity over time. This introduces undesirable,

time-dependent variability to the fabrication process, making the pre-crosslinking method less reproducible. The more common approach of using higher concentrations of alginate (e.g. 3.5%-10% [24, 38, 62]) also benefits its structural stability, but suffers from limitations on biocompatibility. Cells are subjected to increased shear stress during printing [26, 27], and increased alginate concentrations may provide a less favourable biological environment for some cells [24, 28, 29]. In this study, suitable biofabrication parameters were identified to avoid these limitations. A combination of alginate processing temperature and initial viscosity was found to improve printability at low concentrations (2% and 2.5% w/w) without any pre-crosslinking (Fig. 3.6). This finding should assist tissue engineering strategies that require low hydrogel concentrations for biological reasons [63].

To evaluate the biological performance of hybrid constructs, two distinct cell populations isolated from embryonic chick cartilage were assayed for cell viability, proliferation, and secretion of cartilage ECM components during lengthy periods of *in vitro* culture. The "rounded" and "fibroblastic" cell populations were identified in 2D primary cultures based upon morphology (round versus elongated) and adhesive affinity to the culture flask (floating/easily detached versus firmly attached) (Fig. 3.4). After bioprinting into 3D hybrid constructs, these cell populations continued to demonstrate some differences (i.e., timecourse of proliferation and secretion of cartilage ECM) (Figs. 3.8-10), but they both showed high overall biological performance (Fig. 3.7-10).

Focussing first on similarities in the *in vitro* performance of two distinct cell populations in hybrid constructs, both rounded and fibroblastic cells displayed high viability and abundant secretion of cartilage ECM (Figs. 3.7, 9 & 10). Cell viability was over 80% for up to 14 days of culture. Also, abundant Alcian blue staining and Col2 immunostaining in both cell populations (Figs. 3.9,10) reflect secretion of the two major components of cartilage ECM, GAGs and Collagen type II [61], further demonstrating the promising biocompatibility of this 3D biofabrication method. While the majority of impregnated cells appear to maintain a non-hypertrophic, cartilaginous phenotype throughout the examined culture period, a few cells expressed Col10 after long culture time (Fig. 3.11). Col10 expression is characteristic of deep and calcified layers of articular cartilage [64-66], so future work must be done to regulate layer-specific gene expression in engineered cartilage constructs. These are critical results for therapeutic applications of cartilage tissue engineering, since culturing tissue constructs *in vitro*

for a period of time may allow cells to initiate lineage-specific (e.g., chondrocyte) cellular activities prior to *in vivo* implantation [34, 67].

Differences in biological performance of the rounded and fibroblastic cells in hybrid constructs are presumed to rise from intrinsic differences between the two cell populations, since similar results were obtained in many independent experiments. These results raise the general issue of the importance of selecting among alternative cell sources for tissue engineering applications. Rounded and fibroblastic cells showed differences in the timing of cell proliferation and secretion of cartilage ECM (Figs. 3.8-10). A dramatic increase in proliferation of fibroblastic cells compared to rounded cells was observed at later timepoints of 3D hybrid construct culture (Fig. 3.8). Also, statistically larger regions of Alcian blue-stained matrix appeared in fibroblastic cells than in rounded cells at days 7 and 14 of culture (Fig. 3.9), and fibroblastic cell constructs appeared to contain larger areas of Col2-positive matrix than the rounded cells at day 14 of culture (Fig. 3.10). Together, these data suggest that fibroblastic cells secrete abundant cartilage ECM earlier than rounded cells, but they also maintain capacity for proliferation longer than the rounded cells. Both of these features seem beneficial for therapeutic applications of cartilage tissue engineering, and call for an understanding of the mechanistic basis for these observations.

Despite the fact that both rounded and fibroblastic cells were isolated from the same source (embryonic cartilage), I propose that differences in their biological performance in 3D hybrid constructs are explained by the idea that they are at different states of chondrocyte differentiation. Rounded cells have typical chondrocyte morphology [68], suggesting that they may be differentiated chondrocytes. On the other hand, fibroblastic cells have a morphology that is that is typical of many cell types, including stem cells [69]. Given their origin from embryonic cartilage, the fibroblastic cells may be undifferentiated cartilage stem cells (chondroprogenitors) or dedifferentiated chondrocytes. While dedifferentiation of primary cells is common in 2D culture [70, 71], two functional observations support the assertion that fibroblastic cells are cartilage stem cells. Chondroprogenitor cells maintain capacity for cell division [36], and fibroblastic cells demonstrated increased cell proliferation. Also, asymmetric division of progenitor cells give rise to differentiated cells [36, 72], and fibroblastic cells appeared to give rise to rounded cells during 2D culture (Fig. 3.4). Interestingly, when rounded cells were cultured in a 2D environment, some cells attached to the substrate and formed fibroblastic morphology (data not shown), indicating that some rounded cells still have the potential to dedifferentiate and

attach to the tissue culture plate. Similar behaviour of cartilage cells in 2D culture has also been observed in human [73], murine [74, 75], and chick [76, 77] primary embryonic chondrocytes. Moreover, the continued proliferation of the rounded cells in the 3D constructs (Fig. 3.8) suggests that they may not be fully-matured, post-mitotic chondrocytes, which have low proliferation capability [78, 79]. In fact, their proliferative capability is similar to transiently-amplifying chondrocytes that are organized into columns of the developing growth plate [79, 80]. Finally, molecular data support the idea that rounded cells are chondrocytes and fibroblastic cells are chondroprogenitors (Fig. 3.5). qPCR analyses directly after 3D bioprinting showed that rounded cells had significantly higher expression of *Col2a1*, a marker of differentiated chondrocytes [61, 81, 82], while fibroblastic cells expressed significantly higher levels of *Col1a2*, a marker of undifferentiated mesenchymal cells [83, 84].

In total, these functional and molecular data suggest that chondroprogenitors may serve as a better cell source than differentiated chondrocytes in cartilage tissue engineering, since they produce cartilage ECM quicker and proliferate more. Such speculation needs to be supported by rigorous molecular characterization (e.g., transcriptomics) and clonal cell analyses, but would inform a critical, unresolved issue for therapeutic applications of cartilage tissue engineering. Which among the two common cell sources is best: chondroprogenitors from mesenchymal stem cells, or primary chondrocytes isolated from differentiated cartilage [36, 85-88]?

To be clinically relevant, biofabrication methods must work with a variety of cell sources and also be capable of making constructs that match the size of the tissue to be replaced. The cartilage tissue engineering method developed in this study satisfied these objectives. Good biological performance in hybrid constructs was observed using three different cell types and sources: rounded and fibroblastic cells from primary embryonic chick cartilage, as well as a mammalian chondrocytic cell line, ATDC5. While these cells do not have direct application to large animal and human studies, the primary cell isolation method used here from embryonic chick is similar to that used to isolate primary chondrocytes from larger animals and human tissues [89]. Future applications of this hybrid biofabrication method should be explored using primary chondrocytes and mesenchymal stem cells from adult tissues. Furthermore, the hybrid biofabrication method demonstrated good performance when scaled up from two-layer (480 μm) to six-layer (1.44 mm) constructs (Fig. 3.12). These six-layer constructs approximate the average thickness of human articular cartilage (e.g. [55]). Future applications of this hybrid fabrication

method may improve engineering of cartilage and other tissues. Complex structural and biological properties could be designed into constructs that mimic the zonal characteristics of articular cartilage [21, 31]. Such biomimetic tissue constructs may promote more natural ECM formation [90, 91].

In addition to cartilage tissue engineering, the developed biofabrication method could improve functionality of many different soft and hard engineered tissues (such as tendon, ligament, bone and tooth) that require synergistic components with customized properties [92, 93]. Advanced biofabrication technologies build the foundations for hands-free, automated, aseptic, and economic tissue engineering methodologies that are required for large-scale clinical trials [94-96].

3.6 Conclusions

In this study, a 3D printing-based biofabrication technique was developed successfully for making custom-designed, hybrid constructs from polymer and cell-impregnated hydrogel. Demonstrating the potential for advanced cartilage tissue engineering, this hybrid biofabrication enabled promising biological performance (viability, proliferation, and cartilage ECM secretion) of three different cell types (two primary embryonic cell populations and an established chondrocyte line). Statistically significant differences in biological performance of two morphologically distinct cell populations isolated from embryonic chick cartilage were discussed in relation to the strategy of using differentiated vs. progenitor cells in tissue engineering. The hybrid biofabrication method described here can be used to develop sophisticated, biomimetic tissue constructs with more complicated structures and functions.

3.7 References

1. Makris, E.A.; Gomoll, A.H.; Malizos, K.N.; Hu, J.C.; Athanasiou, K.A. Repair and tissue engineering techniques for articular cartilage. *Nat Rev Rheumatol* **2015**, 11, 21-34.

2. Hunziker, E.B.; Lippuner, K.; Shintani, N. How best to preserve and reveal the structural intricacies of cartilaginous tissue. *Matrix Biol* **2014**, 39, 33-43.

3. Athanasiou, K.A.; Darling, E.M.; Hu, J. Articular cartilage tissue engineering, In *Synthesis Lectures on Tissue Engineering*;Editor^Editors, Eds.; Morgan & Claypool: San Rafael, CA, USA, 2009. pp 182.

4. Bian, L.; Fong, J.V.; Lima, E.G.; Stoker, A.M.; Ateshian, G.A.; Cook, J.L.; Hung, C.T. Dynamic mechanical loading enhances functional properties of tissue-engineered cartilage using mature canine chondrocytes. *Tissue Eng Part A* **2010**, 16, 1781-1790.

5. Kisiday, J.D.; Jin, M.; DiMicco, M.A.; Kurz, B.; Grodzinsky, A.J. Effects of dynamic compressive loading on chondrocyte biosynthesis in self-assembling peptide scaffolds. *J Biomech* **2004**, 37, 595-604.

6. Kawanishi, M.; Oura, A.; Furukawa, K.; Fukubayashi, T.; Nakamura, K.; Tateishi, T.; Ushida, T. Redifferentiation of dedifferentiated bovine articular chondrocytes enhanced by cyclic hydrostatic pressure under a gas-controlled system. *Tissue Eng* **2007**, 13, 957-964.

7. Poole, A.R.; Kojima, T.; Yasuda, T.; Mwale, F.; Kobayashi, M.; Laverty, S. Composition and structure of articular cartilage: a template for tissue repair. *Clin Orthop Relat Res* **2001**, S26-33.

8. Chang, C.-H.; Lin, F.-H.; Kuo, T.-F.; Liu, H.-C. Cartilage tissue engineering. *Biomed Eng (Singapore)* **2005**, 17, 61-71.

9. Bryant, S.J.; Anseth, K.S. Hydrogel properties influence ECM production by chondrocytes photoencapsulated in poly(ethylene glycol) hydrogels. *J Biomed Mater Res* **2002**, 59, 63-72.

10. Rahfoth, B.; Weisser, J.; Sternkopf, F.; Aigner, T.; von der Mark, K.; Brauer, R. Transplantation of allograft chondrocytes embedded in agarose gel into cartilage defects of rabbits. *Osteoarthritis Cartilage* **1998**, 6, 50-65.

11. Elisseeff, J.H.; Yamada, Y.; Langer, R. Biomaterials for tissue engineering, In *Tissue engineering and biodegradable equivalents: Scientific and clinical applications*;Editor^Editors, Eds.; Marcel Dekker, Inc.: New York, NY, USA, 2002. pp 23.

12. Li, W.J.; Laurencin, C.T.; Caterson, E.J.; Tuan, R.S.; Ko, F.K. Electrospun nanofibrous structure: a novel scaffold for tissue engineering. *J Biomed Mater Res* **2002**, 60, 613-621.

13. Sechriest, V.F.; Miao, Y.J.; Niyibizi, C.; Westerhausen-Larson, A.; Matthew, H.W.; Evans, C.H.; Fu, F.H.; Suh, J.K. GAG-augmented polysaccharide hydrogel: a novel biocompatible and biodegradable material to support chondrogenesis. *J Biomed Mater Res* **2000**, 49, 534-541.

14. Puppi, D.; Chiellini, F.; Piras, A.M.; Chiellini, E. Polymeric materials for bone and cartilage repair. *Prog Polym Sci* **2010**, 35, 403-440.

15. Moutos, F.T., *Biomimetic Composite Scaffold for the Functional Tissue Engineering of Articular Cartilage*, in *Biomedical Engineering*. 2009, Duke University: Durham, NC, USA. p. 166.

16. Xu, T.; Binder, K.W.; Albanna, M.Z.; Dice, D.; Zhao, W.; Yoo, J.J.; Atala, A. Hybrid printing of mechanically and biologically improved constructs for cartilage tissue engineering applications. *Biofabrication* **2013**, 5, 015001.

17. Jung, Y.; Kim, S.H.; Kim, Y.H.; Kim, S.H. The effect of hybridization of hydrogels and poly(L-lactide-co-epsilon-caprolactone) scaffolds on cartilage tissue engineering. *J Biomater Sci Polym Ed* **2010**, 21, 581-592.

18. Tanaka, Y.; Yamaoka, H.; Nishizawa, S.; Nagata, S.; Ogasawara, T.; Asawa, Y.; Fujihara, Y.; Takato, T.; Hoshi, K. The optimization of porous polymeric scaffolds for chondrocyte/atelocollagen based tissue-engineered cartilage. *Biomaterials* **2010**, 31, 4506-4516.

19. Schagemann, J.C.; Chung, H.W.; Mrosek, E.H.; Stone, J.J.; Fitzsimmons, J.S.; O'Driscoll, S.W.; Reinholz, G.G. Poly-epsilon-caprolactone/gel hybrid scaffolds for cartilage tissue engineering. *J Biomed Mater Res A* **2010**, 93, 454-463.

20. Kawazoe, N.; Inoue, C.; Tateishi, T.; Chen, G. A cell leakproof PLGA-collagen hybrid scaffold for cartilage tissue engineering. *Biotechnol Prog* **2010**, 26, 819-826.

21. Izadifar, Z.; Chen, X.; Kulyk, W. Strategic design and fabrication of engineered scaffolds for articular cartilage repair. *J Funct Biomater* **2012**, 3, 799-838.

22. Pfister, A.; Landers, R.; Laib, A.; Hübner, U.; Schmelzeisen, R.; Mülhaupt, R. Biofunctional rapid prototyping for tissue-engineering applications: 3D bioplotting versus 3D printing. *J Polym Sci A Polym Chem* **2004**, 42, 624-638.

23. Pati, F.; Jang, J.; Ha, D.H.; Won Kim, S.; Rhie, J.W.; Shim, J.H.; Kim, D.H.; Cho, D.W. Printing three-dimensional tissue analogues with decellularized extracellular matrix bioink. *Nat Commun* **2014**, 5, 3935.

24. Kundu, J.; Shim, J.H.; Jang, J.; Kim, S.W.; Cho, D.W. An additive manufacturing-based PCL-alginate-chondrocyte bioprinted scaffold for cartilage tissue engineering. *J Tissue Eng Regen Med* **2013**.

25. Schuurman, W.; Khristov, V.; Pot, M.W.; van Weeren, P.R.; Dhert, W.J.; Malda, J. Bioprinting of hybrid tissue constructs with tailorable mechanical properties. *Biofabrication* **2011**, 3, 021001.

26. Li, M.; Tian, X.; Zhu, N.; Schreyer, D.J.; Chen, X. Modeling process-induced cell damage in the biodispensing process. *Tissue Eng Part C Methods* **2010**, 16, 533-542.

27. Nair, K.; Yan, K.; Sun, W. A Multi-Level Numerical Model for Qunatifying Cell Deformation in Impregnated Alginate Structures. *J Mech Mater Struct* **2007**, 2, 1121-1139.

28. Bohari, S.P.; Hukins, D.W.; Grover, L.M. Effect of calcium alginate concentration on viability and proliferation of encapsulated fibroblasts. *Biomed Mater Eng* **2011**, 21, 159-170.

29. Kong, H.J.; Smith, M.K.; Mooney, D.J. Designing alginate hydrogels to maintain viability of immobilized cells. *Biomaterials* **2003**, 24, 4023-4029.

30. Maher, P.S.; Keatch, R.P.; Donnelly, K.; Mackay, R.E.; Paxton, J.Z. Construction of 3D biological matrices using rapid prototyping technology. *Rapid Prototyp J* **2009**, 15.

31. Klein, T.J.; Malda, J.; Sah, R.L.; Hutmacher, D.W. Tissue engineering of articular cartilage with biomimetic zones. *Tissue Eng Part B Rev* **2009**, 15, 143-157.

32. Chung, C.; Burdick, J.A. Engineering cartilage tissue. *Adv Drug Deliv Rev* **2008**, 60, 243-262.

33. Darling, E.M.; Athanasiou, K.A. Rapid phenotypic changes in passaged articular chondrocyte subpopulations. *J Orthop Res* **2005**, 23, 425-432.

34. Kock, L.; van Donkelaar, C.C.; Ito, K. Tissue engineering of functional articular cartilage: the current status. *Cell Tissue Res* **2012**, 347, 613-627.

35. Discher, D.E.; Mooney, D.J.; Zandstra, P.W. Growth factors, matrices, and forces combine and control stem cells. *Science* **2009**, 324, 1673-1677.

36. O'Sullivan, J.; D'Arcy, S.; Barry, F.P.; Murphy, J.M.; Coleman, C.M. Mesenchymal chondroprogenitor cell origin and therapeutic potential. *Stem Cell Res Ther* **2011**, 2, 8.

37. Li, M.; Tian, X.; Schreyer, D.J.; Chen, X. Effect of needle geometry on flow rate and cell damage in the dispensing-based biofabrication process. *Biotechnol Prog* **2011**, 27, 1777-1784.

38. Lee, H.; Ahn, S.; Bonassar, L.J.; Kim, G. Cell(MC3T3-E1)-printed poly(-caprolactone)/alginate hybrid scaffolds for tissue regeneration. *Macromol Rapid Commun* **2013**, 34, 142-149.

39. Meier, S.; Solursh, M. Ultrastructural analysis of the effect of ascorbic acid on secretion and assembly of extracellular matrix by cultured chick embryo chondrocytes. *J Ultrastruct Res* **1978**, 65, 48-59.

40. Thomas, J.T.; Grant, M.E. Cartilage proteoglycan aggregate and fibronectin can modulate the expression of type X collagen by embryonic chick chondrocytes cultured in collagen gels. *Biosci Rep* **1988**, 8, 163-171.

41. Farjanel, J.; Schurmann, G.; Bruckner, P. Contacts with fibrils containing collagen I, but not collagens II, IX, and XI, can destabilize the cartilage phenotype of chondrocytes. *Osteoarthritis Cartilage* **2001**, 9 Suppl A, S55-63.

42. Walker, E.A.; Verner, A.; Flannery, C.R.; Archer, C.W. Cellular responses of embryonic hyaline cartilage to experimental wounding in vitro. *J Orthop Res* **2000**, 18, 25-34.

43. Hirsch, M.S.; Svoboda, K.H. Establishment of a whole-chick sternum model that recapitulates normal cartilage development. *Biotechniques* **1998**, 24, 632-636.

44. Huang, X.; Zhang, Y.; Donahue, H.J.; Lowe, T.L. Porous thermoresponsive-co-biodegradable hydrogels as tissue-engineering scaffolds for 3-dimensional in vitro culture of chondrocytes. *Tissue Eng* **2007**, 13, 2645-2652.

45. Zhang, Z.; McCaffery, J.M.; Spencer, R.G.; Francomano, C.A. Growth and integration of neocartilage with native cartilage in vitro. *J Orthop Res* **2005**, 23, 433-439.

46. Zhang, Z.; McCaffery, J.M.; Spencer, R.G.; Francomano, C.A. Hyaline cartilage engineered by chondrocytes in pellet culture: histological, immunohistochemical and ultrastructural analysis in comparison with cartilage explants. *J Anat* **2004**, 205, 229-237.

47. Girotto, D.; Urbani, S.; Brun, P.; Renier, D.; Barbucci, R.; Abatangelo, G. Tissue-specific gene expression in chondrocytes grown on three-dimensional hyaluronic acid scaffolds. *Biomaterials* **2003**, 24, 3265-3275.

48. Mayne, R.; Vail, M.S.; Mayne, P.M.; Miller, E.J. Changes in type of collagen synthesized as clones of chick chondrocytes grow and eventually lose division capacity. *Proceedings of the National Academy of Sciences* **1976**, 73, 1674-1678.

49. von der Mark, K.; Gauss, V.; von der Mark, H.; Müller, P. Relationship between cell shape and type of collagen synthesised as chondrocytes lose their cartilage phenotype in culture. **1977**.

50. Tschan, T.; Höerler, I.; Houze, Y.; Winterhalter, K.H.; Richter, C.; Bruckner, P. Resting chondrocytes in culture survive without growth factors, but are sensitive to toxic oxygen metabolites. *The Journal of cell biology* **1990**, 111, 257-260.

51. Glaser, J.H.; Conrad, H.E. Properties of chick embryo chondrocytes grown in serum-free medium. *Journal of Biological Chemistry* **1984**, 259, 6766-6772.

52. Capasso, O.; Gionti, E.; Pontarelli, G.; Ambesi-Impiombato, F.S.; Nitsch, L.; Tajana, G.; Cancedda, R. The culture of chick embryo chondrocytes and the control of their differentiated functions in vitro. I. Characterization of the chondrocyte-specific phenotypes. *Experimental cell research* **1982**, 142, 197-206.

53. Bounelis, P.; Daniel, J.C. Preparation of primary cultures of embryonic chick chondrocytes in agarose. *Journal of tissue culture methods* **1982**, 7, 111-116.

54. Eames, B.F.; Helms, J.A. Conserved molecular program regulating cranial and appendicular skeletogenesis. *Dev Dyn* **2004**, 231, 4-13.

55. Frisbie, D.D.; Cross, M.W.; McIlwraith, C.W. A comparative study of articular cartilage thickness in the stifle of animal species used in human pre-clinical studies compared to articular cartilage thickness in the human knee. *Vet Comp Orthop Traumatol* **2006**, 19, 142-146.

56. Kwon, H.J.; Yasuda, K.; Ohmiya, Y.; Honma, K.; Chen, Y.M.; Gong, J.P. In vitro differentiation of chondrogenic ATDC5 cells is enhanced by culturing on synthetic hydrogels with various charge densities. *Acta Biomater* **2010**, 6, 494-501.

57. Tare, R.S.; Howard, D.; Pound, J.C.; Roach, H.I.; Oreffo, R.O. Tissue engineering strategies for cartilage generation--micromass and three dimensional cultures using human chondrocytes and a continuous cell line. *Biochem Biophys Res Commun* **2005**, 333, 609-621.

58. Rasband, W.S., *ImageJ*. 1997-2014, U. S. National Institutes of Health: Bethesda, Maryland, USA.

59. Radonic, A.; Thulke, S.; Mackay, I.M.; Landt, O.; Siegert, W.; Nitsche, A. Guideline to reference gene selection for quantitative real-time PCR. *Biochem Biophys Res Commun* **2004**, 313, 856-862.

60. Livak, K.J.; Schmittgen, T.D. Analysis of relative gene expression data using real-time quantitative PCR and the 2(-Delta Delta C(T)) Method. *Methods* **2001**, 25, 402-408.

61. Eames, B.F.; de la Fuente, L.; Helms, J.A. Molecular ontogeny of the skeleton. *Birth Defects Res C Embryo Today* **2003**, 69, 93-101.

62. Fedorovich, N.E.; Schuurman, W.; Wijnberg, H.M.; Prins, H.J.; van Weeren, P.R.; Malda, J.; Alblas, J.; Dhert, W.J. Biofabrication of osteochondral tissue equivalents by printing topologically defined, cell-laden hydrogel scaffolds. *Tissue Eng Part C Methods* **2012**, 18, 33-44.

63. Khalil, S.; Sun, W. Bioprinting endothelial cells with alginate for 3D tissue constructs. *J Biomech Eng* **2009**, 131, 111002.

64. Kirsch, T.; von der Mark, K. Isolation of human type X collagen and immunolocalization in fetal human cartilage. *Eur J Biochem* **1991**, 196, 575-580.

65. Eerola, I.; Salminen, H.; Lammi, P.; Lammi, M.; von der Mark, K.; Vuorio, E.; Saamanen, A.M. Type X collagen, a natural component of mouse articular cartilage: association with growth, aging, and osteoarthritis. *Arthritis Rheum* **1998**, 41, 1287-1295.

66. Reichenberger, E.; Aigner, T.; von der Mark, K.; Stoss, H.; Bertling, W. In situ hybridization studies on the expression of type X collagen in fetal human cartilage. *Developmental biology* **1991**, 148, 562-572.

67. Deponti, D.; Di Giancamillo, A.; Mangiavini, L.; Pozzi, A.; Fraschini, G.; Sosio, C.; Domeneghini, C.; Peretti, G.M. Fibrin-based model for cartilage regeneration: tissue maturation from in vitro to in vivo. *Tissue Eng Part A* **2012**, 18, 1109-1122.

68. Glattauer, V.; W.B., T.; White, J.F.; Nigro, J.; Tebb, T.A.; Werkmeister, J.A.; Ramshaw, J.A.M. Direct Use of Resorbable Collagen-Based Beads for Cell Delivery in Tissue Engineering and Cell Therapy Applications, In *Regenerative Medicine and Tissue Engineering - Cells and Biomaterials*;Editor^Editors, Eds.; InTech, 2011.

69. Beyer Nardi, N.; da Silva Meirelles, L. Mesenchymal stem cells: isolation, in vitro expansion and characterization. *Handb Exp Pharmacol* **2006**, 249-282.

70. Benya, P.D.; Padilla, S.R.; Nimni, M.E. Independent regulation of collagen types by chondrocytes during the loss of differentiated function in culture. *Cell* **1978**, 15, 1313-1321.

71. Elima, K.; Vuorio, E. Expression of mRNAs for collagens and other matrix components in dedifferentiating and redifferentiating human chondrocytes in culture. *FEBS Lett* **1989**, 258, 195-198.

72. *The Endocrinology of Growth, Development, and Metabolism in Vertebrates*, ed. M.P. Schreibman;Scanes, C.G.;Pang, P.K.T. 2012, San Diego, CA, USA: Academic Press, Inc.

73. Stokes, D.G.; Liu, G.; Coimbra, I.B.; Piera-Velazquez, S.; Crowl, R.M.; Jimenez, S.A. Assessment of the gene expression profile of differentiated and dedifferentiated human fetal chondrocytes by microarray analysis. *Arthritis Rheum* **2002**, 46, 404-419.

74. Mirando, A.J.; Dong, Y.; Kim, J.; Hilton, M.J. Isolation and Culture of Murine Primary Chondrocytes #, In *T Skeletal Development and Repair*;Editor^Editors, Eds., 2014. pp 267-277.

75. Sautier, J.M.; Nefussi, J.R.; Forest, N. In vitro differentiation and mineralization of cartilaginous nodules from enzymatically released rat nasal cartilage cells. *Biol Cell* **1993**, 78, 181-189.

76. Yasumoto, S.; Kondo, S.; Kato, Y. Growth and differentiation of primary chick embryonic chondrocytes on agar plates. *Jpn J Exp Med* **1980**, 50, 221-224.

77. Guo, J.F.; Jourdian, G.W.; MacCallum, D.K. Culture and growth characteristics of chondrocytes encapsulated in alginate beads. *Connect Tissue Res* **1989**, 19, 277-297.

78. Zhang, J.; Wu, Y.; Thote, T.; Lee, E.H.; Ge, Z.; Yang, Z. The influence of scaffold microstructure on chondrogenic differentiation of mesenchymal stem cells. *Biomed Mater* **2014**, 9, 035011.

79. St-Jacques, B.; Hammerschmidt, M.; McMahon, A.P. Indian hedgehog signaling regulates proliferation and differentiation of chondrocytes and is essential for bone formation. *Genes & development* **1999**, 13, 2072-2086.

80. Lanza, R.; Blau, H.; Gearhart, J.; Hogan, B.; Melton, D.; Moore, M.; Pedersen, R.; Thomas, E.D.; Thomson, J.A.; Verfaillie, C., *Handbook of Stem Cells, Two-Volume Set: Volume 1-Embryonic Stem Cells; Volume 2-Adult & Fetal Stem Cells*. 2004: Academic Press.

81. Eames, B.F.; Allen, N.; Young, J.; Kaplan, A.; Helms, J.A.; Schneider, R.A. Skeletogenesis in the swell shark Cephaloscyllium ventriosum. *J Anat* **2007**, 210, 542-554.

82. Eames, B.F.; Amores, A.; Yan, Y.L.; Postlethwait, J.H. Evolution of the osteoblast: skeletogenesis in gar and zebrafish. *BMC Evol Biol* **2012**, 12, 27.

83. Zhang, H.; Kay, A.; Forsyth, N.R.; Liu, K.K.; El Haj, A.J. Gene expression of single human mesenchymal stem cell in response to fluid shear. *J Tissue Eng* **2012**, 3, 2041731412451988.

84. Kulterer, B.; Friedl, G.; Jandrositz, A.; Sanchez-Cabo, F.; Prokesch, A.; Paar, C.; Scheideler, M.; Windhager, R.; Preisegger, K.H.; Trajanoski, Z. Gene expression profiling of human mesenchymal stem cells derived from bone marrow during expansion and osteoblast differentiation. *BMC Genomics* **2007**, 8, 70.

85. Arai, F.; Ohneda, O.; Miyamoto, T.; Zhang, X.Q.; Suda, T. Mesenchymal stem cells in perichondrium express activated leukocyte cell adhesion molecule and participate in bone marrow formation. *The Journal of experimental medicine* **2002**, 195, 1549-1563.

86. English, A.; Jones, E.; Corscadden, D.; Henshaw, K.; Chapman, T.; Emery, P.; McGonagle, D. A comparative assessment of cartilage and joint fat pad as a potential source of cells for autologous therapy development in knee osteoarthritis. *Rheumatology* **2007**, 46, 1676-1683.

87. De Ugarte, D.A.; Morizono, K.; Elbarbary, A.; Alfonso, Z.; Zuk, P.A.; Zhu, M.; Dragoo, J.L.; Ashjian, P.; Thomas, B.; Benhaim, P. Comparison of multi-lineage cells from human adipose tissue and bone marrow. *Cells tissues organs* **2003**, 174, 101-109.

88. Friedenstein, A.; Piatetzky-Shapiro, I.; Petrakova, K. Osteogenesis in transplants of bone marrow cells. *Journal of embryology and experimental morphology* **1966**, 16, 381-390.

89. Tew, S.R.; Murdoch, A.D.; Rauchenberg, R.P.; Hardingham, T.E. Cellular methods in cartilage research: primary human chondrocytes in culture and chondrogenesis in human bone marrow stem cells. *Methods* **2008**, 45, 2-9.

90. McCullen, S.D.; Autefage, H.; Callanan, A.; Gentleman, E.; Stevens, M.M. Anisotropic fibrous scaffolds for articular cartilage regeneration. *Tissue Eng Part A* **2012**, 18, 2073-2083.

91. Nguyen, L.H.; Kudva, A.K.; Saxena, N.S.; Roy, K. Engineering articular cartilage with spatially-varying matrix composition and mechanical properties from a single stem cell population using a multi-layered hydrogel. *Biomaterials* **2011**, 32, 6946-6952.

92. Longo, U.G.; Lamberti, A.; Maffulli, N.; Denaro, V. Tendon augmentation grafts: a systematic review. *Br Med Bull* **2010**, 94, 165-188.

93. Park, C.H.; Rios, H.F.; Jin, Q.; Bland, M.E.; Flanagan, C.L.; Hollister, S.J.; Giannobile, W.V. Biomimetic hybrid scaffolds for engineering human tooth-ligament interfaces. *Biomaterials* **2010**, 31, 5945-5952.

94. Mironov, V.; Kasyanov, V.; Markwald, R.R. Organ printing: from bioprinter to organ biofabrication line. *Curr Opin Biotechnol* **2011**, 22, 667-673.

95. Mironov, V.; Trusk, T.; Kasyanov, V.; Little, S.; Swaja, R.; Markwald, R. Biofabrication: a 21st century manufacturing paradigm. *Biofabrication* **2009**, 1, 022001.

96. Cohen, D.L.; Malone, E.; Lipson, H.; Bonassar, L.J. Direct freeform fabrication of seeded hydrogels in arbitrary geometries. *Tissue Eng* **2006**, 12, 1325-1335.

CHAPTER 4: COMPUTED TOMOGRAPHY DIFFRACTION ENHANCED IMAGING FOR *IN SITU* VISUALIZATION OF TISSUE SCAFFOLDS IMPLANTED IN CARTILAGE

This chapter has been published as "Izadifar Z., Chapman LD, Chen X. (2014) Computed tomography diffraction-enhanced imaging for in situ visualization of tissue scaffolds implanted in cartilage. *Tissue Engineering Part C: Methods.* 20(2): 140-148". According to the Copyright Agreement, "the authors retain the right to include the journal article, in full or in part, in a thesis or dissertation".

4.1 Abstract

Long-term *in vivo* studies on animal models and advances from animal to human studies must rely on non-invasive monitoring methods. Synchrotron radiation (SR)-diffraction enhanced imaging (DEI) has shown great promise as a non-invasive method for visualizing native and/or engineered tissues and bio-microstructures with appreciable details *in situ*. The objective of this study was to investigate SR-DEI for *in situ* visualization and characterization of tissue engineered scaffolds implanted in cartilage. A piglet stifle joint implanted with an engineered scaffold made from polycaprolactone was imaged using SR computed tomography (CT)-DEI at an X-ray energy of 40 keV. For comparison, *in situ* visualization was also conducted with commonly-used SR CT-phase contrast imaging (PCI) and clinical magnetic resonance imaging (MRI) techniques. The reconstructed CT-DE images show the implanted scaffold with the structural properties much clearer than those in the CT-PC and MR images. Furthermore, CT-DEI was able to visualize microstructures within the cartilage as well as different soft tissues surrounding the joint. These microstructural details were not recognizable using other imaging techniques. Taken together, the results of this study suggest that CT-DEI can be used for non-invasive visualization and characterization of scaffolds in cartilage, representing an advance in tissue engineering to track the success of tissue scaffolds for cartilage repair.

4.2 Introduction

Articular cartilage is a specialized tissue that covers the ends of the bones in diarthrodial joints of the body and facilitates their movements within the joint. Articular cartilage lesions from traumatic joint injuries in children and young adults as well as cartilage degeneration resulting from osteoarthritis (OA; present in ~70% of the population aged 65 years and older [1]) are serious health problems throughout the world. Unfortunately, the natural healing ability of

human articular cartilage is very limited. Available clinical treatments for cartilage repair also have limited success [2] since they do not result in long-term correction of cartilage pathologies [3]. Tissue engineering (TE) aims to replace or repair damaged articular cartilage with an engineered tissue and, as such, holds great promise for joint repair. Most tissue engineering strategies employ 3-dimensional (3D) scaffolds made of biocompatible materials incorporated with viable cells and/or bioactive molecules to promote new tissue generation and functional recovery. To this end, the visualization of the scaffolds, once implanted in animal models or human patients, is essential to track their success. For this, scaffold visualization methods such as biomedical imaging play a significant role.

At the current experimental stages of cartilage TE, conventional histological and imaging techniques, such as light microscopy, scanning electron microscopy, transmission electron microscopy, and confocal laser microscopy, are typically used to visualize and study the success of the tissue engineered scaffolds. These conventional methods are destructive and involve invasive analysis, for which the animal model must be sacrificed. For long-term animal studies, a large number of animals are required for sacrifice throughout the experiments, which makes *in vivo* studies expensive and complicated. Furthermore, as TE strategies will eventually advance from animal to human studies, non-invasive visualization of scaffolds and new tissue generation becomes essential. Although a large number of TE studies have been targeting cartilage tissue, the development of non-invasive monitoring methods with application to cartilage tissue engineering has received limited attention.

Diffraction enhanced imaging (DEI) is an X-ray imaging technique that has shown great promise for non-destructive, quantitative, and qualitative visualization of soft tissues with detailed internal structures. DEI contrast is based on the refraction of X-rays, rather than absorption/attenuation as they travel through the object being imaged. This makes DEI a suitable technique for imaging TE scaffolds and constructs as well as soft tissues (e.g., cartilage) that have very low X-ray attenuation. The main advantage of DEI is that the images can be captured non-invasively and without any exogenous contrast agents. DEI is capable of resolving histological and structural details of articular cartilage [4-7], which are not easily visible using conventional imaging techniques based on absorption contrast. Cartilage consists of ~80% water and, as such, is invisible in conventional radiographs. This is also true for TE scaffolds and constructs made from low density materials [4, 8]. Magnetic resonance imaging (MRI) and

ultrasound are two additional, well-known medical imaging techniques. However, they exhibit some inherent limitations or disadvantages for imaging soft tissues and low density materials such as cartilage [9], including the limits on spatial resolution and the types of tissues/structures that can be resolved. Consequently, investigation of alternative non-invasive imaging techniques (such as DEI) that can overcome these limitations is greatly needed.

With its higher spatial resolution than MRI, synchrotron radiation (SR)-DEI offers considerable promise for providing detailed information of tissues and microstructures [10]. In-line phase contrast imaging (PCI) [11] is one SR X-ray imaging method based on similar, but simpler than DEI, principles and thus offers easier imaging modality. Because of its simplicity and ability to visualize microstructural details in various biological tissues and TE scaffolds [12, 13], PCI has been commonly used in tissue engineering. However, in most reported studies DEI and PCI have been used for imaging TE scaffolds in the *in vitro* or non-*in situ*-like conditions. Examples include imaging of dehydrated TE scaffolds in air [12, 13] and in thin tissue representative medium [8]. Although these studies demonstrate the potential of these techniques, their capacity for real *in vivo* TE studies has not been investigated and reported yet. Planar or 2-dimensional (2D) DEI and PCI have recently been investigated for visualization of low-density TE scaffolds embedded in muscle tissue with a sample thickness of up to 4 cm [8]. As the tissue sample becomes thicker (more than 4 cm) visualization of scaffold may become questionable by using these 2D imaging techniques. With the advance of computed tomography (CT), it is rational to combine these imaging techniques with CT to potentially overcome this limitation with improved capacity for visualization of TE scaffolds in thick tissue samples or *in situ*. To the best of the authors' knowledge, to date there have been no studies reported in this regard. As such, the objective of this study was aimed at investigating CT-DEI for visualization and characterization of TE cartilage scaffolds *in situ*, compared to CT-PCI and clinical MRI, so as to identify the most appropriate imaging technique for use in non-invasive and serial *in situ* monitoring of TE cartilage repair.

4.3 Materials and methods

4.3.1 Scaffold fabrication

The scaffold used in the present study was designed with a porous structure and then fabricated on a 3D-Bioplotter (Envisiontec GmbH, Gladbeck, Germany). The Bioplotter is a

three-axis, computer-controlled additive manufacturing system that can build 3D scaffolds from a variety of biomaterials. Poly-ε-caprolactone (PCL) (Mw 48,000-90,000, Aldrich, Saint Louis, MO, USA) was chosen for the scaffold fabrication due to its wide applications to cartilage tissue engineering. PCL was melted at 65 °C in the high-temperature dispensing head of the Bioplotter and was subsequently dispensed through a metal needle with an internal diameter of 400 µm under a pneumatic pressure of 0.75 MPa (Fig. 4.1A). Scaffolds were fabricated by dispensing melted PCL strands in multiple layers with a strand spacing of 1 mm and a 0°/90° pattern of successive layers (Fig. 4.1B). The scaffold was originally fabricated with an overall size of 10 mm × 10 mm × 1.7 mm and was then trimmed to 4 mm × 4 mm × 1.7 mm for implantation.

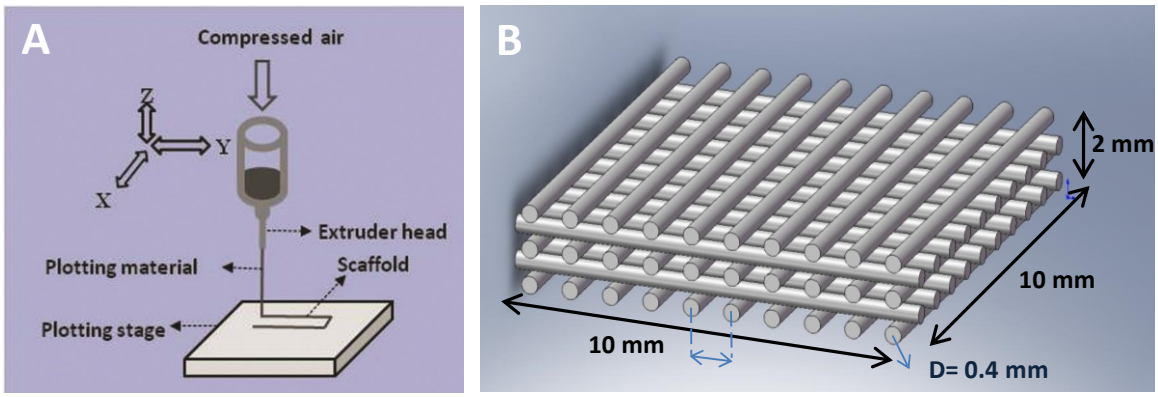

Figure 4.1 (A) Scaffold fabrication by using pneumatic dispenser head and (B) 3D scaffold with five layers of PCL strands.

4.3.2 Sample preparation

Pig joints are usually used for *in vivo* cartilage tissue engineering studies [14] because they better simulate human conditions than small animal models. In this study, the piglet stifle (knee) joint was selected to investigate the non-invasive imaging. Dissected stifle joints of four-week-old cadaver piglets were prepared at the Vaccine and Infection Disease Organization (VIDO, Saskatoon, Canada). For each sample, a full thickness articular defect (4.5 mm × 4.5 mm × 2-2.5 mm depth) was created in the lateral femoral condyle cartilage of the knee and a scaffold as prepared above was then implanted into the created defect area and covered with a piece of periosteum layer [14], which was concurrently harvested from the proximal femur (Fig. 4.2), to mimic the actual surgical procedure used in animal and clinical studies. During the implantation surgery, joint cavity fluid was released and as a result, air was entered the joint cavity and the surrounding soft tissues. It is noted that the trapped air may misrepresent *in vivo* conditions and

cause artifacts in the images. As such, the trapped air must be removed from the joint samples prior to being imagined. For this, joint samples were placed in a sample holder filled with Dulbecco's phosphate buffered saline, which was then placed in a vacuum desiccator for 10-15 min to remove trapped air. It is noted that in live animal/clinical studies, the trapped air may be gradually absorbed and removed from the site via the vascular system/blood circulation postsurgery, and then replaced with synovial and body fluids.

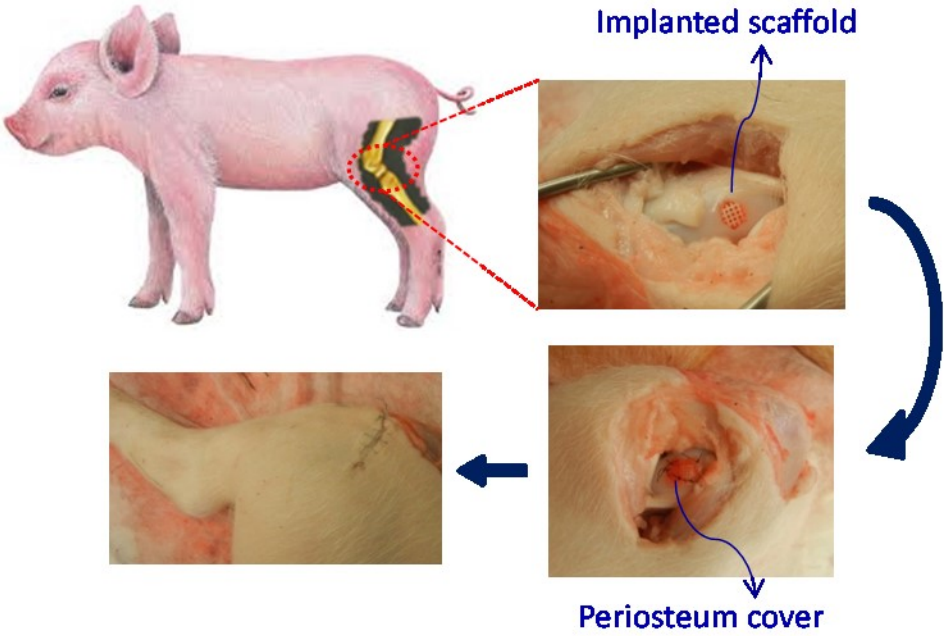

Figure 4.2 Surgical approach used for implanting TE scaffolds in the lateral femoral condyle cartilage of the knee in dissected piglet joints.

4.3.3 Synchrotron based imaging

Imaging was performed at the Biomedical Imaging and Therapy bend magnet (BMIT-BM) beamline of the Canadian Light Source (CLS, Canada). A highly collimated X-ray beam was produced by a bend magnet (1.354T) and monochromatized at 40 keV photon energy by a Si (4,4,0) double crystal monochromator. It is noted that the photon energy is determined by the thickness of tissue sample being imaged, i.e., thicker the sample is, higher photon energy is required. Based on the previous studies [8, 15], 40 keV photon energy and the analyzer reflection plane of Si (4,4,0) were selected and expected to be able to visualize the samples as prepared in this study. A Photonic Science detector (St. Geoirs, France) with an effective pixel size of 37 µm× 37 µm was employed to collect the images, which was selected based on the balance

between the area of interest in the sample and the image resolution, as well as the availability of detectors at the CLS. For each sample, CT images were acquired by rotating it 180° around an axis perpendicular to the incident beam with an angular scanning increment of 0.072°. During the process of imaging, both the beam and detector were stationary and the detector acquisition system was synchronized with the sample angular scanning. The size of the scanned region (field of view) at the detector was 4 mm (vertical) × 74 mm (horizontal). The time required for imaging one sample was 4.9 h for CT-DEI and 1.7 h for CT-PCI. The principles behind both CT-DEI and CT-PCI are outlined as follows.

4.3.3.1 CT-DEI

DEI can dramatically increase the contrast of X-ray images by utilizing a crystal analyzer that enables contrast mechanisms of refraction, ultra small angle x-ray scattering (USAXS), and scatter rejection of small angle x-ray scattering (SAXS) in addition to the absorption mechanism [5]. When the X-rays travel though the sample, they are refracted at the interfaces of organized features/structures in the tissue through angles of a few microradians. The analyzer placed between the object and the detector (Fig. 4.3) uses its angle-dependent reflectivity, or rocking curve (RC), to tune the diffraction of refracted, transmitted X-rays off the analyzer to the detector. At the detector, this is translated into enhanced contrast at the interface of features having different densities from their surroundings. A detailed description of the DEI method can be found in [16]. To obtain DEI refraction images, two sets of images were taken: one on the low angle side (the low-angle image (L)) and one on the high angle side (the high-angle image (H)) of the half maximum point of the analyzer RC (Fig. 4.3). On each side of the RC, tomographic images were acquired by taking 2500 projection images from angular scanning. For normalization of images, flat field (beam without sample) and dark field (without beam) images were also taken at both sides of RC. Refraction angle images were then calculated using the following equation [16]:

$$\Delta\theta_Z = \frac{I_H R(\theta_L) - I_L R(\theta_H)}{I_L(\frac{dR}{d\theta})(\theta_H) - I_H(\frac{dR}{d\theta})(\theta_L)} \quad 4.1$$

where $\Delta\theta_Z$ is the intensity in the refraction angle image, $R(\theta)$ is the analyzer reflectivity, θ is the analyzer angle, and I_H and I_R are the intensity of the images taken on high-angle side (θ_H) and

low-angle side (θ_L), respectively. Obtained refraction images were then processed using SYRMEP software (Elettra Synchrotron Facility, Trieste, Italy) to create CT slices, which were then 3D rendered using Avizo® software (VSG, Burlington, USA).

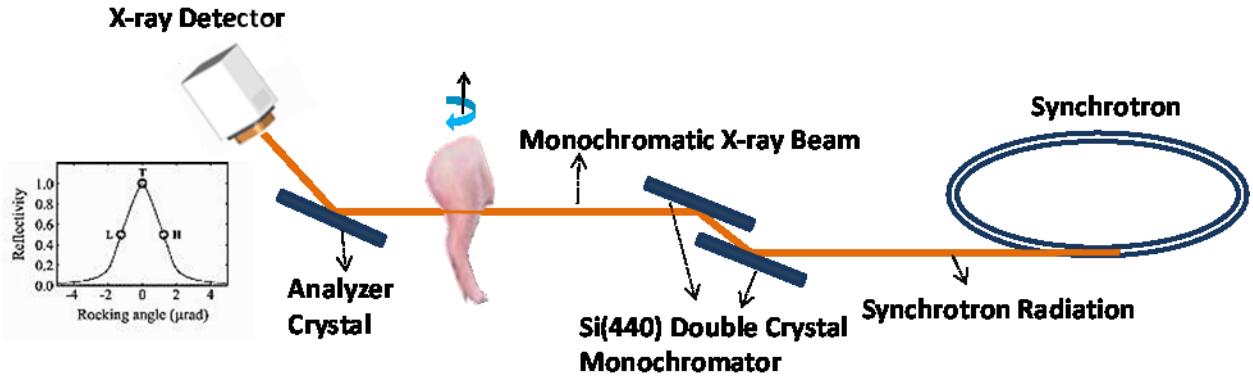

Figure 4.3 Schematic of the DEI set up at the Canadian Light Source used for imaging TE scaffolds in piglet joints. Embedded graph shows the analyzer rocking curve, in which X-ray reflectivity from the analyzer is a function of incident angle.

4.3.3.2 CT-PCI

PCI exploits X-ray refraction at the edges of different features to provide higher image contrast. In in-line PCI, this is made possible by providing a free space between the sample and the detector so that the refracted, transmitted X-rays can freely propagate and interfere to develop informative phase-shifted signals at the detector. Synchrotron radiation provides high coherence X-rays, which is essential to enhancing the quality of PC images. Briefly, the X-rays travel through the object, with the phase information of the beam disturbed by interfaces of features inside the sample that have differing refractive indexes. The phase variation propagated in the free sample-to-detector distance is converted into intensity variation at the detector to visualize the structural features in the object. For PCI of the pig joint samples, a sample-to-detector distance of 85 cm was used. Multiple (3000) images were acquired by rotational (angular) scanning of the sample. Flat field and dark field images were also taken for normalization. Tomographic slices were reconstructed following the same procedure as for CT-DEI.

4.3.3.3 Magnetic resonance imaging (MRI)

MRI of joint samples was performed at the MRI Center, Royal University Hospital, Saskatoon, Canada. The MRI imaging system was a 3T Siemens MAGNETOM® MRI Skyra (Muenchen, Germany), with XQ gradients and 48 channels. T2-weighted spin-echo sequence was used for taking the image and the imaging receiver employed was a hand/wrist 16 channel high resolution receiver coil with a "clamshell design". By using MRI, the time required for imaging one sample was 4 min. Images obtained by MRI were processed by using Numaris/4 software (syngo MR D11, Muenchen, Germany).

4.4 Results

4.4.1 Scaffold characterization

Images of the PCL scaffold fabricated for implantation are shown in Fig. 4.4. The grid structure and morphology of the PCL scaffold are visible from stereo microscope (Ancansco, Canada) image at 2x magnification (Fig. 4.4A). The size of the fabricated scaffold in the z direction is indicated in the isometric view of the scaffold taken by digital camera (Fig. 4.4B). It is noted that the computer-controlled fabrication technique employed in the present study allows for reproducibility of scaffolds with the designed structure and properties, thus limiting the variability of samples for imaging.

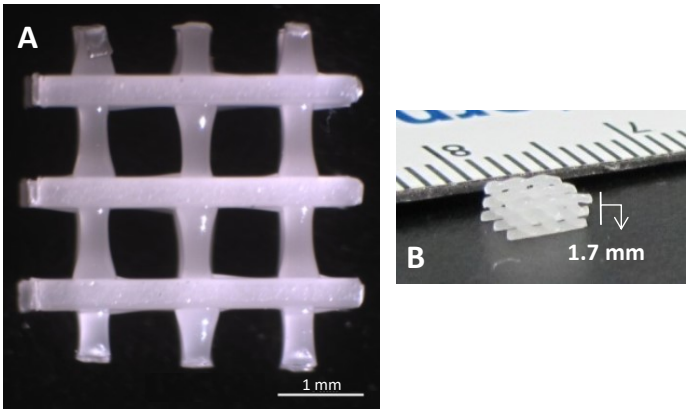

Figure 4.4 Images of the fabricated PCL scaffold by a stereo microscope at 2x magnification (A) and a digital camera (B).

4.4.2 Planar diffraction enhanced imaging

Using the DEI technique, absorption images were obtained along with refraction images. As expected, the absorption image did not provide enough contrast for visualizing the low density scaffold and surrounding tissue microstructures. Consequently, the refraction image, which achieves its contrast solely from refraction of X-rays, is of interest in this study and is exclusively discussed below (referred to as the DE images).

A planar refraction image obtained from the projection DEI of the sample shows a 15 cm long sagittal view of the joint (Fig. 4.5). The planar refraction image was acquired to compare the visibility of the cartilage scaffold *in situ* using 2D imaging modality to tomographic imaging. A weak grid profile of the scaffold can be recognized in the planar DE image (Fig. 4.5); however, the contrast is obviously not sufficient for clear visualization. The limited contrast of the scaffold image may be due to the nature of 2D imaging, in which superposition of information over the thickness of the sample can hinder distinct differentiation of the scaffold structure. As expected, quantitative characterization of scaffold structural properties was also not possible in 2D-DEI. Furthermore, the images of the scaffold that show its grid structure (e.g., Fig. 4.5) can only be acquired in limited projection shots, i.e., at specific spatial/angular positions of the scaffold and the joint itself, but this is inconvenient and impractical. CT imaging can overcome these limitations by producing volumes of data that are used to generate 3D images of the sample.

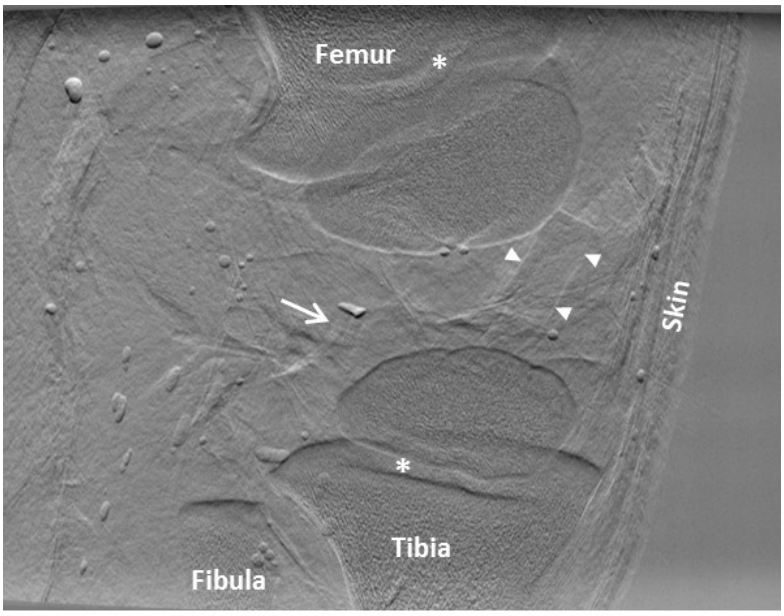

Figure 4.5 Sagittal image of the pig joint using 2D-DEI; the white arrow points to the implanted scaffold in the lateral femoral cartilage. Asterisk (*) indicates the growth plate in a growing joint. The arrowheads show the periphery of a plastic tube placed at the vicinity of the implantation site to direct air bubbles out of the joint.

4.4.3 Computed tomography diffraction enhanced imaging

A volume image was reconstructed from the CT-DEI of the sample. The refraction image of a representative slice (Fig. 4.6) shows a profile through the cartilage of lateral and femoral condyles as well as surrounding soft tissues (e.g., skin, muscle, fat). The interfaces of different soft tissues as well as microstructures of the skin and the infrapatellar fat pad can be identified in the DE image (Fig. 4.6A). In the enlarged image showing the condyles (Fig. 4.6B), a cross-sectional view of the PCL scaffold is clearly recognizable in the lateral femoral cartilage. The PCL strands and their 0°/90° grid pattern of the scaffold structure are clearly visible in the image. Notably, the enhanced contrast at the edges of the strands makes the scaffold contour visible and distinguishable from surrounding low-density tissues. In addition to the implanted scaffold, the DE images show the information on tissue features, including the morphological or structural features of the cartilage (e.g. different appearance of the cartilage tissue in the inner area of the femoral condyle) and the vascular channels within cartilage (Fig. 4.6B and 4.9A).

A 3D rendered image of stacked tomographic slices created a volume image of the joint with a thickness of 4 mm about the region of implantation (Fig. 4.7). The surfaces of the condyle

cartilage at an axial view of the joint are visible (Fig. 4.7A), with the recognizable structural pattern of the implanted scaffold (Fig. 4.4A) clearly depicted in the lateral condyle cartilage. Branches of vascular channels throughout the lateral condyle cartilage are also easily identified in the 3D rendered image. The vascular branches in the medial condyle cartilage are visible in other views. While the cartilage vascular system is most evident in young growing joints, these images show the obvious potential of DEI for visualizing detailed microstructures in soft tissues. An enlarged 3D rendered image of the scaffold (Fig. 4.7B) provides a clear image of the scaffold structure in which some structural properties, such as strands and pore sizes, can be quantitatively characterized. This is of special interest for *in vivo* evaluation of the degradation and mechanical properties of scaffolds during the repair process. For example, one can employ finite element models that use measurable structural parameters as input for simulations that evaluate changes in scaffold mechanical properties with time [17]. Interestingly, even the surgical suture that was used for suturing and closing the inner site of incision was visualized in the DE image (Fig. 4.7B). Furthermore, the soft periosteum tissue layer used to cover and fix the scaffold in place was visible in the CT-DE images (Fig. 4.7C). These are features that can hardly be visualized at this detailed level, if at all, using other imaging techniques. Fig. 4.7A shows the presence of some air bubbles in the joint, which produces strong contrast against other anatomical features imaged in the joint. Although the vacuum dessicator removed the majority of air bubbles from the joint, some remain due to the limited vacuum duration and the formation of bubbles from boiling of the joint sample in the vacuum. The streak artifact that is seen around the scaffold in Fig. 4.6 and Fig.4.7 are caused due to a small copper wire used for quickly locating the scaffold in the joint for the CT scan.

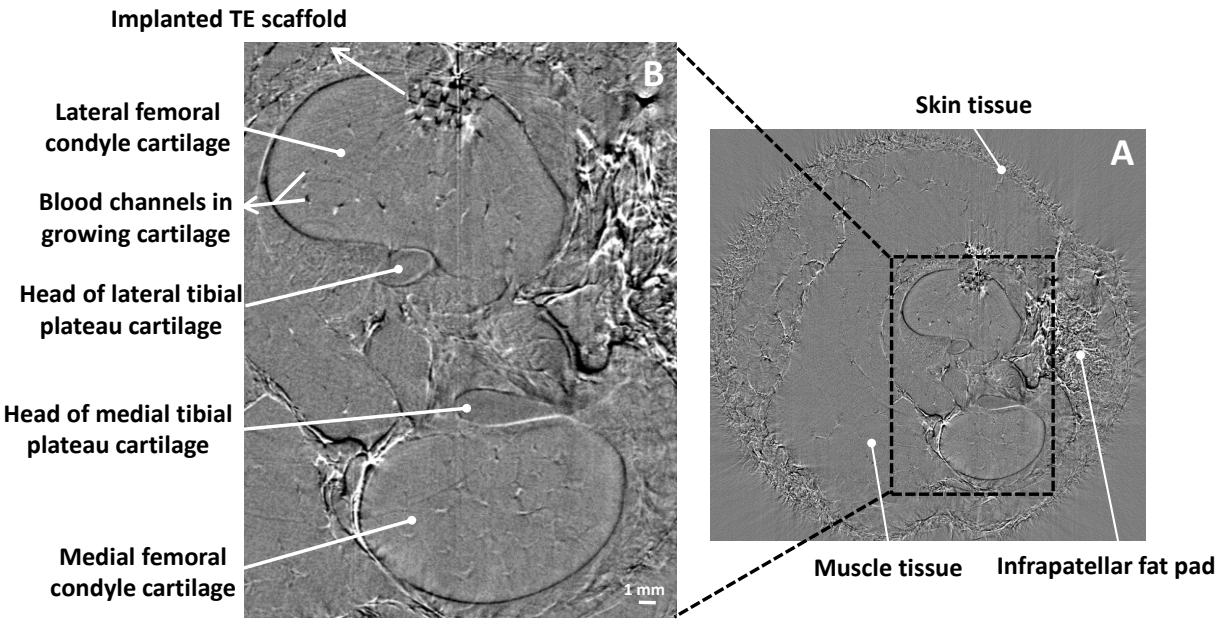

Figure 4.6 Representative tomographic DE image of a pig knee joint implanted with a TE scaffold in the cartilage (image pixel size 37 μm): (A) axial full cross section image of the joint with different soft tissues identified and (B) magnified area of interest clearly showing the profile of the implanted scaffold in the lateral femoral condyle cartilage. Note the enhanced contrast at the edges of the scaffold strands, interfaces of different soft tissues, and contours of vascular channels.

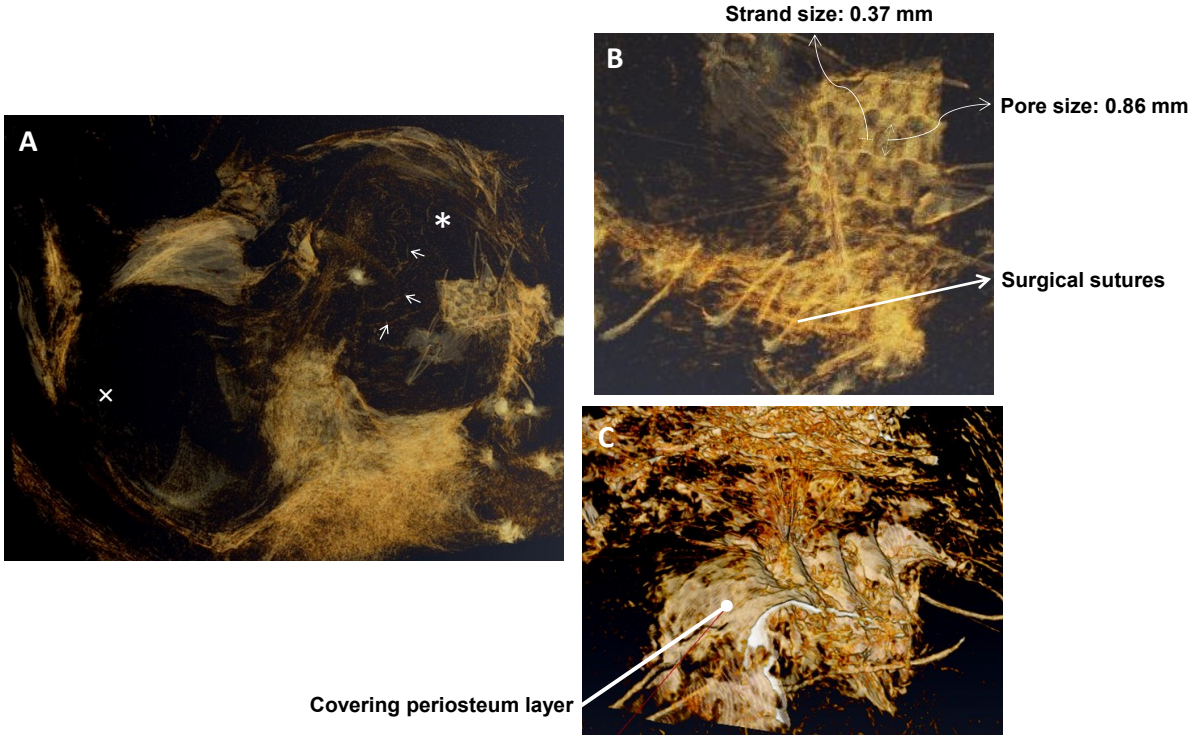

Figure 4.7 Volume rendered DE image of the joint at the site of implantation: (A) axial view of the cartilage surface at lateral (*) and medial (×) femoral condyles, implanted scaffold, and vascular channels in a young growing joint (indicated by arrows), (B) magnified image of the implantation site shows the grid structure of the scaffold with measurable strand and pore sizes and details including the sutures used in the surgery; and (C) grafted periosteum layer covering and fixing the scaffold in place at the site of implantation.

4.4.4 DEI compared to PCI and MRI

The three imaging techniques—CT-DEI, CT-PCI, and MRI—were compared with respect to visualization of the PCL scaffold in cartilage *in situ* (Fig. 4.8). Slices through the joint at the site of implantation were obtained for CT-PCI (Fig. 4.8A) and CT-DEI (Fig. 4.8B). Although the two images represent the same axial view of the joint, the scaffold cannot be perceived in the PC image; however, the DE image clearly shows a profile of the scaffold structure. Structural features in the cartilage and surrounding soft tissues that can be recognized in the DE image (Fig. 4.8B) are not visible in the PC image (Fig. 4.8A). This includes the contours that clearly distinguish the condyle cartilage from surrounding tissues, interfaces that differentiate various soft tissues, and in-cartilage vascular channels. The PCI-induced contrast can apparently only visualize and differentiate bulk features inside the sample (e.g. fat against non-fat soft tissues) and not the fine features required for visualizing microstructures (e.g., the TE scaffold). Consequently, the tested PCI system is unable to provide the information required for imaging and studying TE scaffolds for cartilage repair *in situ*.

The MR image was taken at a resolution of 310 μm pixels. A representative MRI slice shows a cross section through the condyle cartilage and the location of scaffold implantation (Fig. 4.8C). The scaffold profile cannot be identified in the MR image and only the contour of the defect created in the cartilage can be depicted. Expectedly, soft tissues such as cartilage, muscle, fat, and skin are visualized and differentiated in the MR image; however, the scaffold is not visible. In fact, the defect area filled with the scaffold is seen as a void black spot in the MR image, which means that insufficient signal has been produced by the scaffold to make it visible at the detector. Overall, CT-DEI is the most capable method for *in situ* visualization of scaffolds in cartilage among the three imaging methods for comparison.

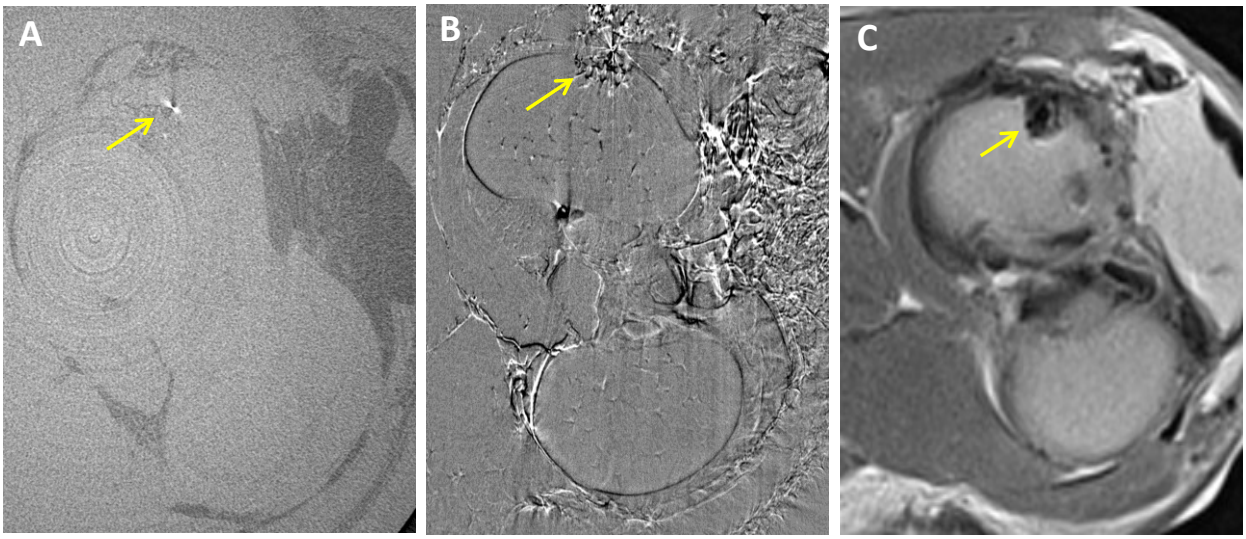

Figure 4.8 Comparison of (A) CT-PCI, (B) CT-DEI, and (C) clinical MRI techniques for visualizing TE scaffold implanted in the lateral femoral cartilage of piglet knee joint. Yellow arrows show the location of the implanted scaffold. Both PC and DE images were taken at a resolution of 37 µm pixels, while MR image taken at a resolution of 310 µm pixels.

4.4.5 Radiation dose

Based on the obtained results, the CT-DEI method evaluated is the most appropriate for visualizing and studying TE scaffolds in thick samples such as knee joints. To extend the application of this imaging method to *in vivo* studies on live animal models or even future clinical human studies, the ionizing radiation dose received by the sample during CT-DEI must be optimized. The irradiation absorbed by the sample is defined as the deposited energy per mass of material in which the radiation is deposited, and is usually characterized by the rate of radiation dose at the surface of the object where the largest dose occurs. The surface dose rate is calculated using

$$\dot{D}(E_{ph}) = \frac{\dot{N}_o E_{ph}}{A} \, {}^{\mu}/_{\rho_{abs}}, \qquad 4.2$$

where $\dot{D}(E_{ph})$ is the rate of surface absorbed dose in gray [Gy] or [J/kg], E_{ph} [eV] is the photon energy, $\dot{N}_o$ is the number of photons that hit the object surface area of A [cm^2] per second, and ${}^{\mu}/_{\rho_{abs}}$ [cm^2/g] is the energy absorption mass attenuation coefficient.

Different tissues and organs respond differently to ionizing radiation based on their radiosensitivity. To account for these differences, a second radiation exposure metric is defined as

$$\dot{D}_{eff} = W_F \times \dot{D}(E_{ph}), \quad 4.3$$

where D_{eff} is the effective dose rate in sieverts (Sv) and W_F is a weighting factor related to the risk for a particular tissue or organ. Tissue weighting factors associated with different tissues and organs are recommended in the annals of International Commission on Radiological Protection (ICRP). The reported effective dose is usually used for measuring the potential detriment or risk to the radiosensitive tissue. The rate of absorbed surface dose, $\dot{D}(E_{ph})$, to the sample imaged by CT-DEI was calculated at 0.34 mGy/s. Considering the total scanning time, the absorbed dose received by the joint sample during the X-ray scan was 6 Gy and with the cartilage tissue weighting factor of 0.01, the total received effective dose was 60 mSv.

4.5 Discussion

The results of this study reveal the feasibility of CT-DEI for *in situ* visualization of a PCL scaffold implanted in pig knee cartilage, which is a critical step to track the scaffold success in the *in vivo* applications. The combination of CT and DEI technique was found essential for *in situ* imaging of the scaffolds embedded in thick samples, thus providing a powerful tool for quantitative evaluation of changes in scaffolds during the tissue repair processes. In the present study, cartilage tissue was imaged with appreciate morphological and structural properties by using CT-DEI. As such, CT-DEI could be employed for studying the success of TE cartilage repair *in situ* by tracking scaffold changes as well as neotissue regeneration. The descriptive information with respect to the cartilage tissue morphology revealed that DE images can also be used for evaluation of the quality of neocartilage as compared to native cartilage. In addition, the CT-DEI presented in the present study was performed without the use of contrast agents or materials. Other methods may be able to provide visual information on the scaffold, but would require the use of contrast materials. In addition to extra work required for scaffold preparation, these contrast agents may also have negative impact on the function of scaffolds and surrounding tissues even after the scaffold completely degrades (i.e., the residual artifact).

In addition to the cartilage tissue targeted in the present study, DEI revealed informative details on the morphology and microstructure of other soft tissues, such as skin, fat, and muscle

(Fig. 4.6A) as well as transverse ligament, anterior cruciate ligament, and menisci (Fig. 4.9A) (in which the striation and the fibrous texture of the ligaments are clearly visible). Notably, these structural features may not be imaged easily, if at all, using clinical imaging techniques. Also, it is noted that CT-DEI has the capacity to image hard tissue. For example, Figure 9B is an axial image of the joint, revealing the cartilage and proximal end of the tibia bone; interestingly, the spongy/porous structure of the bone is also visible (Fig 4.9B-inset). Simultaneous imaging of both soft and hard tissues demonstrates the promising potential of CT-DEI for tissue engineering applications involving a variety of different tissues. This ability is attributed to the non-absorptive, refraction-based contrast mechanism of DEI. One application of this capability in cartilage TE is to monitor and study the repair at the bone-cartilage interface, which involves both soft and hard tissues.

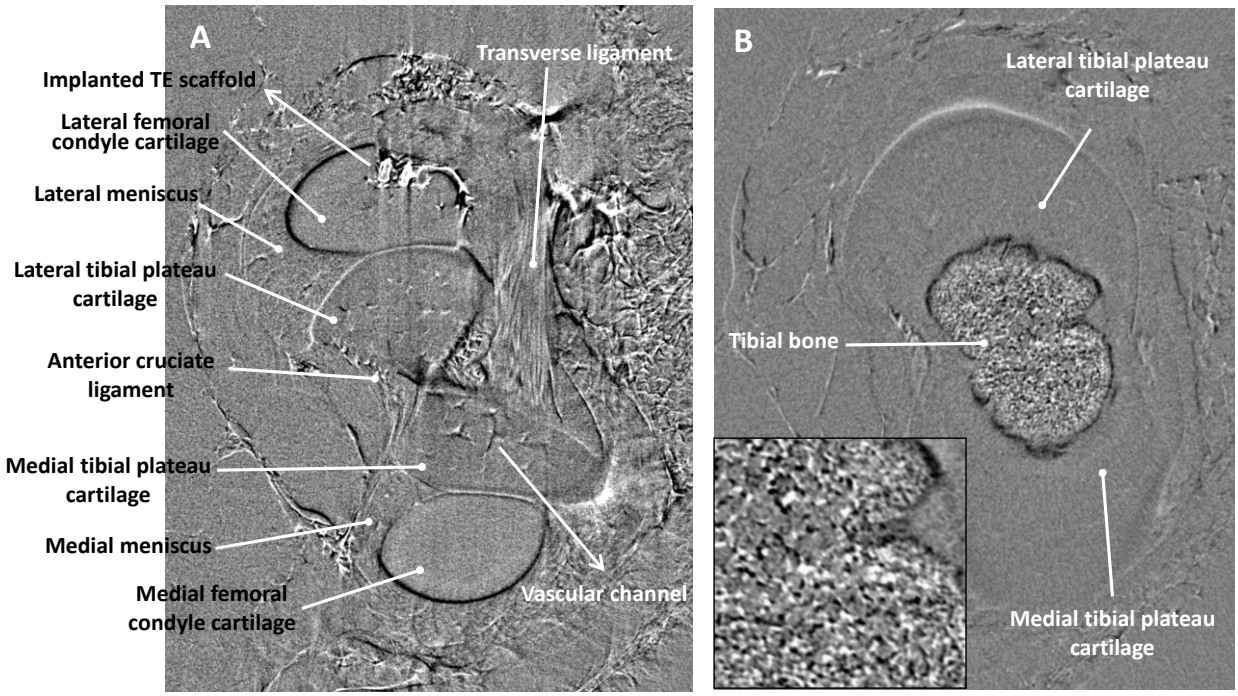

Figure 4.9 Tomographic DEI slices at two different vertical locations of the joint: (A) visualization and differentiation of various soft tissues with some structural details and (B) imaging of both soft (cartilage) and hard (bone) tissues in a DE image, with the inset showing the level of structural detail of the bone tissue.

Compared to CT-DEI, CT-PCI has its limit to visualize scaffolds embedded in thick samples as illustrated in the present study. One main factor in the in-line PCI contrast mechanism is the free propagation of distorted X-rays throughout the sample-to-detector distance. A greater

distance could improve the capability of PCI for visualizing microstructures inside the sample. Low density microstructures such as the implanted TE scaffold and microvascular channels produce small deflections/distortions in the X-rays as they hit the boundaries of the features. The small X-ray phase disturbance induced can propagate and develop over a sufficiently long free space for the features to be visualized at the detector; otherwise, the non-developed phase information of the beam cannot be used to construct the image of the microstructure (e.g., scaffold) at the detector. For this study, a sample-to-detector distance of 85 cm was achievable at the time of experiment in the BMIT-BM experimental hutch; however, the results (Fig. 4.8A) indicate that this sample-to-detector distance was not suitable for visualizing the scaffold inside the cartilage. Longer distances might improve the ability of PCI to image scaffolds *in situ*, and this should be investigated in future experiments. In addition to the free propagating distance, the effective image resolution (i.e., pixel size) has influence on the capability of the PCI technique. A higher spatial resolution (smaller pixel size) could potentially improve the ability of PCI to visualize fine microstructures (i.e., scaffolds), particularly for the cases where a larger sample-to-detector distance is not possible or practical. By doing so, fine distorted phase information (i.e., the one associated with the scaffold structure) could be detected and used for image construction. Although it is theoretically possible to increase image resolution through a longer scanning exposure time, this can dramatically raise the radiation dose received by the sample. For instance, doubling the spatial resolution (decreasing pixel size by half) requires up to a sixteen-fold increase in the exposure time. This means that imaging of scaffolds with the PCI system might be achievable but at the cost of higher radiation doses, which is not suitable for live animal imaging experiments.

In the MRI system, the presence of water and variations in the amounts in different tissues and microstructures are essential for visualization. More precisely, MR imaging is based on the resonation of mobile protons (hydrogen nuclei-H^+) to generate electromagnetic signals using magnetic and radio frequency fields. Protons residing in various tissues/structures resonate at different frequencies, based on the amount of constituent water, and will thus generate different signals. The produced signals are detected by a receiver and used to construct the MR image, which reveals various types of tissues and microstructures. As such, mobile hydrogen nuclei are the source of signal in MRI. The implanted TE scaffold was made of a polyester polymer of PCL, $(C_6H_{10}O_2)_n$, which has hydrogen atoms in its structure. However, constituent protons are

immobilized in the polymer structure (due to strong coupling) and cannot be imaged as easily using MRI as water-containing tissues. The short-lived signals generated by the protons in rigid polymeric materials make their MR imaging difficult. Consequently, no informative electromagnetic signal was received from the scaffold to construct its profile in the MR image (Fig. 4.8C). The only useful information that can be obtained from this MR image is the signal void representing the area in which the scaffold was implanted. In other words, only the external geometry of the implanted scaffold can be visualized in the MR image if the scaffold completely fills the defect geometry, as noted by Stuckey et al. [18]. To improve the signal, strategies such as using a larger magnetic field (e.g., 7T), longer scan time (to accumulate the signals), special pulse sequences (i.e., SPRITE), and elevated temperature in the material [19] may be used. Although these strategies might improve imaging of solid polymeric materials, they may introduce complexities and inefficiencies with respect to the imaging of live animals or humans.

The radiation dose received by the samples in the CT-DEI technique was evaluated from imaging photon energy of 40 keV and detector resolution of 37 μm in the present study. This radiation dose obtained is tolerable for live animals, making it suitable for *in vivo* applications. Notably, lower radiation dose CT-DEI can also be achieved through different strategies. Increasing the imaging photon energy (E_{ph}) can decrease the dose rate at the sample by reducing the photoelectric (PE) component of the energy absorption coefficient (${}^{\mu}/_{\rho_{PEabs}} \propto \frac{1}{{E_{ph}}^3}$) [8]. Therefore, performing CT-DEI at higher energies is one strategy for reducing the radiation dose received. Photon energy of 40 keV was the maximum available at the CLS BMIT-BM beamline that allowed imaging at a sufficient photon flux. Higher photon fluxes can facilitate CT-DEI of the sample at shorter scanning times (faster imaging), which can also considerably reduce the absorbed radiation dose. Both higher photon energies and higher photon fluxes could be achieved by SR X-rays generated by a superconducting wiggler insertion device. Faster scanning will make the CT-DEI method even more convenient for applications to live animals. With the commissioning of the BMIT-ID beamline at the CLS, these strategies can be investigated in the future.

Higher imaging energy may be disadvantageous for all forms of X-ray imaging techniques including PCI and DEI due to the reduced ability to stop X-rays in the detector and the decreased resolution that can occur because of the thick phosphors required in the detector. Additionally,

the increase in photon energy can result in blurring of the image and deterioration of the image quality [8], as higher photon energies increase the X-ray scattering inside the object. However, this problem is prevented in DEI by the analyzer rejecting Compton scattered X-rays that are off the angle and energy of the RC. Consequently, the DEI method is almost scatter free [16], and the increase of photon energy needed to lower the dose rate does not compromise image quality. This property becomes particularly advantageous when imaging large, thick samples is of interest, because this requires an X-ray photon energy sufficient to penetrate throughout the sample and reach the detector. Other strategies that lower the absorbed radiation dose in CT-DEI include reducing the required scan time through imaging a smaller area of interest, lowering the exposure time, and using higher efficiency detectors. This strategy is now being pursued by the authors for developing a lower dose DEI-based imaging method for visualization and monitoring of tissue engineering scaffolds in live animal models. DEI is currently carried out using a synchrotron radiation X-ray source due to its advanced properties (e.g., high photon flux, large range of selectable-energies, high brilliance, small angular divergence, high level of coherence, and monochromatic beam) compared to conventional X-ray sources [20, 21]. Although the same photon flux is not yet achievable without synchrotron sources, studies have been pursued to transfer DEI technology to a desktop X-ray imaging setting [22].

4.6 Conclusion

Non-invasive monitoring methods that can track the success of TE scaffolds *in* situ during repair processes are essential to the future development of TE strategies. In an effort to develop such a method for soft (i.e., cartilage) tissue engineering, CT-DEI was investigated in this study for the visualization and characterization of PCL scaffolds implanted in the knee cartilage of a dissected pig joint. CT-DEI clearly visualized the implanted PCL scaffold, including characterizable structural properties that were not visible in CT-PC and MR images. The contrast mechanism of DEI combined with the CT modality at sufficient X-ray energies enabled successful *in situ* imaging of low density PCL cartilage scaffolds. In addition, CT-DEI also demonstrated its robust capability for distinctly visualizing various soft tissues as well as hard bone tissue with microstructural detail. The present study reveals that information on TE scaffolds, once implanted, as well as the surrounding tissues can be captured by means of CT-

DEI, showing its promise for *in vivo* studies in live animals and eventually for human clinical studies.

4.7 References

1. Gillogly, S.D.; Voight, M.; Blackburn, T. Treatment of articular cartilage defects of the knee with autologous chondrocyte implantation. *J Orthop Sports Phys Ther* **1998**, 28, 241-251.

2. Alford, J.W.; Cole, B.J. Cartilage restoration, part 2: techniques, outcomes, and future directions. *Am J Sports Med* **2005**, 33, 443-460.

3. Moutos, F.T.; Guilak, F. Composite scaffolds for cartilage tissue engineering. *Biorheology* **2008**, 45, 501-512.

4. Muehleman, C.; Zhong, Z.; Williams, J.M.; Kuettner, K.E.; Aurich, M.; Han, B.; Mollenhauer, J.; Chapman, L.D. Diffraction enhanced X-ray imaging of the articular cartilage of experimental animals In *Annual Meeting Orthopaedic Research Society*. Dallas, TX. USA. 2002.

5. Muehleman, C.; Majumdar, S.; Issever, A.S.; Arfelli, F.; Menk, R.H.; Rigon, L.; Heitner, G.; Reime, B.; Metge, J.; Wagner, A.; Kuettner, K.E.; Mollenhauer, J. X-ray detection of structural orientation in human articular cartilage. *Osteoarthritis Cartilage* **2004**, 12, 97-105.

6. Muehleman, C.; Chapman, L.D.; Kuettner, K.E.; Rieff, J.; Mollenhauer, J.A.; Massuda, K.; Zhong, Z. Radiography of rabbit articular cartilage with diffraction-enhanced imaging. *Anat Rec A Discov Mol Cell Evol Biol* **2003**, 272, 392-397.

7. Mollenhauer, J.; Aurich, M.E.; Zhong, Z.; Muehleman, C.; Cole, A.A.; Hasnah, M.; Oltulu, O.; Kuettner, K.E.; Margulis, A.; Chapman, L.D. Diffraction-enhanced X-ray imaging of articular cartilage. *Osteoarthritis Cartilage* **2002**, 10, 163-171.

8. Zhu, N.; Chapman, D.; Cooper, D.; Schreyer, D.J.; Chen, X. X-ray diffraction enhanced imaging as a novel method to visualize low-density scaffolds in soft tissue engineering. *Tissue Eng Part C Methods* **2011**, 17, 1071-1080.

9. Wagner, A.; Aurich, M.; Sieber, N.; Stoessel, M.; Wetzel, W.-D.; Schmuck, K.; Lohmann, M.; Reime, B.; Metge, J.; Coan, P. Options and limitations of joint cartilage imaging: DEI in comparison to MRI and sonography. *Nucl Instrum Methods Phys Res A* **2005**, 548, 47-53.

10. Muehleman, C.; Li, J.; Zhong, Z. Preliminary study on diffraction enhanced radiographic imaging for a canine model of cartilage damage. *Osteoarthritis Cartilage* **2006**, 14, 882-888.

11. Davis, T.; Gureyev, T.; Gao, D.; Stevenson, A.; Wilkins, S. X-ray image contrast from a simple phase object. *Phys Rev Lett* **1995**, 74, 3173.

12. Zehbe, R.; Haibel, A.; Riesemeier, H.; Gross, U.; Kirkpatrick, C.J.; Schubert, H.; Brochhausen, C. Going beyond histology. Synchrotron micro-computed tomography as a

methodology for biological tissue characterization: from tissue morphology to individual cells. *J R Soc Interface* **2010**, 7, 49-59.

13. Zehbe, R.; Goebbels, J.; Ibold, Y.; Gross, U.; Schubert, H. Three-dimensional visualization of in vitro cultivated chondrocytes inside porous gelatine scaffolds: a tomographic approach. *Acta biomater* **2010**, 6, 2097-2107.

14. Chang, C.-H.; Lin, F.-H.; Kuo, T.-F.; Liu, H.-C. Cartilage tissue engineering. *Biomed Eng (Singapore)* **2005**, 17, 61-71.

15. Rhoades, G.; Belev, G.; Rosenberg, A.; Chapman, D. A novel analyzer control system for diffraction enhanced imaging. *J Phys Conf Ser* **2013**, 425, 022003.

16. Chapman, D.; Thomlinson, W.; Johnston, R.E.; Washburn, D.; Pisano, E.; Gmur, N.; Zhong, Z.; Menk, R.; Arfelli, F.; Sayers, D. Diffraction enhanced x-ray imaging. *Phys Med Biol* **1997**, 42, 2015-2025.

17. Bawolin, N.; Li, M.; Chen, X.; Zhang, W. Modeling material-degradation-induced elastic property of tissue engineering scaffolds. *J Biomech Eng* **2010**, 132, 111001.

18. Stuckey, D.J.; Ishii, H.; Chen, Q.-Z.; Boccaccini, A.R.; Hansen, U.; Carr, C.A.; Roether, J.A.; Jawad, H.; Tyler, D.J.; Ali, N.N. Magnetic resonance imaging evaluation of remodeling by cardiac elastomeric tissue scaffold biomaterials in a rat model of myocardial infarction. *Tissue Engineering Part A* **2010**, 16, 3395-3402.

19. MacMillan, B.; Halse, M.; Schneider, M.; Fardy, L.; Chui, Y.; Balcom, B. Magnetic resonance imaging of rigid polymers at elevated temperatures with SPRITE. *Appl Magn Reson* **2002**, 22, 247-256.

20. Dilmanian, F. Computed tomography with monochromatic x rays. *Am J Physiol Imaging* **1991**, 7, 175-193.

21. Bonse, U.; Busch, F. X-ray computed microtomography (μCT) using synchrotron radiation (SR). *Prog Biophys Mol Biol* **1996**, 65, 133-169.

22. Muehleman, C.; Fogarty, D.; Reinhart, B.; Tzvetkov, T.; Li, J.; Nesch, I. In-laboratory diffraction-enhanced X-ray imaging for articular cartilage. *Clin Anat* **2010**, 23, 530-538.

CHAPTER 5: LOW-DOSE PHASE-BASED X-RAY IMAGING TECHNIQUES FOR *IN SITU* SOFT TISSUE ENGINEERING ASSESSMENTS

This chapter has been published as "Izadifar Z., Honaramooz A., Wiebe S., Belev G., Chen X.B., Chapman L.D. (2016) Low-dose phase-based X-ray imaging for *in situ* soft tissue engineering assessments. *Biomaterials.* 82: 151-167*"* and has been accepted for publication as "Izadifar Z., Honaramooz A., Wiebe S., Belev G., Chen X.B., Chapman L.D. (2015) Data of low-dose phase-based X-ray imaging for *in situ* soft tissue engineering assessments. *Data in Brief*". According to the Copyright Agreement, "the authors retain the right to include the journal article, in full or in part, in a thesis or dissertation".

5.1 Abstract

In tissue engineering, non-invasive imaging of biomaterial scaffolds and tissues in living systems is essential to longitudinal animal studies for assessments without interrupting the repair process. Conventional X-ray imaging is inadequate for use in soft tissue engineering due to the limited absorption difference between the soft tissue and biomaterial scaffolds. X-ray phase-based imaging techniques that derive contrast from refraction or phase effects rather than absorption can provide the necessary contrast to see low-density biomaterial scaffolds and tissues in large living systems. This paper explores and compares three synchrotron phase-based X-ray imaging techniques—computed tomography (CT)-diffraction enhanced imaging (DEI), -analyzer based imaging (ABI), and -phase contrast imaging (PCI)—for visualization and characterization of low-density biomaterial scaffolds and tissues *in situ* for non-invasive soft tissue engineering assessments. Intact pig joints implanted with polycaprolactone scaffolds were used as the model to assess and compare the imaging techniques in terms of different qualitative and quantitative criteria. For long-term *in vivo* live animal imaging, different strategies for reducing the imaging radiation dose and scan time—reduced number of CT projections, region of interest, and low resolution imaging—were examined with the presented phase-based imaging techniques. The results demonstrated promising capabilities of the phase-based techniques for visualization of biomaterial scaffolds and soft tissues *in situ*. The low-dose imaging strategies were illustrated effective for reducing the radiation dose to levels appropriate for live animal imaging. The comparison among the imaging techniques suggested that CT-DEI has the highest efficiency in retaining image contrast at considerably low radiation doses.

5.2 Introduction

As tissue engineering aimed at repairing damaged tissues and organs continue to advance, more sophisticated assessment and monitoring techniques are required to evaluate and/or optimize the success of outcomes. The information on the functionality, tissue regeneration, interaction, and integration of engineered constructs with the host tissue post-implantation is essential to the *in situ* evaluation of various therapeutic tissue engineering strategies. Such evaluation or assessment is critical for the strategies seeking approval for clinical application to patients; the approval process typically involves extensive and comprehensive longitudinal *in vivo* studies on large animal models and clinical trials on patients. Notably, conventional biochemical evaluation techniques (e.g., histochemical analysis), which have been widely used for various *in vitro* and *in vivo* studies, are invasive and destructive due to the need to sacrifice animals during the repair process for *ex vivo* analysis. As such, they are inadequate for use in clinically relevant and long-term *in vivo* studies. Furthermore, conventional *ex vivo* techniques cannot provide *de facto* and dynamic information about the *in vivo* repair process, which is the key to developing better regeneration strategies. Most importantly, such invasive assessment techniques have to be relinquished with the advance from animal to human studies. Therefore, the development of non-invasive assessment techniques with applicability to longitudinal live animal studies and eventually to human trials is urgently needed.

Biomedical imaging techniques such as magnetic resonance imaging (MRI) and X-ray imaging are forerunner candidates for non-invasive tissue engineering assessments. MR-based techniques have been explored for non-invasive monitoring in soft (i.e., cartilage) tissue engineering applications [1], but are currently limited to small animal models [1] or require exogenous contrast agents for applications to large animals [2]. Furthermore, MR-based techniques mainly focus on the evaluation of tissue growth [1] and have limitations with respect to *in situ* imaging and evaluation of polymeric tissue scaffolds [3]. With the discovery of synchrotron X-ray source that has superior brilliance, coherence, and a monochromatic (single energy) beam, robust phase-based X-ray imaging techniques have emerged [4-7] and led to breakthroughs in biomedical X-ray imaging of soft tissues and low density microstructures [8-14]. Phase-based X-ray imaging techniques rely on refraction-based and phase shift contrast mechanisms instead of absorption-based mechanisms that do not facilitate imaging of low density materials. In addition, synchrotron phase-based X-ray imaging techniques have the

advantages of being free of contrast agents, providing high imaging resolution (down to 1-2 μm), using a high penetrating beam, and featuring highly sensitive imaging mechanisms. As such, synchrotron phase-based X-ray imaging offers great potential for non-invasive, longitudinal monitoring and assessment applications in large animal and human soft tissue engineering. Although the potential of X-ray phase-based imaging techniques and their capabilities for soft tissue engineering have been shown [3, 15, 16], these techniques are relatively new to the field and several issues remain to be addressed, particularly for use in longitudinal *in vivo* large animal and human studies.

Synchrotron diffraction-enhanced imaging (DEI), analyzer-based imaging (ABI), and propagation-based inline phase contrast imaging (PCI) techniques have been investigated for soft tissue imaging [17-19], particularly for cartilage and joint tissues [12, 20-26]. Recently, these imaging techniques have been drawing considerable attention in soft tissue engineering applications [3, 16, 21, 27-30]. Other phase-based X-ray imaging techniques such as edge-illumination and grating based imaging have also proven great potential for soft tissues [31-38] and low-density materials imaging [39-42]. It is noted that relatively high resolution imaging of large biological samples requires high X-ray energies and big field of view. This can makes the application of grating-based interferometry and edge-illumination techniques more challenging than DEI, ABI, and propagation-based PCI for non-invasive large animal tissue engineering assessments. As such, DEI, ABI, and inline PCI are currently more applicable than other phase-based imaging techniques to large animal imaging applications. Application of the DEI technique to cartilage tissue engineering assessment [3] suggested the necessity of computed tomography (CT) modality for successful and informative *in situ* imaging of engineered tissue scaffolds. Compared to non-CT modalities, however, CT requires collection of multiple 2D images; this often results in a longer scan time and a higher ionizing radiation dose that could prohibit widespread use of newly developed X-ray imaging techniques for live animal and human studies. Although some recent studies have tried to address these issues [31, 43-45], the performance of various imaging techniques for clinically relevant *in vivo* studies involving imaging of large biological objects at safe doses, as compared in terms of imaging quality, radiation dose, and scan time, has not been explored and documented in the literature. Such comparison study provides a platform of different non-invasive assessment techniques for soft tissue engineering, which will greatly facilitate more realistic longitudinal and comprehensive *in*

vivo studies with clinically translatable results that will advance tissue engineering technologies towards clinical patient trials and therapies.

In this study, synchrotron CT-DEI, CT-ABI, and inline CT-PCI (with different propagation distances) were investigated with respect to their potential as non-invasive X-ray monitoring techniques for soft tissue engineering applications. By exemplifying a cartilage tissue engineering application, the capabilities of these phase-based imaging techniques and their practical aspects for longitudinal *in vivo* large animal studies were examined and compared. This included evaluation and comparison of the techniques in terms of imaging features of importance to tissue engineering assessments, scan time, and level of radiation dose delivered. To reduce the scan time and radiation dose, three strategies of reduced number of CT projections, region of interest, and low resolution imaging were investigated and compared with the three imaging techniques. Imaging quality and quantitative contrast of visualized structural features were further probed to identify the most suitable and efficient imaging technique for application to longitudinal *in vivo* animal studies with the potential for possible extension to human trials.

5.3 Materials and methods

5.3.1 Sample preparation

The samples used in this study were prepared by following the procedure developed in my previous study [3]. Briefly, scaffolds were designed with a porous structure featured by a strand spacing of 1 mm and a perpendicular (0°/90°) pattern of strands in successive layers and fabricated from polycaprolactone polymer (Mw 48,000-90,000; Aldrich, St. Louis, MO, USA) on a 3D Bioplotter (Envisiontec, Germany). Polycaprolactone was melted at 75 °C in a cartridge of the Bioplotter and then dispensed through a 22G (400 μm ID) needle under a pneumatic pressure of 0.75 MPa on the Bioplotter stage layer by layer to form a three dimensional (3D) scaffold. The fabricated scaffolds were implanted into the lateral femoral condyles of stifle joints dissected from four-week-old cadaver piglets (prepared at the Western College of Veterinary Medicine (WCVM) and the Vaccine and Infectious Disease Organization (VIDO), Saskatoon, Canada, under the animal use protocol # 20110071 approved by the University of Saskatchewan Animal Research Ethics Board). In each joint, an osteochondral defect (4.5 × 4.5 × 2-2.5 mm depth) was created and filled with the polycaprolactone scaffold and covered with a piece of concurrently harvested periosteum tissue to fix the scaffold in place; this procedure was similar

to the one commonly used in the *in vivo* implantation of cartilage tissue constructs in animals [46]. The implanted intact joints with all surrounding tissues (including skin) were submerged in Dulbecco's phosphate buffered saline (DPBS) and placed under vacuum for 10-15 min to eliminate any air that might have entered the joint cavity during the surgery. It is noted that any trapped air in the joint may cause artifacts in the images and does not represent the actual status of the joint in a living system.

5.3.2 DEI, ABI, and extended-distance PCI

DEI, ABI, and extended-distance PCI were performed at the Biomedical Imaging and Therapy-bend magnet (BMIT-BM) beamline [47], Canadian Light Source (CLS), Canada. The experimental optical setup followed the protocol reported in my previous study [3]. Briefly, for DEI and ABI an analyzer crystal is placed between the object and detector (Fig. 5.1A) so as to induce refraction-based contrast, ultra-small angle X-ray scattering (USAXS), and scatter rejection of small angle X-ray scattering (SAXS). The analyzer crystal is used to convert the change in X-ray refraction angle, caused by interfaces of different microstructures in the tissue, into a change in X-ray photon intensity at the detector, thus resulting in enhanced contrast at the interfaces of features with different densities. Owing to the small X-ray refraction angles (down to a few microradians), the enhanced image contrast allows for visualizing and distinguishing low density microstructures from surroundings. To perform DEI and ABI, a highly collimated, monochromatic 40 keV X-ray beam was produced using a Si (4,4,0) double crystal monochromator to illuminate the sample after passing through 0.221 mm aluminum and 0.276 mm copper filters. The narrow reflective bandwidth of the Si (4,4,0) reflection plane was used in the analyzer crystal and monochromator to allow larger changes in photon intensity upon changes in refraction angle and thus produce sharper contrast at interfaces. The beam height at the sample in the DEI and ABI setups was 4.5 mm.

In DEI mode, two sets of images were taken, at the high and low angle sides of the analyzer rocking curve (RC) at 50% reflectivity angles. The collected images contain contrast from both absorption and refraction mechanisms. Refraction images, which only contain the contrast from diffraction, were extracted using

$$\Delta\theta_Z = \frac{I_H R(\theta_L) - I_L R(\theta_H)}{I_L(\frac{dR}{d\theta})(\theta_H) - I_H(\frac{dR}{d\theta})(\theta_L)}, \quad 5.1$$

where $\Delta\theta_Z$ is the intensity in the refraction angle image, $R(\theta)$ is the analyzer reflectivity, θ is the analyzer angle, and I_H and I_R are the intensity of the images taken on the two sides (high-angle side, θ_H and low-angle side, θ_L) of the RC. In ABI mode, only one set of images was collected at 50% reflectivity of the high angle side of the RC and used to reconstruct the CT slices.

To perform inline PCI, the sample was placed 5.9 m from the detector and illuminated by a 40 keV energy synchrotron X-ray beam produced using a Si (2,2,0) double crystal monochromator and filtered through a 1.04 mm aluminum filter. The beam was then collected at the detector after it exited and traversed the free propagation distance (Fig. 5.1B). At the BMIT-BM beamline, the free propagation distance is adjusted by moving the sample upstream or downstream the X-ray beam, while the detector is kept at a fixed position downstream of the hutch. The X-ray beam has a vertical and horizontal divergence of 0.2 and 10 miliradians, respectively. Thus, the beam height at the sample in the PCI varies with the propagation distance. For the extended propagation distance used in this study the beam height was 3.4 mm at the sample location, while the beam height at the detector position was roughly 4.6 mm, which produces a magnification of 1.35 in vertical direction. In all imaging techniques, the imaged field of view was limited by the beam height at the sample in the vertical direction and the detector size in the horizontal direction, which led to 74 mm (horizontal) × 4.5 mm (vertical) in DEI, ABI, and PCI, and 74 mm × 3.4 mm in extended-distance PCI. Because the scaffold height was smaller than the vertical beam sizes, no vertical scanning was needed for any of the imaging techniques.

The phase contrast signal in PCI system stems from the fact that, when the X-rays travel through the object, their phase information is disturbed at the interface of features having different refractive index. Upon leaving the object, the disturbed phase information develops across the X-ray beam front as it propagates through the free distance before hitting the detector (Fig. 5.1B). Because the propagation distance directly affects the edge-enhanced phase contrast signal [48-50], the maximum available propagation distance of 5.9 m was evaluated and compared to that of 0.85 m, which is commonly used in the PCI setting at the BMIT.

The phase contrast images collected contain both absorption and phase information. A phase retrieval technique [51, 52] was employed to obtain phase information from the images collected by amplifying the phase contrast fringes to background noise and retrieving quantitative results [53]. The phase-retrieval algorithm of the phase-attenuation-duality Paganin

algorithm (PAD-PA) [54], which was developed for single propagation distance PCI and for samples with weak absorption and phase-attenuation duality [55, 56], was employed in this study. Phase retrieval was performed using phase-sensitive X-ray image processing and tomography reconstruction (PITRE) software [53], in which the PAD-PA algorithm is implemented and the phase-retrieved image is reconstructed using [53]:

$$\varphi_\theta(x,y) = F^{-1}\left\{\frac{F\left[\left(I_{Z,\theta}-1\right)/2\right]}{\left(\alpha/\beta\right)^{-1}\cos X+\sin X}\right\}, \quad 5.2$$

$$X = \pi\lambda\, Z\,(u^2+v^2), \quad 5.3$$

where $\varphi_\theta\,(x,y)$ is the phase at the tomography rotation angle θ and at coordinates x and y in the image; F and F^{-1} are the forward and backward Fourier transform operators, respectively; $I_{z,\theta}$ is the photon intensity at sample-to-detector distance z and rotation angle θ; α is the X-ray refractive index decrement; β is the absorption index; λ is the X-ray wavelength; and u and v are Fourier conjugate coordinates of x and y, respectively. In the present study, the values of α and β were chosen as the ones for water, $\alpha = 0.144\times10^{-6}$ and $\beta = 0.0658\times10^{-9}$, given the fact that the joint imaged largely comprises of soft and low density tissues (within the space between femur and tibia). Nonphase-retrieved extended-distance CT slices were also reconstructed for comparison to phase-retrieved images.

All three imaging systems were coupled with CT modality as recommended for *in situ* imaging of thick intact samples [3]. Due to the fixed X-ray beam used in synchrotron-based imaging, CT scanning was performed around the axis perpendicular to the incident beam over 180° degrees in a step and shoot mode with images collected at the detector. The number of projection images collected was in range of 300 to 2500. A Photonic Science detector (St. Geoirs, France) with a physical pixel size of 18.5 ×18.5 μm was used to collect the images. PITRE [53] and X-TRACT [57] were used for reconstruction and CT slice reconstructions of the DEI refraction and ABI images as well as the extended-distance PCI phase-retrieved and non-phase-retrieved images. The intensity signals obtained in the reconstructed CT slices are retuned by the filtered back projection algorithm in the reconstruction software in terms of refraction angle ($\Delta\theta_Z$) in the DE image, X-ray attenuation coefficient (μ) modified for edge-enhancement in the AB image and nonphase-retrieved PC image (referred to as the apparent μ),

and approximate X-ray refractive index decrement (referred to as the approximate α) in phase-retrieved PC image-because the phase retrieval algorithm uses the assumption of constant (α/β) for the sample composition.

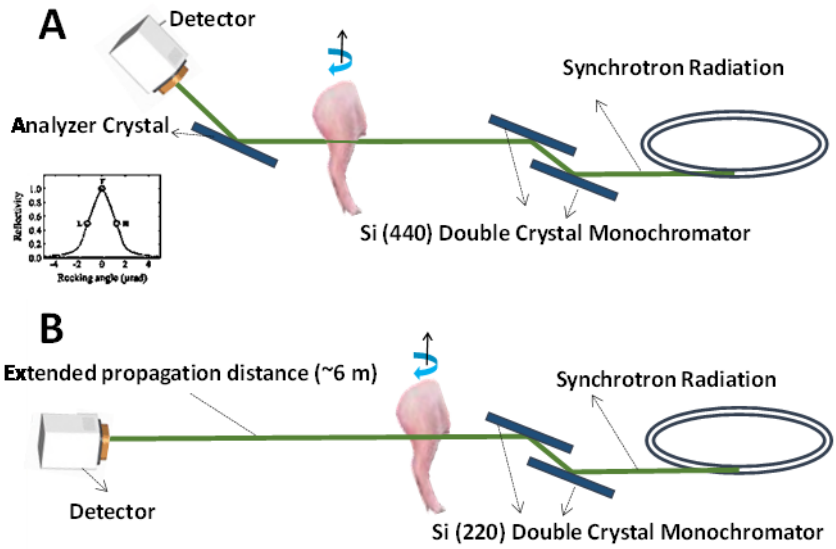

Figure 5.1 Schematic diagrams illustrating the imaging setup for (A) CT-DEI and CT-ABI and (B) extended-distance CT-PCI. Inset in (A) shows the reflectivity function in the analyzer rocking curve.

5.3.3 Radiation dose evaluation

The radiation dose rate delivered in different imaging techniques was obtained using X-ray radiation dosimeters (Luxel® by Landauer (aluminum oxide dosimeter)). The dosimeters measure the shallow dose equivalent, which is the external exposure dose received at the skin or at a tissue depth of 0.007 cm over a 1 cm^2 area [58]. The rate of radiation dose was then calculated from the measured total dose according to

$$\dot{D} = \frac{V}{h} D, \tag{5.4}$$

where $\dot{D}$ is the rate of radiation dose, V is the vertical scanning speed, h is the beam height at the sample location, and D is the total received radiation dose measured by the dosimeter. Two dosimeters were employed to measure the radiation dose for DEI/ABI (both have the same imaging setting despite different data collection procedure) and PCI. Another dosimeter was used to measure the background radiation at the CLS site and served as a control. To measure the radiation from each imaging setup, the dosimeter was attached to a SolidWater® sheet (4.5 mm

in thickness) to simulate radiation back-scattered from the sample to the dosimeter. The dosimeter was then vertically scanned through the beam at a speed of 0.1 mm/s for DEI/ABI and 0.2 mm/s for PCI setups. The vertical beam height was also measured by exposing Linagraph Direct Print papers (Kodak, Type 2167 standard) to the X-rays until a beam mark appeared on the paper.

Total dose received by the sample during CT imaging (D) was calculated according to

$$D = \dot{D} \times \Delta t, \tag{5.5}$$

where $\dot{D}$ is the calculated dose rate and Δt is the total exposure time. The radiation dose is usually reported by two metrics: absorbed dose in Gray (Gy) and effective dose equivalent in Sievert (Sv). Typically, the first metric is used by physicists to report the radiation energy deposited per mass of material, while the second metric is used by clinicians to report the detrimental radiobiological risk of radiation to the exposed tissue or organ. Here, the effective dose equivalent is reported in Sieverts converted according to

$$D(Sv) = D(Gy) \times W_R \times W_T, \tag{5.6}$$

where D is the absorbed dose, W_T is a tissue radio-sensitivity weighting factor, and W_R is a radiation weighting factor. The value of W_R for X-ray photons is 1 [59] and the value of W_T for cartilage tissue was chosen as 0.01 [59]. Although in the report of International Commission on Radiological Protection (ICRP) [59] the value of W_T is not explicitly given for cartilage (considered as a negligibly radiosensitive tissue), for being safe the W_T value for bone surface (0.01) was adopted and used for dose conversions in the present study.

5.3.4 Low-dose CT imaging

Three strategies were investigated to reduce the radiation dose received during CT imaging: (i) reducing the number of projections in CT imaging, (ii) region of interest (ROI) CT imaging, and (iii) lower resolution imaging. These strategies were examined either alone or in combination with CT-DEI, CT-ABI, and extended-distance CT-PCI. The number of projections in CT imaging was reduced by increasing the angular rotation step of tomography scanning stage. A CT scan of 2500 tomographic projections is suggested for standard CT for a field of view of about 74 mm (horizontal) × 4.5 mm (vertical) in DEI, ABI, and PCI (74 × 3.4 mm in extended-distance PCI) and an image pixel size of 37 × 37 μm [3]. To uniformly reduce the

number of tomographic projections collected over the 180° CT, the angular CT steps were increased to collect 1250 (50% of the standard number), 900 (36%), 625 (25%), and 375 (15%) projections for image reconstruction. Standard 2500 projection CT scans performed with all phase-based imaging techniques served as controls. The exposure time per projection was 3.5 s for DEI and ABI and 187 ms for PCI and extended-distance PCI.

Region of interest (ROI) imaging was examined by decreasing the field of view in the horizontal direction to 43 mm using slits to achieve a smaller imaging area that mainly covered the scaffold implanted site at the joint. By following the standard CT scan procedure, 1800 tomographic projections were collected to reconstruct the ROI images. The combination of a lower number of projections and ROI CT imaging was also investigated by performing ROI CT scans of the samples and collecting 900 (50%), 600 (36%), 450 (25%), and 300 (15%) tomographic projections.

The strategy of lower resolution imaging was examined by either performing CT imaging at 74 μm and 111 μm pixel sizes or by using a non-averaging sampling algorithm written in IDL (Interactive Data Language, Exelis Visual Information Solution, Inc., Boulder Colorado, CO, USA) that returns tomographic projections with 74 μm and 111 μm pixel sizes from 2×2 and 3×3 pixel sample areas of 37 μm pixel size projections. The sampling algorithm selects the signal from one of the 4 and 9 pixels to create the 74 and 111 μm pixel size projections, respectively, which simulates the actual signal received during CT imaging at 74 and 111 μm pixel size. The simple binning of data by averaging or summing the values of the pixels was not used in the present study because it leads to improved signal to noise ratio in the simulated projection image. Such signal enhancement is inconsistent with a real CT data collection due to the fact that the AD conversion in the Photonic Science detector is limited to approximately 11.5 bits. The highest imaging resolutions performed in DEI and ABI had a 37 μm pixel size and in extended-distance PCI had an 18.5 μm pixel size. Imaging at a pixel size of 18.5 μm required a projection exposure time of 700-900 ms using extended-distance PCI and 12-16 s using DEI or ABI. This was only practically possible with the extended-distance PCI technique. The scan time could take up to 12 h for a standard CT-DEI at 18.5 μm pixel size; this is extremely large and impractical and therefore was not pursued. The combination of lower resolution and a reduced number of projections was tested by reconstructing 3D images using 1250 (50%), 900 (36%), 625 (25%), and 375 (15%) projections at 74 and 111 μm pixel sizes. The combination of the three low-dose

strategies was also investigated for the imaging techniques that worked well with the individual low-dose strategies.

5.3.5 Image quality assessment

To evaluate the image quality as well as the effectiveness of the aforementioned low-dose strategies, quantitative and qualitative criteria were used in evaluation and comparison of the imaging techniques. The criteria examined include image intensity profile, quantitative image similarity/correlation to the standard (100% projections) image, contrast to noise ratio, total effective dose, total scan time, and qualitative observer image quality score. Quantitative analysis was performed on a square-shape area in the images that contained the structured feature of the scaffold. An area of the same size at a non-structured region of the image was used as the background noise area. The image intensity profile was obtained and compared among images for a line drawn across the structured scaffold region. In each technique, the similarity between the lower dose images and the standard reference image was represented by the image correlation coefficient (R) obtained using the ImageJ correlation plugin [60]. Contrast to noise ratio (CNR) was defined as the contrast of a structured region in the image (e.g. scaffold) to the noise of the background calculated according to

$$CNR = \frac{\sigma_s}{\sigma_b}, \tag{5.7}$$

where σ_s is the standard deviation across the selected structured area and σ_b is the standard deviation of a non-structured background region. The relative CNR values for each image was calculated by multiplying the CNR of the reference standard image (100% projections) to the image correlation coefficient (R) associated with low- dose image. In order to enable an equitable comparison among the CT-DEI, CT-ABI, and extended-distance CT-PCI techniques, the relative CNR values of standard and low dose images were normalized with respect to the associated dose and pixel size resolution by

$$NCNR = \frac{CNR \times R}{D \times px}, \tag{5.8}$$

where *NCNR* is the normalized contrast to noise ratio [mSV^{-1} mm^{-1}], *R* is the image correlation coefficient, *D* [msV] is the total absorbed effective dose and *px* [mm] is the image pixel size. To produce the error bar, the relative CNR values were obtained from the original structured and non-structured square-shape areas (~ 5 mm × 5 mm) and 8 other areas of the same size, but with

the center shifted 1 mm in eight directions of the following angles: 0°, 45°, 90°, 135°, 180° 225°, 270°, 315°. For the observer image quality assessments, a 5-point scoring system was employed to describe the image quality, where 5 was “best”, 4 was “optimal”, 3 was “adequate”, 2 was “insufficient”, and 1 was “poor”. A clinical radiologist used the scoring scale to grade the quality of images in terms of level of visualization and characterization of the implanted scaffold as well as different microstructural and anatomical features. The given image quality score (IQS) was used to represent the clinically relevant quality of the image.

5.4 Results

5.4.1 CT-DEI, CT-ABI, and CT-PCI

The initial comparison to identify the most suitable phase-based X-ray imaging technique(s) for *in situ* scaffold visualization was performed with images captured by using standard CT imaging modality (using 2500 projections) at a pixel size of 37 μm. In the CT-DEI and CT-ABI produced images, the scaffolds implanted in cartilage were clearly visualized *in situ* (Fig. 5.2A,B), while not detectable in the PCI with a sample-to-detector distance of <1 m (Fig. 5.2D). Increasing the propagation distance for inline PCI was found to be essential for *in situ* imaging of the scaffold and low absorbing soft tissues of the joint (Fig. 5.2C,E). DEI, ABI, and extended-distance PCI did not exhibit similar image contrasts, but the contrast mechanism employed in each technique was sufficient for resolving the desired low density features with appreciable structural detail. All three techniques produced images of the implanted scaffolds that included the characteristic lattice structure. Furthermore, distinct interfaces and structures of the surrounding soft tissues, e.g., condyle cartilage, meniscus, fibrous ligament, tendon, muscle, and fat tissues, were visible in the CT-DE, CT-AB, and extended-distance CT-PC images (Fig. 5.2A-C, E).

The DE and AB images showed stronger edge contrast than extended-distance PC images at the 37 μm resolution. CNR of the scaffold region was determined as 4.07, 2.13, 1.49, and 1.19 in the DE, AB, and phase-retrieved and nonphase-retrieved extended-distance PC images, respectively, which confirms the contrast difference observed among different methods (Fig. 5.2 A-C, and E). Very small and detailed structural features of soft tissues, such as micro-vascular channels in the cartilage, bundled fibrous texture of the ligaments and tendon, and loose, non-oriented fibrous structure of the fat tissue, were identified with more distinct interfaces in the DE

and AB images than in the extended-distance PC images (Fig. 5.2A-C, and E). DEI produced a sharper edge contrast than ABI due to the ABI's combined refraction-absorption contrast signal (Fig. 5.2F and G). The dual imaging in the DEI technique enabled extraction of a pure refraction signal that produced a stronger edge-enhanced contrast with better visualization of small features (Fig. 5.2A and F). In extended-distance PCI, the tissue and structural contours were identifiable but had less edge-enhanced contrast than DEI and ABI (Fig. 5.2F-H, and J). The nonphase-retrieved PC image showed less sharp edge contrast than the phase-retrieved PC images (Fig. 5.2C and E), which appeared to be due to the large background noise that supressed the edge-enhanced contrast signal in the image profile (Fig. 5.2H and J). In the phase-retrieved PC image, the contrast difference between bulk tissues was more recognizable by sudden changes in pixel intensity (Fig. 5.2H). For example, the fat tissue is seen as a darker, less absorbing material with much lower pixel intensity than muscle and cartilage (Fig. 5.2C and H). The intensity profile of the phase-retrieved extended-distance CT-PC images also shows a subtle difference between pixel intensity in muscle and cartilage tissues (Fig. 5.2H). Furthermore, the cartilage defect cavity implanted with the scaffold and filled with DPBS was distinguishable in the phase-retrieved extended-distance PC image as a lower density material compared to the surrounding cartilage tissue (Fig. 5.2C and H). This subtle bulk density information was not visualized in the DE and AB images. The nonphase-retrieved PC image illustrated the low density fat tissue as a darker, less absorbing material, but it fell short in revealing the detailed information that was depicted in phase-retrieved PC image (Fig. 5.2C, E, H, and J).

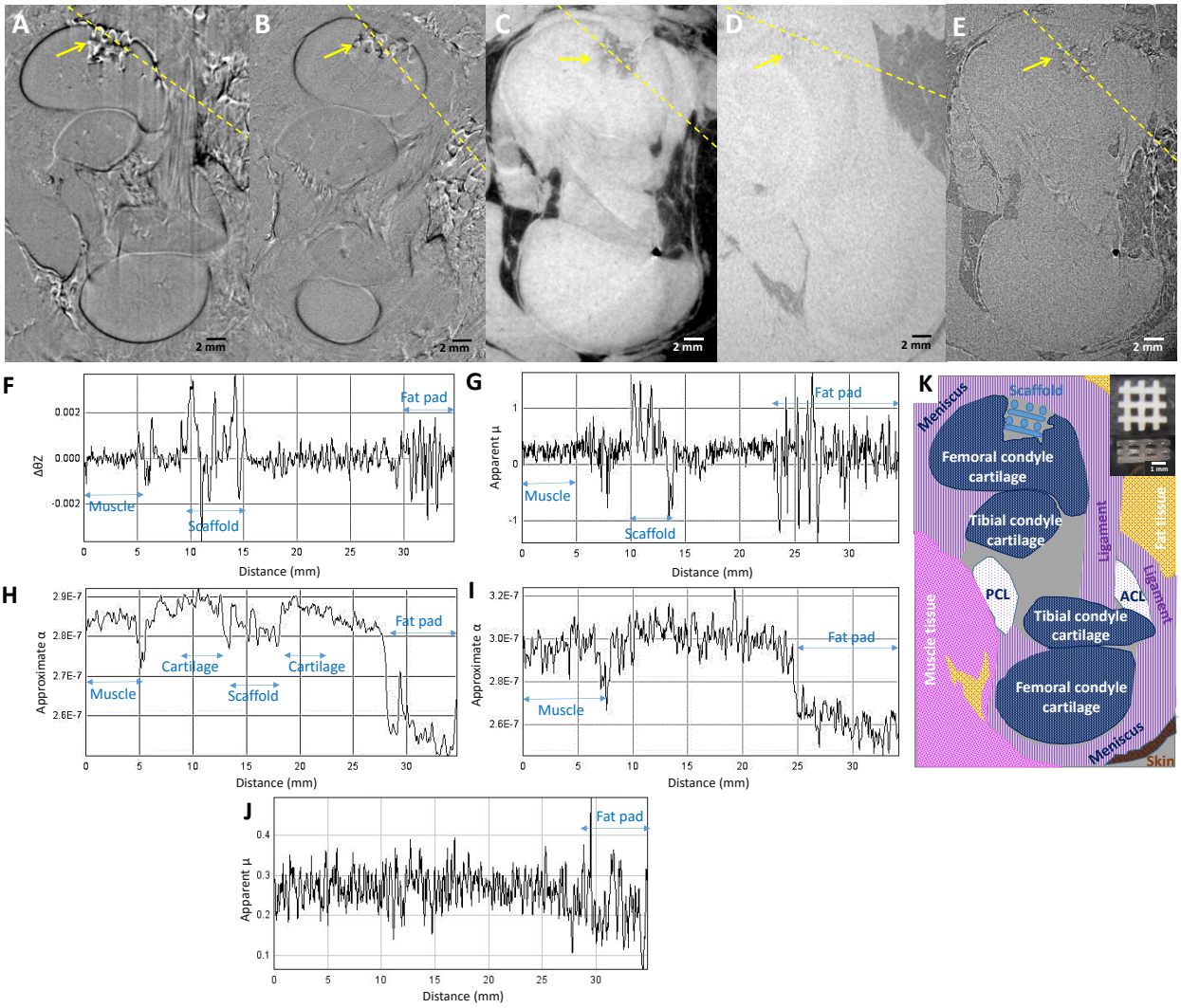

Figure 5.2 Imaging *in situ* cartilage scaffold using different phase-based X-ray imaging techniques. Reconstructed CT slices from (A) DEI, (B) ABI, (C) phase-retrieved PCI and (E) nonphase-retrieved PCI at extended sample-to-detector distance of 5.9 m and (D) PCI at a sample-to-detector distance of 85 cm. All images are at a pixel size resolution of 37 μm. Yellow arrows point to the implanted scaffold. The intensity profile across the yellow dashed line in the (A-E) images is shown in (F–J) respectively. (K) A schematic view of the joint cross section with labeled main components. Inset images in panel (K) are the digital planar view (top) and the light microscopic cross section view (bottom) of polycaprolactone tissue scaffold.

5.4.2 Radiation dose of phase-based X-ray imaging

The radiation doses delivered by the imaging methods considered were 10.31 mGy for DEI and ABI and 117.40 mGy for PCI. The calculated rate of radiation dose was 0.2 mGy/s for DEI and ABI and 6.43 mGy/s for PCI. The higher dose rate in PCI is due to the higher X-ray photon flux reflected from the Si (2,2,0) planes vs. the Si (4,4,0) planes used for DEI. The Si

(4,4,0) reflection plane in the DEI and ABI systems provides a narrow reflection bandwidth in the rocking curve for higher refraction sensitivity and stronger edge contrast, but this results in a lower photon flux and consequently longer scan times and larger exposures.

The total exposure time for a standard CT scan (2500 tomographic projections), was about 4.9 h for DEI, 2.5 h for ABI, and 8 min for PCI. The total dose received by the samples during these scans was calculated as 3.4 Gy for CT-DEI, 1.7 Gy for CT-ABI, and 3 Gy for extended-distance CT-PCI. Despite their considerably different dose rates, DEI and PCI methods have similar total delivered doses due to their large difference in scan times. ABI has a smaller dose rate than PCI and shorter scan time than DEI, resulting in a lower total dose than the other techniques. Considering the 0.01 tissue weighting factor (W_F) for cartilage and surrounding soft tissues, the equivalent effective dose rate for CT-DEI and CT-ABI was 2 μSv/s and for extended-distance PCI was 64.3 μSv/s. The total equivalent effective dose received by the sample was 34 mSv for CT-DEI, 17 mSv for CT-ABI, and 30 mSv for extended-distance CT-PCI.

5.4.3 Low-dose CT phase-based imaging

5.4.3.1 Reduced number of CT projections imaging

The strategy of reducing the number of projections was investigated by reconstructing the CT-DEI, CT-ABI, and extended-distance CT-PCI slices using 50, 36, 25, and 15% of the projections collected during a standard CT scan at 37 μm image pixel size. Although the number of projections collected was considerably reduced, the CT slices were successfully reconstructed with the key features and information preserved. The scaffold structure and the joint soft tissues were detectable and characterizable in the DE, AB, and phase-retrieved extended-distance PC images constructed using 50, 36, 25, and 15% of the usual number of projections without considerable loss of contrast compared to a standard (100%) image (Fig. 5.3A-O). However, reducing the number of tomographic projections made the noise signal more recognizable, which slightly affected the overall quality of the reconstructed DE, AB, and phase-retrieved extended-distance PC slices. The noise signal was particularly apparent in the 25 and 15% extended-distance PC images compared to the corresponding DE and AB images (Fig. 5.3 D, E, I, J, N and O). In the nonphase-retrieved extended-distance PCI, reducing the number of projections, even by 50%, led to noticeably poor image contrast and quality (Fig. 5.3P-T). The bright area seen in

the center of the phase-retrieved image appears to be the start of the ossification center at the femoral condyle, which is also more easily visualized in the phase-retrieved image than nonphase-retrieved image (Fig. 5.3K-T). Comparing image intensity profile across the structured scaffold illustrated the well-preserved image signal in DEI upon reduction of the tomographic projections up to 85% (Fig. 5.4A and E-I). In ABI and phase-retrieved extended-distance PCI, the coarse changes in the signal associated with more distinct features were observed to be sufficiently preserved, while fine changes were to some extent affected as the number of projections was reduced (Fig. 5.4B, C, and J-S). The nonphase-retrieved PC image profile shows the apparent suppression of the structure signal by the strong noise when the number of projections were reduced (Fig.5. 4D, and T-X).

Furthermore, the image correlation coefficient results confirmed the superior performance of DEI compared to other methods by consistently high image correlation coefficient of at least 0.85 to the standard reference image (100% projections) when the number of projections were reduced to 15% (Fig. 5.4Y). The minimum number of projections that can efficiently preserve DE image information was 15% CT projections; R dropped considerably at 10 and 5% CT projections (Fig. 5.4Y). ABI and extended-distance PCI showed reduced image correlation with lowering the number of projections (Fig. 5.4Y). Lower image quality and R values reduced to 0.5 or less were observed at 15% projections with ABI and phase-retrieved extended-distance PCI, and at 50% projections with nonphase-retrieved extended-distance PCI. This appears to be a threshold R value below which the image quality and information may be compromised considerably (Fig. 5.4Y). The high CNR of the DEI technique along with the high image correlations resulted in persistently high relative CNR (>3.9) across lower number of projections images (50%-15%) (Fig. 5.4Z). This indicates the robustness of this technique compared to other methods with respect to maintaining contrast at a reduced number of projections. ABI showed slightly higher relative CNR than extended-distance PCI at 100% projections (2.1 vs 1.5), however, the difference diminishes as the number of projections is reduced (Fig. 5.4Z). The nonphase-retrieved extended-distance PCI showed the lowest CNR value (1.2) among the methods, which reduces to 0.5 at 50% projections and eventually to zero at 15 % projections (Fig. 5.4Z).

Reducing the number of projections substantially lowered the received dose and scan time for all three imaging techniques (Table 5.1). For example, reducing the number of projections to

15% in CT-DEI reduced the scan time and dose from 4.9 h and 34.5 mSv in standard CT imaging to ~45 min and 5.5 mSv, respectively. Similarly, the dose in CT-ABI dropped from 17.2 to 2.6 mSv and in extended-distance CT-PCI dropped from 30.1 to 4.5 mSv. The scan times dropped to <25 min for CT-ABI and <2 min for CT-PCI (Table 5.1). By reducing the number of projections in CT-DEI by 50%, a comparable dose and scan time to standard (100%) CT-ABI is achieved while maintaining superior image contrast (Fig. 5.4). The observer image quality assessments indicated that the reduced CT projection strategy for all the methods, except nonphase-retrieved extended-distance PCI, did not affect the capability of the techniques in imaging the implanted scaffold, image quality scores (IQS)>3 (Table 5.1). This illustrates the potential of this strategy to reduce time and dose without compromising image contrast. Since the nonphase-retrieved extended-distance PCI demonstrated an inferior and insufficient capability among other methods for imaging scaffolds at standard and lower projection imaging, it was excluded from further intensity profile and observer image quality assessments.

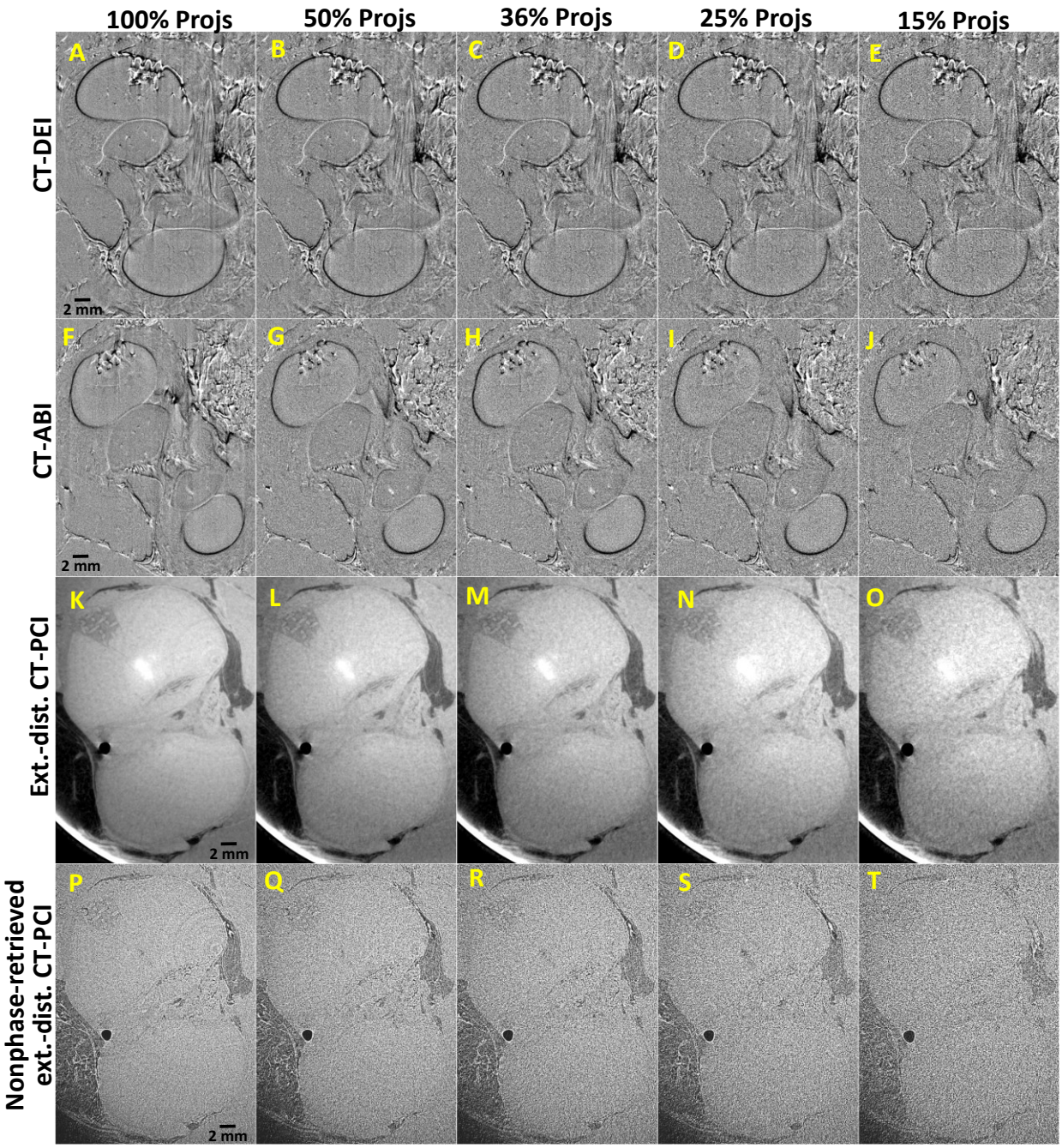

Figure 5.3 Qualitative image comparison in CT phase-based imaging using a lower number of projections. (A–E) CT-DEI, (F–J) CT-ABI, and (K–O) phase-retrieved and (P–T) nonphase-retrieved extended-distance (ext.-dist.) CT-PCI at (A, F, K, P) 100%, (B, G, L, Q) 50%, (C, H, M, R) 36%, (D, I, N, S) 25%, and (E, J, O, T) 15% of the standard number of projections. The bright spot visible in panels (K–O) corresponds to the start of the ossification center, and are better visualized in the phase-retrieved images than the nonphased retrieved images (P–T).

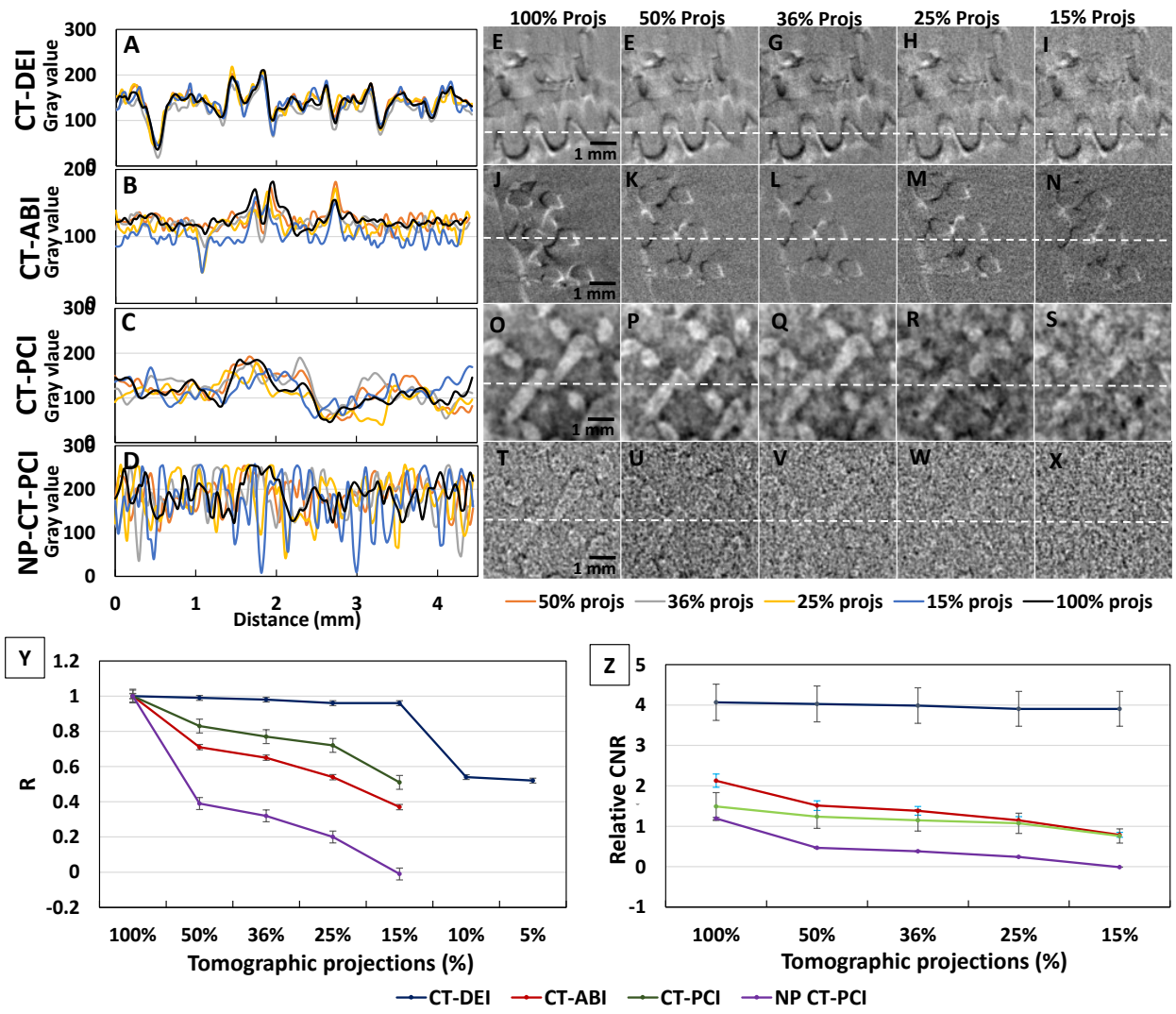

Figure 5.4 Quantitative image comparison in lower number of projections CT phase-based imaging. Comparison of the image intensity profile across a 4.5 mm white dashed line shown in the structured scaffold area of (A, E–J) CT-DE, (B, J–N) CT-AB, (C, O–S) phase-retrieved extended distance CT-PCI, and (D, T–X) nonphase-retrieved extended distance CT-PCI (NP-CT-PCI) as the number of tomographic projections decreases from 100 to 15% of the standard number. (Y) Image correlation coefficient(R) with the reference image (100% projection) and (Z) relative contrast to noise ratio (CNR) for CT-DEI, CT-ABI, and phase-retrieved and nonphase-retrieved CT-PCI with reduced number of tomographic projections.

Table 5.1 Total effective dose, scan time, and observer image quality score (IQS) for visualizing scaffolds *in situ* with the strategy of reducing the number of projections in CT imaging.

% Proj	CT-DEI			CT-ABI			Extended-distance CT-PCI			
	Dose*	Scan time**	IQS	Dose	Scan time	IQS	Dose	Scan time	IQS	IQS(NP×)
100%	34.5	294.6	5	17.2	147.3	4	30.1	7.8	4	3
50%	17.2	147.3	4	8.6	73.7	4	15.1	3.9	4	2
36%	12.4	106.1	4	6.2	53.1	4	10.8	2.8	4	2
25%	8.6	73.7	4	4.3	36.9	4	7.5	2.0	3	1
15%	5.2	44.3	3	2.6	22.1	3	4.5	1.2	3	1

* Total effective dose in (mSv), ** total scan time in (min), × Nonphase-retrieved

5.4.3.2 Region of interest (ROI) CT imaging

Performing the CT scan on a smaller area of the sample that mainly covered the implantation site, i.e., ROI imaging, was also found to be an effective strategy for reducing the radiation dose and scan time. Reducing the scan area resulted in a smaller number of pixels in the field of view and a smaller number of required tomographic projections to be collected in a CT scan. In a standard CT scan of the whole joint at 37 μm pixel size, 2500 projections are collected; this was reduced to ~1800 projections for a CT scan of the selected ROI. Compared to standard images (Fig. 5.3A, F, and K), reconstructed ROI slices did not show any notable negative effects on the visualization of the scaffold and surrounding soft tissues (Fig. 5.5A, F, and K). Image intensity profile analysis showed similar performance of the techniques at ROI imaging as that observed in the reduced number of projection strategy (Fig. 5.6). Intensity profile of ROI DE images at reduced number of projections showed the smallest variation from the reference standard image (non-ROI, 100% projections) compared to those in ROI AB and phase-retrieved PC images (Fig. 5.6A-C). This observation was also confirmed quantitatively by the consistently higher R values (>0.85) of ROI DE images than ROI AB and extended-distance PC images at reduced number of projections (Fig. 5.6S). Although the image correlation of ROI AB and PC images dropped with decreasing the number of tomographic projections, ABI demonstrated better R values than extended-distance PCI particularly at 15% projections (Fig. 5.6S). The considerably higher relative CNR values of ROI DE images than ROI AB and extended-distance PC images indicated that DEI maintained high contrast in the ROI imaging compared to ABI and extended-distance PCI (Fig. 5.6T). At 25% and 15% projections, R and

relative CNR values of ROI PC images drop to relatively low value which reflects the somewhat affected image quality observed (Fig. 5.6Q-T).

ROI imaging reduced the radiation dose from 34.5 to 24.8, 17.2 to 12.4, and 30.1 to 19.4 mSv for CT-DEI, CT-ABI, and extended-distance CT-PCI, respectively (Table 5.2). When ROI imaging was combined with a reduced number of projections, the delivered dose and scan time declined further (Table 5.2). For example, the CT-DEI radiation dose dropped from 34.5 to 24.8 mSv by reducing the imaging area, and then use of 15% of the standard number of projections further decreased the total delivered dose to 4.1 mSv. The observer IQSs for visualizing the scaffold remained relatively high at these settings. The reconstructed ROI AB and extended-distance PC images also maintained sufficient image contrast at a low number of projections for visualizing both the scaffold and anatomical features of the joint; however, the subtle structural details were less clear in ROI ABI and extended-distance PCI than in DEI (Fig. 5.5).

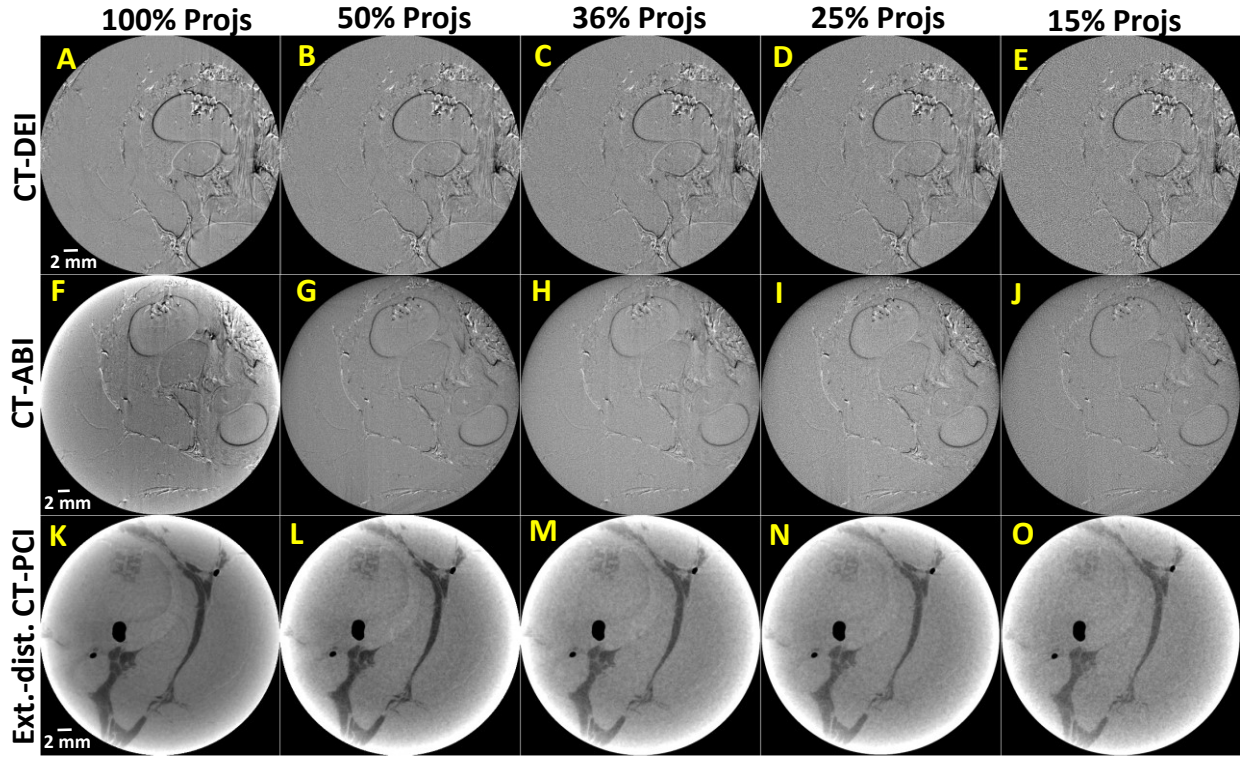

Figure 5.5 Region of interest (ROI) and CT imaging at reduced number of projections: (A-E) CT-DEI, (F-J) CT-ABI, and (K-O) extended-distance (ext.-dist) CT-PCI at (A, F, K) 100%, (B, G, L) 50%, (C, H, M) 36%, (D, I, N) 25%, and (E, J, O) 15% of the standard number.

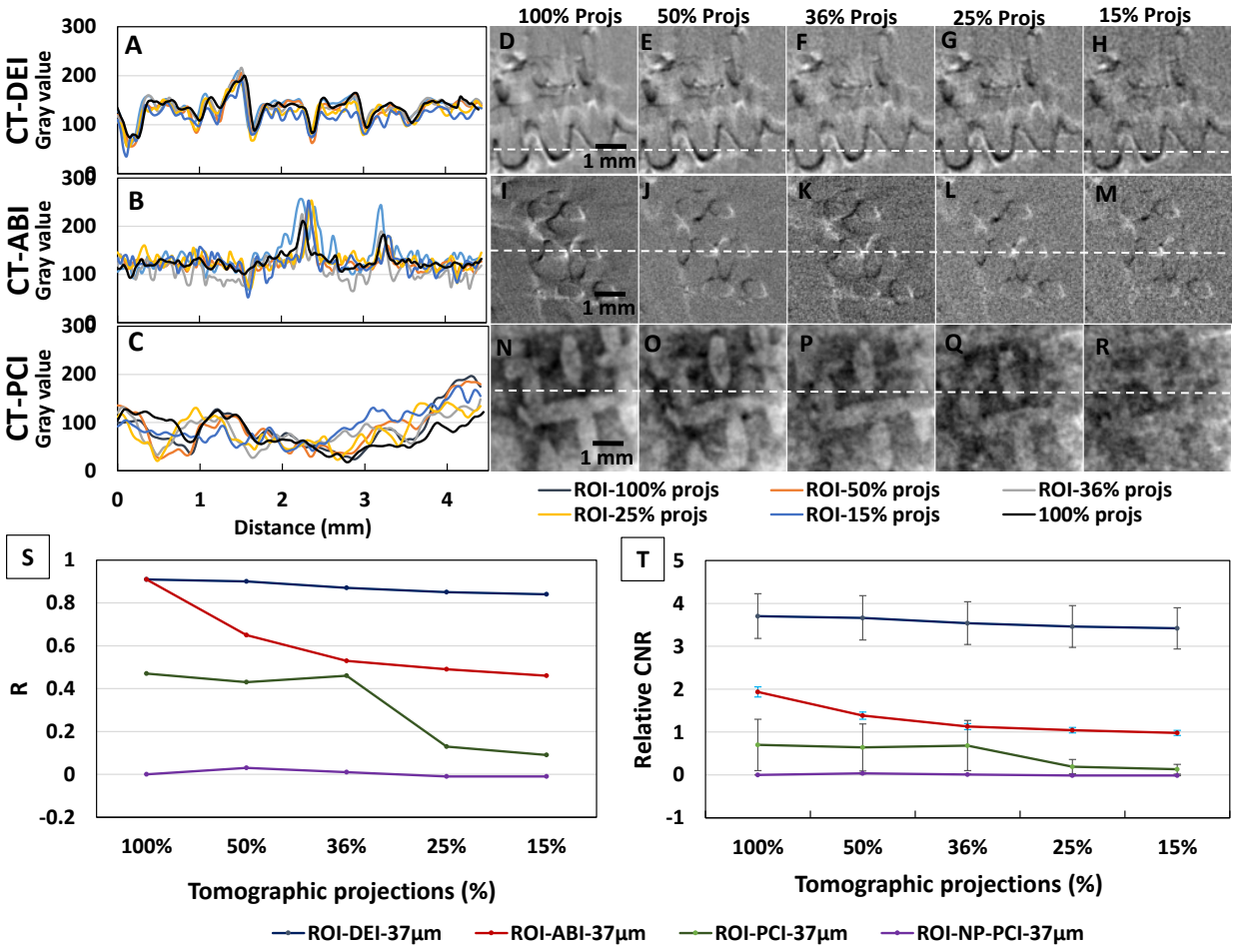

Figure 5.6 Quantitative image comparison in ROI and lower number of projections CT phase-based imaging. Comparison of the image intensity profile across a 4.5 mm white dashed line shown in the scaffold area of region of interest (ROI) (A, D–H) CT-DE, (B, I–M) CT-AB, and (C, N–R) phase-retrieved extended distance CT-PC images as the number of tomographic projections decreases from 100 to 15% of the standard number. The black intensity profiles in panels A–C are associated with the standard non-ROI images at 100% projections. (S) Image correlation coefficient (R) to the standard image and (T) relative contrast to noise ratio (CNR) for ROI CT-DEI, CT-ABI, phase-retrieved CT-PCI, and nonphase-retrieved CT-PCI (NP–PCI) with decrease of the number of tomographic projections.

Table 5.2 Total effective dose, scan time, and observer image quality score (IQS) for visualizing scaffolds *in situ* with the strategy of reducing the region of interest (ROI) combined with reduced number of projections in CT imaging.

% Proj	CT-DEI			CT-ABI			Extended-distance CT-PCI		
	Dose*	Scan time**	IQS	Dose	Scan time	IQS	Dose	Scan time	IQS
100%	24.8	212.1	4	12.4	106.0	4	19.4	5.0	4
50%	11.5	98.3	4	6.2	53.1	4	9.5	2.5	4
36%	8.6	73.7	4	4.3	36.9	4	6.3	1.6	3
25%	6.9	59.0	4	3.1	26.6	3	4.8	1.2	3
15%	4.1	35.4	3	2.1	17.7	2	3.2	0.8	3

* Total effective dose in (mSv), ** total scan time in (min)

5.4.3.3 Lower resolution imaging

To further reduce the radiation dose and scan time, imaging at a lower resolution was investigated. Lowering the resolution or increasing the pixel size results in higher photon counts per pixel per second, which reduces the required exposure times and thus scan times and radiation dose. The scaffold structure as well as anatomical and structural details of different surrounding tissues were well preserved in the lower resolution DE and AB images, with negligible image quality deterioration compared to standard 37 μm pixel size images (Fig. 5.7 A-F). In the extended-distance PC images, lowering the resolution resulted in a noticeable deterioration of image quality (increased noise, blurred edges and interfaces) compared to DEI and ABI at the same resolution (Fig. 5.7 G-I). However, the images still were of sufficient quality to visualize the scaffold and anatomical features of the joint. The intensity profile analysis showed that the signal changes across the structured feature are well preserved in DE images at lower pixel size resolutions of 74 and 111 μm (Fig. 5.8A, and D-F), although a slight drop in the intensity level was observed at 111 μm pixel size. The superior performance of low resolution DEI was also quantitatively confirmed by the high R values (>0.72) at 100% as well as reduced number of projections images (Fig. 5.8M). Lower resolution ABI and extended-distance PCI captured the coarse intensity changes across the structured region (Fig. 5.8B-L) at 100% tomographic projections, however, reducing the number of projections dropped the image correlation values for both imaging techniques (Fig. 5.8M). Relative CNR values indicated that DEI maintained high contrast, compared to ABI and extended-distance PCI, as both image resolution and the number of tomographic projections reduced (Fig. 5.8N).

Decreasing the image resolution in CT-DEI and CT-ABI decreased the exposure time per projection from 3.5 s (at 37 μm pixel size) to 900 ms (at 74 μm pixel size) and 410 ms (at 111 μm pixel size). In extended-distance CT-PCI, the exposure time per projection decreased from 776 ms (at 18.5 μm pixel size) to 187 ms (at 37 μm pixel size), 60 ms (at 74 μm pixel size), and 21 ms (at 111 μm pixel size). For all three imaging techniques, the considerable drop in exposure time decreased the radiation dose and the total scan time by approximately four-fold (at 74 μm) and nine-fold (at 111 μm) (Table 5.3). Imaging at 74 μm pixel size combined with reducing the number of projections further decreased the radiation dose, by 16-fold to <3 mSv at 25% in CT-DEI and CT-ABI, and by 8.6-fold to 3.5 mSv in extended-distance CT-PCI at 36% (Table 5.3). Based on the given observer IQSs, the contrast signal in these settings remained sufficient to visualize the scaffold structure (Fig. 5.7 J, L, and N; Table 5.3).

The scan time (at 74 μm and 25%) was also considerably reduced in DEI and ABI to < 20 and 10 min, respectively, and in extended-distance PCI (at 74 μm and 36%) to <1 min (Table 5.3). At 111 μm pixel size, CT-DEI, CT-ABI, and extended-distance CT-PCI can be performed at a reduced number of tomographic projections to further lower the radiation dose and scan time while maintaining adequate image quality for visualizing the scaffold structure (Fig. 5.7 K, M, and O; Table 5.3). Reducing the number of projections to 25% at 111 μm pixel size lowered the total delivered dose and scan time in CT-DEI and CT-ABI to 1 and 0.5 mSv and 8.6 and 4.3 min, respectively (Table 5.3). The radiation dose and scan time in extended-distance CT-PCI could also be reduced to 1.5 mSv and 0.4 s by imaging at 111 μm pixel size and collecting 50% of the standard number of tomographic projections while maintaining sufficient detail to reconstruct the scaffold structure (Table 5.3). Imaging at the highest image resolution, 18.5 μm pixel size, was only practically feasible with extended-distance CT-PCI (the scan time for CT-DEI or CT-ABI at 18.5 μm pixel size is 16 times longer than at 37 μm pixel size), although the radiation dose was very high at 187 mSv.

The combination of the three strategies can further reduce the dose and scanning time without considerably affecting image quality for visualization and characterization of scaffolds *in situ*. This was particularly effective with the DEI technique due to its strong image contrast. Region of interest CT-DEI using 25% of the standard number of projections reduced the effective radiation dose and scan time to 1.77 mSv and 15 min at 74 μm pixel size and to 0.81 mSv and 7 min at 111 μm pixel size. Region of interest CT-ABI at 25% of the standard number

of projections reduced the effective radiation dose and scan time to 0.88 mSv and 7.5 min at 74 µm pixel size and to 0.4 mSv and 3.4 min at 111 µm pixel size (image not shown).

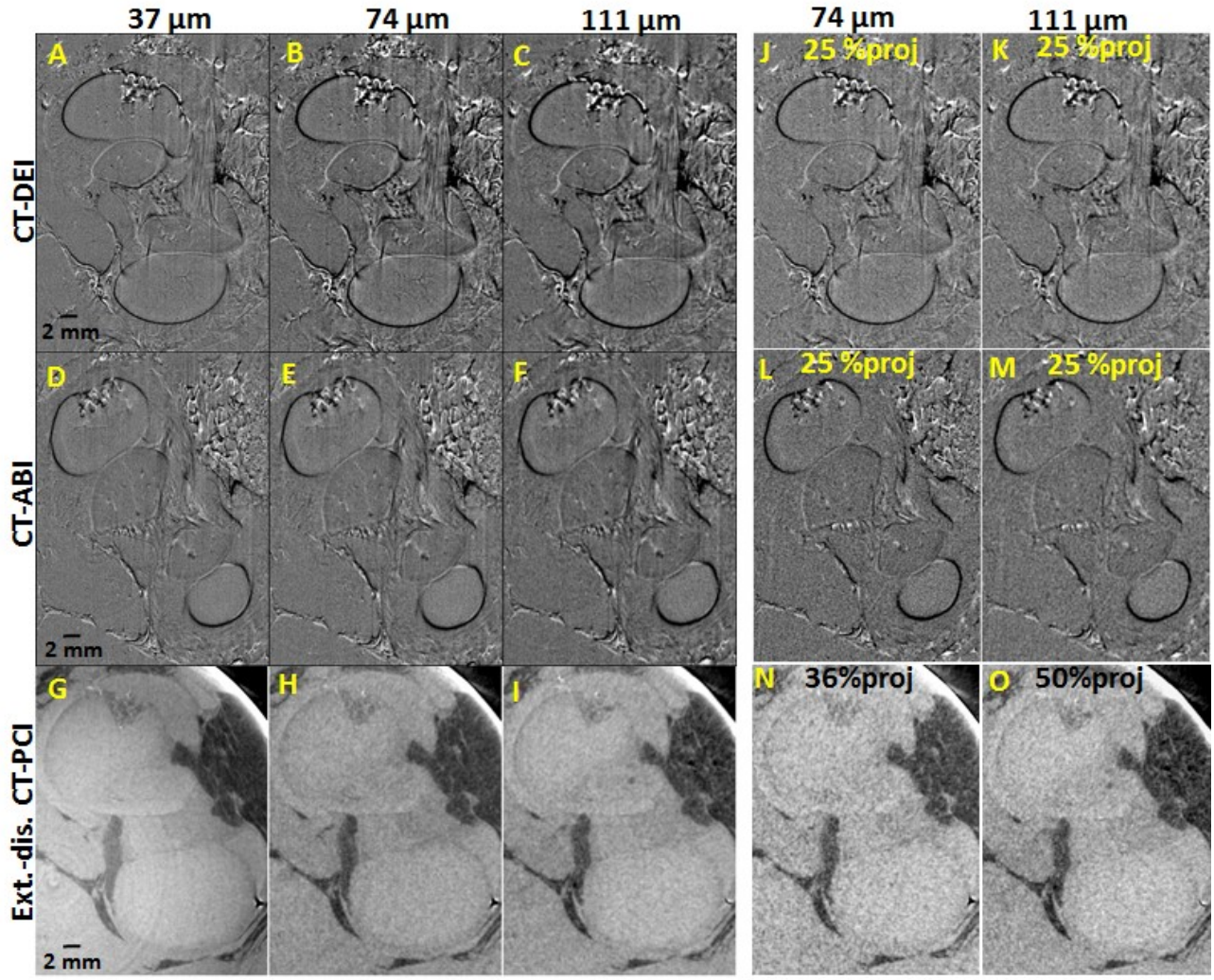

Figure 5.7 Comparison of representative images from lower resolution CT phase-based imaging. CT-DEI (A–C, J, K), CT-ABI (D–F, L, M), and phase-retrieved extended-distance (ext.-dist.) CT-PCI (G–I, N, O) using 100% (A–I), 25% (J–M), 36% (N), and 50% (O) of standard projections at 37 µm (A, D, G), 74 µm (B, E, H, J, L, N), and 111 µm (C, F, I, K, M, O).

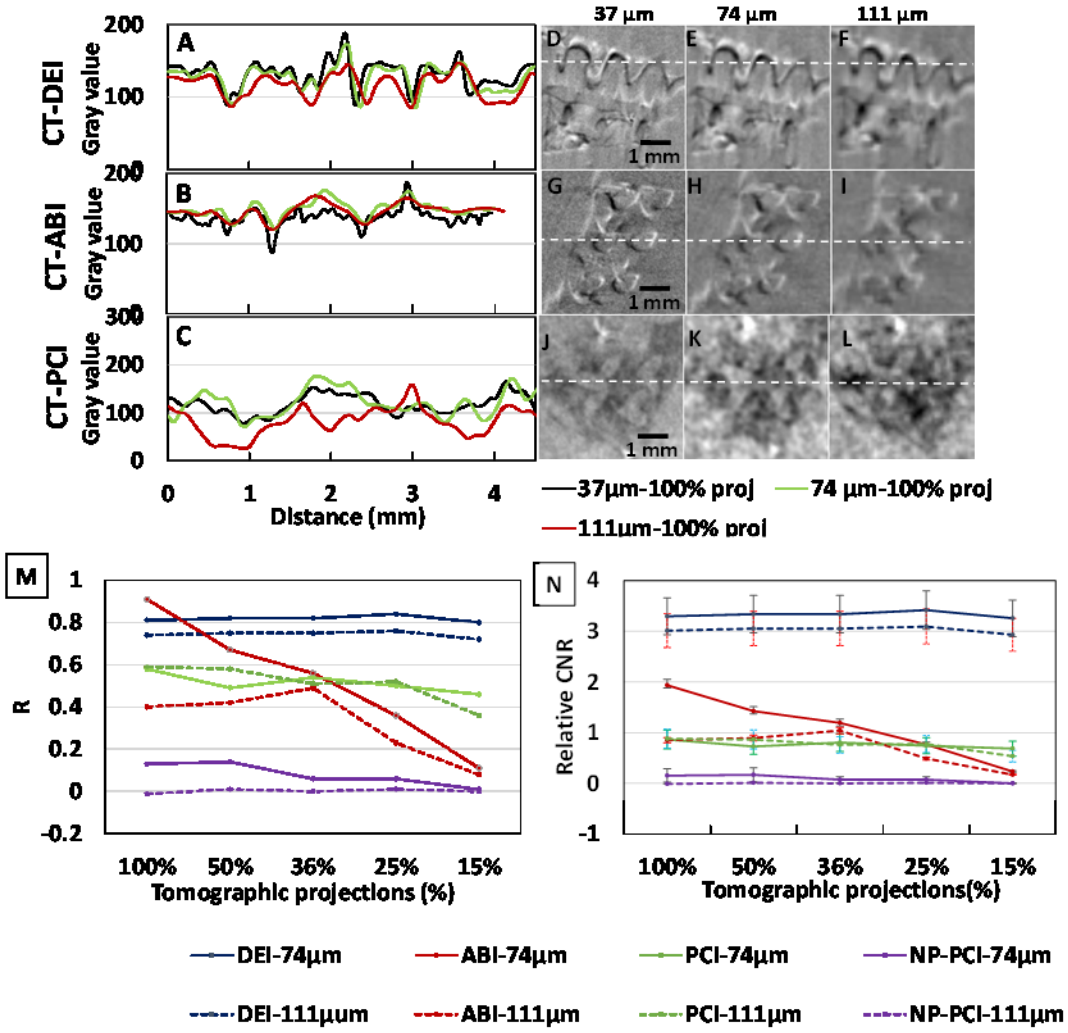

Figure 5.8 Quantitative image comparison in lower resolution and reduced number of projections CT phase-based imaging. Comparison of the image intensity profile across a 4.5 mm white dashed line shown in the scaffold area of low resolution (A, D–F) CT–DE, (B, G–I) CT-AB, and (C, J–L) phase-retrieved extended distance CT-PC images at 37 (D,G, J), 74 (E, H, K), and 111 µm (F, I, L) pixel size resolutions. (M) Image correlation coefficient (R) to the standard 100% projections images at 37 µm resolution and (T) relative contrast to noise ratio (CNR) for CT-DEI, CT-ABI, phase-retrieved CT-PCI, and nonphase-retrieved CT-PCI (NP-PCI) at 74 and 111 µm resolutions as the number of tomographic projections decreases from 100 to 15% of the standard number..

Table 5.3 Total effective dose, scan time, and observer image quality score (IQS) for visualizing scaffolds *in situ* with the strategy of lowering imaging resolution combined with reduced number of projections in CT imaging.

CT-DEI	37 µm			74 µm			111 µm		
	Dose*	Scan time**	IQS	Dose	Scan time	IQS	Dose	Scan time	IQS
100%	34.5	294.6	5	8.8	75.3	4	4.0	34.4	4
50%	17.2	147.3	4	4.4	37.7	4	2.0	17.2	3
36%	12.4	106.1	4	3.2	27.1	4	1.4	12.4	3
25%	8.6	73.7	4	2.2	18.8	3	1.0	8.6	3
15%	5.2	44.3	3	1.3	11.3	2	0.6	5.2	2
CT-ABI	37 µm			74 µm			111 µm		
	Dose	Scan time	IQS	Dose	Scan time	IQS	Dose	Scan time	IQS
100%	17.2	147.3	4	4.4	37.7	4	2.0	17.2	4
50%	8.6	73.7	4	2.2	18.8	4	1.0	8.6	4
36%	6.2	53.1	4	1.6	13.6	4	0.7	6.2	3
25%	4.3	36.9	4	1.1	9.4	3	0.5	4.3	3
15%	2.6	22.1	3	0.7	5.7	2	0.3	2.6	2
Ext.-dist. CT-PCI	18.5 µm			37 µm			74 µm			111 µm		
	Dose	Scan time	IQS	Dose	Scan time	IQS	Dose	Scan time	IQS	Dose	Scan time	IQS
100%	187.0	48.5	5	30.1	7.8	5	9.6	2.5	4	3.4	0.9	3
50%				15.1	3.9	4	5.8	1.5	3	1.5	0.4	3
36%				10.8	2.8	4	3.5	0.9	3	1.2	0.3	2
25%				7.5	2.0	3	2.4	0.6	2	0.8	0.2	1
15%				4.5	1.2	3	1.4	0.4	2	0.5	0.1	1

* Total effective dose in (mSv), ** total scan time in (min)

5.4.3.4 Lowe-dose CT-DEI vs CT-ABI vs extended-distance CT-PCI

In order to perform a more reasonable comparison among the methods for identifying the more effective low dose imaging settings, the low dose images were compared based on the normalized CNR (NCNR) that accounts for the dose and image resolution associated with the achieved image contrast. At 100% tomographic projections (standard setting), DEI, ABI, and extended-distance PCI demonstrated similar performances. In other words, at standard CT imaging all three methods provided comparable image contrast per mm pixel size of the image and per mSv delivered dose (Fig. 5.9). This, however, changes as the lower dose strategies are applied. The lower dose DEI demonstrates an increase in its performance, higher than other methods, as the lower CT projection, ROI, lower resolution, or a combination of these strategies are implemented (Fig. 5.9). At the lowest dose image settings, 15% projections, ROI-15% projections, 74 or 111µm-15% projections, the NCNR of DEI demonstrated the largest

difference from the other methods that indicates its superior performance for the same image resolution and amount of delivered dose (Fig. 5.9). Furthermore, ABI demonstrated better performance than extended-distance PCI at ROI and reduced CT projection imaging (Fig. 5.9). At lower resolution-reduced CT projections imaging, DEI exhibits considerably better image contrast than the other methods per mm pixel size and mSv delivered dose (Fig. 5.9B).

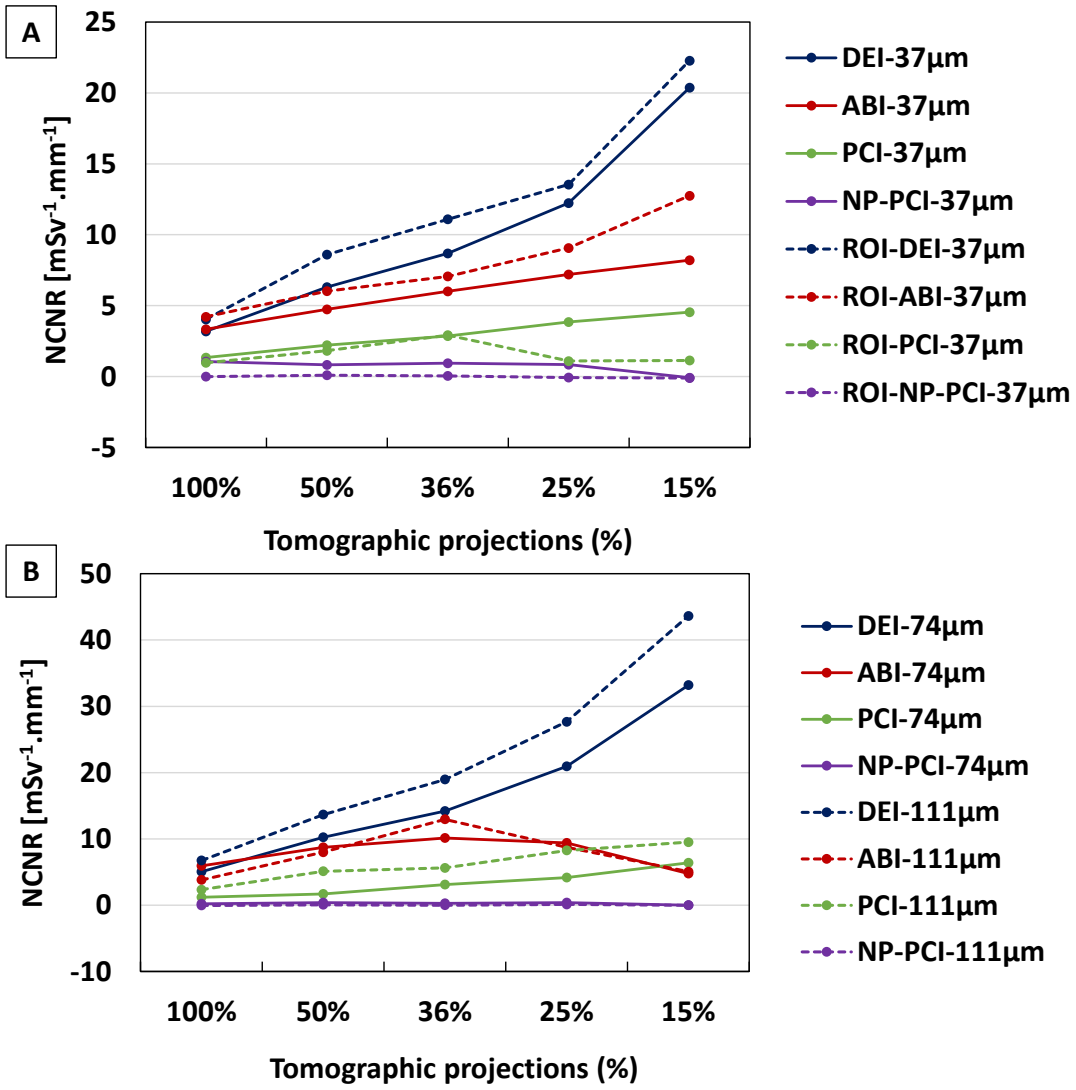

Figure 5.9 Quantitative comparison of low dose CT-DEI, CT-ABI, phase-retrieved extended-distance CT-PCI, and nonphase-retrieved extended-distance CT-PCI (NP-PCI) techniques. Comparison of normalized contrast to noise ratio (NCNR) for (A) reduced number of CT projections and region of interest (ROI) imaging, and (B) lower resolution imaging strategies at 100, 50, 36, 25, and 15% of the standard number of projections.

5.4.4 Imaging low density microstructural features using CT phase-based imaging

In addition to the implanted tissue scaffold, the phase-based imaging techniques investigated here revealed various other soft tissues and microstructural features present in the joint. CT-DEI and CT-ABI demonstrated similar visualization of these features at the standard setting and, as such, only DE and phase-retrieved extended-distance PC images are discussed further. The low density structural features are more readily detectable with a higher level of detail in DE axial and sagittal images than those in extended-distance PC images (Fig. 5.10). A video of 3D rendered DE images better shows such structural details [see Appendix B]. As described in the methodology, the beam height at the sample was smaller in the extended distance PCI than DEI and, as such, a smaller vertical view of the joint is seen in the sagittal plane of the PC image compared to that in the DE image. If a longer experimental X-ray hutch is available, the sample can be placed at the same location as in DEI (or even further away from the source) to illuminate a larger area of the object while maintaining the required long sample to detector distance.

Among the low density structures visualized in the CT-DE, CT-AB, and extended-distance CT-PC image stacks, the following features were identified and evaluated using the observer image quality assessments: perimeter of the created defect area, cartilage anatomy including its interfaces with surrounding tissues and in-cartilage vascular channels, fat tissue perimeters and its loose fibrous structure, perimeters of ligaments and tendons and their bundled fibrous structure, muscle tissue, distortion of tissue parenchyma caused during implantation procedure, strands of the surgery suture, and the covering periosteum patch (Fig. 10). Image quality scores associated with the visualization level of these features at standard and low dose imaging modes are given in (Table 5.4). In standard imaging mode, all three imaging techniques demonstrated high scores for visualization of different microstructural features. In low dose imaging modes, the difference between the techniques becomes more evident. Generally speaking, CT-DEI maintained higher IQSs than CT-ABI and extended-distance CT-PCI while CT-ABI had higher IQSs than extended-distance CT-PCI for visualizing low density structures (Table 5.4). In other words, applying the three strategies to lower the radiation dose had a more noticeable effect on the quality of extended-distance PC images than DE and AB images (Table 5.4). Visualization and characterization of subtle features, such as in-cartilage vascular channels or the covering periosteum patch, appear to be more affected by the low dose strategies than the

more obvious structures, such as cartilage, fat, and ligament tissues and some of their structural characteristics.

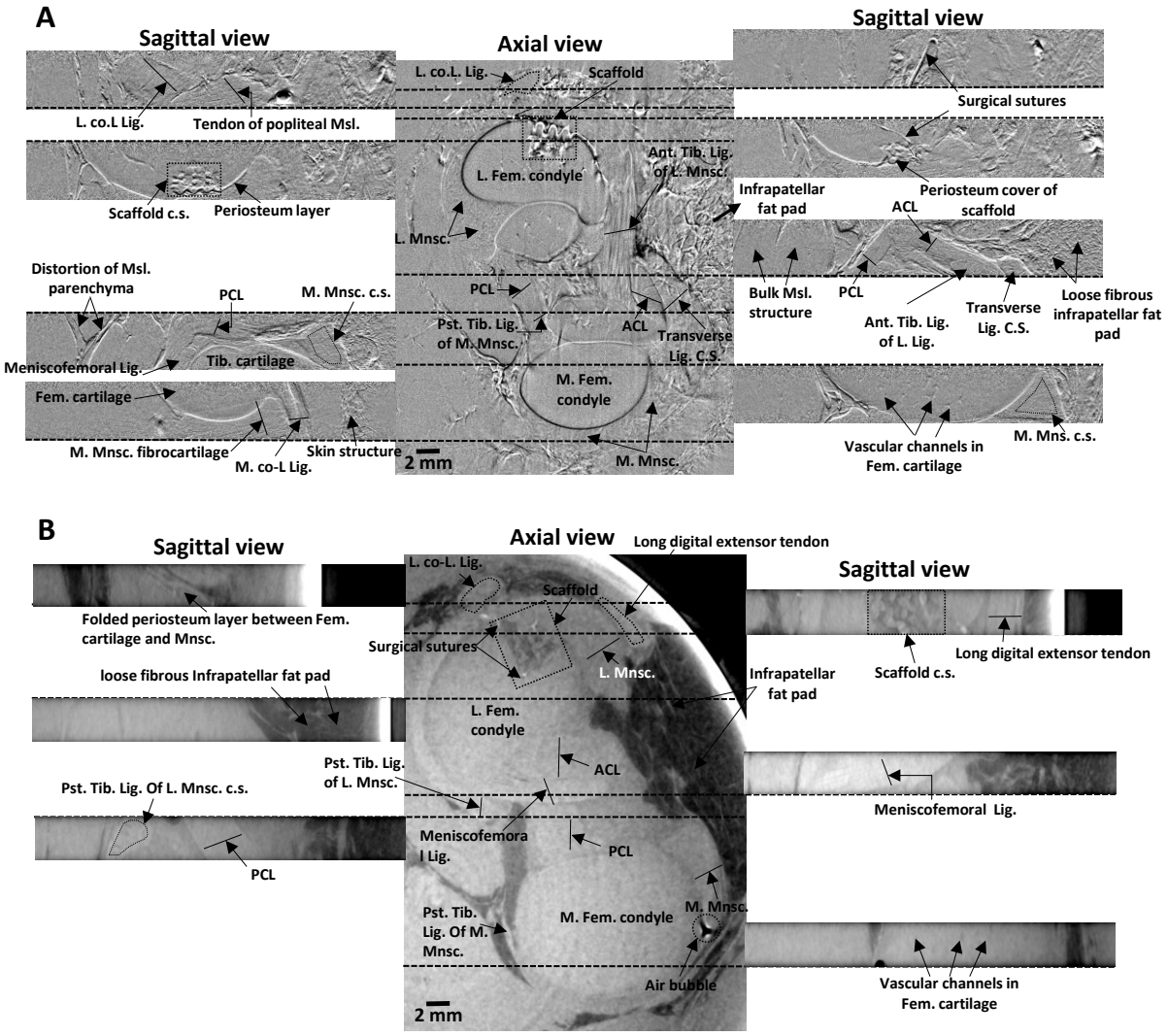

Figure 5.10 Visualization of different low density microstructural features in axial and sagittal views of 3D reconstructed (A) DE and (B) extended-distance phase-retrieved PC slices of the joint. L: lateral, co-L: collateral, M: medial, Ant: anterior, Pst: posterior, Fem: femoral, Tib: tibial, Lig: ligament, Msl: muscle, Mncs: meniscus, PCL: posterior cruciate ligament, ACL: anterior cruciate ligament, c.s.: cross section. Periosteum was used to cover the scaffold at the site of implantation. Anterior and posterior are equivalent to cranial and caudal locations, respectively, in animals.

Table 5.4 Image quality scoring for *in situ* visualization of soft microstructural features captured by the phase-based CT imaging with low-dose imaging strategies or in their combination.

Microstructural features	Cartilage defect perimeters	Cartilage anatomy/distinct interfaces	In-cartilage vascular channels	Fat tissue perimeters & internal structure	Ligament anatomy & internal structure	Muscle tissue perimeters	Distortion of tissue parenchyma	Surgery suture	Covering periosteum patch
CT-DEI (37 μm)									
100%	5	5	5	4	5	5	5	5	5
50%	4	4	4	4	4	4	4	4	4
36%	4	4	4	4	4	4	4	4	4
25%	4	4	4	4	4	4	4	4	4
15%	3	3	3	3	3	3	3	3	3
ROI CT-DEI (37 μm)									
100%	4	4	4	4	4	4	4	4	4
50%	4	4	4	4	4	4	4	4	4
36%	4	4	4	4	4	4	4	4	4
25%	4	4	3	3	4	4	4	4	4
15%	3	3	3	3	3	3	3	3	3
CT-DEI (74 μm)									
100%	4	4	4	4	4	4	4	4	4
50%	4	4	4	3	4	4	4	4	3
36%	3	4	4	3	4	3	3	3	2
25%	2	3	3	3	3	3	2	3	1
15%	2	3	2	3	3	2	1	3	1
CT-DEI (111 μm)									
100%	3	4	4	3	4	4	4	4	4
50%	3	4	3	3	3	3	3	3	3
36%	3	3	2	3	3	3	3	3	2
25%	2	3	2	3	2	2	2	2	1
15%	2	2	1	2	2	2	2	2	1
CT-ABI (37 μm)									
100%	4	5	4	4	5	4	4	5	4
50%	4	4	4	4	4	4	4	4	4
36%	4	4	4	3	4	4	4	4	4
25%	4	4	4	3	4	4	4	4	3
15%	3	3	3	2	3	3	3	3	3
ROI CT-ABI (37 μm)									
100%	4	4	4	3	4	4	4	4	4
50%	3	3	3	3	4	3	3	4	3
36%	3	3	3	3	3	3	3	4	3

25%	3	3	3	3	3	3	3	3	3
15%	2	2	2	2	2	2	2	2	2
CT-ABI (74 μm)									
100%	4	4	4	4	4	3	3	4	4
50%	4	3	3	3	3	3	3	4	4
36%	3	3	3	3	3	3	3	3	3
25%	2	3	2	2	2	2	2	3	2
15%	2	1	1	1	1	1	1	2	2
CT-ABI (111 μm)									
100%	4	4	3	3	3	3	3	4	4
50%	4	3	3	3	3	3	3	4	4
36%	3	3	2	3	2	2	2	3	2
25%	2	2	2	2	2	2	2	3	2
15%	2	1	1	1	1	1	1	2	2
Extended-distance CT-PCI (37 μm)									
100%	5	4	5	5	4	4	4	4	4
50%	4	4	4	4	4	4	4	3	3
36%	4	3	3	4	3	3	3	2	2
25%	3	2	2	3	2	2	2	2	2
15%	2	1	1	2	2	2	2	1	1
ROI Extended-distance CT-PCI (37 μm)									
100%	4	3	3	4	4	3	4	4	3
50%	4	3	3	4	3	3	4	3	3
36%	3	2	2	4	3	2	3	2	2
25%	3	2	2	3	2	2	3	2	2
15%	2	1	1	2	2	2	2	1	1
Extended-distance CT-PCI (74 μm)									
100%	4	3	3	4	3	3	3	3	3
50%	3	3	2	3	3	2	3	3	2
36%	3	2	2	3	3	2	3	2	2
25%	3	2	1	2	2	2	2	2	2
15%	2	1	1	2	2	2	2	1	1
Extended-distance CT-PCI (111 μm)									
100%	3	3	2	4	3	3	3	3	3
50%	3	3	2	3	3	2	3	3	2
36%	2	2	2	2	3	2	2	2	2
25%	1	1	1	2	2	2	2	2	2
15%	1	1	1	1	1	1	1	1	1

5.5 Discussion

This study shows the promise of CT-DEI, CT-ABI, and extended-distance PCI for *in situ* imaging of tissue scaffolds implanted in pig knee joints. Phase-based X-ray imaging techniques have great utility for soft tissue engineering and diagnosis applications, and being non-invasive and *in situ* make them particularly suitable for longitudinal live animal studies as well as for possible clinical translation to human trials. The imaging techniques examined in the present study produce image contrast based on the X-ray refractive properties of low absorbing materials albeit through relatively different mechanisms. In the PCI technique, the sample-to-detector propagation distance was found to be a critical factor for achieving desirable image contrast. A large propagation distance (~6 m) was shown to be essential for adequate phase contrast and visualization of structural features similar to DEI and ABI. Phase-retrieval processing of the PC images was also observed to be beneficial and preferable for visualization and interpretation of low density features.

Although the main features of interest, such as the tissue scaffold and surrounding soft tissues, were successfully imaged in all three systems investigated, some differences were observed among the reconstructed images. Higher sensitivity of DEI and ABI in imaging small structural features, as compared to extended-distance PCI, could be employed to assess details of tissue repair processes, such as evaluating the quality of tissue construct integration and/or interaction with host tissues. In order to achieve a similar level of details, extended-distance PCI requires imaging at higher spatial resolutions, which increases the exposure time, scan time, and delivered radiation dose. On the other hand, the capability of extended-distance PCI to visualize the difference in the density of bulk materials is particularly applicable to monitoring new cartilage tissue formation by assessing its bulk resemblance to natural healthy cartilage tissue during the repair process. The contrast in extended-distance PC images constitutes of both phase and attenuation signals. Therefore, the interface of low density structures and tissues (from the phase component) as well as the bulk density difference of various materials (from the absorption component) could be visualized. This is an advantage when both types of information are of interest for tissue repair assessment. Although the contrast in ABI is also obtained from both refraction and absorption signals, the change in material bulk density is not as clear as in extended-distance PCI (Fig. 5.2B and C). This may be due to the higher intensity of the refraction signal that conceals the absorption signal in the images.

The DEI and PCI techniques also offer the potential for quantitative tissue engineering assessment. The X-ray refractive index decrement (α) is a material-specific property that can be extracted from phase-based images and used as a characterization parameter for soft tissues and engineered constructs. In DEI, the refraction image gives the refraction angle ($\Delta\theta_Z$) that arises from gradients of the thickness and/or density of different materials and structures, which, if employed along with the geometrical information of the features, can return the refractive index of distinct materials. In PCI, the pure phase image that returns the specific refractive indices of materials can be obtained by performing inline PCI at two or more propagation distances, and then using consecutive phase retrieval analysis to obtain pure phase images with extracted refractive indices [52, 61]. Although feasible, this technique is not very practical for live animal imaging. Collecting projection images at shorter exposure time may be a possible solution to address the increased scan time and radiation dose. However, in case of live animal imaging where the propagation distance is adjusted by moving the anesthetized animal rather than the detector, the application of multiple distance PC imaging becomes risky due to potential complications from animal motion. This issue and increased noise to contrast ratio at shorter exposure times make multiple distance PCI less practical for live animal imaging compared to DEI and ABI. In this case, DEI is preferable over PCI because with a comparable total does it requires two sets of scans, during which the location of the object is not changed.

To identify the most suitable imaging technique(s) for applications to longitudinal live animal studies, factors that influence the practicality and safety of the techniques should be evaluated in addition to the quality and level of information obtained. These factors include the total delivered dose, the rate at which the dose was delivered, imaging scan time, and the ease of performing the imaging technique on a living object. Standard CT-ABI delivered an effective radiation dose (17.2 mSv) within the range delivered in a clinical abdomen or pelvic CT scan (10-20 mSv [62]), while the effective radiation doses delivered by standard CT-DEI (34.5 mSv) and extended-distance CT-PCI (30.1 mSv) were slightly higher than that conventionally delivered in a clinical PET/CT scan (25 mSv [62]). However, the report of International Commission on Radiological Protection (ICRP) [59] indicates absorbed doses up to ~100 mSv are low radiation doses at which no tissues show clinically relevant functional deterioration [63]. Furthermore, the available literature and clinical experience with radiation therapy show that normal tissues exhibit tolerance to much larger radiation doses. For example, bone,

temporomandibular joints, and skin tissues have demonstrated total dose tolerance of up to 52, 65, and 55-70 Gy, respectively, if irradiated over a 4-10 cm^2 area [64]. With a tissue weighting factor of 0.01 for bone and skin tissues [59], the effective tolerance dose would be 520, 650, and 550-700 mSv for bone, temporomandibular joint, and skin, respectively. This is in agreement with the annual dose limit suggested by the ICRP, i.e. 500 mSv, for skin, hands, and feet [63]. Radiation dose is conventionally fractionated and delivered in bearable portions of 1.8-5 Gy (18-50 mSv equivalent dose) per day of treatment [64, 65]. These reported tolerance doses are based on the standard probability of 5% complications within five years after treatment [66]. Overall, the total doses delivered by phase-based CT imaging techniques at standard settings (2500 tomographic projections at 37 μm resolution) do not appear to be largely concerning or impractical, particularly for live animal *in vivo* studies. Nevertheless, the minimally possible radiation dose from these systems is always preferred and encouraged for live object imaging.

The measured dose rates for CT-DEI and CT-ABI (0.2 mGy/s) and extended-distance PCI (6.43 mGy/s) were in a range similar to that delivered during conventional clinical radiation therapy. Depending on the size of the target area, therapy radiation doses are delivered at a rate between 0.27 and 25 mGy/s [67]. Therefore, the dose rate associated with the phase-based imaging techniques in this study appears to be practical for live animal imaging. DEI and extended-distance PCI delivered a comparable total dose; however, the dose rate was >30× larger in extended-distance PCI than with DEI and ABI due to the different monochromator reflection plane used in the PCI system. The Si (4,4,0) planes used in DEI and ABI have a small reflection bandwidth that reduces the X-ray photon flux and results in a smaller dose rate. In extended-distance PCI, the Si (2,2,0) plane is used to gain a higher photon flux and shorter scan time through wider reflection bandwidth, which results in a larger dose rate. If a smaller dose rate comparable to that of DEI is of interest for extended-distance PCI, Si (4,4,0) or an alternative reflection plane can simply be adopted; however, this comes at the cost of increased scan time. For instance, using Si (4,4,0) in extended-distance PCI instead of Si (2,2,0) increases the scan time from 7.8 to 83 min. The use of Si (4,4,0) in DEI and ABI was necessary to increase the sensitivity ~~to~~ of the contrast mechanism, which is not the case for the extended-distance PCI technique.

Among the three imaging techniques examined, extended-distance CT-PCI had the shortest scan time (<10 min), which was 37 times shorter than CT-DEI and 19 times shorter than

CT-ABI. Faster imaging is highly preferred for practical implementation and clinical translation of techniques for live animal or possible human applications. Moreover, extended-distance PCI benefits from a simple imaging setup comparable to conventional clinical radiography, while CT-DEI and CT-ABI require more technical apparatus. The less demanding extended-distance PCI system makes it a more user-friendly technique with easier translation to clinical X-ray sources. The CT-DEI technique requires two sets of CT scans during which the object must remain still with negligible to no movement to perfectly align the two sets of CT scans for obtaining the refraction image. Maintaining the position of a live object throughout the scan time could be practically challenging, although the use of an anesthetic may alleviate such concerns. Such motion sensitivity is considerably reduced in the CT-ABI technique by collecting only one set of CT scan data. Nevertheless, the long scan time in both standard CT-DEI and CT-ABI increases the chance of motion artifact production in the images and also imposes discomfort to the living object being imaged. One approach to reducing the scan time is to use a higher photon flux X-ray source, such as a synchrotron wiggler insertion device [68]. The associated higher flux can reduce the scan time by up to 25 times compared to a bend magnet X-ray source (to <12 and <6 min for CT-DEI and CT-ABI, respectively). This can make the methods more efficient and practical for live object imaging. Overall, extended-distance CT-PCI may be more readily implementable to live animal imaging at standard CT scan settings. However, standard CT-DEI and CT-ABI could also be adapted for practical live animal imaging with improved X-ray sources.

As discussed earlier, the radiation doses delivered by standard CT-DEI, CT-ABI, and extended-distance CT-PCI were in a feasible dose range; however, ICRP [59] requires consideration of effective dose reduction to 20-100 mSv [63]. The common dose range of 0.001 to 25 mSv for clinical X-ray scans has been associated with negligible to moderate risk levels [62]. The dose of the phase-based imaging methods investigated here (17-34.5 mSv) is associated with the low to upper end of the moderate risk level. To implement these imaging techniques in live animal studies and possible human trials, action must be further taken to reduce the dose. The low dose imaging strategies investigated in this study successfully reduced the radiation doses to a risk level of low (10 mSv) to very low (0.3 mSv), which is comparable to most clinical X-ray scans [62] while largely preserving the quality and information in the images obtained. By applying the low dose imaging strategies, the impractically-long scan times for CT-

DEI and CT-ABI were reduced to a range from 5-10 mins to <1 h, which is realistic for anesthetized live animals. At the settings with the scan time less than 5 min, imaging human patients may also become possible.

Among the three low dose strategies investigated, reducing the number of projections and imaging at lower resolution (111 μm pixel size) were shown to be the most effective. These approaches reduced the delivered dose and scan time up to 7 and 9 times, respectively, over standard CT-DEI, CT-ABI, and extended-distance CT-PCI. The advantage of these approaches is the preservation of contrast and image information despite a significant reduction in image resolution and the number of tomographic projections. Although low resolution imaging (74 μm pixel size) and ROI imaging strategies also reduced the dose and scan time, their combination with reduced number of projections achieved reductions in dose and scan time to suitably low levels. In all three phase-based imaging techniques, dose and scan time were reduced up to 10 times when ROI imaging was performed using 15% of the standard number of CT projections. The dose and scan time were also reduced up to 15 and 35 times when CT scans were performed using 25% of the number of standard projections at 74 μm and 111 μm image pixel sizes. Although ROI imaging was the smallest contributor to decreasing radiation dose, it could become more effective when relatively-large objects are being imaged and/or if reducing the dose and scan time to a minimally reasonable level is critical or preferred, such as in human imaging. Depending on the features-of-interest in the samples and the technique used, another strategy to further reduce the radiation dose can be decreasing the projection exposure time. By reducing the projection exposure time to half in the CT-DEI technique, for example, the delivered dose can be reduced by 50%. This strategy was simulated in CT-DEI technique by reducing the gray value by 50% in the originally-collected images in CT-DEI-15% projections (as the DEI technique showed the highest performance among the others in visualizing scaffold at the 15% projection condition (Fig. 5.4)). Comparison of the reconstructed slices from half-exposure DEI to that from standard DEI at 15% of projections showed that the image correlation is almost in the same level as that for the case of full exposure time. This shows that in the case of CT-DEI technique, reduction of the projection exposure time may be feasible for further dose reduction.

The low dose imaging strategies were most compatible and effective for the CT-DEI technique. The strong refraction contrast signal combined with the scatter-free characteristic of

DEI made it the most resistant method to impaired signal contrast when low dose strategies were applied. This particular feature makes CT-DEI a superior technique for high quality and detailed assessment imaging with reasonably low and practical radiation doses. The lack of such a mechanism in extended-distance CT-PCI led to greater deterioration of the image quality because background noise increased as the number of tomographic projections and image resolution decreased. This might be addressed by increasing the sample-to-detector propagation distance to increase the intensity of the phase-contrast fringes and compensate for the increased background noise. However, there is a limit to this approach depending on the properties of the employed imaging station. In BMIT-BM beamline with the vertical and horizontal source sizes (σ) of 51 and 173 μm, respectively, and source to sample distance of 21 m, workable propagation distance in PCI at 40 keV is limited by the detector resolution and penumbral blurring effect. The most suitable propagation length for PCI at 40 keV and 37 μm resolution in BMIT-BM end-station was found to be in the range of 4.6 to 6 m, based on the method descried in [49]. Beyond this range the penumbral blurring effect increasingly dominates the phase fringe width at the detector. The given suitable range is associated with the Frensel regime zone of the X-ray wave front that gives rise to edge contrast in the phase image and followed by the Fraunhofer regime zone where the phase-contrast fringes become blurred and image quality is impaired. Since the suitable range for PCI propagation distance is dependent on the properties of imaging end-station and setup, it is suggested that the workable propagation distance be calculated for different X-ray sources and imaging setups. Where longer propagation distance is an option for an imaging end-station, it would be interesting to discover the influence of longer propagation distance on the background noise increased by applying the low dose strategies.

5.6 Conclusions

In this study, synchrotron phase-based X-ray imaging techniques of CT-DEI, CT-ABI, and extended-distance CT-PCI have been demonstrated promising for visualizing low density scaffolds and soft tissues *in situ*, thus will facilitate applications to longitudinal non-invasive tissue engineering assessments in *in vivo* animal studies. Low-dose imaging strategies of decreasing the number of CT projections, region of interest, and low resolution imaging were examined and illustrated effective for reducing the radiation dose and scan time without considerable loss of the image quality, owing to the strong image contrast from the synchrotron phase-based X-ray imaging techniques. The low-dose imaging strategies reduced the radiation

does and scan time to the levels comparable to clinical CT scans and practical for longitudinal live animal studies. Compared to other examined techniques, CT-DEI exhibited the highest performance and dose efficiency in low-dose imaging. The reduced number of CT projections and low resolution imaging were observed to be more effective than other strategy in reducing the imaging dose.

5.7 References

1. Kotecha, M.; Klatt, D.; Magin, R.L. Monitoring cartilage tissue engineering using magnetic resonance spectroscopy, imaging, and elastography. *Tissue Eng Part B Rev* **2013**, 19, 470-484.
2. Kwack, K.S.; Cho, J.H.; Kim, M.M.; Yoon, C.S.; Yoon, Y.S.; Choi, J.W.; Kwon, J.W.; Min, B.H.; Sun, J.S.; Kim, S.Y. Comparison study of intraarticular and intravenous gadolinium-enhanced magnetic resonance imaging of cartilage in a canine model. *Acta Radiol* **2008**, 49, 65-74.
3. Izadifar, Z.; Chapman, L.D.; Chen, X. Computed tomography diffraction-enhanced imaging for in situ visualization of tissue scaffolds implanted in cartilage. *Tissue Eng Part C Methods* **2014**, 20, 140-148.
4. Chapman, D.; Thomlinson, W.; Johnston, R.E.; Washburn, D.; Pisano, E.; Gmur, N.; Zhong, Z.; Menk, R.; Arfelli, F.; Sayers, D. Diffraction enhanced x-ray imaging. *Phys Med Biol* **1997**, 42, 2015-2025.
5. Momose, A.; Fukuda, J. Phase-contrast radiographs of nonstained rat cerebellar specimen. *Med Phys* **1995**, 22, 375-379.
6. Momose, A.; Takeda, T.; Itai, Y.; Hirano, K. Phase-contrast X-ray computed tomography for observing biological soft tissues. *Nat Med* **1996**, 2, 473-475.
7. Snigirev, A.; Snigireva, I.; Kohn, V.; Kuznetsov, S.; Schelokov, I. On the possibilities of x-ray phase contrast microimaging by coherent high-energy synchrotron radiation. *Rev Sci Instrum* **1995**, 66, 5486-5492.
8. Lin, X.; Miao, P.; Mu, Z.; Jiang, Z.; Lu, Y.; Guan, Y.; Chen, X.; Xiao, T.; Wang, Y.; Yang, G.Y. Development of functional in vivo imaging of cerebral lenticulostriate artery using novel synchrotron radiation angiography. *Phys Med Biol* **2015**, 60, 1655-1665.
9. Huang, S.; Kou, B.; Chi, Y.; Xi, Y.; Cao, Y.; Cui, W.; Hu, X.; Shao, Z.; Guo, H.; Fu, Y.; Xiao, T.; Sun, J.; Zhao, J.; Wang, Y.; Wu, J. In-line phase-contrast and grating-based phase-contrast synchrotron imaging study of brain micrometastasis of breast cancer. *Sci Rep* **2015**, 5, 9418.
10. Luan, X.; Campanucci, V.A.; Nair, M.; Yilmaz, O.; Belev, G.; Machen, T.E.; Chapman, D.; Ianowski, J.P. Pseudomonas aeruginosa triggers CFTR-mediated airway surface liquid secretion in swine trachea. *Proc Natl Acad Sci U S A* **2014**, 111, 12930-12935.
11. Muehleman, C.; Li, J.; Zhong, Z. Preliminary study on diffraction enhanced radiographic imaging for a canine model of cartilage damage. *Osteoarthritis Cartilage* **2006**, 14, 882-888.
12. Muehleman, C.; Majumdar, S.; Issever, A.S.; Arfelli, F.; Menk, R.H.; Rigon, L.; Heitner, G.; Reime, B.; Metge, J.; Wagner, A.; Kuettner, K.E.; Mollenhauer, J. X-ray detection of structural orientation in human articular cartilage. *Osteoarthritis Cartilage* **2004**, 12, 97-105.
13. Dreossi, D.; Abrami, A.; Arfelli, F.; Bregant, P.; Casarin, K.; Chenda, V.; Cova, M.A.; Longo, R.; Menk, R.H.; Quai, E.; Quaia, E.; Rigon, L.; Rokvic, T.; Sanabor, D.; Tonutti, M.; Tromba, G.; Vascotto, A.; Zanconati, F.; Castelli, E. The mammography project at the SYRMEP beamline. *European journal of radiology* **2008**, 68, S58-62.
14. Quai, E.; Longo, R.; Zanconati, F.; Jaconelli, G.; Tonutti, M.; Abrami, A.; Arfelli, F.; Dreossi, D.; Tromba, G.; Cova, M.A. First application of computed radiology to mammography with synchrotron radiation. *La Radiologia medica* **2013**, 118, 89-100.

15. Appel, A.A.; Larson, J.C.; Garson, A.B., 3rd; Guan, H.; Zhong, Z.; Nguyen, B.N.; Fisher, J.P.; Anastasio, M.A.; Brey, E.M. X-ray phase contrast imaging of calcified tissue and biomaterial structure in bioreactor engineered tissues. *Biotechnol Bioeng* **2015**, 112, 612-620.
16. Zhu, N.; Chapman, D.; Cooper, D.; Schreyer, D.J.; Chen, X. X-ray diffraction enhanced imaging as a novel method to visualize low-density scaffolds in soft tissue engineering. *Tissue Eng Part C Methods* **2011**, 17, 1071-1080.
17. Lewis, R.; Hall, C.; Hufton, A.P.; Evans, S.; Menk, R.; Arfelli, F.; Rigon, L.; Tromba, G.; Dance, D.; Ellis, I. X-ray refraction effects: application to the imaging of biological tissues. *The British journal of radiology* **2014**.
18. Lewis, R. Medical phase contrast x-ray imaging: current status and future prospects. *Physics in medicine and biology* **2004**, 49, 3573.
19. Zhang, L.; Luo, S. Micro Soft Tissues Visualization Based on X-Ray Phase-Contrast Imaging. *The Open Medical Informatics Journal* **2011**, 5, 19-25.
20. Horng, A.; Brun, E.; Mittone, A.; Gasilov, S.; Weber, L.; Geith, T.; Adam-Neumair, S.; Auweter, S.D.; Bravin, A.; Reiser, M.F.; Coan, P. Cartilage and soft tissue imaging using X-rays: propagation-based phase-contrast computed tomography of the human knee in comparison with clinical imaging techniques and histology. *Invest Radiol* **2014**, 49, 627-634.
21. Olubamiji, A.D.; Izadifar, Z.; Chen, D.X. Synchrotron imaging techniques for bone and cartilage tissue engineering: potential, current trends, and future directions. *Tissue Eng Part B Rev* **2014**, 20, 503-522.
22. Muehleman, C.; Zhong, Z.; Williams, J.M.; Kuettner, K.E.; Aurich, M.; Han, B.; Mollenhauer, J.; Chapman, L.D. Diffraction enhanced X-ray imaging of the articular cartilage of experimental animals In *Annual Meeting Orthopaedic Research Society*. Dallas, TX. USA. 2002.
23. Mollenhauer, J.; Aurich, M.E.; Zhong, Z.; Muehleman, C.; Cole, A.A.; Hasnah, M.; Oltulu, O.; Kuettner, K.E.; Margulis, A.; Chapman, L.D. Diffraction-enhanced X-ray imaging of articular cartilage. *Osteoarthritis Cartilage* **2002**, 10, 163-171.
24. Li, J.; Zhong, Z.; Connor, D.; Mollenhauer, J.; Muehleman, C. Phase-sensitive X-ray imaging of synovial joints. *Osteoarthritis and Cartilage* **2009**, 17, 1193-1196.
25. Coan, P.; Wagner, A.; Bravin, A.; Diemoz, P.C.; Keyriläinen, J.; Mollenhauer, J. In vivo x-ray phase contrast analyzer-based imaging for longitudinal osteoarthritis studies in guinea pigs. *Phys Med Biol* **2010**, 55, 7649.
26. Langer, M.; Cloetens, P.; Hesse, B.; Pacureanu, A.; Raum, K.; Lafage-Proust, M.; Peyrin, F. Propagation based X-ray phase microtomography of multi-material objects for simultaneous bone and soft tissue visualisation. In *Biomedical Imaging (ISBI), 2012 9th IEEE International Symposium on*. IEEE. 2012.
27. Zehbe, R.; Haibel, A.; Riesemeier, H.; Gross, U.; Kirkpatrick, C.J.; Schubert, H.; Brochhausen, C. Going beyond histology. Synchrotron micro-computed tomography as a methodology for biological tissue characterization: from tissue morphology to individual cells. *J R Soc Interface* **2010**, 7, 49-59.
28. Zehbe, R.; Haibel, A.; Brochhausen, C.; Gross, U.; Kirkpatrick, C.J.; Schubert, H. Characterization of oriented protein-ceramic and protein-polymer-composites for cartilage tissue engineering using synchrotron μ-CT. *Int J Mater Res* **2007**, 98, 562-568.

29. Zehbe, R.; Goebbels, J.; Ibold, Y.; Gross, U.; Schubert, H. Three-dimensional visualization of in vitro cultivated chondrocytes inside porous gelatine scaffolds: a tomographic approach. *Acta biomater* **2010**, 6, 2097-2107.
30. Appel, A.A.; Larson, J.C.; Somo, S.; Zhong, Z.; Spicer, P.P.; Kasper, F.K.; Garson, A.B., 3rd; Zysk, A.M.; Mikos, A.G.; Anastasio, M.A.; Brey, E.M. Imaging of poly(alpha-hydroxy-ester) scaffolds with X-ray phase-contrast microcomputed tomography. *Tissue Eng Part C Methods* **2012**, 18, 859-865.
31. Hagen, C.K.; Munro, P.R.; Endrizzi, M.; Diemoz, P.C.; Olivo, A. Low-dose phase contrast tomography with conventional x-ray sources. *Med Phys* **2014**, 41, 070701.
32. Hagen, C.K.; Diemoz, P.C.; Endrizzi, M.; Rigon, L.; Dreossi, D.; Arfelli, F.; Lopez, F.C.; Longo, R.; Olivo, A. Theory and preliminary experimental verification of quantitative edge illumination x-ray phase contrast tomography. *Opt Express* **2014**, 22, 7989-8000.
33. Diemoz, P.C.; Vittoria, F.A.; Hagen, C.K.; Endrizzi, M.; Coan, P.; Brun, E.; Wagner, U.H.; Rau, C.; Robinson, I.K.; Bravin, A.; Olivo, A. Single-image phase retrieval using an edge illumination X-ray phase-contrast imaging setup. *J Synchrotron Radiat* **2015**, 22, 1072-1077.
34. Pelliccia, D.; Vaz, R.; Svalbe, I.; Morgan, K.S.; Marathe, S.; Xiao, X.; Assoufid, L.; Anderson, R.A.; Topczewski, J.; Bryson-Richardson, R.J. Comparison of different numerical treatments for x-ray phase tomography of soft tissue from differential phase projections. *Phys Med Biol* **2015**, 60, 3065-3080.
35. Herzen, J.; Willner, M.S.; Fingerle, A.A.; Noel, P.B.; Kohler, T.; Drecoll, E.; Rummeny, E.J.; Pfeiffer, F. Imaging liver lesions using grating-based phase-contrast computed tomography with bi-lateral filter post-processing. *PloS one* **2014**, 9, e83369.
36. Grandl, S.; Willner, M.; Herzen, J.; Sztrokay-Gaul, A.; Mayr, D.; Auweter, S.D.; Hipp, A.; Birnbacher, L.; Marschner, M.; Chabior, M.; Reiser, M.; Pfeiffer, F.; Bamberg, F.; Hellerhoff, K. Visualizing typical features of breast fibroadenomas using phase-contrast CT: an ex-vivo study. *PloS one* **2014**, 9, e97101.
37. Noel, P.B.; Herzen, J.; Fingerle, A.A.; Willner, M.; Stockmar, M.K.; Hahn, D.; Settles, M.; Drecoll, E.; Zanette, I.; Weitkamp, T.; Rummeny, E.J.; Pfeiffer, F. Evaluation of the potential of phase-contrast computed tomography for improved visualization of cancerous human liver tissue. *Zeitschrift fur medizinische Physik* **2013**, 23, 204-211.
38. Hetterich, H.; Fill, S.; Herzen, J.; Willner, M.; Zanette, I.; Weitkamp, T.; Rack, A.; Schuller, U.; Sadeghi, M.; Brandl, R.; Adam-Neumair, S.; Reiser, M.; Pfeiffer, F.; Bamberg, F.; Saam, T. Grating-based X-ray phase-contrast tomography of atherosclerotic plaque at high photon energies. *Zeitschrift fur medizinische Physik* **2013**, 23, 194-203.
39. Sarapata, A.; Chabior, M.; Cozzini, C.; Sperl, J.I.; Bequé, D.; Langner, O.; Coman, J.; Zanette, I.; Ruiz-Yaniz, M.; Pfeiffer, F. Quantitative electron density characterization of soft tissue substitute plastic materials using grating-based x-ray phase-contrast imaging. *Review of Scientific Instruments* **2014**, 85, 103708.
40. Sarapata, A.; Stayman, J.W.; Finkenthal, M.; Siewerdsen, J.H.; Pfeiffer, F.; Stutman, D. High energy x-ray phase contrast CT using glancing-angle grating interferometers. *Med Phys* **2014**, 41, 021904.
41. Wang, Z.; Stampanoni, M. Quantitative x-ray radiography using grating interferometry: a feasibility study. *Phys Med Biol* **2013**, 58, 6815-6826.

42. Szafraniec, M.B.; Millard, T.P.; Ignatyev, K.; Speller, R.D.; Olivo, A. Proof-of-concept demonstration of edge-illumination x-ray phase contrast imaging combined with tomosynthesis. *Phys Med Biol* **2014**, 59, N1-10.
43. Pacile, S.; Brun, F.; Dullin, C.; Nesterest, Y.I.; Dreossi, D.; Mohammadi, S.; Tonutti, M.; Stacul, F.; Lockie, D.; Zanconati, F.; Accardo, A.; Tromba, G.; Gureyev, T.E. Clinical application of low-dose phase contrast breast CT: methods for the optimization of the reconstruction workflow. *Biomedical optics express* **2015**, 6, 3099-3112.
44. Mirone, A.; Brun, E.; Coan, P. A dictionary learning approach with overlap for the low dose computed tomography reconstruction and its vectorial application to differential phase tomography. *PloS one* **2014**, 9, e114325.
45. Zhou, T.; Lundström, U.; Larsson, D.H.; Hertz, H.M.; Burvall, A. Low-dose phase-contrast X-ray imaging: a comparison of two methods. In *Journal of Physics: Conference Series*. IOP Publishing. 2013.
46. Chang, C.-H.; Lin, F.-H.; Kuo, T.-F.; Liu, H.-C. Cartilage tissue engineering. *Biomed Eng (Singapore)* **2005**, 17, 61-71.
47. Wysokinski, T.W.; Chapman, D.; Adams, G.; Renier, M.; Suortti, P.; Thomlinson, W. Beamlines of the biomedical imaging and therapy facility at the Canadian light source—Part 1. *Nucl Instrum Methods Phys Res A* **2007**, 582, 73-76.
48. Bartels, M., *Cone-beam x-ray phase contrast tomography of biological samples: Optimization of contrast, resolution and field of view*. Vol. 13. 2013: Universitätsverlag Göttingen.
49. Nesterets, Y.I.; Wilkins, S.W.; Gureyev, T.E.; Pogany, A.; Stevenson, A.W. On the optimization of experimental parameters for x-ray in-line phase-contrast imaging. *Review of Scientific Instruments* **2005**, 76, 093706.
50. Suortti, P.; Thomlinson, W. Medical applications of synchrotron radiation. *Phys Med Biol* **2003**, 48, R1-35.
51. Nugent, K.A.; Gureyev, T.E.; Cookson, D.J.; Paganin, D.; Barnea, Z. Quantitative Phase Imaging Using Hard X Rays. *Phys Rev Lett* **1996**, 77, 2961-2964.
52. Cloetens, P.; Ludwig, W.; Baruchel, J.; Van Dyck, D.; Van Landuyt, J.; Guigay, J.P.; Schlenker, M. Holotomography: Quantitative phase tomography with micrometer resolution using hard synchrotron radiation x rays. *Appl Phys Lett* **1999**, 75, 2912-2914.
53. Chen, R.C.; Dreossi, D.; Mancini, L.; Menk, R.; Rigon, L.; Xiao, T.Q.; Longo, R. PITRE: software for phase-sensitive X-ray image processing and tomography reconstruction. *J Synchrotron Radiat* **2012**, 19, 836-845.
54. Gureyev, T.E.; Davis, T.J.; Pogany, A.; Mayo, S.C.; Wilkins, S.W. Optical phase retrieval by use of first Born- and Rytov-type approximations. *Appl Opt* **2004**, 43, 2418-2430.
55. Paganin, D.; Mayo, S.C.; Gureyev, T.E.; Miller, P.R.; Wilkins, S.W. Simultaneous phase and amplitude extraction from a single defocused image of a homogeneous object. *J Microsc* **2002**, 206, 33-40.
56. Wu, X.; Liu, H.; Yan, A. X-ray phase-attenuation duality and phase retrieval. *Opt Lett* **2005**, 30, 379-381.
57. Gureyev, T.E.; Nesterets, Y.; Ternovski, D.; Thompson, D.; Wilkins, S.W.; Stevenson, A.W.; Sakellariou, A.; Taylor, J.A. Toolbox for advanced x-ray image processing. In *SPIE 8141, Advances in Computational Methods for X-Ray Optics II*. San Diego, California, USA. 2011.

58. United States Nuclear Regulatory Commission (U.S.NRC). *Shallow-Dose Equivalent (SDE)*. 2015 [cited 2015 June 28]; Available from: http://www.nrc.gov/reading-rm/basic-ref/glossary/shallow-dose-equivalent-sde.html.
59. The 2007 Recommendations of the International Commission on Radiological Protection. ICRP publication 103. *Ann ICRP* **2007**, 37, 1-332.
60. Chinga, G.; Syverud, K. Quantification of paper mass distributions within local picking areas. *Nord Pulp Paper Res J* **2007**, 22, 441-446.
61. Ren, Y.; Chen, C.; Chen, R.; Zhou, G.; Wang, Y.; Xiao, T. Optimization of image recording distances for quantitative X-ray in-line phase contrast imaging. *Opt Express* **2011**, 19, 4170-4181.
62. Radiological Society of North America (RSNA). *Radiation Dose in X-Ray and CT Exams*. 2015 [cited 2015 June 28]; Available from: http://www.radiologyinfo.org/en/safety/?pg=sfty_xray.
63. Wrixon, A.D. New ICRP recommendations. *J Radiol Prot* **2008**, 28, 161-168.
64. Emami, B.; Lyman, J.; Brown, A.; Coia, L.; Goitein, M.; Munzenrider, J.E.; Shank, B.; Solin, L.J.; Wesson, M. Tolerance of normal tissue to therapeutic irradiation. *Int J Radiat Oncol Biol Phys* **1991**, 21, 109-122.
65. Barendsen, G.W. Dose fractionation, dose rate and iso-effect relationships for normal tissue responses. *Int J Radiat Oncol Biol Phys* **1982**, 8, 1981-1997.
66. Rubin, P.; Casarett, G. A Direction for Clinical Radiation Pathology:The Tolerance Dose. In *6th Annual San Francisco Cancer Symposium*. San Francisco, Calif.: Basel, Karger, and University Park Press. 1972.
67. Steel, G.G.; Deacon, J.M.; Duchesne, G.M.; Horwich, A.; Kelland, L.R.; Peacock, J.H. The dose-rate effect in human tumour cells. *Radiother Oncol* **1987**, 9, 299-310.
68. Wysokinski, T.W.; Chapman, D.; Adams, G.; Renier, M.; Suortti, P.; Thomlinson, W. Beamlines of the biomedical imaging and therapy facility at the Canadian light source–part 3. *Nuclear Instruments and Methods in Physics Research Section A: Accelerators, Spectrometers, Detectors and Associated Equipment* **2015**, 775, 1-4.

CHAPTER 6: CONCLUSIONS AND FURTHER RESEARCH

6.1 Conclusions

This research was aimed at addressing two key issues: hybrid-construct bioprinting and synchrotron-based non-invasive assessment for cartilage tissue engineering. Hybrid constructs with solid polymeric and hydrogels components are promising for use in cartilage repair as they can provide both biological and biomechanical properties as desired. Fabrication of such hybrid constructs is, however, still in its infancy due to the issues related to the structural integrity and the functions of cells incorporated in the constructs. One aim of this thesis was to address these issues by developing 3D printing biofabrication processes that uses cytocompatible melted-polymer and soft, low concentration hydrogel for making hybrid cartilage tissue constructs with physically stable and biologically conducive properties. Development of such suitable fabrication processes make it possible to develop constructs with synergistic properties without compromising physical and structural fidelity for biological functionality.

Synchrotron phase-based X-ray imaging techniques rely on X-ray refraction properties of materials, rather than their absorption, for producing image contrast. As such, these techniques have shown great promises in imaging soft tissues and biological microstructures *in situ*. With the high penetration depth of X-rays, these methods are promising candidates for non-invasive soft tissue engineering monitoring and assessments, thus enabling the longitudinal evaluation of animal models and even human patients throughout the repair process without the need to scarify the animal and interrupt the repair process. The other aim of this research was to explore various phase-based X-ray imaging techniques for developing non-invasive methods appropriate for *in situ* assessments of scaffold-based cartilage and soft tissue engineering strategies.

Followings are the main conclusions drawn from this research:

1. The 3D printing-based biofabrication process is able to fabricate hybrid cartilage tissue constructs with two complementary structural components of solid framework and hydrogel matrix, similar to biphasic nature of cartilage tissue, thus providing both mechanical and biological supports for the impregnated cells during tissue regeneration.
2. The materials properties of both PCL polymer and alginate hydrogel as well as the processing conditions (such as dispensing temperatures) were illustrated critical for

maintaining the structural integrity and cell functions of the hybrid constructs, and if properly determined they enable a cytocompatible hybrid 3D-pritning process that preserves cell functions and maintains the structural integrity of the constructs throughout the fabrications.

3. The hybrid constructs developed in this research are able to provide the conducive environment for promising biological activities (viability, proliferation, and cartilage ECM secretion) of cells during long-term tissue regeneration process *in vitro*.
4. The phased-based X-ray imaging techniques of CT-DEI, CT-ABI, and extended-distance CT-PCI have been shown suitable for *in situ* imaging and characterization of low density cartilage tissues constructs, moreover with better performance than clinical gold standard MRI technique as examined by means of a pig animal model in this research.
5. It has been demonstrated that the CT-DEI, CT-ABI, and extended-distance CT-PCI techniques have the capability for distinctly visualizing tissue constructs, various soft tissues, and hard tissues with detailed microstructural features, favorable for non-invasive assessment and monitoring applications of cartilage as well as other soft and hard tissues engineering repair.
6. Low dose imaging strategies including lower number of projection CT imaging, region of interest imaging, and low resolution imaging, have been developed and successfully adopted to the phase-based imaging techniques with reduced effective doses comparable to the dose for clinical X-ray scans, and without compromising the image quality.
7. Among the tested phase-based imaging techniques, CT-DEI exhibited the highest performance by maintaining a high image contrast and information at substantially low dose imaging settings. In other words, CT-DEI contrast mechanism allowed making the best use of reduced number of photons at low dose imaging, and, as such, is the most efficient method for substantially low-dose imaging in live animals.

6.2 Recommendation for future research

This research has shown the promising biological functionality and chondrogenic matrix production of the 3D hybrid constructs by means of the *in vitro* studies. It is suggested that these constructs be further implanted in animal models such as immunodeficient mice, for investigating the integrity of the construct and continuation of the cartilage tissue regeneration over long term *in vivo*. Moving forward with *in vivo* studies, upon obtaining successful results

from subcutaneous *in vivo* cartilage tissue growth in immunocompetent mice the functionality of the hybrid constructs can then be investigated for repairing damaged cartilage of load bearing, articular joints in larger animal models, such as pig and goat. Particularly, the effectiveness of the hybrid construct strategy over clinically-relevant long term *in vivo* period (such as 8-10 month) in large animal models is interesting to be probed in the future. Furthermore, with the capability of making customized, defect-matching shape constructs, the 3D hybrid construct bioprinting can be explored for repairing complex-shape defects from osteoarthritis in osteoarthritic animal models. It is noteworthy to mention that identifying the optimum implantation time of the hybrid constructs or the required *in vitro* culture time before *in vivo* implantation, is important to successful integration with host tissue and the maturation of newly regenerated tissue, and is recommended to be searched in the future.

The biocompatibility of the hybrid 3D bioprinting for incorporating viable cells during construct fabrication was demonstrated in this study, suggesting the potential for incorporating other biological components, such as bioactive molecules and growth factors, along with the cells during construct bioprinting. It would be interesting to explore the 3D hybrid bioprinting for localized and spatially designed deposition of bioactive molecules in the 3D construct to promote biomimetic, non-uniform cell differentiation (e.g. when mesenchymal stem cells are used), and/or ECM formation as seen in the natural cartilage or other spatially-organized tissues in the body. This is particularly suggested to be investigated for biomimetic cartilage tissue engineering where regenerating zonal structure of cartilage is important for natural-like functionality of the new tissue substitute. Designing and biofabricating hybrid constructs that have zonal cells and bioactive molecules distribution and/or zonal mechanical stimulation pattern (through zonal architectural designs) are suggested to be explored for biomimetic cartilage tissue engineering. To facilitate such biomimetic strategy, it is needed that the mechanical properties of the hybrid constructs after fabrication and following abandon cartilage matrix formation be investigated for constructs with different architectural designs, with or without mechanical stimulations during the culture time. Such comprehensive study will be very beneficial to the field and is suggested to be considered in the future research.

Although the developed hybrid biofabrication process used PCL, alginate and cartilage cells as the construct materials, the technique has the capability to use multiple dissimilar materials and cells for making complex, heterogeneous tissue constructs. Such potential is worth

examining for the regeneration of composite tissues and organs or tissue interfaces made of both soft and hard tissues. The developed 3D hybrid biorpinting technique used non-cross-linked, low concentration alginate, which is a hydrogel material commonly used in cartilage and soft tissue engineering applications. This fabrication method is, however, not limited to the alginate hydrogel and has the potential to be used with other soft, non-cross-linked hydrogel materials (e.g. hyalouronic acid, gelatin). Further exploration of this hybrid 3D bioprinting method with other hydrogel materials suitable for engineering other tissues is suggested for future research.

In this research, the synchrotron-based X-ray imaging techniques were shown to be promising methods for visualization and characterization of soft tissue scaffolds *in situ* in a dissected animal model joint. With the lower dose imaging strategies adopted with these techniques, future studies are recommended to investigate these non-invasive methods for scaffold and tissue regeneration assessments in live animal models during longitudinal *in vivo* studies. To identify how far non-invasive assessment methods could replace the conventional methods for cartilage and soft tissue engineering applications, the level of information that can be obtained from non-invasive imaging is urged to be compared with the information obtained from the conventional assessment methods.

This research focused mainly on the qualitative assessment aspects of scaffold imaging. However, the presented methods have great potential to be explored in the future for providing quantitative information on the scaffold material and the natural and regenerated cartilage tissue both *in situ* and *in vitro* (e.g. in culture plate or bioreactor). Evaluating the similarity of the regenerated cartilage tissue density to that of host healthy tissue *in vitro* and particularly *in vivo*, studying the degradation profile of tissue scaffolds, and regeneration profile of the newly formed tissue by time *in vivo* during long-term studies using the proposed non-invasive techniques will considerably improve cartilage tissue engineering strategies-through design of better materials and scaffolds- and improve the current knowledge-state of the tissue engineering repair. Future studies are encouraged to apply the presented imaging-based assessment methods to these research issues. The combination of non-invasive imaging-based assessments with other analyzing methods, such as finite element modeling, is interesting to be explored in order to generate more sophisticated evaluation methods such as tracking the change in biomechanical properties of scaffold *in situ* during the repair process.

By developing more accessible X-ray sources that can produce X-rays with essential synchrotron-X-ray properties, phase-based imaging technique could become more available to a wider range of researchers and clinicians in the field of tissue engineering and regenerative medicine to perform longitudinal non-invasive assessments. It is recommended that more accessible X-ray sources suitable for phase-based X-ray imaging be investigated and developed.

Appendix A

Video of 3D bioprinting process: 3D bioprinting process of creating cell-impregnated hybrid tissue constructs by co-deposition of PCL and cell-embedded alginate hydrogel.

Appendix B

Video of 3D synchrotron imaging: 3D volumetric visualization of tissue scaffold and soft tissues in a piglet joint *in situ* using computed tomography diffraction enhanced X-ray imaging (CT-DEI).